Passive Millimeter-Wave Retrieval of Global Precipitation Utilizing Satellites and a Numerical Weather Prediction Model

by

Chinnawat Surussavadee

B.Eng. Electrical Engineering
King Mongkut's Institute of Technology at Ladkrabang (1999)
M.S. Electric Power Engineering
Rensselaer Polytechnic Institute (2001)

Submitted to the Department of Electrical Engineering and Computer Science
in partial fulfillment of the requirements for the degree of

Doctor of Philosophy

at the

MASSACHUSETTS INSTITUTE OF TECHNOLOGY

November 2006

Author …………………………………………………………………………...
Department of Electrical Engineering and Computer Science
November 30, 2006

Certified by ……………………………………………………………………...
David H. Staelin
Professor of Electrical Engineering
Thesis Supervisor

Accepted by ……………………………………………………………………..
Arthur C. Smith
Chairman, Department Committee on Graduate Students

Passive Millimeter-Wave Retrieval of Global Precipitation Utilizing Satellites and a Numerical Weather Prediction Model

by

Chinnawat Surussavadee

Submitted to the Department of Electrical Engineering and Computer Science
on November 30, 2006, in partial fulfillment of the
requirements for the degree of
Doctor of Philosophy

Abstract

This thesis develops and validates the MM5/TBSCAT/F(λ) model, composed of a mesoscale numerical weather prediction (NWP) model (MM5), a two-stream radiative transfer model (TBSCAT), and electromagnetic models for icy hydrometeors (F(λ)), to be used as a global precipitation ground-truth for evaluating alternative millimeter-wave satellite designs and for developing methods for millimeter-wave precipitation retrieval and assimilation. The model's predicted millimeter-wave atmospheric radiances were found to statistically agree with those observed by satellite instruments [Advanced Microwave Sounding Unit-A/B (AMSU-A/B)] on the United States National Ocean and Atmospheric Administration NOAA-15, -16, and -17 satellites over 122 global representative storms. Whereas such radiance agreement was found to be sensitive to assumptions in MM5 and the radiative transfer model, precipitation retrieval accuracies predicted using the MM5/TBSCAT/F(λ) model were found to be robust to the assumptions. Appropriate specifications for geostationary microwave sounders and their precipitation retrieval accuracies were studied. It was found that a 1.2-m micro-scanned filled-aperture antenna operating at 118/166/183/380/425 GHz, which is relatively inexpensive, simple to build, technologically mature, and readily installed on a geostationary satellite, could provide useful observation of important global precipitation with ~20-km resolution every 15 minutes. AMSU global precipitation retrieval algorithms for retrieving surface precipitation rate, peak vertical wind, and water-paths for rainwater, snow, graupel, cloud water, cloud ice, and the sum of rainwater, snow, and graupel, over non-icy surfaces were developed separately using a statistical ensemble of global precipitation predicted by the MM5/TBSCAT/F(λ) model. Different algorithms were used for land and sea, where principal component analysis was used to attenuate unwanted noises, such as surface effects and angle dependence. The algorithms were found to perform reasonably well for all types of precipitation as evaluated against MM5 ground-truth. The algorithms also work over land with snow and sea ice, but with a strong risk of false detections. AMSU surface precipitation rates retrieved using the algorithm developed in this thesis reasonably agree with those retrieved for the Advanced Microwave Scanning Radiometer for the Earth Observing System (AMSR-E) aboard the Aqua satellite over both land and sea. Surface precipitation rates retrieved using the Advanced Microwave Sounding Unit (AMSU) aboard NOAA-15 and -16 satellites were further compared with four similar products derived from other systems that also observed the United States Great Plains (USGP) during the summer of 2004. These systems include AMSR-E aboard the Aqua satellite, the Special Sensor Microwave/Imager (SSM/I) aboard the Defense Meteorological Satellite Program (DMSP) F-13, -14, and -15 satellites, the passive Tropical Rainfall Measuring Mission (TRMM) Microwave Imager (TMI) aboard the TRMM satellite, and a surface precipitation rate product (NOWRAD), produced and marketed by Weather Services International Corporation (WSI) using observations from the Weather Surveillance Radar-1988 Doppler (WSR-88D) systems of the Next-Generation Weather Radar (NEXRAD) program. The results show the reasonable agreement among these surface precipitation rate products where the difference is mostly in the retrieval resolution, which depends on instruments' characteristics. A technique for assimilating precipitation information from observed millimeter-wave radiances to MM5 model was proposed. Preliminary study shows that wind and other correction techniques could help align observations at different times so that information from observed radiances is used at appropriate locations.

Thesis Supervisor: David H. Staelin
Title: Professor of Electrical Engineering

Acknowledgments

I would like to thank my thesis supervisor, Prof. David H. Staelin, for guiding me through my Ph.D. study. I am very lucky to have a chance to work with him in the Remote Sensing and Estimation Group (RSEG) at MIT. I consider him as an exceptional thesis supervisor. He is very nice, generous, supportive, hard-working, patient, enthusiastic, and creative. He is always available for his students even in the weekends or holidays. I sometimes call him at his home in weekends and holidays to ask questions about research, and he always enthusiastically gives great advice. He always has great suggestions and helps students to find ways to solve problems, not only academic problems but also any problems students have. He also taught me how to teach by allowing me to work as his teaching assistant in the MIT course 6.013. I am so grateful for all of his generous helps.

I would like to thank my parents, Gowit and Niramon Surussavadee, and my sister, Kamonrat (Pook) Surussavadee. They are the most important people in my life. "Everything and every success in my life could not be possible at all without endless love, great advice, and all strong support from my Dad and my Mom." They are always there for me. I am so lucky to have them as my parents. My Dad is very reasonable and always has the best advice. Every advice from him guides me to all accomplishments in my life. During my Ph.D. at MIT, he came from Thailand to stay with me to help me on everything. I really mean everything. For example, he helped me choose to work at RSEG. He came to the lab with me almost every night for ~2 years. My Mom is very reasonable and supportive. She always sends her endless love oversea to me. I am so grateful for everything they have been giving me.

I would like to thank my thesis readers, including Dr. Phil W. Rosenkranz for all helpful discussions about my research throughout my Ph.D. study and all helps with some of his computer programs especially TBSCAT and his cloud-liquid water retrieval program; Prof. Jin Au Kong for being the person who made me love electromagnetic theory and all of his valuable suggestions as my academic advisor, one of my research qualifying exam committee, and my thesis reader; and Prof. Dennis McLaughlin for co-authoring a paper on comparison of AMSU surface precipitation rate retrievals with those retrieved from other instruments presented in Chapter 8 of this thesis and for all of his valuable suggestions.

I would like to thank the Pennsylvania State University and the University Corporation for Atmospheric Research for providing us with MM5 and technical support, the Alliance for Computational Earth Science at MIT for assistance with computer resources, B. T. Draine and P. J. Flatau for making DDSCAT6.1 available, the National Center for Atmospheric Research for assistance with NCEP global tropospheric analyses, M. W. Shields for antenna pattern computations, A. J. Gasiewski, B. Bizzarri, and F. J. Solman, III for helpful discussions on geostationary microwave sounders, Ross Hoffman and Christopher Grassotti for providing us NOWRAD data set, David Flagg for providing us NOWRAD, SSM/I, and TMI data sets, Prof. Dara Entekhabi and Virat Chadarong for coauthoring a paper on comparison of AMSU surface precipitation rate retrievals with those retrieved from other instruments presented in Chapter 8 of this thesis, and the National Snow and Ice Data Center and the Remote Sensing Systems for making AMSR-E precipitation rate retrievals available.

I would like to thank the people of RSEG, including Seth Hall, Laura von Bosau, Scott Bressler, Choongyeun Chuck Cho, Siddhartan Govindasamy, Keith Herring, Danielle Hinton, Andrew Mui, Bill Blackwell, R. Vince Leslie, Fred W. Chen, Jack Holloway, Jessica Loparo, and Filip Antic, for all helpful discussions and their friendships. I would like to specifically thank Seth Hall for all dependable computer supports, Laura von Bosau for all administrative helps, and R. Vince Leslie and Fred W. Chen for their guides when I first joined RSEG.

My life at MIT has been more enjoyable because of having good friends. I would like to thank all Thai students at MIT (TSMIT) and Thai friends in Boston area, particularly Kittiwit Matan, Warit Wichakool, Ratchatee Techapiesancharoenkij, Watcharapan Suwansantisuk, and Watjana Lilaonitkul. I would like to thank Xudong Chen, who is my both good friend and good teaching assistant. I would also like to thank all members of my traditional Thai music and guitar bands, and all my tennis partners. I had great fun with all of you.

I would like to thank all financial sponsors for my graduate study, including the Royal Thai Government, who first gave me the opportunity to study aboard, NASA under Grant NAG5-13652 and Contract NAS5-31376, and NOAA under Contract DG133E-02-CN-0011.

Contents

List of Figures

List of Tables

Chapter 1

Introduction

Global monitoring of precipitation is important because of its significant human consequences. However, accurate global observations of precipitation using satellites have been impeded by lack of reliable global ground truth. Rain gauges, ground-based and satellite-borne radars, visible and infrared sensors, and various passive microwave sensors all have deficiencies. For example, rain inhomogeneities, wind, and the lack of good global coverage significantly degrade rain gauge measurements. Infrared satellite observations only see the tops of clouds, and almost all remote sensors respond to precipitation aloft, not that reaching the ground. Radar is expensive and global coverage is sparse. Both ground-based radars and passive microwave satellite sensors sense precipitation aloft and are generally unable to discern how much of that precipitation evaporates before impact. Both are also sensitive to unknown local hydrometeor size, form, and vertical velocity distributions, as are simple single-frequency radars on satellites. In addition, existing radar and satellite precipitation retrieval algorithms are largely based on error-prone backscattered signals and coincident rain gauge observations. The resulting lack of adequate ground truth seriously complicates development and validation of global precipitation sensing methods.

1.1 Problem Statement

This thesis is composed of 6 main studies; five out of six were documented in five separate manuscripts for publication [1]-[5]. First, to overcome the lack of accurate global ground truth, this thesis starts by developing and validating the use of the MM5/TBSCAT/F(λ) model composed of a Numerical Weather Prediction (NWP) Model, MM5 [6], a forward radiance program, TBSCAT [7], and electromagnetic scattering models (F(λ)) for icy hydrometeors aloft [1], as a rich new statistical form of ground truth for global precipitation. The MM5/TBSCAT/F(λ) model was validated by comparing its predicted brightness temperature distributions 50-191 GHz with those simultaneously observed by the Advanced Microwave Sounding Unit (AMSU) on operational NOAA-15, -16, and -17 satellites for a global set of 122 storms between 83N and 73S over a year between July 2002 and June 2003 [1]. Second, sensitivity of predicted radiances to assumptions in MM5 and the radiative transfer model, and the robustness of predicted retrieval accuracies of millimeter-wave instruments were studied [2]. Third, appropriate specifications for geostationary microwave satellites and their precipitation retrieval accuracies were studied [3]. Fourth, a new global precipitation retrieval algorithm for AMSU was developed by using information from the MM5/TBSCAT/F(λ) model as a global ground-truth [4]. AMSU surface precipitation rates retrieved using the algorithm developed in this thesis were compared to those retrieved from the Advanced Microwave Scanning Radiometer for the Earth Observing System (AMSR-E) aboard the Aqua satellite [8]-[9] over both land and sea. Fifth, AMSU surface precipitation rates retrieved using the algorithm developed in this thesis were compared to the surface precipitation rate product (NOWRAD) [10] that was retrieved by the Weather Services International (WSI) from the Weather Surveillance Radar-1988 Doppler (WSR-88D) systems of the Next-Generation Weather Radar (NEXRAD) program and to those retrieved for the Advanced Microwave Scanning Radiometer for the Earth Observing System (AMSR-E) aboard the Aqua satellite [9], the passive Tropical Rainfall Measuring Mission (TRMM) Microwave Imager (TMI) aboard the TRMM satellite [11], and the Special Sensor Microwave/Imager (SSM/I) aboard the Defense Meteorological Satellite Program (DMSP) F-13, -14, and -15 satellites [11], over the United States Great Plains from June to August of 2004 [5], where all observations are within the same 15-minute period. Sixth, this thesis also explores possibilities to assimilate satellite radiances into MM5 with the objective of improving the model forecasts so that they are close to satellite observations as possible. To help navigate this thesis, Table 1.1 lists important questions, short answers, and consequences of these 6 main studies appearing in chapters 4-10.

TABLE 1.1
IMPORTANT QUESTIONS, ANSWERS, AND CONSEQUENCES OF
RESULTS FROM CHAPTERS 4-10

Chapter	Question	Answer	Consequence
4	1. How well does MM5/TBSCAT/ F(λ) model match coincident satellite millimeter-wave observations?	1. Reasonably well for convective, stratiform, snow, and non-glaciated precipitation using the Goddard explicit cloud model, TBSCAT with two streams, and Mie scattering from spheres with ice densities F(λ) found using DDSCAT for graupel and snow	1. The MM5/TBSCAT/ F(λ) model could be used to simulate and evaluate alternative precipitation observation and retrieval concepts
5	1. How sensitive are the simulated radiances to assumptions in MM5, the radiative transfer model? 2. How well should millimeter-wave surface precipitation rate retrievals perform using AMSU, ATMS and GEostationary Microwave satellites (GEM)? 3. Are the predicted	1. Fairly sensitive 2. Reasonably well above ~1 mm/h 3. Not very sensitive	1. With the findings in Chapter 5, assumptions in the MM5/TBSCAT/F(λ) model and the MM5 prediction should be close to reality 2. MM5/TBSCAT/F(λ) model could be used as a global ground-truth for evaluating alternative millimeter-wave satellite designs and for developing methods for

	accuracies sensitive to imperfections of MM5, TBSCAT, and F(λ)?		retrieval and assimilation
6	1. What specifications for Geo-microwave sounders appear attractive? 2. How well should such Geo-microwave sounders perform? 3. Does image sharpening technique help for filled-aperture antennas?	1. 1.2-m micro-scanned filled-aperture antennas operating at 118/166/183/380/425 GHz 2. Reasonably well except cell tops below 2 km 3. Yes, especially for small and isolated precipitation	1. Simple, practical, technologically mature geo-microwave sounders could be implemented 2. Geo-microwave sounders could provide useful continuous mapping of important global precipitation at ~15 minute intervals 3. Image sharpening technique can increase resolution for filled-aperture antennas and help capture small and isolated precipitation
7	1. How good is the retrieval accuracy using the new algorithm AMSU? 2. How do AMSU precipitation rate retrievals compare to those of AMSR-E?	1. Reasonably good above ~1 mm/h (better for stratiform, worse for convective rain) 2. Reasonably well	1. The newly developed AMSU surface precipitation retrieval algorithm could be used operationally with reasonable accuracy
8	1. How do AMSU precipitation rate retrievals compare to those of other instruments over land?	1. Reasonably well	1. This emphasizes that the newly developed AMSU surface precipitation retrieval algorithm could be used operationally
9	1. What are the difficulties in assimilating brightness temperatures into MM5?	1. Rapid evolution, translation, and evaporation of precipitation 2. Very large number of atmospheric variables	1. Wind and other correction techniques could help align observations at different times 2. Projected-principal component analysis

		compared to number degrees of freedom in satellite radiance observations	could help find key degrees of freedom that should be adjusted

1.2 Prior Work

This thesis constitutes 6 main studies appearing in Chapters 4-9. Prior work for each main study is described in the introductions to these chapters.

1.3 Thesis Outline

Chapter 2 addresses background that helps understand this thesis, including thermal radiation, microwave interaction with atmospheric constituents, radiative transfer equation, image sharpening, aperture antennas, principal component analysis, neural network, and descriptions for AMSU. Chapter 3 addresses details about MM5 model and globally representative storm systems used in this thesis.

Chapters 4-9 address 6 main studies and were written in order of how this thesis has evolved. All results presented in Chapters 4-8 are from [1]-[5], respectively. Chapter 4 validates the MM5/TBSCAT/F(λ) model against AMSU observations. Chapter 5 addresses the sensitivity of predicted radiances to assumptions in MM5 and the radiative transfer model, and the robustness of predicted retrieval accuracies of millimeter-wave instruments. Chapter 6 addresses appropriate specifications for geostationary microwave sounders and their precipitation retrieval accuracies. Chapter 7 addresses the development of a new global precipitation retrieval algorithm for AMSU by using information from the MM5/TBSCAT/F(λ) model as a global ground-truth. Chapter 8 compares AMSU surface precipitation rates retrieved using the new algorithm developed in this thesis with those retrieved by other radar and microwave instruments. Chapter 9 presents the idea, difficult issues, and preliminary results for assimilating satellite radiances into MM5 with the objective of improving the model forecasts. Chapter 10 summarizes and concludes the thesis.

Chapter 2

Background

2.1 Thermal Radiation

The solar electromagnetic radiation is the main source of energy in the planet. From thermodynamic principles, absorbed electromagnetic energy by a material medium will be transformed to thermal energy that produces a rise in the temperature of the material. Hence, a substance has to radiate the same thermal energy it absorbs in order to have a finite absolute temperature. This process is called thermal emission.

A blackbody is ideally defined as a material that absorbs all the incident radiation at all frequencies without any reflection and is thus also a perfect emitter. From Planck's radiation law, a blackbody radiates uniformly in all directions with an intensity of

$$I_{bb}(f,\theta,\phi) = \frac{2hf^3}{c^2}\left(\frac{1}{e^{hf/kT}-1}\right) \quad [\mathrm{Wm^{-2}sr^{-1}Hz^{-1}}] \tag{2.1}$$

where $I_{bb}(f,\theta,\phi)$ = blackbody radiation intensity [$\mathrm{Wm^{-2}sr^{-1}Hz^{-1}}$]
h = Planck's constant = 6.63×10^{-34} [J]
f = frequency [Hz]
k = Boltzmann's constant = 1.38×10^{-23} [$\mathrm{JK^{-1}}$]
T = physical temperature [K]
c = velocity of light = 3×10^{8} [$\mathrm{ms^{-1}}$]

The factor of two in the numerator of (2.1) accounts for both polarizations. In the Rayleigh-Jeans limit where $hf/kT << 1$, (2.1) is reduced to

$$I_{bb}(f,\theta,\phi) \cong \frac{2kT}{\lambda^2} \qquad [\mathrm{Wm^{-2}sr^{-1}Hz^{-1}}] \tag{2.2}$$

Hence, the intensity, $I_{bb}(f,\theta,\phi)$, is directly proportional to absolute temperature in the microwave region. The brightness of a blackbody having a temperature T over a narrow frequency bandwidth Δf centered at a frequency f is

$$B_{bb}(\theta,\phi) = I_{bb}(f,\theta,\phi)\Delta f = \frac{2kT}{\lambda^2}\Delta f \qquad [\mathrm{Wm^{-2}sr^{-1}}] \tag{2.3}$$

Real materials, called grey bodies, reflect some incident energy and hence emit less than a blackbody does. The brightness temperature, $T_B(\theta,\phi)$ [K], for a homogeneous material having a uniform physical temperature of T is defined as

$$B(\theta,\phi) = \frac{2k}{\lambda^2} T_B(\theta,\phi)\Delta f \qquad [\mathrm{Wm^{-2}sr^{-1}}] \tag{2.4}$$

Or

$$T_B(\theta,\phi) = \frac{\lambda^2}{2k} I(\theta,\phi) \tag{2.5}$$

and the emissivity, $\varepsilon(\theta,\phi)$, is defined as

$$\varepsilon(\theta,\phi) = \frac{B(\theta,\phi)}{B_{bb}} = \frac{T_B(\theta,\phi)}{T} \tag{2.6}$$

where $B(\theta,\phi) \le B_{bb}$ and thus, $0 \le \varepsilon(\theta,\phi) \le 1$ and $T_B(\theta,\phi) \le T$. The reflectivity, $R(\theta,\phi)$, is the fraction of incident power reflected from the object. Hence, from conservation of energy principles, $R(\theta,\phi) + \varepsilon(\theta,\phi) = 1$.

2.2 Microwave Interaction with Atmospheric Constituents

The interaction between electromagnetic wave and atmospheric constituents could be divided into two main categories, including absorption and emission by atmospheric gases, and extinction and emission by hydrometeors.

2.2.1 Absorption and Emission by Gases

In the microwave spectrum, oxygen and water vapor are the only constituents of the various gases in the earth's atmosphere that exhibit significant absorption bands below the stratopause. The oxygen molecule has absorption bands in the vicinity of 54, 118, and 425 GHz among others. Water vapor has absorption bands in the vicinity of 22, 183, and 380 GHz among others. Fig. 2.1 shows zenith opacity for the microwave spectrum for a ground-based zenith-observing radiometer in the clear sky situation. The opacity of the atmosphere, τ_θ, is the optical depth of the entire atmosphere along a path at a zenith angle θ, and is defined as

$$\tau_\theta = \int_0^\infty \alpha_e(z) \sec\theta dz \tag{2.7}$$

where $\alpha_e(z)$ is the extinction coefficient. Fig. 2.1 shows the opacity spikes around the oxygen and water vapor absorption bands, and the spectral coverage for microwave instruments. Hence, satellite-borne radiometers having frequency channels observing at these frequencies would sense high in the atmosphere. These channels are called opaque channels. On the other hand, those observing at frequencies far away from these frequencies would be sensitive to the surface and are called window channels. Temperature and water vapor profiles are strongly correlated with precipitation. The Advanced Microwave Sounding Unit (AMSU) observed primarily near the 54-GHz oxygen band and the 183-GHz water vapor band.

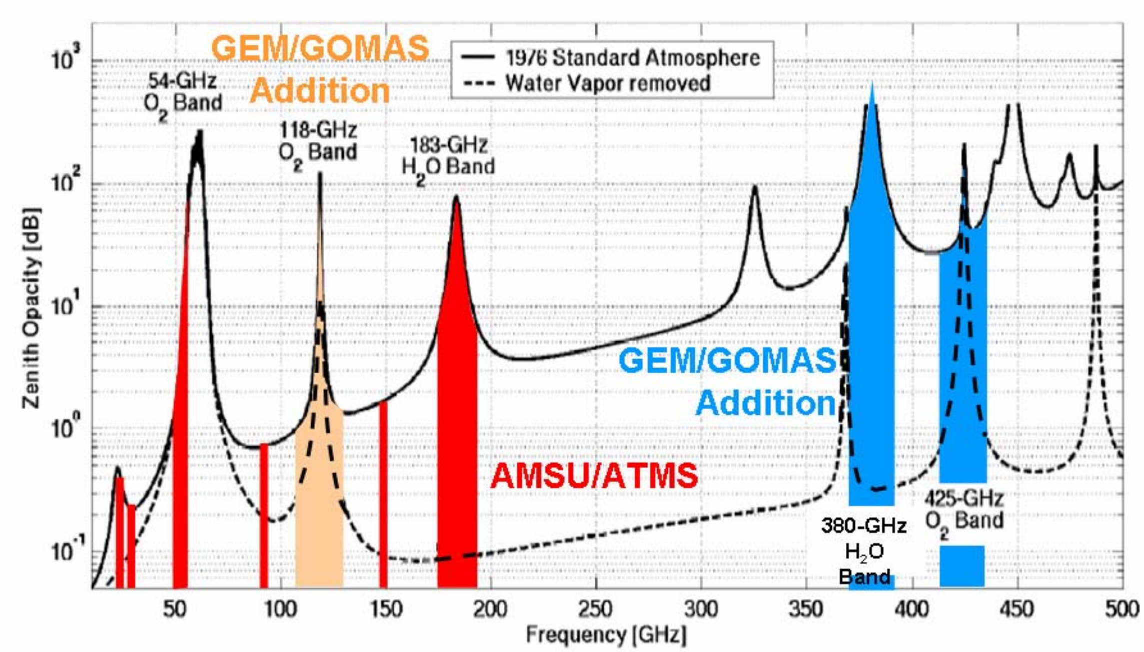

Fig. 2.1. Zenith opacity for the microwave spectrum for a ground-based zenith-observing radiometer in the clear sky situation and spectral coverage for microwave instruments.

2.2.2 Extinction and Emission by Clouds and Hydrometeors

Hydrometeors are liquid or frozen water particles either suspended or falling in the atmosphere, including rain water, cloud liquid water, cloud ice, snow, and hail/graupel, for example. Consider an electromagnetic wave with the power density S_i [Wm^{-2}] that propagates in the atmosphere and is incident upon a suspended material particle of geometrical cross-sectional area A. The particle could be a rain drop, snow, graupel/hail, or a cloud ice particle, for example. Some part of the energy will get absorbed by the particle and some will be scattered in all directions. The absorption cross-section Q_a is the ratio of absorbed power P_a to incident power density S_i:

$$Q_a = \frac{P_a}{S_i} \qquad [\mathrm{m}^2] \tag{2.8}$$

and the absorption efficiency factor ξ_a is the ratio of Q_a to the physical cross-section A, which is

$$\xi_a = \frac{Q_a}{\pi r^2} \tag{2.9}$$

for a spherical particle of radius r, $A = \pi r^2$. The scattering cross-section Q_s and the scattering efficiency factor ξ_s are similarly defined as

$$Q_s = \frac{P_s}{S_i} \qquad [\mathrm{m}^2] \tag{2.10}$$

$$\xi_s = \frac{Q_s}{\pi r^2} \tag{2.11}$$

where P_s is the total power scattered by the particle.

The total power removed from the incident wave is $P_a + P_s$, and the corresponding extinction cross-section Q_e and efficiency ξ_e are

$$Q_e = Q_a + Q_s \qquad [\mathrm{m}^2] \tag{2.12}$$

$$\xi_e = \xi_a + \xi_s \tag{2.13}$$

The scattering and absorption of electromagnetic waves by a dielectric sphere of arbitrary radius r could be solved by Mie's theory [12] using an iterative computational procedure [13]. Rayleigh approximations could be used when the particle size is much smaller than the wavelength of the incident wave. The scattering and absorption of electromagnetic waves by arbitrary shapes could be approximated using the Discrete-Dipole Approximation method [14], which is described later in Section 4.3.1. These cross-sections are functions of mass, size, frequency, dielectric permittivity, shape, orientation, and polarization. Dielectric permittivity is a function of temperature and frequency and is computed using [15] and [16] for water and ice, respectively.

Consider a volume of rain or ice where particles are randomly distributed so that there are no coherent phase relationships between fields scattered by these particles. The total scattering cross-section of a given volume is thus equal to the sum of the scattering cross-sections of all particles contained in the volume. The scattering coefficient is equal to

$$\alpha_s = \int_{r_1}^{r_2} p(r) Q_s(r) dr \qquad [\text{Np m}^{-1}] \tag{2.14}$$

where $p(r)$ is the drop-size distribution describing number of particles having different drop radii, r [m], in the volume. Similarly, absorption (α_a) and extinction (α_e) coefficients are, respectively

$$\alpha_a = \int_{r_1}^{r_2} p(r) Q_a(r) dr \qquad [\text{Np m}^{-1}] \tag{2.15}$$

and

$$\alpha_e = \int_{r_1}^{r_2} p(r) Q_e(r) dr \qquad [\text{Np m}^{-1}] \tag{2.16}$$

2.2.3 Dielectric Constant of Ice and Ice Factor (F(λ))

Snow and graupel are heterogeneous materials composed of ice and air. In an attempt to reproduce an approximate electromagnetic description of these materials, a mixing rule [17]-[18] is used to compute the effective permittivity. The effective permittivity of a random medium, ε_{eff}, is defined as:

$$\overline{D} = \varepsilon_{eff} \overline{E} \tag{2.17}$$

where $\overline{D}$ = average displacement
$\overline{E}$ = average electric field
with the limitation that the inhomogeneity has to be smaller scale than the wavelength.

The effective permittivity of a random medium, ε_{eff}, is characterized by the ice factor, F(λ), which is a fractional volume of ice in an air matrix. Since the density of ice is ~1 [g cm^{-3}], ice factor is an inherent density of the heterogeneous mixture. For a given mass, it gives the volume of the mixture.

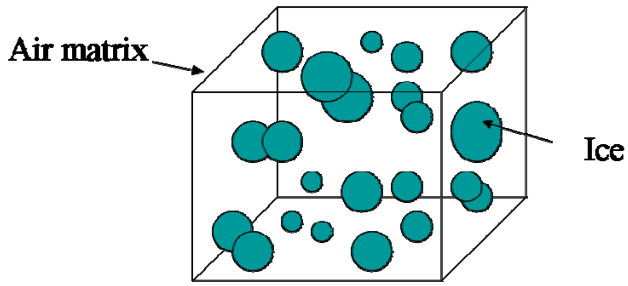

Fig. 2.2. A mixture model for icy hydrometeors.

Equations (13) and (14) in [17] were used to compute the effective permittivity for a mixture of air and ice, and υ was from equation (22) in [18], where spherical ices with complex permittivity $\varepsilon_1 = \varepsilon_1^{'} - j\varepsilon_1^{''}$ are inclusions occupying a volume fraction F(λ), and air with permittivity ε_0 is the background material, as Fig. 2.2 shows. If the losses of the inclusions are small and the background material is lossless, the real and imaginary parts of the effective permittivity $\varepsilon_{eff} = \varepsilon_{eff}^{'} - j\varepsilon_{eff}^{''}$ can be solved approximately as:

$$\varepsilon_{eff}^{'} = \frac{\sqrt{b^2 + 4\upsilon c} - b}{2\upsilon} \tag{2.18}$$

where

$$b = \varepsilon_1^{'} + 2\varepsilon_0 - 2\upsilon\varepsilon_0 - F(\lambda)(\varepsilon_1^{'} - \varepsilon_0)(1+\upsilon) \tag{2.19}$$

$$c = \varepsilon_0[\varepsilon_1^{'} + (2-\upsilon)\varepsilon_0 + F(\lambda)(2-\upsilon)(\varepsilon_1^{'} - \varepsilon_0)] \tag{2.20}$$

$$\varepsilon_{eff}^{''} = \varepsilon_1^{''} \cdot \frac{-(\varepsilon_{eff}^{'} - \varepsilon_0) + F(\lambda)[\varepsilon_{eff}^{'} + 2\varepsilon_0 + \upsilon(\varepsilon_{eff}^{'} - \varepsilon_0)]}{[\varepsilon_1^{'} + 2\varepsilon_0 + 2\upsilon(\varepsilon_{eff}^{'} - \varepsilon_0)] - F(\lambda)(1+\upsilon)(\varepsilon_1^{'} - \varepsilon_0)} \tag{2.21}$$

It is interesting to consider two extremes. First, $F(\lambda) = 0$ means that the mixture is purely air without ice. ε_{eff} has to be equal to ε_0. Second, $F(\lambda) = 1$ means the mixture is purely ice without air. ε_{eff} has to be equal to $\varepsilon_1 = \varepsilon_1^{'} - j\varepsilon_1^{''}$. Let us consider these two extremes in detail.

When $F(\lambda) = 0$,

From, (2.19) $$b = \varepsilon_1^{'} + 2\varepsilon_0 - 2\upsilon\varepsilon_0 \tag{2.22}$$

From, (2.20) $$c = \varepsilon_0\varepsilon_1^{'} + (2-\upsilon)\varepsilon_0^{\;2} \tag{2.23}$$

$$b^2 = [\varepsilon_1^{'} + 2\varepsilon_0 - 2\upsilon\varepsilon_0]^2 = \varepsilon_1^{'2} + 4\varepsilon_0\varepsilon_1^{'} - 4\upsilon\varepsilon_0\varepsilon_1^{'} - 8\upsilon\varepsilon_0^{\;2} + 4\varepsilon_0^{\;2} + 4\upsilon^2\varepsilon_0^{\;2} \tag{2.24}$$

$$4\upsilon c = 4\upsilon\varepsilon_0\varepsilon_1^{'} + 8\upsilon\varepsilon_0^{\;2} - 4\upsilon^2\varepsilon_0^{\;2} \tag{2.25}$$

$$b^2 + 4\upsilon c = \varepsilon_1^{'2} + 4\varepsilon_0\varepsilon_1^{'} + 4\varepsilon_0^{\;2} = (\varepsilon_1^{'} + 2\varepsilon_0)^2 \tag{2.26}$$

$$\sqrt{b^2 + 4\upsilon c} = \varepsilon_1^{'} + 2\varepsilon_0 \quad (2.27)$$

$$\varepsilon_{eff}^{'} = \frac{\sqrt{b^2 + 4\upsilon c} - b}{2\upsilon} = \frac{2\upsilon\varepsilon_0}{2\upsilon} = \varepsilon_0 \quad (2.28)$$

From (2.21),

$$\varepsilon_{eff}^{''} = \varepsilon_1^{''} \cdot \frac{-(\varepsilon_{eff}^{'} - \varepsilon_0)}{[\varepsilon_1^{'} + 2\varepsilon_0 + 2\upsilon(\varepsilon_{eff}^{'} - \varepsilon_0)]} \quad (2.29)$$

Substitute (2.28) in (2.29), $\varepsilon_{eff}^{''} = 0$. Hence, when $F(\lambda) = 0$, $\varepsilon_{eff} = \varepsilon_0$ as it should be.

When $F(\lambda) = 1$,

From (2.19),

$$b = \varepsilon_1^{'} + 2\varepsilon_0 - 2\upsilon\varepsilon_0 - (\varepsilon_1^{'} - \varepsilon_0)(1 + \upsilon) \quad (2.30)$$

$$= \varepsilon_1^{'} + 2\varepsilon_0 - 2\upsilon\varepsilon_0 - \varepsilon_1^{'} - \varepsilon_1^{'}\upsilon + \varepsilon_0 + \varepsilon_0\upsilon \quad (2.31)$$

$$= 3\varepsilon_0 - \varepsilon_0\upsilon - \varepsilon_1^{'}\upsilon \quad (2.32)$$

$$b^2 = (3\varepsilon_0 - \varepsilon_0\upsilon - \varepsilon_1^{'}\upsilon)^2 \quad (2.33)$$

$$= 9\varepsilon_0^{\ 2} - 6\varepsilon_0^{\ 2}\upsilon - 6\varepsilon_0\varepsilon_1^{'}\upsilon + 2\varepsilon_0\varepsilon_1^{'}\upsilon^2 + \varepsilon_0^{\ 2}\upsilon^2 + \varepsilon_1^{'2}\upsilon^2 \quad (2.34)$$

From (2.20),

$$c = \varepsilon_0[\varepsilon_1^{'} + 2\varepsilon_0 - \upsilon\varepsilon_0 + 2\varepsilon_1^{'} - 2\varepsilon_0 - \upsilon\varepsilon_1^{'} + \upsilon\varepsilon_0] \quad (2.35)$$

$$= \varepsilon_0[3\varepsilon_1^{'} - \upsilon\varepsilon_1^{'}] = 3\varepsilon_0\varepsilon_1^{'} - \upsilon\varepsilon_0\varepsilon_1^{'} \quad (2.36)$$

$$4\upsilon c = 12\upsilon\varepsilon_0\varepsilon_1^{'} - 4\upsilon^2\varepsilon_0\varepsilon_1^{'} \quad (2.37)$$

$$b^2 + 4\upsilon c = 9\varepsilon_0^{\ 2} - 6\varepsilon_0^{\ 2}\upsilon + 6\upsilon\varepsilon_0\varepsilon_1^{'} - 2\upsilon^2\varepsilon_0\varepsilon_1^{'} + \varepsilon_0^{\ 2}\upsilon^2 + \varepsilon_1^{'2}\upsilon^2 = (3\varepsilon_0 - \varepsilon_0\upsilon + \varepsilon_1^{'}\upsilon)^2 \quad (2.38)$$

$$\sqrt{b^2 + 4\upsilon c} = 3\varepsilon_0 - \varepsilon_0\upsilon + \varepsilon_1^{'}\upsilon \quad (2.39)$$

$$\varepsilon_{eff}^{'} = \frac{\sqrt{b^2 + 4\upsilon c} - b}{2\upsilon} = \frac{2\varepsilon_1^{'}\upsilon}{2\upsilon} = \varepsilon_1^{'} \quad (2.40)$$

From (2.21),

$$\varepsilon_{eff}^{''} = \varepsilon_1^{''} \cdot \frac{-\varepsilon_{eff}^{'} + \varepsilon_0 + \varepsilon_{eff}^{'} + 2\varepsilon_0 + \upsilon\varepsilon_{eff}^{'} - \upsilon\varepsilon_0}{\varepsilon_1^{'} + 2\varepsilon_0 + 2\upsilon\varepsilon_{eff}^{'} - 2\upsilon\varepsilon_0 - \varepsilon_1^{'} + \varepsilon_0 - \upsilon\varepsilon_1^{'} + \upsilon\varepsilon_0} \quad (2.41)$$

$$= \varepsilon_1^{''} \cdot \frac{3\varepsilon_0 + \upsilon\varepsilon_{eff}^{'} - \upsilon\varepsilon_0}{3\varepsilon_0 + 2\upsilon\varepsilon_{eff}^{'} - \upsilon\varepsilon_1^{'} - \upsilon\varepsilon_0} \quad (2.42)$$

Substitute (2.40) in (2.42), $\varepsilon_{eff}^{''} = \varepsilon_1^{''}$. Hence, when $F(\lambda) = 1$, $\varepsilon_{eff} = \varepsilon_1$ as it should be.

2.3 Radiative Transfer Equation

Radiative transfer is the equation describing the flow of radiant energy to be measured by a radiometer. In the non-scattering atmosphere, contributions to observed brightness temperature at the top of the atmosphere are from four components [19]

$$T_B = RT_c e^{-2\tau_o} + \mathrm{R}e^{-\tau_o}\int_0^L T(z)\alpha_a(z)e^{-\int_0^z \alpha_a(z)dz}dz + \varepsilon T_s e^{-\tau_o} + \int_0^L T(z)\alpha_a(z)e^{-\int_z^L \alpha_a(z)dz}dz \text{ [K]} \quad (2.43)$$

, as Fig. 2.3 shows, where $\tau(z) = \int_z^L \alpha_a(z)dz$ is the optical depth, and $\alpha_a(z)$ is the absorption coefficient [Np m^{-1}]. The first term is the contribution from the sky brightness, T_c, propagating downward and reflecting from the ground back to the top of the atmosphere. Energy is attenuated twice by the atmosphere ($e^{-2\tau_o}$). The second term corresponds to radiation emitting downward by the atmosphere and then reflected back upward by the surface. The third term is the energy radiated from the surface, which is equal to the surface emissivity ε times the ground temperature T_s, attenuated once by $e^{-\tau_o}$. The fourth term is the direct emission by the atmosphere. The surface reflectivity R is equal to $1-\varepsilon$.

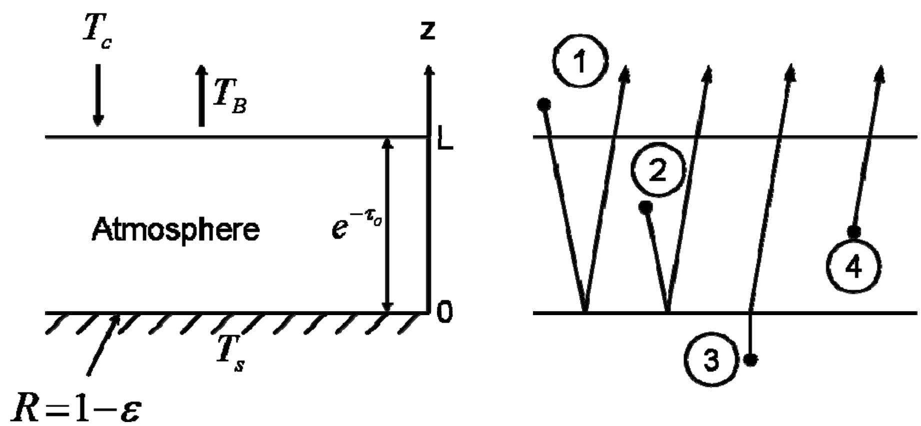

Fig. 2.3. Geometry for observed radiation, including reflected components [19].

Radiometers operating in the 50-60 GHz oxygen band are used to derive temperature profiles in clear and cloudy atmospheres. Measurements around the 22-GHz water-vapor line are used to obtain column water abundance and the measurements around the 183-GHz water vapor line are used to obtain humidity profiles. To see effect of temperature and water vapor profiles on observed brightness temperatures, assume the surface reflectivity $R = 0$ for simplicity. (2.43) is reduced to

$$T_B = \varepsilon T_s e^{-\tau_o} + \int_0^L T(z)\alpha_a(z)e^{-\int_z^L \alpha_a(z)dz}dz = \varepsilon T_s e^{-\tau_o} + \int_0^L T(z)W(f,z)dz \quad (2.44)$$

where $W(f,z) = \int_0^L \alpha_a(z)e^{-\int_z^L \alpha_a(z)dz}dz$ is called the weighting function.

Consider a more general situation involving scattering. Since clouds and rain cells have horizontally large scales compared to their vertical scale, a plane-parallel atmosphere is often useful for computing brightness temperatures. Fig. 2.4 shows the geometry for a plane-parallel atmosphere. Three processes are involved in the change in intensity, I, as it propagates through a layer of atmosphere. The first, second, and third terms are due to attenuation by extinction, multiple scattering, and emission from the layer, respectively. The general equation of radiative transfer for plane-parallel atmospheres is

$$\frac{dI(z;\mu,\phi)}{dz/\mu} = -\alpha_e I(z;\mu,\phi) + \alpha_s \int_0^{2\pi}\int_{-1}^{1} I(z;\mu',\phi') \frac{P(\mu,\phi,\mu',\phi')}{4\pi} d\mu' d\phi' + \alpha_a B[T(z)] \quad (2.45)$$

where $\mu = \cos\theta$, ϕ is the azimuthal coordinate, α_a, α_s, and α_e are the absorption, scattering, and extinction coefficients, respectively, and $P(\mu,\phi,\mu',\phi')$ is the phase function denoting the redirection of the incoming intensity defined by (μ',ϕ') to the outgoing intensity defined by (μ,ϕ). Define the single-scattering albedo $\omega = \frac{\alpha_s}{\alpha_e}$ or $1-\omega = \frac{\alpha_a}{\alpha_e}$ and the optical depth $\tau = \int_z^{\infty} \alpha_e dz'$ or $d\tau = -\alpha_e dz$. (2.45) becomes

$$\mu\frac{dI(z;\mu,\phi)}{\alpha_e dz} = -I(z;\mu,\phi) + \frac{\omega}{4\pi}\int_0^{2\pi}\int_{-1}^{1} I(z;\mu',\phi')P(\mu,\phi,\mu',\phi')d\mu' d\phi' + (1-\omega)B[T(z)] \quad (2.46)$$

$$-\mu\frac{dI(\tau;\mu,\phi)}{d\tau} = -I(\tau;\mu,\phi) + \frac{\omega}{4\pi}\int_0^{2\pi}\int_{-1}^{1} I(\tau;\mu',\phi')P(\mu,\phi,\mu',\phi')d\mu' d\phi' + (1-\omega)B[T(\tau)] \quad (2.47)$$

$$-\mu\frac{dT_B(\tau;\mu,\phi)}{d\tau} = -T_B(\tau;\mu,\phi) + \frac{\omega}{4\pi}\int_0^{2\pi}\int_{-1}^{1} T_B(\tau;\mu',\phi')P(\mu,\phi,\mu',\phi')d\mu' d\phi' + (1-\omega)T(\tau) \quad (2.48)$$

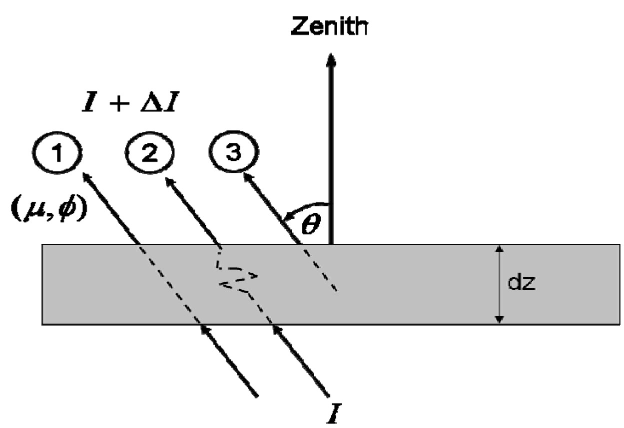

Fig. 2.4. Geometry for plane parallel atmosphere.

2.3.1 Method of Successive Orders of Scattering

(2.48) can be solved many ways [20]. The successive orders of scattering method is very intuitive and gives good physical understanding. Number of times that photons scatter and contributions of each scattering time to the total brightness temperature for a given atmospheric profile could be computed. Since (2.48) is linear, superposition can be applied, that is,

$$T(\tau;\mu,\phi) = T(\tau;\mu,\phi,0th) + T(\tau;\mu,\phi,1st) + T(\tau;\mu,\phi,2nd) + ... \tag{2.49}$$

where $T(\tau;\mu,\phi,0th)$, $T(\tau;\mu,\phi,1st)$, $T(\tau;\mu,\phi,2nd)$ are brightness temperature components from no scattering, scattering once, and scattering twice, respectively. From (2.48), the zeroth-order scattering component, $T(\tau;\mu,\phi,0th)$, is

$$-\frac{dT(\tau;\mu,\phi,0th)}{d\tau} = -T(\tau;\mu,\phi,0th) + (1-\omega)T(\tau) \tag{2.50}$$

Multiply both sides by $e^{-\tau}$ and integrate over thickness dz from τ to τ_1 leading to

$$\int_{\tau}^{\tau_1}\left\{-\frac{dT(\tau;\mu,\phi,0th)}{d\tau}e^{-\tau}\right\}d\tau = \int_{\tau}^{\tau_1}\left\{-T(\tau;\mu,\phi,0th)e^{-\tau} + (1-\omega)T(\tau)e^{-\tau}\right\}d\tau \tag{2.51}$$

From $-\dfrac{d\left(T(\tau;\mu,\phi,0th)e^{-\tau}\right)}{d\tau} = Te^{-\tau} - e^{-\tau}\dfrac{dT(\tau;\mu,\phi,0th)}{d\tau}$, (2.51) becomes

$$-\int_{\tau}^{\tau_1}\frac{d\left(T(\tau;\mu,\phi,0th)e^{-\tau}\right)}{d\tau} = \int_{\tau}^{\tau_1}(1-\omega)T(\tau)e^{-\tau}d\tau \tag{2.52}$$

Consider a slab with an equilibrium temperature T_1 and optical depth τ_1. (2.52) becomes

$$T(0;\mu,\phi,0th) - T(\tau_1;\mu,\phi,0th)e^{-\tau_1} = (1-\omega)T_1(1-e^{-\tau_1}) \tag{2.53}$$

Hence, we have

$$T(0;\mu,\phi,0th) = T(\tau_1;\mu,\phi,0th)e^{-\tau_1} + (1-\omega)T_1(1-e^{-\tau_1}) \tag{2.54}$$

The successive order method is very intuitive and is best illustrated by a simple example. Fig. 2.5 shows a simple atmospheric model composed of 2 layers. Let us compute observed brightness temperature at the top of the atmosphere. Left of the 1st layer is the ground, and right of the 2nd layer is the sky. Assume α_a = 0.01, α_s = 0.09, and Δz = 1 km for both layers. Hence, α_e = 0.1 and $\Delta\tau$ = 0.1. Consider two-stream, forward and backward, situation with asymmetry g = 0.5 for both layers and assume I is independent of azimuthal coordinate. In the two-stream situation, fractions of power scattering forward and backward are equal to $0.5(1+g)$ and $0.5(1-g)$, respectively. Calculations below show how the method of successive orders of scattering works.

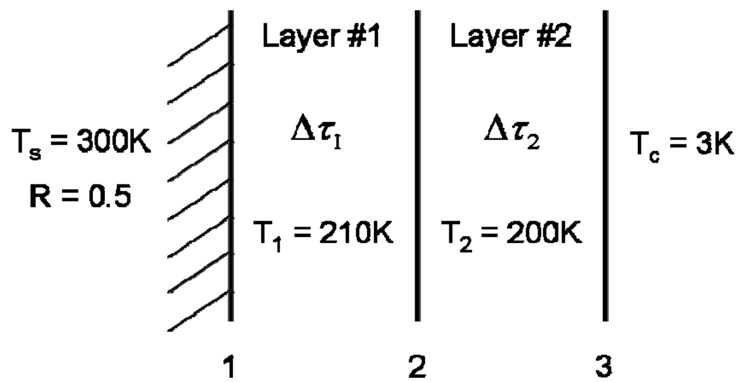

Fig. 2.5. Geometry for SOS example (1).

Step 1: compute zeroth-order brightness temperatures at boundaries as power propagates downward from the top of the atmosphere.

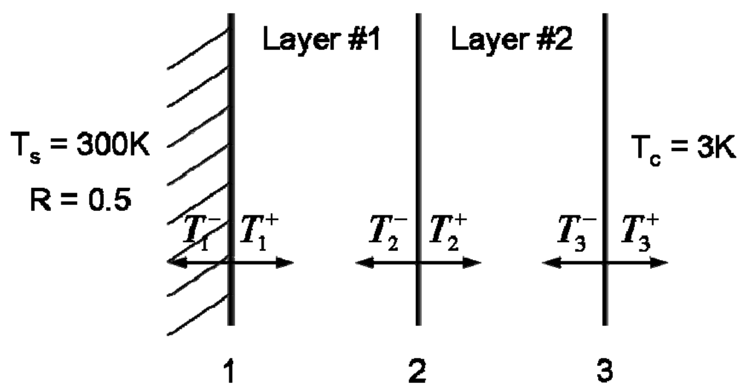

Fig. 2.6. Geometry for SOS example (2).

Apply (2.54), we have

$T_3^-(0th) = 3$

$T_2^-(0th) = 3e^{-0.1} + 200(1-0.9)(1-e^{-0.1}) = 4.6178$

$T_1^-(0th) = 4.6178e^{-0.1} + 210(1-0.9)(1-e^{-0.1}) = 6.1768$

$T_1^+(0th) = 6.1768 \cdot 0.5 + 300(1-0.5) = 153.0884$

$T_2^+(0th) = 153.0884e^{-0.1} + 210(1-0.9)(1-e^{-0.1}) = 140.5185$

$T_3^+(0th) = 140.5185e^{-0.1} + 200(1-0.9)(1-e^{-0.1}) = 129.0496$

where these components are illustrated in Fig. 2.6.

Step 2: compute intensity lost from 1st scattering in both layers.

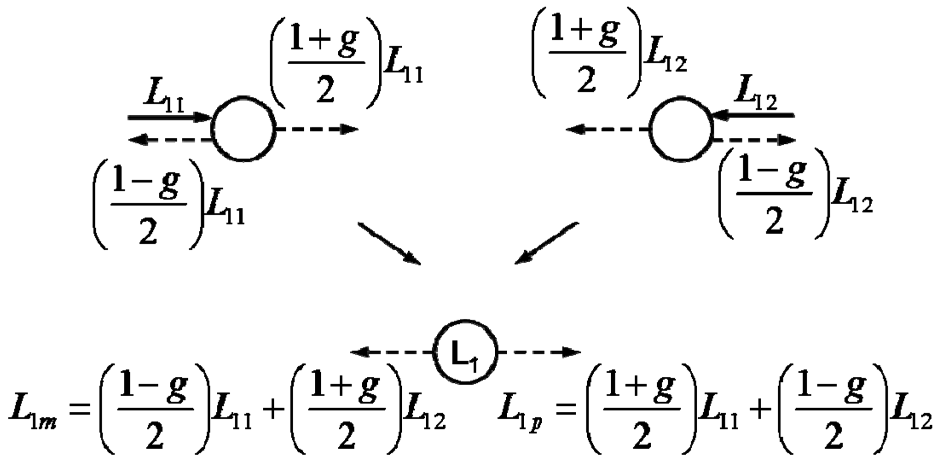

Fig. 2.7. Geometry for SOS example (3).

Layer #1:

$$L_{11}(0th) = T_1^+(0th)(1-e^{-\alpha_{s1}dz}) = 153.0884(1-e^{-0.09}) = 13.1761$$
$$L_{12}(0th) = T_2^-(0th)(1-e^{-\alpha_{s1}dz}) = 4.6178(1-e^{-0.09}) = 0.3974$$
$$L_{1p}(0th) = \left(\frac{1+g}{2}\right)L_{11} + \left(\frac{1-g}{2}\right)L_{12} = 9.9814$$
$$L_{1m}(0th) = \left(\frac{1-g}{2}\right)L_{11} + \left(\frac{1+g}{2}\right)L_{12} = 3.5921$$

where L_{11} and L_{12} are scattering losts due to propagation of $T_1^+(0th)$ and $T_2^-(0th)$ through the atmospheric layer #1, respectively. $L_{1p}(0th)$ and $L_{1m}(0th)$ are illustrated in Fig. 2.7.

Similarly, Layer #2:

$$L_{21}(0th) = T_2^+(0th)(1-e^{-\alpha_{s2}dz}) = 140.5185(1-e^{-0.09}) = 12.0943$$
$$L_{22}(0th) = T_3^-(0th)(1-e^{-\alpha_{s2}dz}) = 3(1-e^{-0.09}) = 0.2582$$
$$L_{2p}(0th) = \left(\frac{1+g}{2}\right)L_{21} + \left(\frac{1-g}{2}\right)L_{22} = 9.1353$$
$$L_{2m}(0th) = \left(\frac{1-g}{2}\right)L_{21} + \left(\frac{1+g}{2}\right)L_{22} = 3.2172$$

Step 3: compute sources, J_{ij}, from scattering, as illustrated in Fig. 2.8, to be used for computation of next order brightness temperatures.

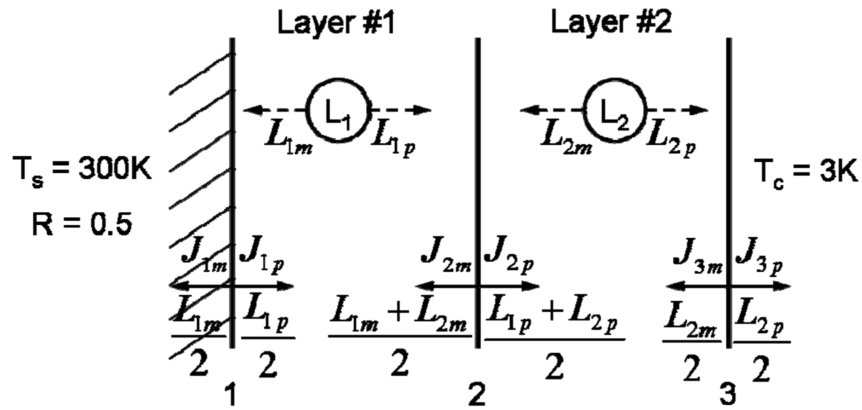

Fig. 2.8. Geometry for SOS example (4).

$$J_{1m}(0th) = \frac{L_{1m}(0th)}{2} = \frac{3.5921}{2} = 1.7960$$
$$J_{2m}(0th) = \frac{L_{1m}(0th) + L_{2m}(0th)}{2} = \frac{3.5921 + 3.2172}{2} = 3.4047$$
$$J_{3m}(0th) = \frac{L_{2m}(0th)}{2} = \frac{3.2172}{2} = 1.6086$$
$$J_{1p}(0th) = \frac{L_{1p}(0th)}{2} = \frac{9.9814}{2} = 4.9907$$
$$J_{2p}(0th) = \frac{L_{1p}(0th) + L_{2p}(0th)}{2} = \frac{9.9814 + 9.1353}{2} = 9.5584$$
$$J_{3p}(0th) = \frac{L_{2p}(0th)}{2} = \frac{9.1353}{2} = 4.5677$$

Step 4: compute 1st order brightness temperatures.

$$T_3^-(1st) = J_{3m}(0th) = 1.6086$$
$$T_2^-(1st) = T_3^-(1st)e^{-\Delta\tau_2} + J_{2m} = 1.6086e^{-0.1} + 3.4047 = 4.8602$$
$$T_1^-(1st) = T_2^-(1st)e^{-\Delta\tau_1} + J_{1m} = 4.8602e^{-0.1} + 1.7960 = 6.1937$$
$$T_1^+(1st) = R \cdot T_1^-(1st) + J_{1p} = 0.5 \times 6.1937 + 4.9907 = 8.0876$$
$$T_2^+(1st) = T_1^+(1st)e^{-\Delta\tau_1} + J_{2p} = 8.0876e^{-0.1} + 9.5584 = 16.8764$$
$$T_3^+(1st) = T_2^+(1st)e^{-\Delta\tau_2} + J_{3p} = 16.8764e^{-0.1} + 4.5677 = 19.8381$$

Now, iterate steps 2, 3, and 4, respectively, that is,

Compute lost from scattering in both layers.

$$L_{11}(1st) = T_1^+(1st)(1 - e^{-\alpha_{s1}dz}) = 8.0876(1 - e^{-0.09}) = 0.6961$$
$$L_{12}(1st) = T_2^-(0th)(1 - e^{-\alpha_{s1}dz}) = 4.8602(1 - e^{-0.09}) = 0.4183$$

$$L_{1p}(1st) = \left(\frac{1+g}{2}\right)L_{11} + \left(\frac{1-g}{2}\right)L_{12} = 0.6267$$
$$L_{1m}(1st) = \left(\frac{1-g}{2}\right)L_{11} + \left(\frac{1+g}{2}\right)L_{12} = 0.4878$$

$$L_{21}(1st) = T_2^+(1st)(1-e^{-\alpha_{s2}dz}) = 16.7864(1-e^{-0.09}) = 1.4448$$
$$L_{22}(1st) = T_3^-(1st)(1-e^{-\alpha_{s2}dz}) = 1.6086(1-e^{-0.09}) = 0.1385$$
$$L_{2p}(1st) = \left(\frac{1+g}{2}\right)L_{21} + \left(\frac{1-g}{2}\right)L_{22} = 1.1182$$
$$L_{2m}(1st) = \left(\frac{1-g}{2}\right)L_{21} + \left(\frac{1+g}{2}\right)L_{22} = 0.4651$$

Compute source from scattering to be used to compute next order brightness temperatures.

$$J_{1m}(1st) = \frac{L_{1m}(1st)}{2} = \frac{0.4878}{2} = 0.2439$$
$$J_{2m}(1st) = \frac{L_{1m}(1st) + L_{2m}(1st)}{2} = \frac{0.4878 + 0.4651}{2} = 0.4765$$
$$J_{3m}(1st) = \frac{L_{2m}(1st)}{2} = \frac{0.4651}{2} = 0.2326$$
$$J_{1p}(1st) = \frac{L_{1p}(1st)}{2} = \frac{0.6267}{2} = 0.3134$$
$$J_{2p}(1st) = \frac{L_{1p}(1st) + L_{2p}(1st)}{2} = \frac{0.6267 + 1.1182}{2} = 0.8725$$
$$J_{3p}(1st) = \frac{L_{2p}(1st)}{2} = \frac{1.1182}{2} = 0.5591$$

Compute 2nd order brightness temperatures.

$$T_3^-(2nd) = J_{3m}(1st) = 0.2326$$
$$T_2^-(2nd) = T_3^-(2nd)e^{-\Delta\tau_2} + J_{2m}(1st) = 0.2326e^{-0.1} + 0.4765 = 0.6870$$
$$T_1^-(2nd) = T_2^-(2nd)e^{-\Delta\tau_1} + J_{1m}(1st) = 0.6870e^{-0.1} + 0.2439 = 0.8655$$
$$T_1^+(2nd) = R \cdot T_1^-(2nd) + J_{1p}(1st) = 0.5 \times 0.8655 + 0.3134 = 0.7462$$
$$T_2^+(2nd) = T_1^+(2nd)e^{-\Delta\tau_1} + J_{2p}(1st) = 0.7462e^{-0.1} + 0.8725 = 1.5477$$
$$T_3^+(2nd) = T_2^+(2nd)e^{-\Delta\tau_2} + J_{3p}(1st) = 1.5477e^{-0.1} + 0.5591 = 1.9595$$

Keep repeating these steps until T_3^+ becomes a very small number. The brightness temperature observed at the top of the atmosphere is equal to $T_b = T_3^+(0th) + T_3^+(1st) + T_3^+(2nd) + ... +$ higher order terms. Application of method of successive orders of scattering is illustrated in Section 7.3.5.

2.3.2 TBSCAT

TBSCAT is an efficient radiative transfer program by P. W. Rosenkranz, where the radiative transfer equation (2.48) in a planar-stratified atmosphere with multiple scattering is solved by numerically integrating an ensemble of trial functions that are constructed to satisfy the boundary conditions at the top of the atmosphere [7] and the boundary conditions at the surface are imposed after integration through the atmosphere. It assumes that the radiance I is independent of azimuthal coordinate and the phase function is scalar. Its two-stream variant is used here in this thesis.

2.4 Image Sharpening

The power spectrum propagating down a single-mode transmission line [19] from a matched load at temperature T is

$$P_+(f) \cong \frac{hf}{e^{hf/kT}-1} \qquad [\mathrm{WHz}^{-1}] \tag{2.55}$$

In the Rayleigh-Jeans limit where $hf << kT$, (2.55) is reduced to

$$P_+(f) \cong kT \qquad [\mathrm{WHz}^{-1}] \tag{2.56}$$

Hence, the total thermal power within some bandwidth B [Hz] is

$$P \cong kTB \quad [\mathrm{W}] \tag{2.57}$$

If a transmitter having antenna gain $G_T(\theta,\phi)$ transmits a power of P_T, with the assumption that the signals arriving from different directions are statistically independent, the power received at the receiver at a distance R away from the transmitter is

$$P_r(f) = \int_{4\pi} A_r(f,\theta,\phi)\cdot I_r(f,\theta,\phi)d\Omega \quad [\mathrm{WHz}^{-1}] \tag{2.58}$$

where $A_r(f,\theta,\phi)$ is the effective area of the receiver's antenna and has relationship with the gain of the receiver's antenna $G_r(f,\theta,\phi)$ as

$$A_r(f,\theta,\phi) = \frac{\lambda^2}{4\pi}G_r(f,\theta,\phi) \qquad [\mathrm{m}^2] \tag{2.59}$$

and $I_r(f,\theta,\phi)$ [Wm^{-2}Hz^{-1}ster^{-1}] is the intensity at the receiver and is equal to

$$I_r(f,\theta,\phi) = \frac{P_T}{4\pi R^2} G_T(f,\theta,\phi) \quad [\mathrm{Wm^{-2}Hz^{-1}ster^{-1}}] \tag{2.60}$$

Power received at the antenna is generally coupled to a coaxial cable, which is a TEM transmission line. In the Rayleigh-Jeans limit, power spectrum in (2.56) and (2.60) are equal. Hence, the antenna temperature can be obtained by equating (2.56) and (2.60)

$$kT_A = \int_{4\pi} A_r(\theta,\phi) I_r(\theta,\phi) d\Omega \qquad [\mathrm{WHz^{-1}}] \tag{2.61}$$

If the antenna can intercept both polarizations, then each polarization would yield its own separate T_A. Substituting the Rayleigh-Jeans expression for intensity $I_r = kT_B/\lambda^2$ for each polarization yields

$$T_A = \frac{1}{\lambda^2} \int_{4\pi} A(\theta,\phi) T_B(\theta,\phi) d\Omega \qquad [\mathrm{K}] \tag{2.62}$$

$$T_A = \frac{1}{4\pi} \int_{4\pi} G(\theta,\phi) T_B(\theta,\phi) d\Omega \quad [\mathrm{K}] \tag{2.63}$$

The following explains how to estimate the true sky brightness distribution $T_B(\overline{\phi}_S)$ as a function of the two-dimensional source angle $\overline{\phi}_S$, where the overbar signifies a vector quantity. The finite resolution antenna is pointed at angle $\overline{\phi}_A$ at any instant, and the antenna response to radiation arriving from the source angle $\overline{\phi}_S$ depends on the antenna gain in that direction, $G(\overline{\phi}_A - \overline{\phi}_S)$. If the radiation arriving from different angles is uncorrelated, then (2.63) applies and the antenna temperature $T_A(\overline{\phi}_A)$ becomes

$$T_A(\overline{\phi}_A) = \frac{1}{4\pi} \int_{4\pi} G(\overline{\phi}_A - \overline{\phi}_S) T_B(\overline{\phi}_S) d\Omega_S \quad [\mathrm{K}] \tag{2.64}$$

$$= \frac{1}{4\pi} G(\overline{\phi}) * T_B(\overline{\phi}) \qquad [\mathrm{K}] \tag{2.65}$$

where "$*$" signifies two-dimensional convolution. Fourier transforming (2.65) from angular coordinates $\overline{\phi}$ into angular frequency coordinates $\overline{s}$ [cycles/radian],

$$\underline{T_A}(\overline{s}) = \frac{1}{4\pi} \underline{G}(\overline{s}) \cdot \underline{T_B}(\overline{s}) \tag{2.66}$$

Where

$$\underline{G}(s_x, s_y) = \iint G(\phi_x, \phi_y) e^{-2j\pi(\phi_x s_x, \phi_y s_y)} d\phi_x d\phi_y \tag{2.67}$$

and underbar signifies a complex quantity.

From (2.65), the antenna brightness temperature, $T_A(\overline{\phi}_A)$, is a blurred function of the true brightness temperature, $T_B(\overline{\phi}_A)$. We can see from (2.66) that $T_B(\overline{\phi}_A)$ can be estimated as

$$\hat{T}_B(\overline{\phi}_A) = F^{-1}\left\{\frac{4\pi \underline{T_A}(\overline{s})}{\underline{\underline{G}}(\overline{s})} \cdot W(\overline{s})\right\}$$

(2.68)

where ^ signifies estimated value and F^{-1} is the inverse Fourier transform. In the no-noise situation, the optimum window function $W_{optimum}(\overline{s})$ for deblurring is a 2-D boxcar just to avoid the singularity introduced at angular frequencies $\overline{s}$ for which the gain is zero. In general situation, the antenna temperature $T_A(\overline{\phi}_A)$ is corrupted by noise. With the reasonable assumption that the antenna temperature and receiver noise contributions are uncorrelated, the optimum window function can be shown [19] to be

$$\underline{W_{optimum}}(\overline{s}) = \left(1 + E\left[\left|\underline{N}(\overline{s})\right|^2\right] \Big/ E\left[\left|\underline{T_A}(\overline{s})\right|^2\right]\right)^{-1} \tag{2.69}$$

which is a 2-D boxcar tapered gently to zero where the signal-to-noise-ratio (SNR) is low. From (2.68), the sharpening pattern is

$$G_{sharpening}(\overline{\phi}) = F^{-1}\left\{W(\overline{s})\right\} \tag{2.70}$$

Application of image sharpening is illustrated in Section 6.3.2.

2.5 Aperture Antennas

Fig. 2.9 shows an aperture in the x-y plane picking up multiple plane waves arriving from different directions (φ_x, φ_y). Typically these waves are statistically independent and that is assumed here. By integrating contributions from all separate plane wave arriving from different directions, $\underline{\overline{E}}(\varphi_x, \varphi_y)$, over 4π steradians, the total observed complex electric field distribution on the aperture, $\underline{\overline{E}}(x, y)$, can be written as [19]

$$\underline{\overline{E}}(x, y) \cong \int_{4\pi} \underline{\overline{E}}(\varphi_x, \varphi_y) e^{+j\frac{2\pi}{\lambda}(x\sin\varphi_x + y\sin\varphi_y)} d\Omega \tag{2.71}$$

where an underbar and upperbar denote a complex quantity and a vector, respectively.

The electric field pattern, $\underline{\overline{E}}(\varphi_x, \varphi_y)$, can be written as

$$\underline{\overline{E}}(\varphi_x, \varphi_y) \cong \frac{1}{\lambda^2} \int_A \underline{\overline{E}}(x, y) e^{-j\frac{2\pi}{\lambda}(x\varphi_x + y\varphi_y)} dxdy \tag{2.72}$$

where A is the area of the aperture and λ is the wavelength.

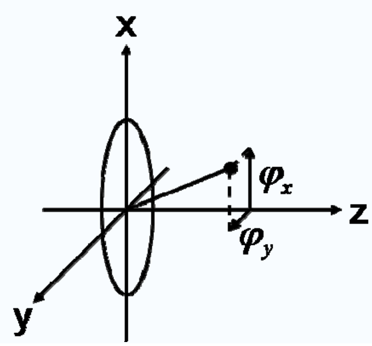

Fig. 2.9. An aperture antenna [19].

By defining $x_\lambda = x/\lambda$ and $y_\lambda = y/\lambda$, (2.71) and (2.72) become

$$\underline{\overline{E}}(x, y) \cong \int_{4\pi} \underline{\overline{E}}(\varphi_x, \varphi_y) e^{+j2\pi(x_\lambda\varphi_x + y_\lambda\varphi_y)} d\Omega \tag{2.73}$$

and

$$\underline{\overline{E}}(\varphi_x, \varphi_y) \cong \frac{1}{\lambda^2} \int_A \underline{\overline{E}}(x, y) e^{-j\frac{2\pi}{\lambda}(x_\lambda\varphi_x + y_\lambda\varphi_y)} dx_\lambda dy_\lambda \tag{2.74}$$

(2.73) and (2.74) are a Fourier transform pair. Hence, the autocorrelation function, $\underline{R}_{\underline{E}}(\overline{\tau}_\lambda)$, of the electric field distribution in the aperture, $\underline{\overline{E}}(x_\lambda, y_\lambda)$, can be related to the angular intensity, $I(\varphi_x, \varphi_y)$, of transmitting or arriving electric fields, $\underline{\overline{E}}(\varphi_x, \varphi_y)$, in different directions as

$$
\begin{array}{ccc}
\underline{\overline{E}}(x_\lambda, y_\lambda)\quad [V/m] & \overset{\sim}{\leftrightarrow} & \underline{\overline{E}}(\varphi_x, \varphi_y)\quad [V/m\cdot radian] \\
\downarrow & & \downarrow \\
\underline{R}_{\underline{E}}(\overline{\tau}_\lambda)\quad [V/m]^2 & \overset{\sim}{\leftrightarrow} & \left|\underline{\overline{E}}(\varphi_x, \varphi_y)\right|^2 \;\propto\; 2\eta_o I(\varphi_x, \varphi_y) \;\propto\; G(\varphi_x, \varphi_y)
\end{array}
\tag{2.75}
$$

where $\overset{\sim}{\leftrightarrow}$ denotes a Fourier transform pair, $\downarrow$ denotes one way relationship, which is not reversible, $\underline{R}_{\underline{E}}(\overline{\tau}_\lambda) = \int_{-\infty}^{\infty}\int_{-\infty}^{\infty} \underline{\overline{E}}(\overline{r}_\lambda)\underline{\overline{E}}^*(\overline{r}_\lambda - \overline{\tau}_\lambda)dx_\lambda dy_\lambda$, $G(\varphi_x, \varphi_y)$ is the antenna gain of the transmitting antenna, and η_o is the characteristic impedance of the free space equal to $\sqrt{\mu_o/\varepsilon_o} = 120\pi$ [Ω].

For narrowband uncorrelated stochastic signals, (2.75) becomes

$$
\begin{array}{ccc}
\underline{\overline{E}}(x_\lambda, y_\lambda, t)\quad [V/m] & \overset{\sim}{\leftrightarrow} & \underline{\overline{E}}(\varphi_x, \varphi_y, t) \\
\downarrow & & \downarrow \\
\phi_{\underline{E}}(\tau_{x_\lambda}, \tau_{y_\lambda})\quad [V/m]^2 & \overset{\sim}{\leftrightarrow} & E\left[\left|\underline{\overline{E}}(\varphi_x, \varphi_y, t)\right|^2\right]\quad [V/m\cdot radian]^2
\end{array}
\tag{2.76}
$$

and

$$
\begin{array}{ccc}
\phi_{\underline{E}}(\tau_{x_\lambda}, \tau_{y_\lambda}, t)/2\eta_o B\quad [Wm^{-2}] & \overset{time/\,freq}{\leftrightarrow} & \phi_{\underline{E}}(\tau_{x_\lambda}, \tau_{y_\lambda}, f)/2\eta_o B\quad [Wm^{-2}Hz^{-1}] \\
& & \updownarrow space/\,angle \\
& & I(\overline{\varphi}, f) = \dfrac{kT_B(\overline{\varphi}, f)}{\lambda^2}\quad [Wm^{-2}Hz^{-1}ster^{-1}]
\end{array}
\tag{2.77}
$$

where $E[]$ is the expectation operator, $\phi_{\underline{x}}(\tau) = E[\underline{x}^*(t-\tau)\underline{x}(t)]$, $I(\overline{\varphi}, f)$ is the intensity, $T_B(\overline{\varphi}, f)$ is the brightness temperature, and $\leftrightarrow$ and $\updownarrow$ are time/frequency and space/angle Fourier transforms, respectively.

2.5.1 Filled-Aperture Antennas

(2.75) shows that the antenna gain of the transmitting antenna, $G(\varphi_x, \varphi_y)$, is proportional to a magnitude squared of the Fourier transform of the electric field distribution in the aperture, $\underline{\overline{E}}(x_\lambda, y_\lambda)$. Hence, a uniformly-illuminated circular aperture with a diameter D [m], which has a Fourier transform equal to a sinc function, yields 3-dB beamwidth $\theta_B \cong \dfrac{1.2\lambda}{D}$ radians. In practice, there is a tradeoff between the antenna resolution and the amplitude of sidelobes. The electric field distribution is generally tapered toward the edges to reduce sidelobes. A reasonable illumination tapering yields $\theta_B \cong \frac{1.3\lambda}{D}$ radians. As discussed in Section 2.4, Nyquist sampling and image sharpening can increase the resolution with some noise amplification.

2.5.2 Passive Aperture Synthesis

Passive aperture synthesis combines signals intercepted by multiple small apertures to yield the angular response characteristics of much larger antennas. (2.77) illustrates the important relationship between autocorrelation function, $\phi_{\underline{E}}(\overline{\tau_\lambda}, f)$, and angular distribution of the intensity, $I(\overline{\varphi}, f)$.

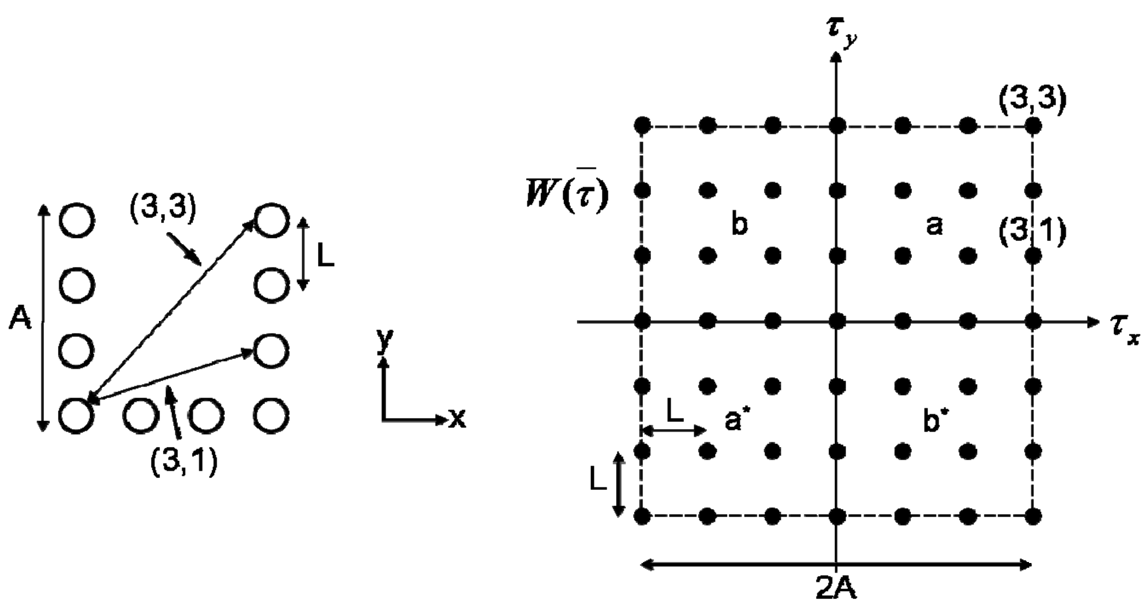

Fig. 2.10. A U-shaped antenna array and its corresponding observed space of autocorrelation function.

Fig. 2.10 shows a U-shaped antenna array with three equal length arms of length A and the spacing between adjacent antennas equal to L and its corresponding observed space of autocorrelation, which is equivalent to the weighting function $W\left(\overline{\tau_\lambda}\right)$ times the true autocorrelation function $\phi_{\underline{E}}(\overline{\tau_\lambda}, f)$. Note that an autocorrelation function is conjugate symmetric, that is, $\phi_{\underline{E}}(\overline{\tau_\lambda}, f) = \phi_{\underline{E}}^*(-\overline{\tau_\lambda}, f)$. The dimension of the observed autocorrelation function is a square of 2A×2A. Note that the observations of $\phi_{\underline{E}}(\overline{\tau_\lambda}, f)$ is composed of discrete samples arranged on a square. Hence, what is actually observed is

$$[\phi_{\underline{\bar{E}}}(\overline{\tau_\lambda}, f)/2\eta_o B]\cdot W(\overline{\tau_\lambda}) \leftrightarrow I(\bar{\varphi}, f) * W(\bar{\varphi}) \tag{2.78}$$

where $*$ is the convolution. Fig. 2.11 shows graphically the effect of discrete sampling of an autocorrelation function.

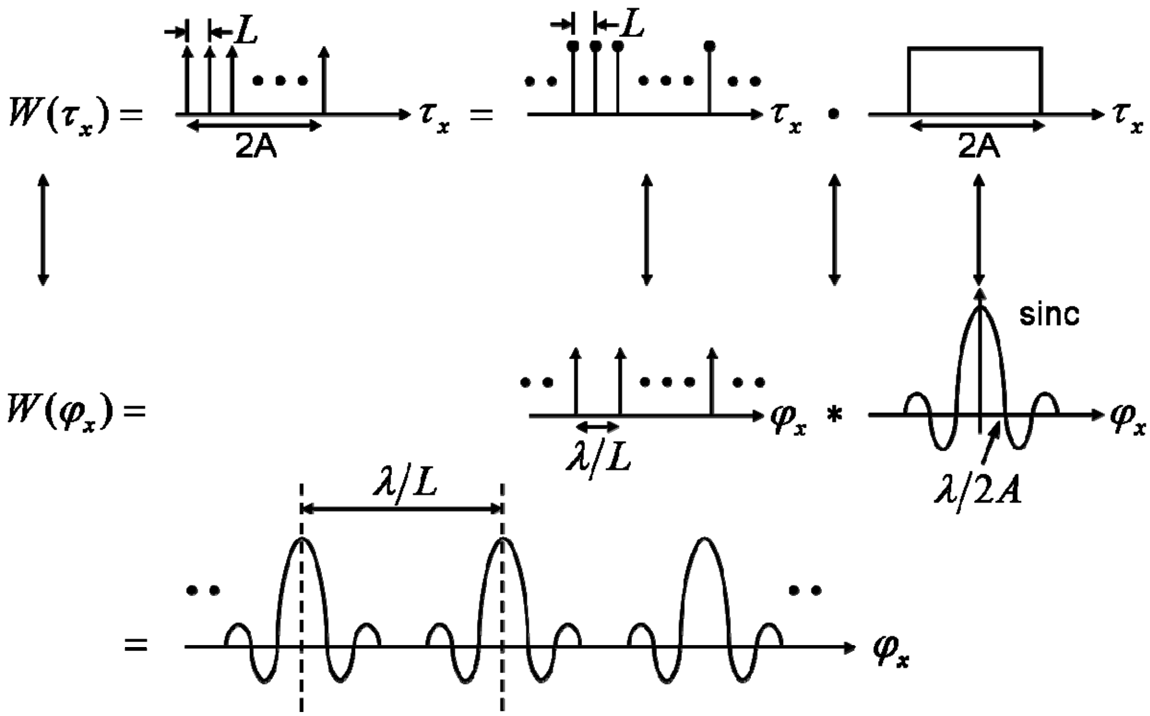

Fig. 2.11. Resolution and aliasing of synthesized images due to discrete samples of autocorrelation function [19].

Hence, the antenna beamwidth $\theta_B = \dfrac{\lambda}{2A}$ and there is aliasing in synthesized images every $\dfrac{\lambda}{L}$ because of the discrete nature of observation, as Fig. 2.12 shows. $\dfrac{\lambda}{L}$ has to be chosen appropriately so that the effect of aliasing is acceptable. Since a sinc function is infinitely long, there is still aliasing no matter how large $\dfrac{\lambda}{L}$ is, but its effect will be less as the amplitude of a sinc function gets smaller for increasing $\dfrac{\lambda}{L}$. Application of aperture antenna concept is illustrated in Chapter 6.

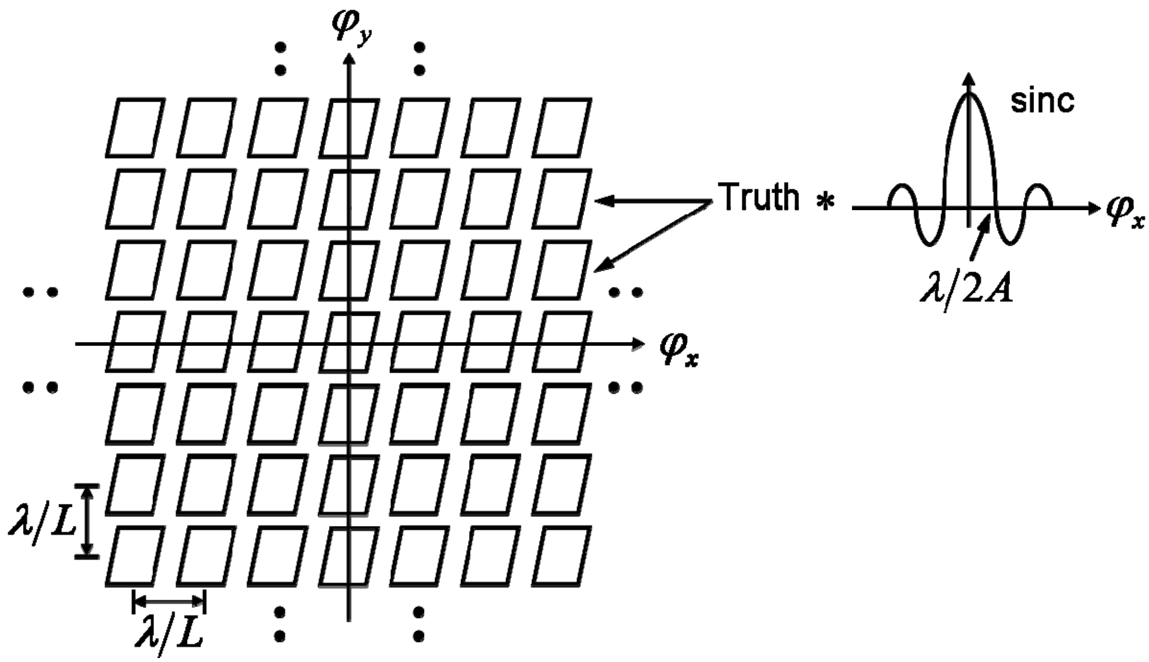

Fig. 2.12. Synthesized image with aliasing [19].

2.6 Principal Component Analysis (PCA)

A multivariate dataset, such as brightness temperatures observed by satellites, generally contains a large number of variables with high correlations among them. This multi-dimensional dataset can be compressed to lower dimensions with little loss of information using principal component analysis (PCA) to eliminate correlations among the variables. PCA is also called as Karhunan-Loeve expansion. It could also be used to get rid of unwanted noise in the dataset, which is illustrated later in Section 7.4. There are variants of PCA with different objectives.

2.6.1 Basic PCA

Let x be a zero-mean random vector with dimension of n, that is, $x = [x_1 \quad x_2 \quad \cdots \quad x_n]^T$. A reduced-dimension data vector is $y = [y_1 \quad y_2 \quad \cdots \quad y_m]^T = W^T x$ with dimension of m where m<n could be found using PCA with the main objective to optimally minimize mean-square reconstruction error, where W is an n-by-m transform matrix. The cost function is

$$C(\cdot) = E[(x - \hat{x})^T (x - \hat{x})] \tag{2.79}$$

where $\hat{x}$ is the reconstruction estimate of the original data, x. PCA is also often used to get rid of noises or unwanted signals that are embedded in the original data, x. PCA linearly transforms the data to a new coordinate system such that projection of the data on the first coordinate, called the first principal component, has the greatest variance, projection of the data on the second coordinate, called the second principal component, has the second greatest variance, and so on.

The first principal component is $w_1^T x$, where w_1 is defined as

$$w_1 = \arg\max_{\|w\|=1} E\{[w^T x]^2\} \tag{2.80}$$

w_1 has the same dimension, n, as x. Having found the first k-1 principal components, the k-th principal component is $w_k^T x$, where

$$w_k = \arg\max_{\|w\|=1} E\{[w^T (x - \sum_{i=1}^{k-1} w_i w_i^T x)]^2\} \tag{2.81}$$

The reduced-dimension data y has dimension m, where m<n can be obtained by

$$y = [w_1 \mid w_2 \mid \cdots \mid w_m]^T x \tag{2.82}$$

and the reconstructed estimate of x is

$$\hat{x} = WW^T x \tag{2.83}$$

Computation of w_i could be shown [21] to be eigenvectors of C_{xx} corresponding to n largest eigenvalues. Intuitively, $W_n = [w_1 \mid w_2 \mid \cdots \mid w_n]$ spans subspace of C_{xx}. So, if we want to reduce the dimension of the subspace spanning by w_i from n dimensions to m dimensions with the cost function in (2.79), we want to keep m eigenvectors w_i that capture most variance in x. Application of basic PCA is illustrated in Section 7.4.

2.6.2 Projected Principal Component Analysis (PPC)

PPC is a flavor of PCA. Let us assume that a multivariate signal, x, is a random vector with a dimension of n. The main objective of PPC is to find a reduced-dimension data vector $y = W^T x$ with a dimension m, where m<n, from the original data x such that the resulting mean-square error is minimized when we linearly estimate s from y. That is a reduced-dimension data y keeps information about s in x as much as possible in the linear least-square sense for a given dimension of y. The linear least-squares estimate $\hat{s}$ of s is

$$\hat{s} = C_{sy}C_{yy}^{-1}y = C_{sx}W[W^T C_{xx} W]^{-1} W^T x \tag{2.84}$$

where C_{sx} is the cross-covariance of s and x. The cost function to be minimized is

$$C(\cdot) = E[(s - \hat{s})^T (s - \hat{s})] \tag{2.85}$$

W that minimizes (2.85) can be shown [21] to be the m right eigenvectors with highest singular values of the reduced-rank regression matrix L_m

$$L_m = V_m V_m^T C_{sx} C_{xx}^{-1} \tag{2.86}$$

where $V_m = [v_1 \mid v_2 \mid \cdots \mid v_m]$ are m most-significant eigenvectors of $C_{sx}C_{xx}^{-1}C_{xs}$.

PPC could be understood intuitively. Say, we want to estimate a zero-mean random vector s from x having a dimension of n by using linear least-squares estimation, the linear- least-squares estimate of s is $\hat{s} = C_{sx}C_{xx}^{-1}x = Lx$ where $L = C_{sx}C_{xx}^{-1}$ is the regression matrix. The error covariance is equal to $C_{ss} - C_{sx}C_{xx}^{-1}C_{xs}$. Let eigenvectors $V_n = [v_1 \mid v_2 \mid \cdots \mid v_n]$ span the subspace of $C_{sx}C_{xx}^{-1}C_{xs}$. To minimize the error covariance $C_{ss} - C_{sx}C_{xx}^{-1}C_{xs}$, we want $C_{sx}C_{xx}^{-1}C_{xs}$ to be as large as possible. So, if we want to reduce the dimension of the subspace spanning by $V_n = [v_1 \mid v_2 \mid \cdots \mid v_n]$ from n dimensions to m dimensions with the cost function in (2.85), we want to keep m most significant eigenvectors of V_n. Hence, the reduced-rank regression matrix L_m becomes (2.86) and PPC of x is equal to $W^T x$, where W is the m right eigenvectors with highest singular values of the reduced-rank regression matrix L_m. Application of PPC is illustrated in Section 9.2.

2.7 Neural Network (NN)

The relationship between atmospheric parameters and brightness temperatures observed by satellites is very complex and nonlinear. Hence, the optimal estimator should be nonlinear. A neural network is composed of interconnecting artificial neurons working in parallel. It was designed to mimic biological nervous system. It can be used to learn and compute complex functions for which the relationships between inputs and outputs are unknown or computationally complex and is useful for pattern recognition, classification, and estimation. Fig. 2.13 shows a multilayer neural network, where x_i is the ith input, n is the number of inputs, w_{ij} is the weight associated with the ith input to the jth node, b_i is the bias of the ith neuron, m is the number of neurons in the hidden layer, f is the transfer function in the hidden layer, v_i is the weight between the ith neuron and the output neuron, c is the bias of the output neuron, g is the transfer function of the output node, and y is the output, which is

$$y = g\left(\sum_{j=1}^{m} v_j f\left(\sum_{i=1}^{n} w_{ij} y_i + b_j\right) + c\right) \tag{2.87}$$

In this thesis, f(x) was chosen to be a nonlinear function to capture nonlinear relationship between inputs and output, and g(x) is a linear function, that is, $f(x) = \tanh x = \frac{e^x - e^{-x}}{e^x + e^{-x}}$, and $g(x) = x$.

The most important assumption when applying a neural network is that the training data composed of vectors of inputs and output is a good representative of most, if not all, possible relationships. To train a neural network, a general practice is to divide training data into three disjoint sets, including training, validation, and testing sets. The training set is used by the neural network to adjust its weights and biases during the training to minimize a defined cost function. The validation set is used to determine when the training should stop to avoid over-training the neural network. The testing set is used to evaluate the resulting neural network. Applications of neural networks are illustrated in Chapters 4-9.

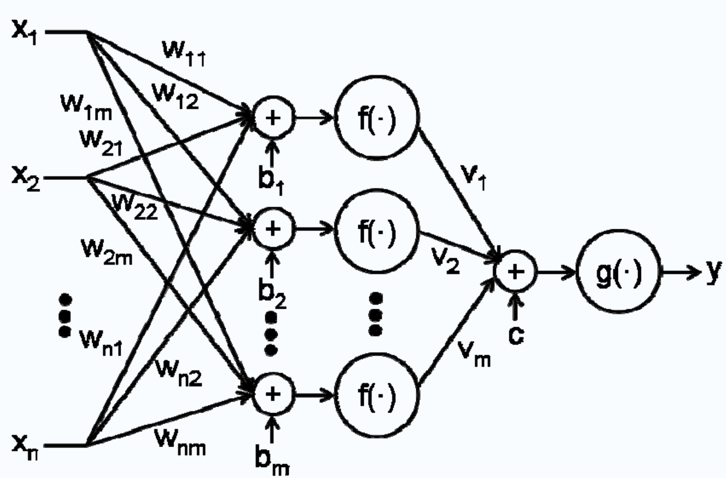

Fig. 2.13. A 2-layer feedforward neural network with one output node [22].

2.8 Advanced Microwave Sounding Unit (AMSU)

The Advanced Microwave Sounding Units (AMSU) on the operational satellites NOAA-15, -16, and -17, and -18 have been providing extensive observations of millimeter-wave spectral images of Earth at 20 frequencies (19 on NOAA-18) since May, 1998. AMSU is composed of two units, AMSU-A and AMSU-B (the Microwave Humidity Sounder (MHS) replaces AMSU-B on NOAA-18), and observes the frequencies and bandwidths shown in Tables 2.1 and 2.2. AMSU-A observes 15 channels centered mostly in oxygen absorption bands with 50-km resolution near nadir, and AMSU-B observes five channels near water vapor resonances with 15-km resolution near nadir [23]-[24].

AMSU-A and AMSU-B scan cross-track ±48.33 and ±48.95 degrees from nadir, respectively, mapping a ~2200 km swath beneath the spacecraft with 30 AMSU-A views and 90 AMSU-B views. Similar microwave sounding instruments include AMSU/Humidity Sounder for Brazil (HSB) [25] on the NASA Aqua satellite and the future Advanced Technology Microwave Sounder (ATMS) [26] on NPOESS. HSB resembles AMSU-B with the lack of the 89-GHz channel, and the spatial resolution of the AMSU-A channels are improved to ~33 km on ATMS, along with the addition of two channels. Tables 2.1 and 2.2 list for each AMSU channel the frequencies, bandwidths, and altitudes where the temperature weighting function peaks, based on nadir views of the 1976 U.S. standard atmosphere over a non-reflecting surface. Fig. 2.14 shows weighting functions for AMSU-A and AMSU-B channels.

TABLE 2.1

FREQUENCIES, BANDWIDTHS, WEIGHTING FUNCTION PEAK HEIGHTS COMPUTED USING THE 1976 US STANDARD ATMOSPHERE AT NADIR OVER A NONREFLECTIVE SURFACE, AND RADIOMETRIC SENSITIVITY VALUES FOR AMSU-A

Ch	Channel Frequencies (MHz)	Bandwidth (MHz)	Weighting Function Peak Height (km)	NEΔT Measured at 18 degree C
1	23,800±72.5	2×125	0	0.211
2	31,400±50	2×80	0	0.265
3	50,300±50	2×80	0	0.219
4	52,800±105	2×190	0	0.143
5	53,596±115	2×168	4	0.148
6	54,400±105	2×190	8	0.154
7	54,940±105	2×190	9.5	0.132
8	55,500±87.5	2×155	12.5	0.141
9	57,290.344±87.5	2×155	16.5	0.236
10	57,290.344±217	2×77	20.5	0.250
11	57,290.344±322.2±48	4×35	24.5	0.280
12	57,290.344±322.2±22	4×15	29.5	0.400
13	57,290.344±322.2±10	4×8	34.5	0.539
14	57,290.344±322.2±4.5	4×3	40.5	0.914

15	89,000±1000	2×1000	0	0.116

TABLE 2.2
FREQUENCIES, BANDWIDTHS, WEIGHTING FUNCTION PEAK HEIGHTS COMPUTED USING THE 1976 US STANDARD ATMOSPHERE AT NADIR OVER A NONREFLECTIVE SURFACE, AND RADIOMETRIC SENSITIVITY VALUES FOR AMSU-B

Ch	Channel Frequencies (GHz)	Bandwidth (GHz)	Weighting Function Peak Height (km)	NEΔT Measured at 16 degree C
1	89±0.9	2×1	0	0.35
2	150±0.9	2×1	0	0.76
3	183.31±1	2×0.5	6.1	0.98
4	183.31±3	2×1	4.0	0.68
5	183.31±7	2×2	1.8	0.55

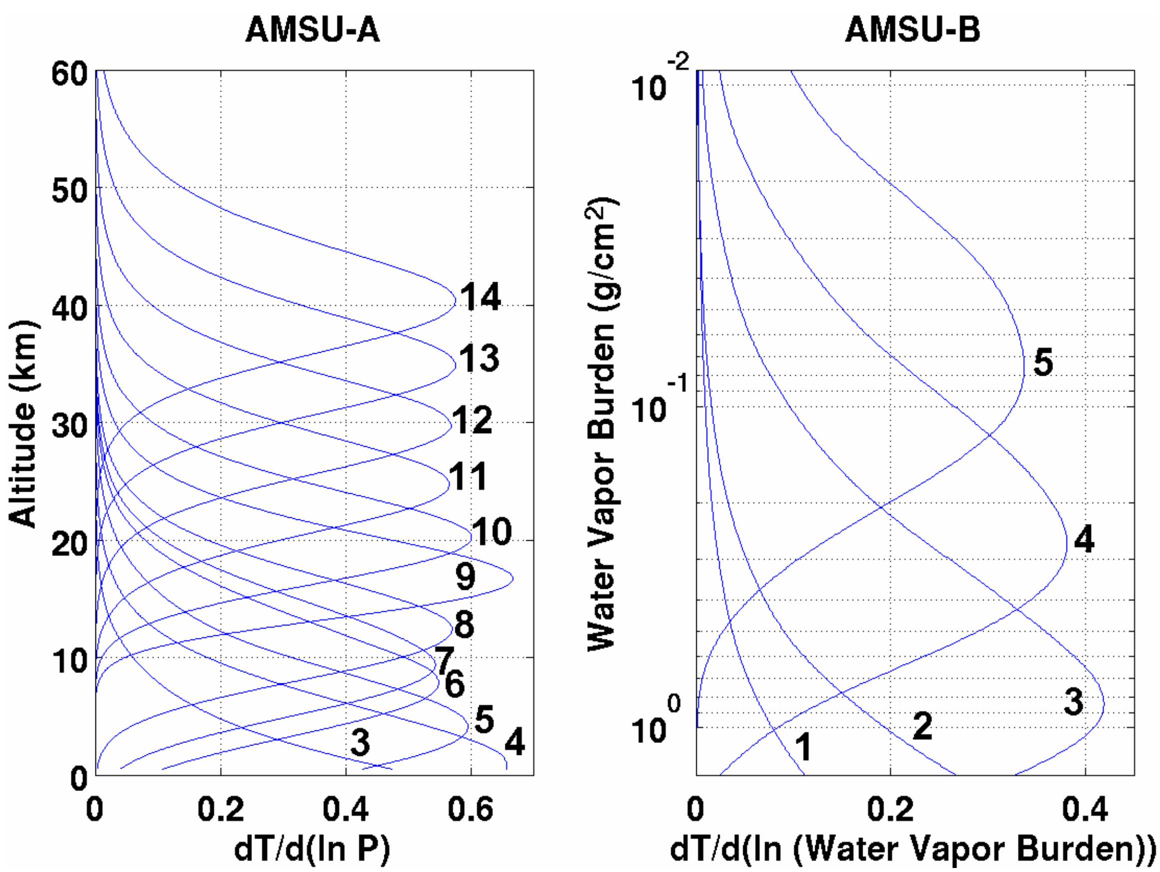

Fig. 2.14. AMSU-A and AMSU-B weighting functions, where numbers indicate channel numbers.

Chapter 3

A Numerical Weather Prediction Model MM5

MM5 [6] is the fifth-generation NCAR/Penn State Mesoscale Model used for numerical weather prediction research and mesoscale modeling applications. It is a nonhydrostatic, three-dimensional, limited-area, primitive-equation, nested grid model with a terrain-following vertical coordinate. NOAA NCEP global atmospheric analyses (http://dss.ucar.edu/datasets/ds083.2/) from the National Center for Atmospheric Research (NCAR) were used for temporal and spatial boundary conditions in this study. These analyses have 1-degree resolution at 0Z, 6Z, 12Z, and 18Z for 24 pressure levels extending to 10 mbar. MM5 employs nested grids or domains, where the outermost grids have reduced resolution, as listed in Table 3.1 along with domain sizes and time steps. All domains are co-centered and have thirty-four terrain-following levels. Planetary boundary layer parameterization for the Medium-Range Forecast model [27] was used for all three domains.

Although the positions of MM5-predicted 15-km scale convective cells are meaningful only on the ~100-km scales of the NCEP initialization data, the statistics of their predicted microwave emission on a 15-km scale are generally consistent with satellite observations for ice habits observed aloft, as Chapter 4 shows later.

3.1 MM5 Physic Options and Domain Configurations

MM5 offers 7 implicit schemes and 8 explicit schemes for treating precipitation [6] and one of each is chosen for each domain. The explicit and implicit schemes treat resolved and unresolved precipitation, respectively, where unresolved precipitation is characterized by the aggregate nature and effects of precipitation averaged over a region that could, for example, include multiple independent convective cells. Kain-Fritsch has been shown to perform best among implicit schemes [28], and a newer version, Kain-Fritsch 2 [29], was used in this study for the lower resolution grids--domain1 and domain2. The implicit output of Kain-Fritsch 2 does not include the hydrometeor profiles needed to compute brightness temperatures, although it does forecast surface precipitation rates. Since the domain3 5-km grid size is so small, no implicit scheme is needed there and only the explicit scheme is used [6].

Only three explicit schemes available to us--Goddard [30], Reisner 2 [31], and Schultz [32]--have complete sets of frozen hydrometeor types. These three options were tested while keeping other options identical. Whereas Goddard and Reisner 2 agreed well with coincident satellite observations, Schultz generally predicted too little precipitation coverage and intensity, as illustrated in Fig. 3.1 for a representative storm. Note the general agreement between AMSU observations and MM5 predictions, although the detailed positions of convective cells differ somewhat due to coarse initialization and the role of chaos. Since Reisner 2 required 17 percent more computer time than Goddard, Goddard was used in this study. Goddard microphysics includes a parameterized Kessler-type two-category liquid water scheme, including cloud water and rain, and parameterized three-category ice-phase schemes [33], including cloud ice, snow, and hail/graupel. Table 3.1 shows MM5 domain configurations.

Hydrometeors are assumed in the Goddard model [30] to have size distributions that are inverse-exponential functions of diameter (D) [cm] as

$$N(D) = N_o \exp(-\lambda D) \tag{3.1}$$

where N(D) [cm^{-4}] is the number of drops per cubic centimeter, per centimeter of diameter D. The intercept values, $N_o = N(0)$, for rain, snow, and graupel are assumed to be 0.08, 0.04, and 0.04 cm^{-4}, respectively. By assumption the decay rate $\lambda = (\pi\rho N_o/\rho_o q)^{0.25}$ [cm^{-1}] where ρ is the density for rain, snow, and graupel, and q is the mass mixing ratio given by MM5 for each species as a function of altitude; ρ_o is the density of moist air. All cloud ice is assumed to have a single diameter $D = 2\times10^{-3}$ cm and a density of 0.917 $g\cdot cm^{-3}$. The same expression (3.1) was used when computing brightness temperatures, but with $\rho = F(\lambda)$, as given later in Table 4.2. The dependence of N(D) upon ρ shifts the size distribution for graupel to larger D values than for snow because of graupel's lower values for $F(\lambda)$. If the densities used within MM5/Goddard are used in the N(D) expression instead of $F(\lambda)$, then the radiance histograms presented later shift only very slightly; these Goddard densities are 1, 0.1, and 0.4 g cm^{-3} for rain, snow, and graupel, respectively.

Because the available global initialization data from NCEP was on a ~110-km grid, MM5 required ~4 hours or more to generate realistic 15-km resolution precipitation profiles. Each satellite overpass considered in Chapter 4 occurred between 4 and 6 hours after MM5 initialization. Predictions further than 6 hours become less reliable at the 15-km scale. The output data used in the forward radiance program was interpolated to 42 equally spaced pressure levels, 10 to 1000 mbar. More details about submodels of MM5 and assumptions used are presented in Appendix A.2.

TABLE 3.1
MM5 DOMAIN CONFIGURATIONS

Domain	Number of cells	Cell size (km)	Implicit scheme	Explicit scheme	Time step (sec)
1	100*100	45	Kain-Fritsch 2	Goddard	40
2	190*190	15	Kain-Fritsch 2	Goddard	13.33
3	190*190	5	None	Goddard	4.44

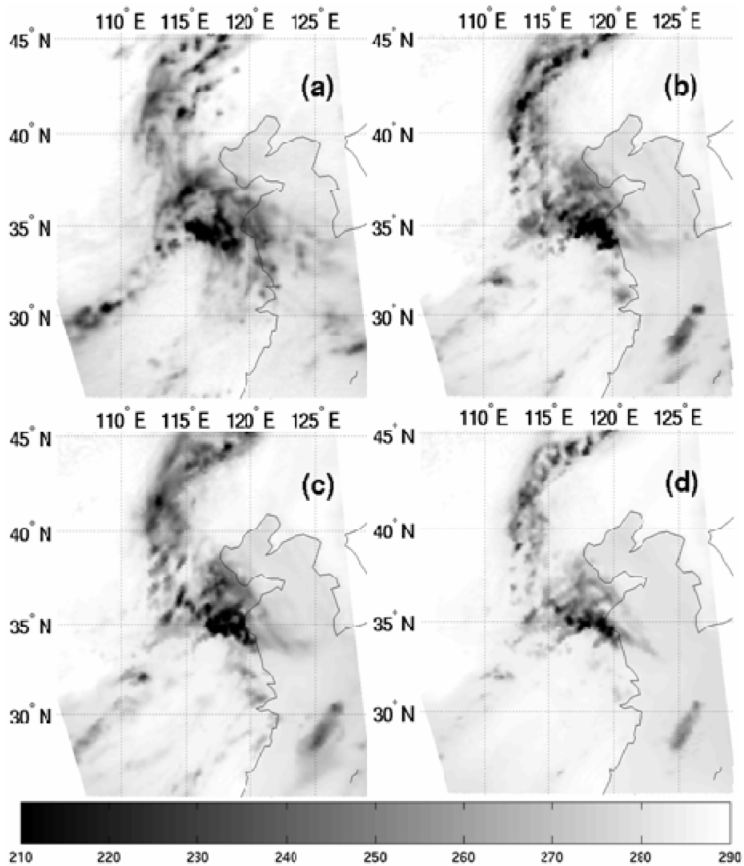

Fig. 3.1. Brightness temperatures (K) at 150 GHz for AMSU and three explicit physics schemes for a storm system viewed 0555 UTC 22 June 2003 at: (a) AMSU-B, (b) Goddard, (c) Reisner 2, and (d) Schultz.

3.2 Ensemble of Global Precipitation

To span a wide range of precipitation types and rates, 255 globally representative storm systems July 2002 – June 2003 were selected by examining AMSU data. These storms included 20 for each month plus 15 that were not glaciated (~warm rain). Unglaciated pixels are defined here as those with microwave ice signatures too weak to be flagged as precipitation [34], but for which more than 0.25-mm of cloud liquid water is retrieved [35]. These satellite passes typically overlap with MM5 storm systems over an area ~ 2200 km × 2200 km.

One challenge in initializing MM5 with low-spatial-resolution data is that the morphology of the MM5 forecast can sometimes differ significantly from the reality sensed by satellite, as illustrated by two extreme examples in Fig. 3.2. The dominant discrepancies between AMSU observations and co-located 4-6 hour MM5 forecasts are in the positions and character of precipitation rather than in radiance values. For example, the concentrated convection shown in Fig. 3.2(b) resulted directly from a strong feature in the initial NCEP field, as did the oversized typhoon eye shown in Fig. 3.2(d). Such obvious morphological discrepancies, as well as storms embracing either pole or very high mountains, led to deletion of approximately half the initial set of 255 storms, leaving 122 storms for further study. Discrepancies in radiance values were not used as a deletion criterion. Analysis of the causes of morphological disagreements between MM5 and AMSU could be informative, but was beyond the scope of this study. Fig. 3.3 shows examples of MM5 forecasts that morphologically agree with coincident AMSU observations and were used further in this study.

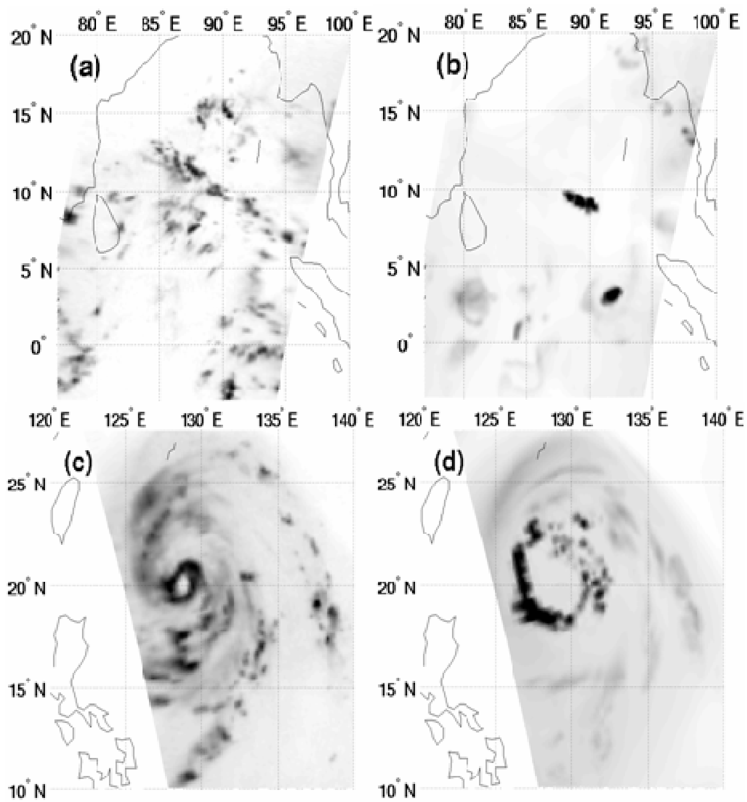

Fig. 3.2. Examples of unacceptable forecast/AMSU differences. Brightness temperatures at 183±7 GHz: (a) T_B observed by AMSU at 0420 UTC 7 October 2002, (b) T_B predicted by NCEP/MM5 for (a), (c) T_B observed by AMSU at 0438 UTC 2 July 2002, (d) T_B predicted by NCEP/MM5 for (c).

Fig. 3.4 shows the locations and months of 122 representative storm systems that agree morphologically with coincident AMSU observations and were chosen for this study from the initial set of 255. The numbers 1-12 indicate the months of the storms, January through December, and the number 14 indicates the predominantly non-glaciated storms. These storm systems were chosen to be diverse and globally representative in terms of location, time of year, and precipitation type and rate. Typhoon Pongsona over Guam at 1625 UTC 8 December 2002 and Hurricane Isidore over Gulf of Mexico at 1642 UTC 22 September 2002 are included. Table 3.2 presents the numbers of precipitating 15-km MM5 pixels in various categories for the 122 chosen storms. Over 640 thousand precipitating 15-km MM5 pixels were studied, where a pixel is designated as precipitating if MM5 rain water or snow at 1000 mbar is non-zero. The categories were defined using AMSU and MM5 data as explained later in Section 4.5.2. The most under-represented category is perhaps pure snow. For purposes of analyzing AMSU observations of snow in Section 4.5.2.2, pure snow (no mixed rain) was defined as precipitation for which the MM5 surface temperatures were below 266K, and only 3200 pixels satisfied these criteria. That these pure-snow criteria are too strict is indicated by the fact that there are 44,000 MM5 rain-free precipitating pixels. Detailed list of the initial set of 255 global storms and 15 storms over the North Pole, which were simulated using MM5 but were not used in this study because it is very difficult to model icy surface correctly, could be found in Appendix A.1.

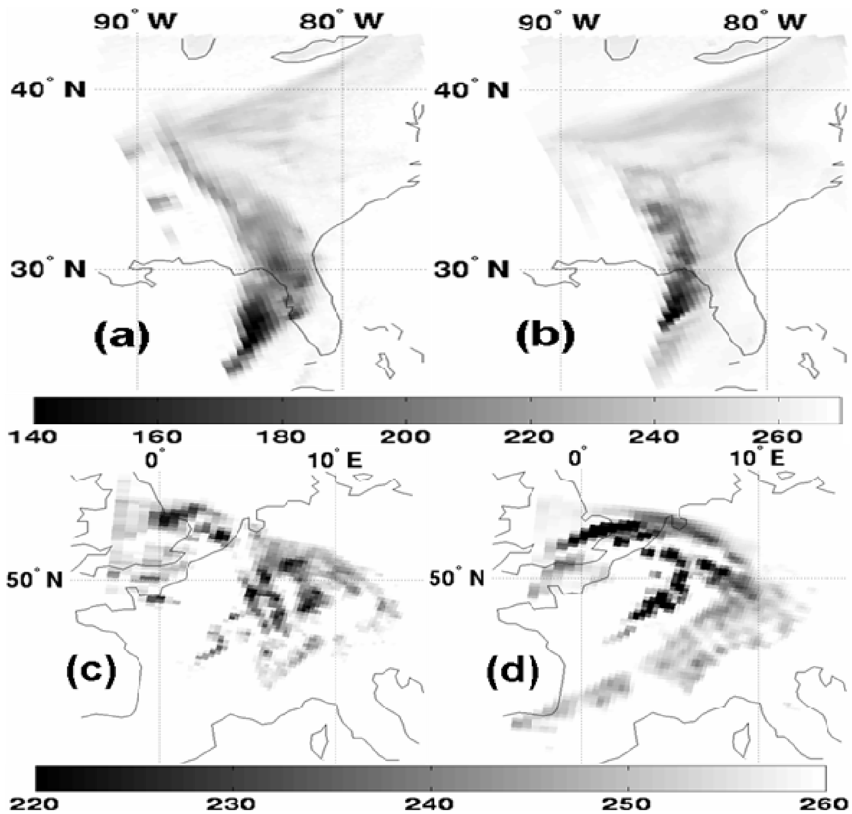

Fig. 3.3. Examples of acceptable forecast/AMSU. Brightness temperatures at 183±7 GHz: (a) T_B observed by AMSU at 2344 UTC 31 December 2002, (b) T_B predicted by NCEP/MM5 for (a), (c) T_B observed by AMSU at 1003 UTC 2 January 2003, (d) T_B predicted by NCEP/MM5 for (c).

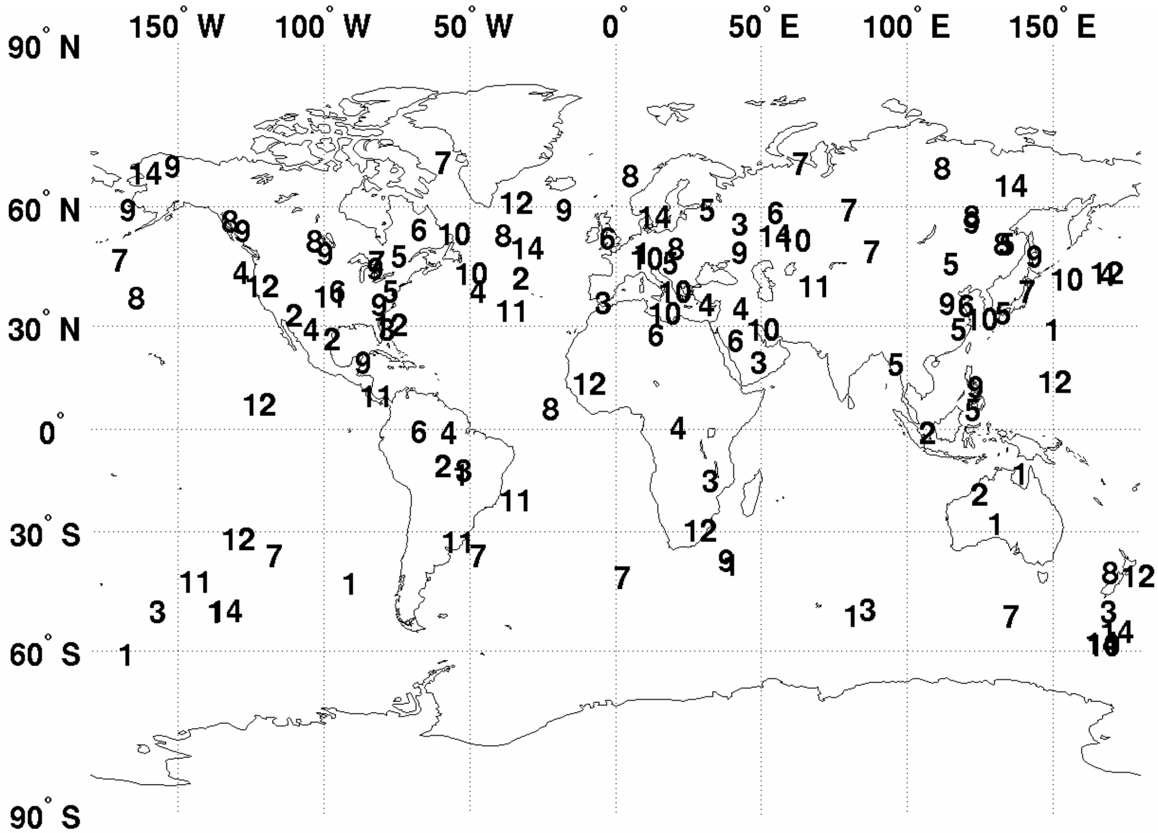

Fig. 3.4. 122 representative storm systems; the numbers 1-12 stand for January-December, and 14 indicates largely unglaciated cases.

TABLE 3.2
NUMBERS OF MM5 PRECIPITATING PIXELS (IN THOUSANDS)
IN VARIOUS PRECIPITATION CATEGORIES

Category	Pixels (000)	Category	Pixels (000)
$\lvert lat\rvert \le 25$	112	Winter	115
$25 < \lvert lat\rvert \le 55$	356	Spring	132
$55 < \lvert lat\rvert \le 90$	172	Summer	173
Convective	10	Autumn	221
Stratiform	631	Rain only	558
Non-glaciated (Land)	37	Mixed rain, snow	39
Non-glaciated (Ocean)	35	Snow only (per MM5)	44
		Snow only (surface T < 266K)	3

Chapter 4

AMSU vs MM5/TBSCAT Radiances, and EM Models for Hydrometeors

All results in this chapter are from [1].

4.1 Abstract

This chapter addresses: 1) millimeter-wave scattering by icy hydrometeors, and 2) the consistency between histograms of millimeter-wave atmospheric radiances observed by satellite instruments (AMSU-A/B) and those predicted by a mesoscale numerical weather prediction (NWP) model (MM5) in combination with a two-stream radiative transfer model (TBSCAT). This observed consistency at 15-km resolution supports use of MM5/TBSCAT as a useful simulation tool for designing and assessing global millimeter-wave systems for remotely sensing precipitation and related parameters at 50-200 GHz. MM5 was initialized by NCEP NWP analyses on a 1-degree grid approximately 5 hours prior to each AMSU transit and employed the Goddard explicit cloud physics model. The scattering behavior of icy hydrometeors, including snow and graupel, was assumed to be that of spheres having an ice density F(λ) and the same average Mie scattering cross-sections as computed using a discrete-dipole approximation implemented by DDSCAT for hexagonal plates and 6-pointed rosettes, respectively, which have typical dimensional ratios observed aloft. No tuning beyond the stated assumptions was employed. The validity of these approximations was tested by varying F(λ) for snow and graupel so as to minimize discrepancies between AMSU and MM5/TBSCAT radiance histograms over 122 global storms. Differences between these two independent determinations of F(λ) were less than ~0.1 for both snow and graupel. Histograms of radiances for AMSU and MM5/TBSCAT generally agree for 122 global storms and for subsets of convective, stratiform, snowy, and non-glaciated precipitation.

4.2 Introduction

Global monitoring of precipitation is important because of its significant human consequences. However, the multiplicity of hydrometeor types and their small- and large-scale spatial inhomogeneity make accurate measurements difficult. For example, rain gauge measurements are significantly impaired by wind, poor global coverage, and the non-uniformity of rain. Both ground-based radars and passive microwave satellite sensors sense precipitation aloft and are generally unable to discern how much of that precipitation evaporates before impact. Both are also sensitive to unknown local hydrometeor size, form, and vertical velocity distributions, as are simple single-frequency radars on satellites. The resulting lack of adequate ground truth seriously complicates development and validation of global precipitation sensing methods.

Fortunately, mesoscale and cloud-scale numerical weather prediction models such as the fifth-generation NCAR/Penn State Mesoscale Model (MM5) [6] have evolved to the point that they can provide substantially improved understanding of retrieval errors and their origins, as demonstrated in a preliminary way in this chapter.

The general goals of this chapter are therefore as follows: 1) to describe and evaluate a software testbed (NCEP/MM5/TBSCAT/F(λ)) that should enable more detailed understanding of the strengths and weaknesses of alternative millimeter-wave-based precipitation and hydrometeor profile estimation algorithms than can conventional ground-truth instruments; 2) to describe and evaluate a millimeter-wave radiative transfer algorithm (TBSCAT/F(λ)) useful in such a testbed; and 3) to describe and evaluate a configuration of MM5 appropriate for the same testbed.

Numerous references describe alternative radiative transfer algorithms useful at millimeter wavelengths [7], [36], [37], and others characterize MM5 modules that predict hydrometeor populations in explicit cloud models [30]-[32]. The principal contribution of this chapter is the demonstration that simple radiative transfer assumptions and simple models for icy hydrometeors are sufficient to match histograms of satellite-observed 50-190 GHz radiances to those based on coincident mesoscale weather prediction models incorporating explicit cloud models. Furthermore we found that this match is sensitive to relatively small departures from those assumptions, as discussed later.

Development of scattering models for various types of icy hydrometeors is described in Section 4.3. The initialization of MM5 and computation of predicted radiances using a radiative transfer program (TBSCAT) are then described in Section 4.4. Comparison of these predicted radiances with those observed by the Advanced Microwave Sounding Unit (AMSU) [23]-[24] on the United States National Ocean and Atmospheric Administration NOAA-15, -16, and -17 satellites is described in Section 4.5 together with an alternative characterization of scattering by graupel and snow that maximizes agreement between histograms of the predicted and AMSU-observed radiances. Section 4.6 compares the satellite and MM5 radiance histograms for a variety of precipitation types, showing that a single simple pair of ice factors F(λ) for graupel and snow results in reasonable agreement between MM5 and AMSU at all ice-affected frequencies and for essentially all precipitation types evaluated, including convective, stratiform, snow, and unglaciated precipitation. Section 4.7 then summarizes and concludes the chapter.

4.3 Electromagnetic Models for Known Ice Habits

Frozen hydrometeors usually assume habits resembling hexagonal columns, hexagonal plates, or rosettes. Since evaluation of electromagnetic wave interactions with these complex shapes is computationally expensive, icy hydrometeors were approximated by spheres that are mixtures of ice and air having average densities F(λ) ($0 < F < 1$) that depend on habit and wavelength λ. Hereafter this density parameter is called the ice factor F(λ). It is important to note that the density F(λ) can be quite different from the density of the ice itself (~0.9 g cm^{-3}) and different from the average ice density within an envelop bounding the hydrometeor. That is, F(λ) is defined as that density which yields the correct Mie scattering cross-section, as explained below, and can differ from common perceptions, as discussed in Section 2.2.3.

Liu [38] and others [39] have utilized this spherical approximation to hydrometeors at millimeter wavelengths, which simplifies computations because spherical hydrometeors are readily characterized by Mie scattering. For a sphere of given mass, F(λ) determines its volume; therefore the effective size distribution for a given set of spheres becomes a function of wavelength in this approximation.

The density F was then used to determine an effective complex electric permittivity ε of each sphere using an ice-air mixing model in which ice inclusions are distributed within an air matrix [17]-[18]. As explained further below, to find F(λ) the average electromagnetic scattering cross-section of each ice habit was computed using the Discrete Dipole Approximation program, DDSCAT6.1 [14], and equated to the Mie scattering cross-section of an equal-mass sphere having the ice factor F(λ).

4.3.1 Discrete Dipole Approximation Program DDSCAT6.1

The discrete dipole approximation represents the target by a dense finite array of polarizable points. It can approximate electromagnetic extinction, scattering, and absorption by arbitrary geometries with dimensions smaller than a few wavelengths [14].

4.3.2 Ice Models

The ice models studied include spheres, hexagonal columns, hexagonal plates, and bullet rosettes having the densities and shapes of observed ice habits [40]-[42]. Bullet rosettes here comprise three long orthogonal hexagonal columns joined at their centers to form a three-dimensional orthogonal cross. These model densities and shapes are listed in Table 4.1, where S and L are the small and large dimensions, respectively. The shapes and dimensions are also illustrated in Fig. 4.3. The hydrometeor lengths varied from 0.2 to 5 mm. Snow was modeled as hexagonal plates and graupel was modeled as 6-point bullet rosettes. Cloud ice and all liquid hydrometeors, including rain water and cloud liquid water, were ultimately modeled as spheres.

TABLE 4.1
OBSERVED ICE HABIT DIMENSIONS AND DENSITIES

Ice Habit	Dimensional Ratios (mm)	Densities [40] (g cm^{-3})
Column	$S = 0.238 \cdot L^{0.938}$ [41]	$0.848 \cdot L^{-0.014}$
Plate	$S = 0.0478 \cdot L^{0.474}$ [42]	0.9
Rosette	$S = 0.185 \cdot L^{0.532}$ [40]	$0.848 \cdot L^{-0.014}$

4.3.3 Ice Factors of Spheres Best Imitating Snow and Graupel

Fig. 4.1 illustrates the method used to find F(λ) for spheres having the same mass and the same Mie scattering cross-sections as hexagonal plates (snow) and rosettes (graupel) computed by DDSCAT. The scattering and absorption cross-sections computed using DDSCAT6.1 were averaged over 125 target orientations of the ice models; some orientations were redundant, depending on hydrometeor geometry. To simplify the DDSCAT computations, ice temperatures of -15°C were assumed since the permittivity of cold ice is a weak function of temperature. Since the absorption cross-sections for ice were much smaller than the scattering cross-sections, they did not influence F(λ). Although functions of the angular scattering behavior other than the average scattering cross-section could have been matched between Mie and DDSCAT, this simplification worked well, as shown in Sections 4.5 and 4.6. This is not entirely unexpected since the average permittivity over all habit orientations would be spherically symmetric.

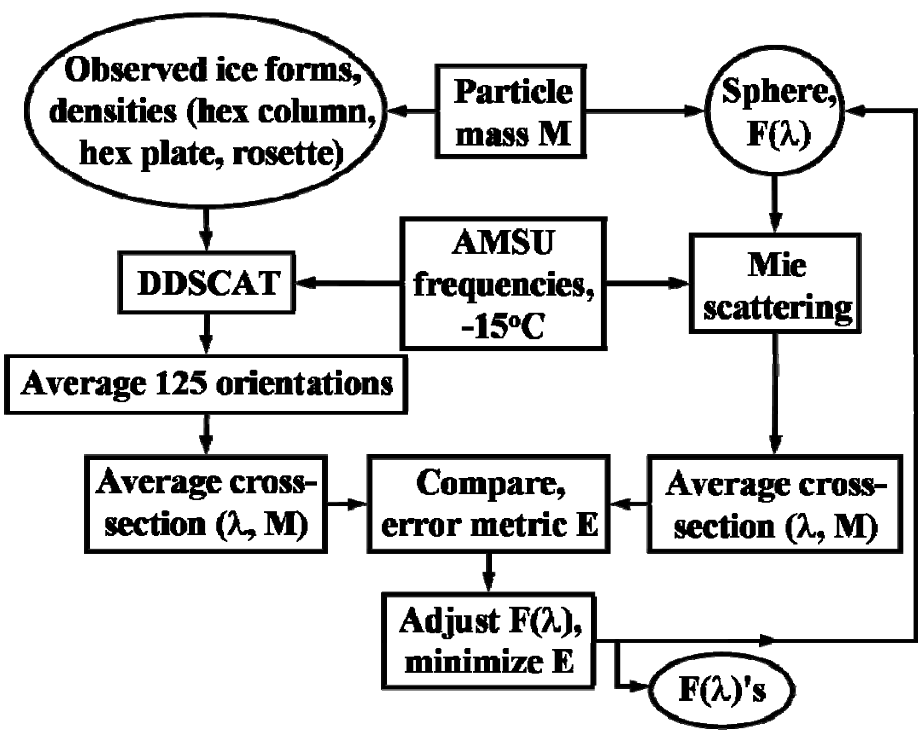

Fig. 4.1. Method for using DDSCAT to yield ice factors F(λ) for graupel and snow.

4.3.4 Results

Fig. 4.2 illustrates the sensitivity of the computed scattering cross-sections to both F(λ) and particle size L for the representative cases of hexagonal plates at 89.9 GHz and rosettes at 183±7 GHz. Thus the illustrated scattering cross-sections of hexagonal plates and equal-mass spheres are equal if F(λ) = 0.2±0.02. Fig. 4.2 also reveals the important fact that F(λ) is largely independent of particle size L for hexagonal plates and rosettes, so assumptions in MM5/TBSCAT about hydrometeor size distributions do not impact F(λ), although they do impact the computed scattering itself. Although hexagonal columns exhibit some dependence on L, they appear to be less influential in controlling emission spectra, as discussed in Section 4.5.1. Fig. 4.2 also shows the back-scattering fraction β for hexagonal plates, rosettes, and spheres for specific cases. In a two-stream radiative transfer model β is the fraction of the scattered energy directed backwards. For both snow and graupel β decays monotonically with length, although for graupel the decay for equal-mass spheres is more rapid, potentially leading to TBSCAT overestimates of graupel brightness temperatures. One possible implication of this is addressed in Section 4.7.

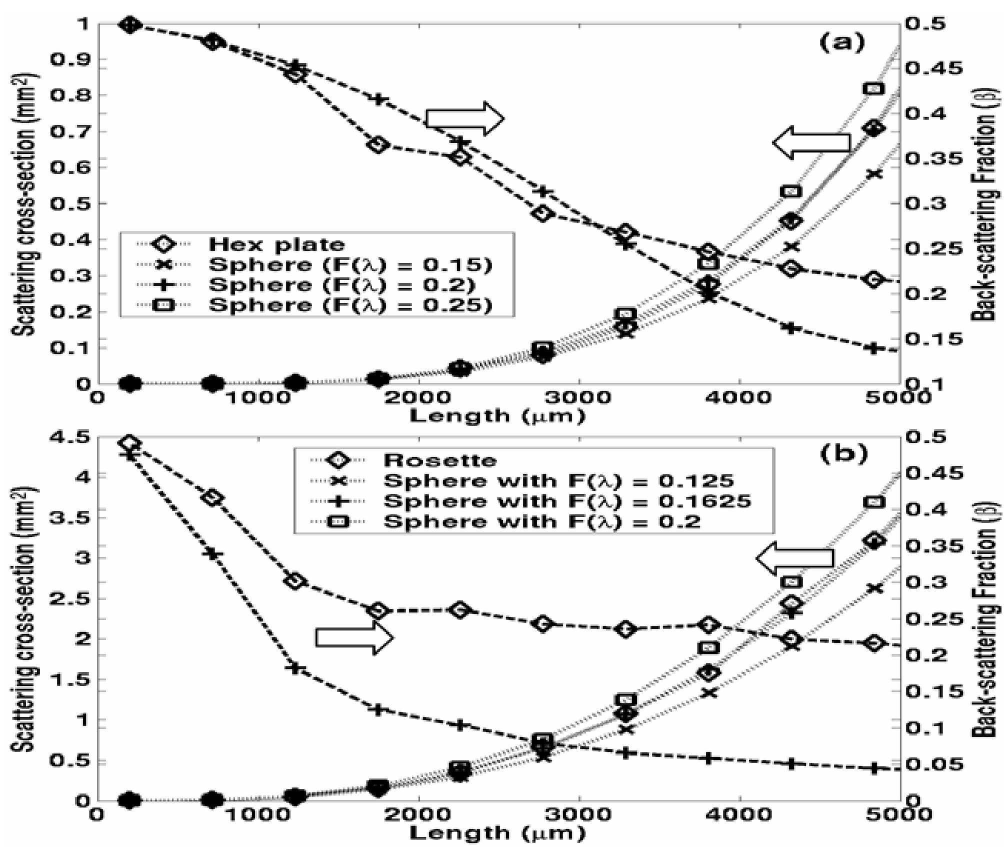

Fig. 4.2. Scattering cross-sections and back-scattering fractions as a function of particle length L for (a) hexagonal plates at 89.9 GHz and (b) rosettes at 183±7 GHz, both compared to those of equal-mass spheres having three different values for F(λ).

Such estimates for F(λ) for all AMSU frequencies are plotted in Fig. 4.3 for spheres, columns, plates, and rosettes. Those for hexagonal plates (snow) and rosettes (graupel) are fit to a minimum-square-error straight-line function of λ. Table 4.2 presents equations for the best-fit ice factors F(λ) for snow, graupel, and cloud ice (spheres), as derived from DDSCAT. These expressions lose some validity above 200 GHz because F(λ) becomes size dependent, and because expressions for permittivity become less certain. The formulas in Table 4.2 are generally consistent with the findings of Liu [38] that at the longer millimeter wavelengths lower density (softer) ice spheres match DDSCAT computations better. The weak dependence of F(λ) upon hydrometeor size distribution below 200 GHz reduces any incentive to make F(λ) size or altitude dependent. Although F(λ) for graupel is less than for snow for a given length L, implying that graupel might scatter less, this effect is compensated by the tendency for graupel to be larger and to have water paths several times greater; stronger scattering by graupel relative to snow is evident later in the simulated brightness images of Figs. 3.1 – 3.3.

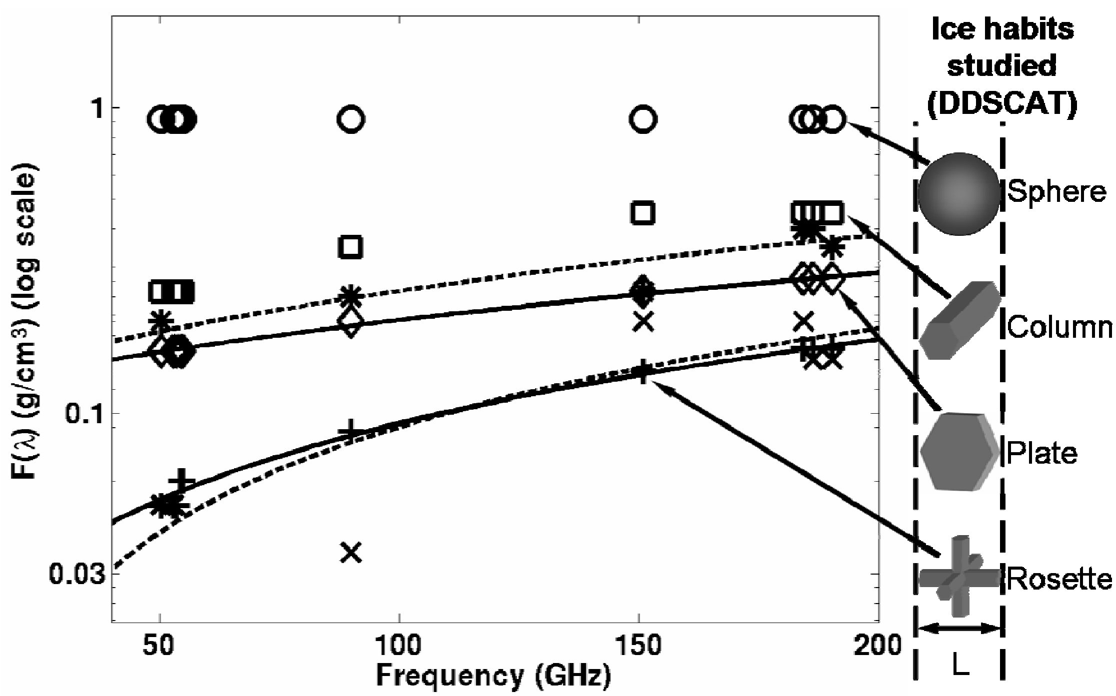

Fig. 4.3. Values for F(λ) that match the scattering cross-sections of spheres (○), hexagonal columns (□), hexagonal plates (◊), and rosettes (+) found using DDSCAT, and the corresponding best-fit linear approximations (solid lines). Best-fit values for $F_{opt}(\lambda)$ for snow (*) and graupel (x) found from MM5/AMSU comparisons, and the corresponding best-fit linear approximations (dashed lines).

TABLE 4.2
ICE FACTORS FOR SNOW, GRAUPEL, AND CLOUD ICE BASED ON DDSCAT

Ice Species	Ice Factors ($F(\lambda)$) ($g\ cm^{-3}$)
Snow	$0.863 \cdot f_{THz} + 0.115$
Graupel	$0.815 \cdot f_{THz} + 0.0112$
Cloud ice	0.917

f_{THz} is frequency in units of THz.

4.4 Computation of MM5/TSCAT Predicted Radiances

The generation of microwave brightness temperature images from numerical weather prediction models had several steps. First, United States National Center for Environmental Prediction (NCEP) analyses at ~110-km resolution were interpolated to times 4-6 hours prior to passage of the satellites over storm systems, and were then used to initialize MM5 at the outermost domain (45-km resolution). The atmospheric states predicted by MM5 at the time of satellite transit were input to the radiative transfer program TBSCAT [7] in its two-stream formulation to simulate AMSU millimeter-wave brightness temperatures (T_B's) using the $F(\lambda)$ values presented in Table 4.2. All brightness temperature comparison presented in this chapter is over 122 global storms from July 2002 to June 2003 with details discussed earlier in Section 3.2.

AMSU-A and AMSU-B radiances were simulated by using a forward radiance program, TBSCAT, in its two-stream Mie-scattering approximation. TBSCAT was developed and provided by P. W. Rosenkranz (personal communication) based on his radiative transfer algorithm [7], improvements on standard millimeter-wave atmospheric transmittance models [43]-[44], and the complex permittivities for water and ice given by [15] and [16], respectively. To simulate brightness temperatures using TBSCAT, all hydrometeors were assumed to be spherical and homogeneous [45]-[46] with size distributions that are inverse-exponential functions of diameter as given in (3.1), where $F(\lambda)$ for each ice species was used in place of the density ρ. Because $F(\lambda)$ is generally not dependent upon hydrometeor diameters below 200 GHz, $F(\lambda)$ was made independent of altitude or size distribution functions.

The surface emissivity for ocean was computed using FASTEM [47], where the sea surface temperature and wind at 10 meters were provided by MM5. This program includes the effects of geometric optics, Bragg scattering, and foam coverage. Since there was no prior knowledge of land emissivity, it was assumed to be uniformly distributed randomly between 0.91 and 0.97, which are typical values [48]. The atmosphere is sufficiently opaque at these frequencies that surface emissivity errors are usually secondary except over dry snow (e.g. the coldest pixels in Fig. 4.12(a) at 89 and 150 GHz), and over water misclassified as land (e.g. a few pixels along the Amazon river; see Fig. 4.12(b) at 89 GHz and Fig. 4.14 at 89 and 150 GHz). Furthermore, although random land emissivities within the assumed range noticeably alter the simulated brightness for individual pixels, such random shuffling does not alter the brightness histograms much.

Since computing MM5 forecasts with 5-km resolution over the full swath width observed by satellites would have been prohibitively time consuming, only the 15-km MM5 domain-2 output was utilized, even though the inner ~1000-km domain-3 block had 5-km resolution. To validate MM5 domain-2 outputs at 15-km resolution, brightness temperatures for AMSU channels above 85 GHz simulated by using MM5 domain-2 outputs (15-km resolution) were compared with those simulated by using MM5 domain-3 outputs (5-km resolution) for 24 test cases, where the 5-km resolution brightness temperatures were first smoothed using a Gaussian filter with a full-width-half-maximum (FWHM) resolution of 15 km. A sample histogram comparison is shown in Fig. 4.4, which exhibits good agreement. Based on this agreement and the excessive computer time that would have been required for TBSCAT simulations at 5-km resolution over comparable global areas, all MM5 comparisons with satellite data were performed using MM5 domain-2 outputs at 15-km resolution.

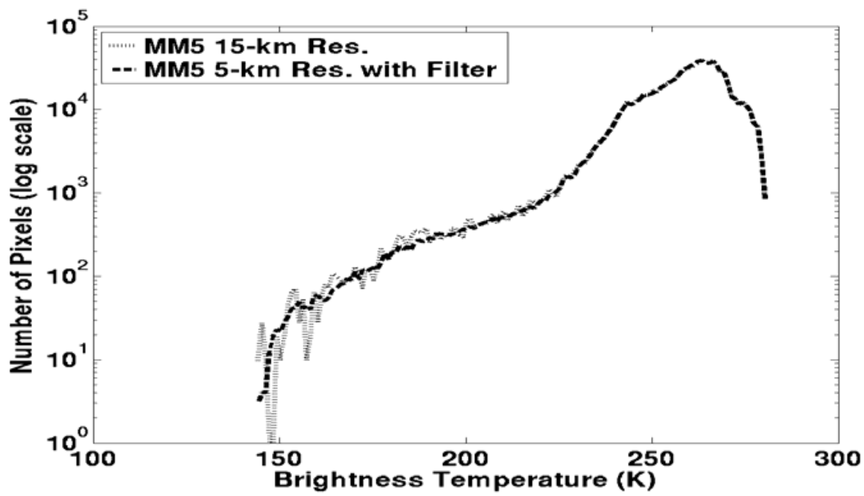

Fig. 4.4. Comparison of MM5 183.3±7 GHz brightness temperatures at 15-km resolution with those simulated by filtering MM5 5-km resolution output with a 15-km Gaussian filter. The histograms present the numbers of samples within each 1-K interval.

To simulate AMSU-A radiances, a Gaussian filter with 50-km FWHM resolution was used to smooth 15-km resolution MM5 radiances. Radiances were computed using TBSCAT at the appropriate incidence angle, and assuming constant 50-km resolution without compensating for blurring at extreme scan angles.

4.5 Comparison of MM5/TBSCAT and AMSU Radiances

The radiance-simulation algorithm NCEP/MM5/TBSCAT/F(λ) has no discretionary parameters other than the choice of this particular combination of routines and physical models. The validity of the resulting radiance simulations were evaluated by comparing them to AMSU observations in two ways. First the AMSU radiance histograms were compared to those generated using NCEP/MM5/TBSCAT/F(λ) for the same global set of 122 storms. Section 4.5 presents a preliminary comparison and Section 4.6 presents comparisons for specific types of precipitation. Second, the MM5/TBSCAT/F(λ) simulated radiance histograms were made to approximate those observed by AMSU by adjusting F(λ) for each of snow and graupel to see how well these empirically optimized values of F(λ) agreed with those derived in Section 4.3.4 using DDSCAT.

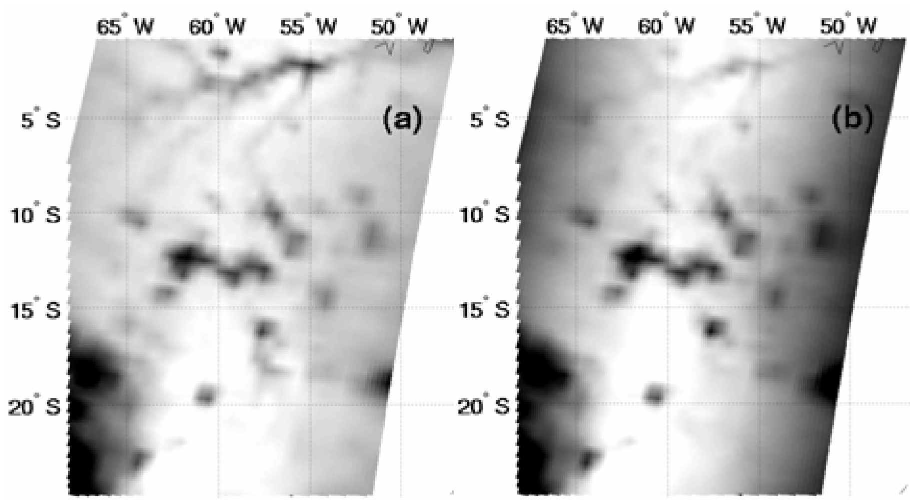

Fig. 4.5. Satellite radiances near 50.3 GHz (a) and 52.8 GHz (b); precipitation appears colder (darker), similar to the limb effects seen in (b).

Because the ice factor F(λ) is a weak function of λ, it suffices to evaluate F at only one representative frequency in the 54-GHz band--that frequency with the best ice signature relative to surface "noise". The strongest ice signatures in the 54-GHz band appear in the most transparent channels at 50.3 and 52.8 GHz. The other channels in this band sound levels above some or all of the ice aloft. Fig. 4.5(b) shows that the 52.8-GHz channel of AMSU-A exhibits limb effects at larger scan angles that resemble the signatures from ice aloft, while the 50.3-GHz channel (Fig. 4.5(a)) distinguishes precipitation much more clearly. Therefore only the 50.3-GHz channel was analyzed in this band.

The surface effects for the window channels, including AMSU-A channels 1-4 and AMSU-B channels 1-2, were diminished by evaluating only pixels over land at those frequencies, thus reducing the effects of highly reflective water surfaces that mimic icy signatures. For example, the AMSU and MM5 land/sea flags excluded from the radiance histograms most of the Amazon River pixels visible in the top part of Fig. 4.5(a). Low radiances in these channels produced by highly reflective high-altitude snow were largely avoided by excluding pixels having |lat| > 60^o and terrain elevation above 500 m. Because icy hydrometeor signatures generally do not contribute to brightness temperatures above ~260K, histogram inconsistencies there are generally insensitive to F(λ).

Subject to the restrictions noted above, the radiance histograms in Fig. 4.6(a) suggest that good agreement was obtained between MM5-simulated and satellite-observed radiances over 122 representative storm systems that contain over 185,580 AMSU-A (23-90 GHz) and 1,674,964 AMSU-B (88-191 GHz) footprints. In the figure the AMSU channels are arranged in order of increasing opacity: 50.3, 89, 150, 183±7, 183±3, and 183±1 GHz; the 89 GHz data was observed by AMSU-B. The high sensitivity of this comparison to the ice factor F(λ) used in TBSCAT is indicated in Fig. 4.6(b), for which F(λ) was increased by 0.05 at all frequencies for both snow and graupel; the effects of the small cloud ice particles are not evident in these histograms. The small differences between Figs. 4.6(a) and 4.6(b) at certain wavelengths suggest that ice effects near 50.3 GHz are also small and that the 183±1 GHz weighting function peaks above most ice aloft. The largest differences between AMSU and MM5 in Fig. 4.6(a) (at 150 GHz) are small compared to those induced when the ice factor is increased slightly (Fig. 4.6(b)).

Histograms like those in Fig. 4.6 are used extensively in this chapter. Their main purpose is to illustrate the differences between AMSU and MM5 brightnesses, not their absolute values, which are included with stated offsets. These differences between AMSU and MM5 histograms are generally smaller than those induced by minor adjustments of the model itself, as Fig. 4.6(b) illustrates.

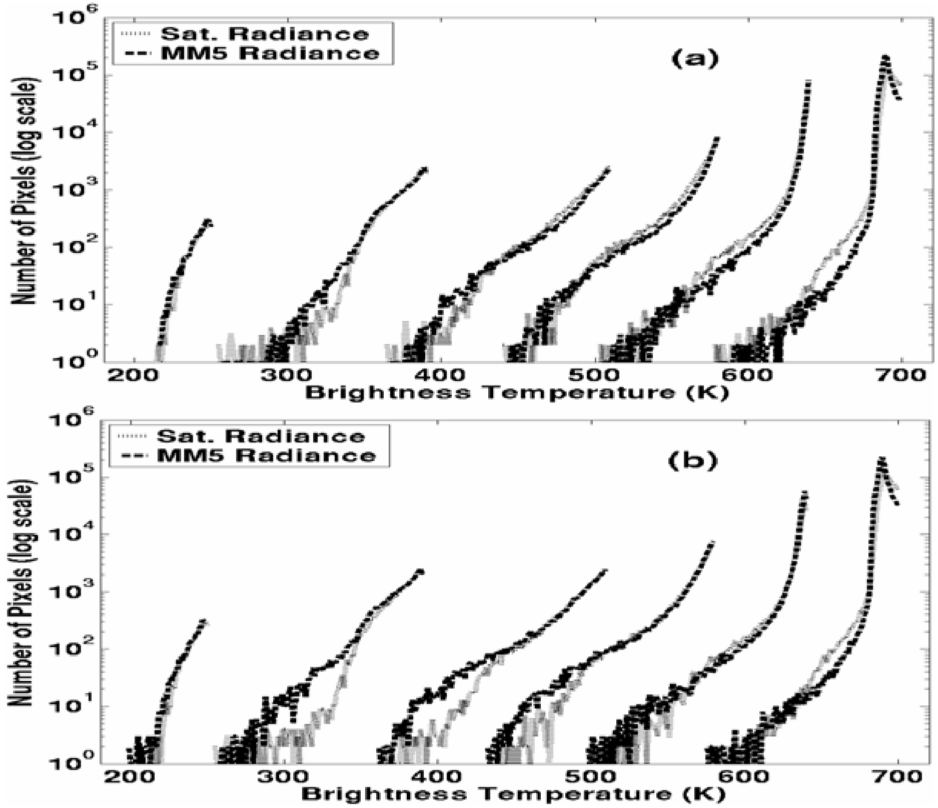

Fig. 4.6. Brightness temperature histograms (pixels per degree K) for channels near 50.3, 89, 150, 183±7, 183±3, and 183±1 GHz, in order of increasing opacity from left to right, for 122 storms using: (a) F(λ) and (b) F(λ)+0.05. Only T_B's below 250 K are plotted. For clarity, the absolute T_B's were shifted to the right by 0, 140, 260, 330, 390, and 450 K, respectively.

4.5.1 Best-fit Ice Factors for Snow and Graupel

To help validate the values of F(λ) found for snow and graupel using DDSCAT, F(λ) for these two species was also found empirically by minimizing at each frequency separately the difference between radiance histograms produced by AMSU and NCEP/MM5/TBSCAT/F(λ) for 122 storms. Since cloud ice particles are generally too small to affect millimeter-wave brightness temperatures, the value for F(λ) in Table 4.2 was used instead. The error metric for the difference between two histograms is defined as:

$$E = \sum_{i=1}^{n}\left[\left(N_{SAT_i} - N_{MM5_i}\right)^2 \Big/ \left(N_{SAT_i} + N_{MM5_i}\right)^2\right] \quad (4.1)$$

where each bin i corresponds to a brightness temperature, and N_{SATi} and N_{MM5i} are, respectively, the number of satellite-observed radiance pixels and MM5-simulated radiance pixels falling in radiance bin i for all 122 storms. The denominator normalizes the histogram, increasing the relative contribution to E of the coldest ice-sensitive pixels relative to the far more numerous brighter pixels unaffected by ice. The algorithm used to find the values F(λ) that minimize E is presented in Fig. 4.7.

The resulting values of $F_{opt}(\lambda)$ for snow and graupel are presented in Fig. 4.3, and are fit to straight lines that minimize mean-square-error on a linear scale. The best-fit straight line to F(λ) for snow differs from that for hexagonal plates, as computed using DDSCAT, no more than 0.096 out of 0.38 (25 percent), this worst case being at 200 GHz. The best-fit line for graupel differs from that computed for rosettes no more than 0.015 out of 0.19 (8 percent). The F values for hexagonal columns and spheres deduced from DDSCAT differ so greatly from the graupel and snow values found from the MM5/AMSU comparisons that these ice habits are unlikely to be major contributors to AMSU observations, as expected.

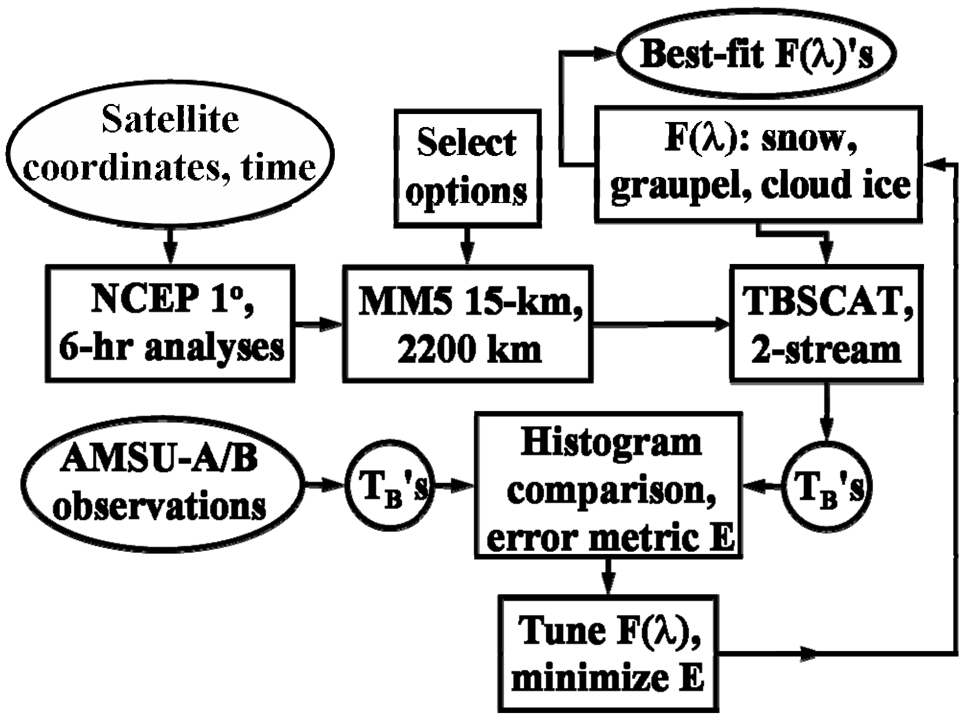

Fig. 4.7. Method for comparing AMSU observations with MM5/TBSCAT radiance predictions to yield best-fit ice factors $F_{opt}(\lambda)$ for graupel and snow.

4.6 Tests of Ice Factor Validity

To test the validity of the values for F(λ) given by the DDSCAT experiment results, brightness temperatures were computed using MM5/TBSCAT/F(λ) for 122 storms. The

T_B histograms in Fig. 4.6 suggest that the DDSCAT values of $F(\lambda)$ are usually within ~0.1 of those providing optimum agreement. This global agreement was then tested further by separating the data into different latitude bands and precipitation types. Note that part of the discrepancy between histograms considered below could be due to misclassification of precipitation type.

4.6.1 Histogram Comparisons for Different Latitude Bands

The 122 storm systems were divided into three different latitude bands: $|lat| \leq 25$; $25 < |lat| \leq 55$; and $55 < |lat| \leq 83$. Each latitude band continues to show good agreement at all frequencies, as illustrated in Fig. 4.8. The worst discrepancy, somewhat less than that due to a modest ice factor increment of 0.05 (see Fig. 4.6), occurs at 89 GHz in the tropics, where MM5/TBSCAT/$F(\lambda)$ produces too many cold pixels. This residual discrepancy could originate from: 1) any of the radiative transfer approximations, 2) excessively concentrated convection arising from the initial NCEP fields, as suggested in Fig. 3.2(b), or 3) excessive convective strength and graupel production by MM5. Radiative transfer approximations include use of: $F(\lambda)$ for Mie spheres, a two-stream scattering model, the assumed hydrometeor form factors, and the method of fitting $F(\lambda)$ to total DDSCAT scattering cross-section rather than to some other angular scattering function. Further extensive comparisons of models and observations would be required to evaluate these alternative explanations. The mismatches for the ~100 coldest pixels in Fig. 4.8(c) at 183±3 and 183±1 GHz are generally not due to MM5 or radiative transfer flaws, but to extremely dry air that was not anticipated by NCEP/MM5 and that exposes highly reflective dry snow.

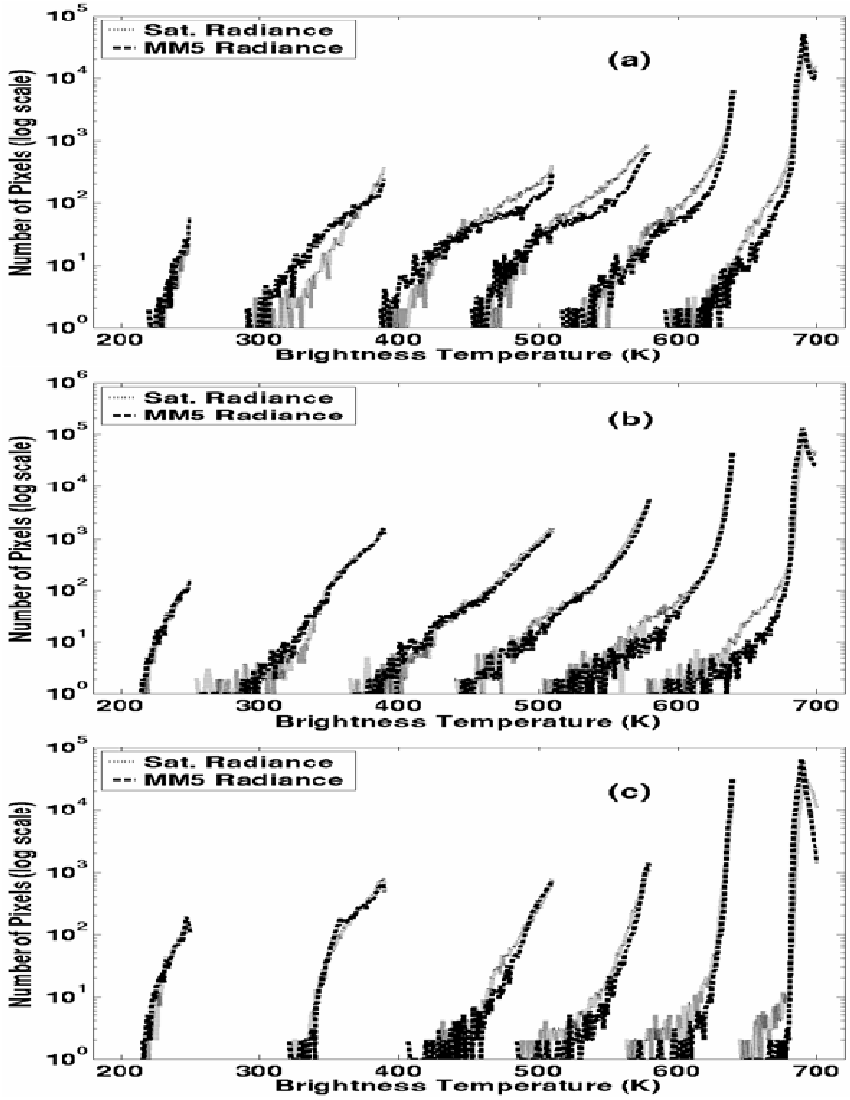

Fig. 4.8. Brightness temperature histograms (pixels per degree K) for channels near 50.3, 89, 150, 183±7, 183±3, and 183±1 GHz, in order of increasing opacity from left to right, for 122 storms: (a) |lat| ≤ 25, (b) 25 < |lat| ≤ 55, and (c) 55 < |lat| ≤ 83. Only T_B's below 250 K are plotted. For clarity, the absolute T_B's were shifted to the right by 0, 140, 260, 330, 390, and 450 K, respectively.

4.6.2 Histogram Comparisons for Various Precipitation Types

To further test these results, the precipitating pixels in the 122 storm systems were categorized as convective, stratiform, snow storm, and non-glaciated. The same radiance algorithm was used for classifying both AMSU and MM5 pixels, although this categorization selected different pixels for AMSU and MM5 data because their convective cells were located differently. Since our purpose here is only to support histogram comparisons that might reveal weaknesses in the observed global consistency of MM5/TBSCAT/F(λ)/AMSU comparisons, perfect separation by precipitation type is not required.

4.6.2.1 Convective versus Stratiform Precipitation

The estimated peak vertical wind (w_{peak}) for each pixel was used to distinguish convective from stratiform precipitation. Pixels were flagged as convective when the estimated peak vertical wind exceeded 0.45 ms^{-1}. Higher wind threshold values would be more appropriate for spatial resolutions of 5 km or less, as opposed to the 15-km resolution velocities used here. The 0.45 ms^{-1} threshold was that value which balanced and minimized the errors when dividing pixels into convective and stratiform classes using the neural network described below.

Fifteen percent of the MM5-simulated radiances and corresponding vertical winds were used as statistical ground-truth to train a neural network to estimate peak layer vertical wind by using AMSU-B observations at the three frequencies near 183 GHz, which have ice signatures strongly correlated with vertical wind speed. The MM5 peak vertical wind was negatively correlated with brightness temperatures at 150, 183±7, 183±3, and 183±1 GHz with correlation coefficients of -0.2, -0.53, -0.43, and -0.25, respectively, for the test ensemble of storms. These correlation coefficients were less than 0.08 for the other AMSU channels. Different neural network configurations were tested for their ability to estimate peak vertical wind. The best configuration employed three layers comprising 10, 5, and 1 neurons. Tan-sigmoid transfer functions were used for neurons in the first two layers, and a linear transfer function was used at the output. The Levenberg-Marquardt [49] training algorithm has been shown to be efficient [22] and was used. To facilitate convergence of the neural net weights during training, the weights of the neural net were initialized by using the Nguyen-Widrow method [50].

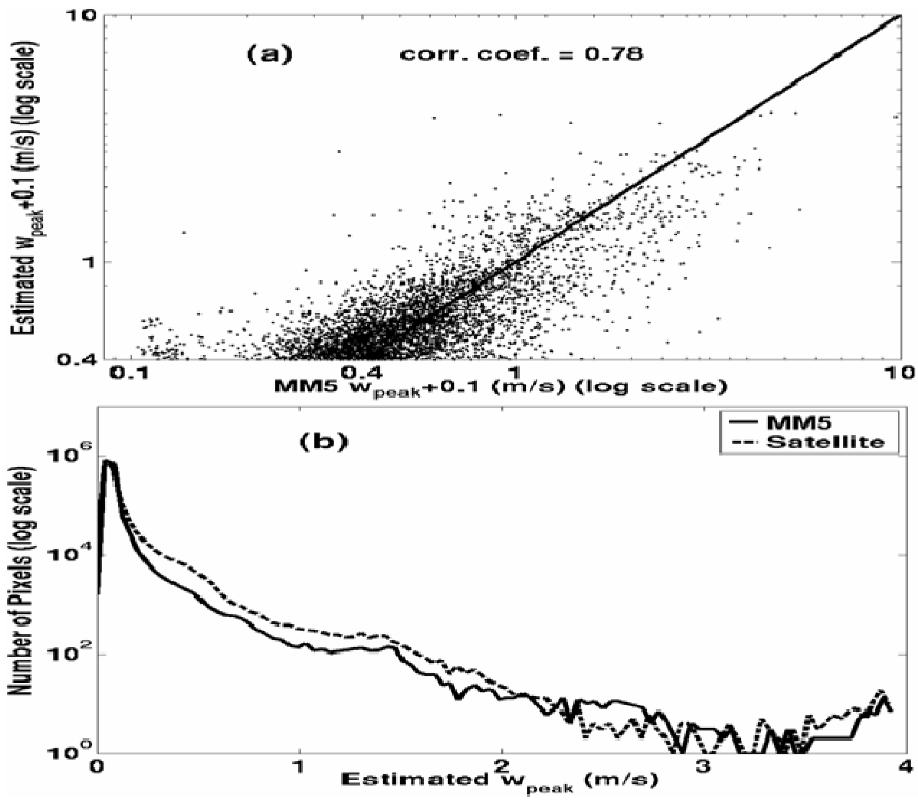

Fig. 4.9. Performance of the peak vertical wind (w_{peak}) estimator: (a) Every 5th pixel of estimated w_{peak} vs. MM5 truth, and (b) histogram comparisons over 100 linear-scale bins of MM5-estimated and satellite estimated w_{peak} values.

Fig. 4.9(a) plots every 5th pixel of estimated MM5 peak vertical wind w_{peak} versus MM5 truth. This estimator misclassifies 25 and 26.6 percent of MM5 stratiform and convective pixels, respectively. Fig. 4.9(b) exhibits general agreement between histograms for w_{peak} estimated by using AMSU and MM5-simulated radiances, with AMSU sensing roughly twice as many "convective" pixels, presumably due to the larger sizes of AMSU-sensed cirrus anvils relative to the convective columns below. Based on this classification, Fig. 4.10 exhibits good agreement between MM5/TBSCAT and AMSU brightness temperature histograms for both convective and stratiform precipitation. The small differences between simulated and observed radiances in the stratiform case could be due to surface effects, small values for F(λ, stratiform), or weak MM5 stratiform hydrometeor production; these differences are again smaller than those associated with an ice factor increment of 0.05.

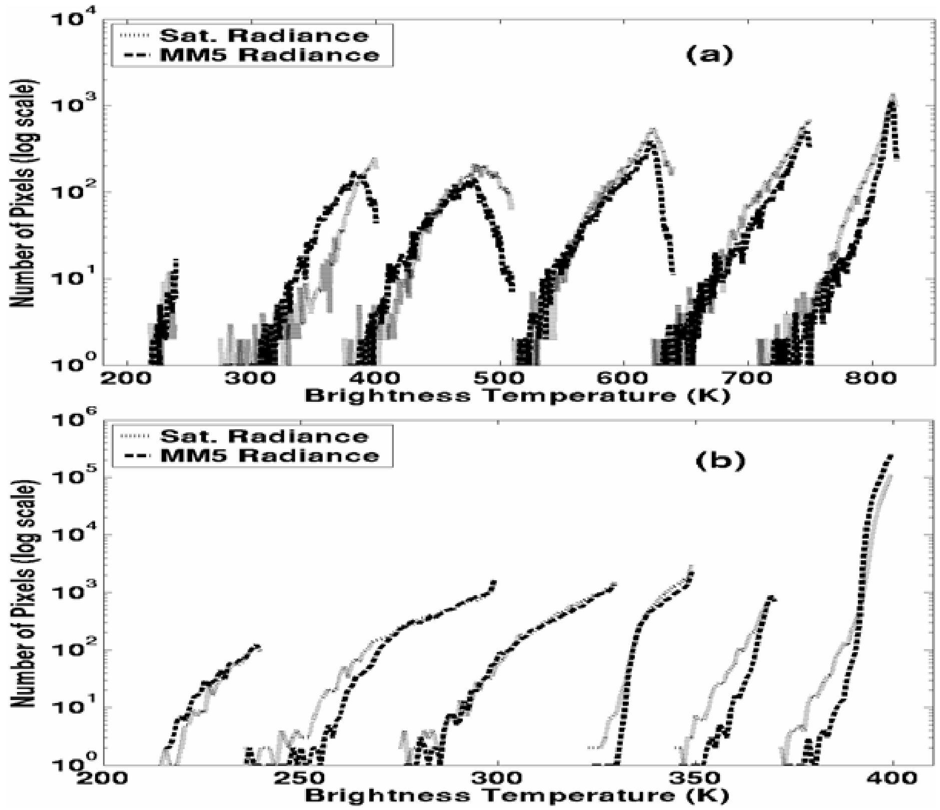

Fig. 4.10. Brightness temperature histograms (pixels per degree K) for AMSU and MM5 channels near 50.3, 89, 150, 183±7, 183±3, and 183±1 GHz, in order of increasing opacity from left to right: (a) convective pixels, and (b) stratiform pixels. Only T_B's below 240 K are plotted. For clarity, the absolute T_B's were shifted to the right by 0, 160, 270, 400, 510, and 580 K, respectively, for (a), and 0, 60, 90, 110, 130, and 160 K, respectively, for (b).

4.6.2.2 Snow versus Rain

All precipitating pixels in the set of 122 storms were divided into rain and snow categories using MM5 surface temperature as the predictor and the hydrometeor state at the MM5 1000-mbar level as the criterion, as illustrated in Fig. 4.11. To reduce the risk of pixel misclassification, only those with MM5 surface temperatures below 266K were designated "snow", and only those above 294K were designated "rain". Based on this classification, Fig. 4.12 exhibits good agreement between MM5/TBSCAT and AMSU brightness temperature histograms for both rain and snow. The substantial discrepancies at 89 and 150 GHz are most likely due to our simplified assumption that land surface emissivities range randomly between 0.91 and 0.97, whereas the emissivity of dry fallen snow can drop below 0.8 to produce the histograms presented in Figure 4.12(a). Under this hypothesis the observed histogram agreement at 50.3 and 183±7 GHz could result if the fallen snow were sufficiently shallow that it could still be penetrated at 50 GHz, and if the humidity were sufficiently high that 183±7 GHz retained some limited opacity. Since "snow" was defined as those few pixels where the MM5 surface temperature was below 266K, these results could be due to only ~1600 shallow-snow pixels out of ~3000, and less than one-tenth of a single MM5 image. The alternative hypothesis that falling snow has an unexpectedly high albedo near 89-150 GHz is not readily reconciled with the noticeably higher brightness temperatures seen at 183±7 GHz, a frequency that normally penetrates at least to the upper levels of any snowstorm so as to be similarly affected. Thus validating dry snowfall observations requires knowledge of the surface emissivity spectrum for those channels that sense it, where this spectrum may depend on snow depth, temperature, and history [51]. The small gaps in Fig. 4.12(b) near 210K in these histograms are most likely due to excessive upper tropospheric humidity in the NCEP initializations, as explained later in Section 7.3.4.

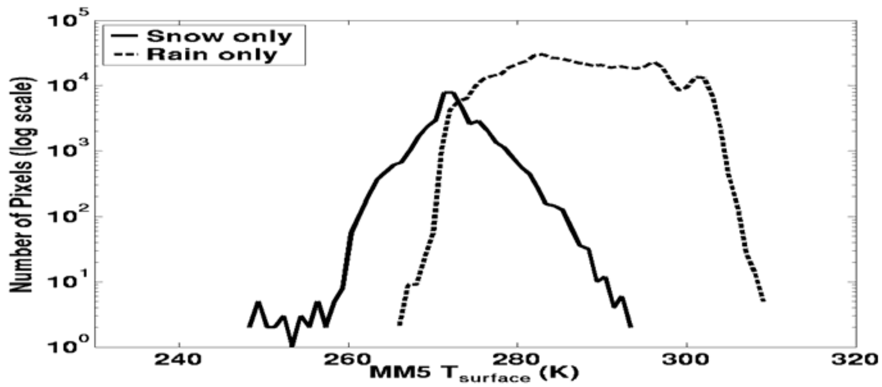

Fig. 4.11. Histograms (pixels per degree K) for MM5 surface rain and snow classifications, as a function of MM5 predicted surface temperature.

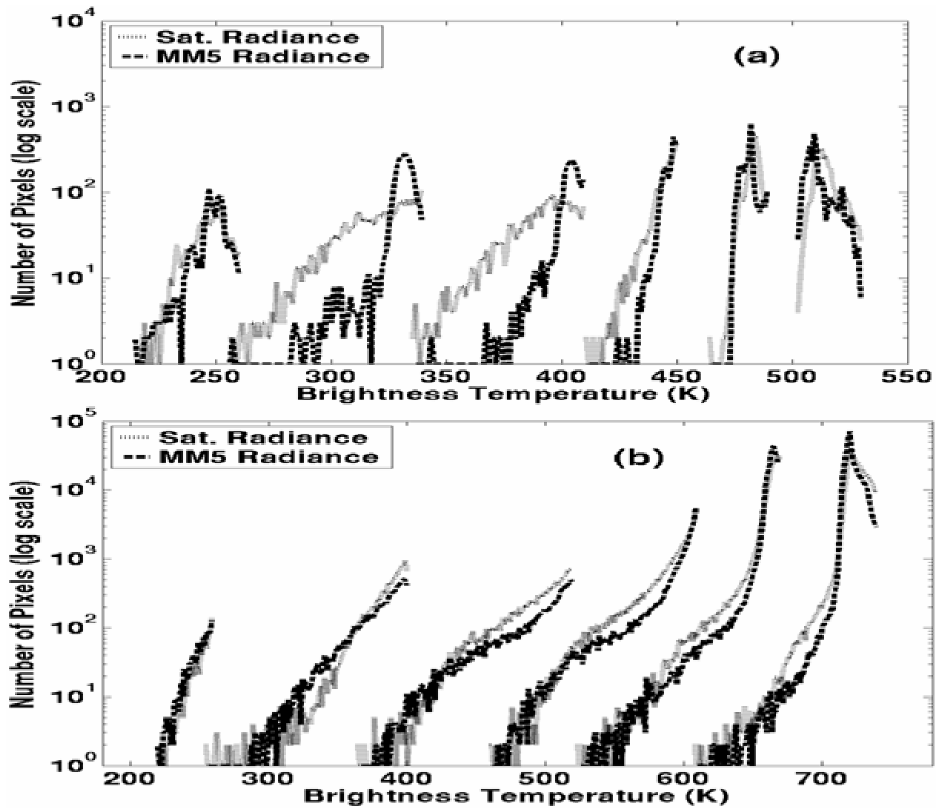

Fig. 4.12. Brightness temperature histograms (pixels per degree K) for AMSU and MM5 channels near 50.3, 89, 150, 183±7, 183±3, and 183±1 GHz, in order of increasing opacity from left to right: (a) snowing pixels, and (b) raining pixels. Only T_B's below 260 K are plotted. For clarity, the absolute T_B's were shifted to the right by 0, 80, 150, 190, 230, and 270 K for (a) and 0, 140, 260, 350, 410, and 480 K for (b).

4.6.2.3 Non-glaciated Rain

A pixel was classified as non-glaciated rain if T_B(183±7 GHz) ≥ 250 K, and over 0.1-mm integrated rain water W were retrieved. The neural network used for estimating W was trained using 15 percent of the MM5 simulations for 122 storms; the inputs were brightness temperatures at all five AMSU frequencies above 85 GHz. Tests of various network architectures led to the same architecture found for estimating vertical winds. Every 50th estimate of the rain water W is plotted versus the corresponding "true" MM5 value in Fig. 4.13(a), and Fig. 4.13(b) exhibits general agreement between histograms for W values estimated by using AMSU and MM5-simulated radiances. Utilizing this classification scheme, Fig. 4.14 exhibits good agreement between MM5 and observed AMSU brightness temperature histograms for non-glaciated rain (e.g., warm rain). The limited brightness range shown for 183±7 GHz is due to the definition used here for non-glaciated precipitation—T_B must be equal or greater than 250K, and only T_B's below 260K are plotted. Those few pixels that AMSU observed at 89 and 150 GHz with brightness temperatures of ~220K, about 10 degrees below MM5 predictions, may have been glaciated despite having been classified otherwise, or may backscatter more efficiently than expected.

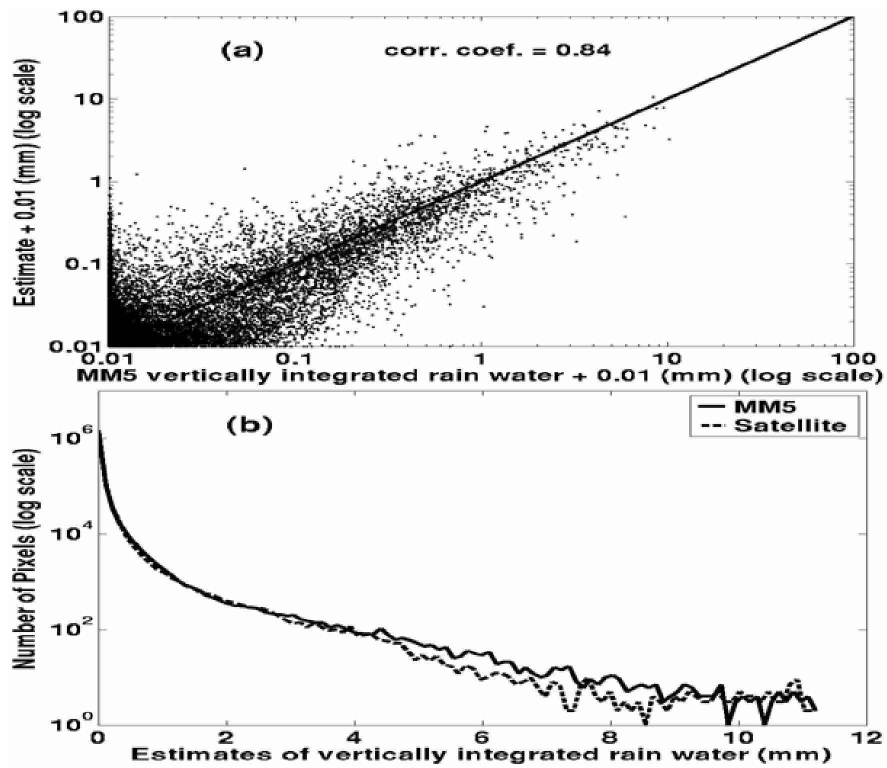

Fig. 4.13. Performance of the integrated rain water (W) estimator: (a) estimated W vs. MM5 truth, and (b) histogram comparisons over 100 linear-scale bins of MM5-estimated and satellite-estimated W values.

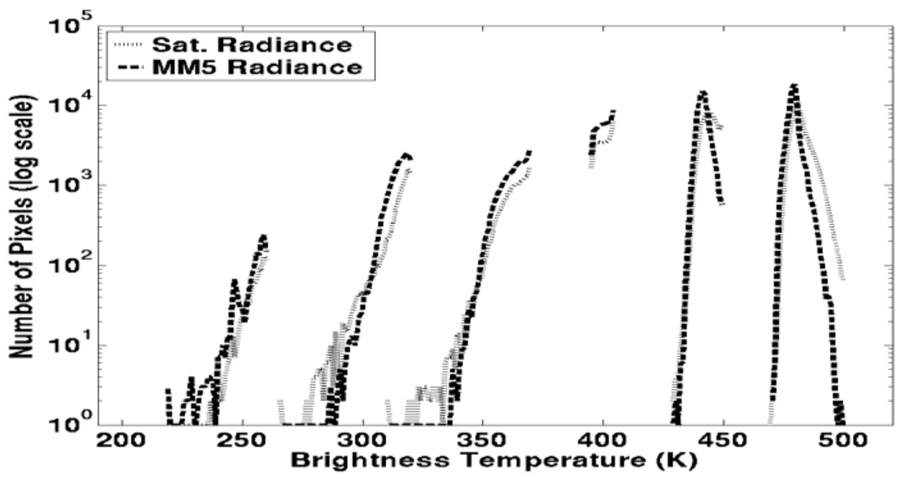

Fig. 4.14. Brightness temperature histograms (pixels per degree K) for AMSU and MM5 channels observing non-glaciated rain near 50.3, 89, 150, 183±7, 183±3, and 183±1 GHz, in order of increasing opacity from left to right. Only T_B's below 260 K are plotted. For

clarity, the absolute T_B's were shifted to the right by 0, 60, 110, 145, 190, and 240 K, respectively.

4.6.2.4 Sensitivity to Errors in MM5 and F(λ)

To determine the sensitivity of observed brightness temperatures to the MM5 convective cloud models, the amounts of snow, graupel, and cloud ice were arbitrarily increased 25 percent to yield the brightness temperature histograms presented in Fig. 4.15. The resulting discrepancies associated with the reduced MM5 radiances are comparable to the consequences of increasing F(λ) by 0.05, shown in Fig. 4.6b. The discrepancies in Fig. 4.15 are largest for those channels most sensitive to ice aloft (89-183±7 GHz), whereas 50 GHz responds well only to the very largest hydrometeors, and water vapor partially shields the two most opaque 183-GHz channels from most hydrometeors at lower altitudes. Interestingly, the increase in MM5 ice production has closed the small gap between AMSU and MM5 183±1 GHz radiances shown in Fig. 4.6(a). Thus the icy hydrometeor production of the Goddard explicit cloud model in MM5 appears to be generally consistent with AMSU observations within perhaps 10-15 percent, assuming the TBSCAT/F(λ) model is correct.

The high sensitivity of such histograms to changes in F(λ) were illustrated earlier in Fig. 4.6(b). Unfortunately, due to the spatial offsets and morphological differences between MM5-predicted and AMSU-sensed precipitation, same-storm brightness histograms for precipitation types of interest constitute the most robust comparison metric available. Only simulated comparisons such as those illustrated in Figs. 4.6(b) and 4.15 and others presented in Chapter 5 yield discrepancy probability distributions as a function of given parameters. The results in Chapter 5 corroborate the relatively high sensitivity of brightness histograms to altered MM5 and radiative transfer assumptions. They also demonstrate the considerable hydrometeor water path retrieval capabilities of millimeter-wave sensors, and the strong correlation of virga effects (~0.5 correlation coefficient) with surface precipitation rate retrieval errors.

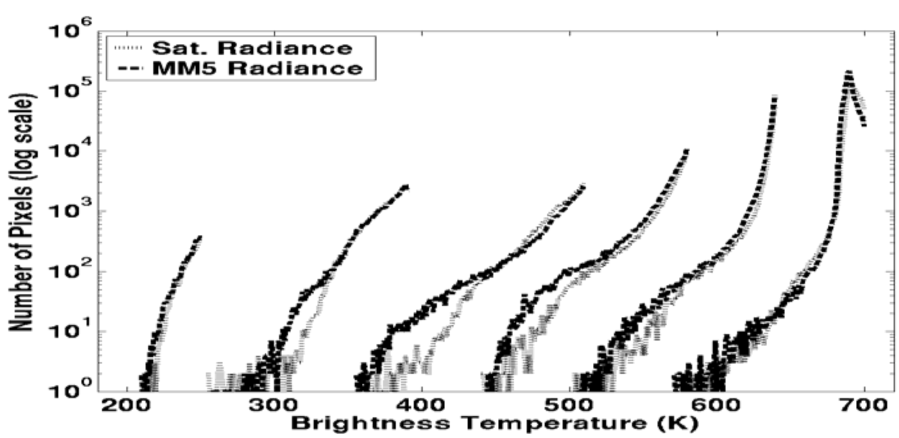

Fig. 4.15. Brightness temperature histograms (pixels per degree K) for AMSU and MM5 channels near 50.3, 89, 150, 183±7, 183±3, and 183±1 GHz, in order of increasing opacity from left to right, using 1.25 times the amount of MM5-predicted snow, graupel, and cloud ice. Only T_B's below 250 K are plotted. For clarity, the absolute T_B's were shifted to the right by 0, 140, 260, 330, 390, and 450 K, respectively.

4.7 Summary and Conclusions to Chapter 4

A method has been demonstrated for generating millimeter-wave brightness temperature spectra for precipitating regions that approximate well those observed by AMSU on polar-orbiting satellites viewing the same events at frequencies 50-190 GHz. A two-stream radiative transfer model (TBSCAT) generates these spectra using the temperature, humidity, and hydrometeor profiles predicted by a mesoscale NWP model (MM5) incorporating an explicit cloud model (Goddard). Only histograms of brightness temperatures can be matched because four hours are generally required for MM5 to create small realistic precipitation features from one-degree initialization data, and their locations and intensities have a random element that precludes perfect co-registration with satellite observations. These brightness temperature histograms generally matched well near 50, 89, 150, and 183 GHz for all types of precipitation tested, including convective, stratiform, cold snowfall, unglaciated, tropical, and snow-free rain.

Since millimeter-wave scattering phenomena and explicit cloud models are complex, the general agreement between these two sets of brightness histograms for AMSU and MM5 in five frequency bands and for multiple categories of precipitation is somewhat unexpected. This is particularly so because only Mie scattering from spheres with ice densities $F(\lambda)$ was assumed, where $F(\lambda)$ was chosen to match the total scattering cross-section deduced from DDSCAT for hexagonal plates and rosettes, the two habits found to dominate the spectrum. Improvements in MM5 and its initialization, and in the radiative transfer algorithm, would presumably further increase this agreement. Study of residual disagreements could be rewarding; preliminary examination suggests weaknesses in the NCEP initialization field are often involved.

The sensitivity to assumptions of the link between NWP initialization data and predicted millimeter-wave spectra was tested in three ways using the observed spread between AMSU and MM5 brightness histograms. First the ice factor was increased by 0.05, i.e., five percent of its dynamic range, and the resulting histogram spread exceeded that observed in essentially all comparisons. Next the ice production by MM5 was increased at all altitudes by twenty-five percent with a similar result. Finally, $F(\lambda)$ for snow and graupel was independently determined by minimizing empirically the histogram spread for a 122-storm global data set, leading in most cases to values within ~0.1 of those determined using DDSCAT. Thus the histogram comparison technique provides a reasonably sensitive metric for evaluating alternative means for generating realistic millimeter-wave spectra.

The reasons why relatively simple radiative transfer assumptions work so well might include the following. First, using principal component analysis of MM5/TBSCAT millimeter-wave spectra for 122 storms we found that the normalized variances of the first three principal components of the hydrometeor-induced perturbations of AMSU-A channels 1-8 and AMSU-B channels 1-5 are 95.72, 3.16, and 0.67, respectively, where the hydrometeor-induced perturbations are the differences in brightness temperatures simulated using normal MM5 outputs and those simulated by setting all MM5 icy hydrometeors to zero. This means that over 99.5 percent of all variance in icy-hydrometeor-induced perturbations 50-190 GHz was explained by only three degrees of freedom, consistent, for example, with dominance of the spectrum by cell-top altitude and the abundances of snow and graupel. Second, the angular scattering properties of hydrometeors might deviate from our assumptions and yet small adjustments in abundances might plausibly compensate for any errors in snow or graupel albedo, or for errors resulting from the two-stream approximation in TBSCAT; such abundance adjustments presumably are less than ~25 percent, as suggested by Fig. 4.15. Larger abundance adjustments would be allowed if graupel production were traded for snow production. For example, replacing half the graupel with a roughly equal mass of snow would not change brightness temperatures much, as suggested by Fig. 5.5. Such substitution could occur simultaneously with an increase in $F(\lambda)$ for graupel that would narrow the gap in β between DDSCAT and Mie scattering shown in Fig. 4.2(b); optimization of such model adjustments is studied further in Section 7.3.5 of this thesis.

Finally, it may be that the average scattering behavior over any ensemble of icy hydrometeor shapes, sizes, and orientations approximates the scattering behavior of a spherically symmetric dilute object having an electric permittivity distribution in space that declines with radius. An ensemble of homogeneous dilute spheres having inverse-exponential size distributions, as assumed in our model, would also have a spherically symmetric dilute permittivity that declines with radius, and perhaps two such models for hydrometeors and spheres would be observationally similar. These issues will be further discussed in Section 7.3.5.

Because there may be small residual errors in the MM5/TBASCAT/$F(\lambda)$ model presented here, any use of it for training operational precipitation retrieval algorithms should be tuned against traditional precipitation measurements; such tuning is beyond the scope of this chapter. The immediate application of these results might therefore be to simulation and evaluation of alternative precipitation observation and retrieval concepts, for which any residual errors in the model are less critical. As will be shown in Chapter 5, the precipitation retrieval accuracies predicted using this model are relatively insensitive to the values of $F(\lambda)$ chosen. Finally, we have found that extending DDSCAT above 200 GHz leads to $F(\lambda)$ values that are more dependent on the size distribution, warranting caution in their use.

Chapter 5

Sensitivity of Simulated Radiances and Predicted Retrieval Accuracies to MM5/RTM Assumptions

All results in this chapter are from [2].

5.1 Abstract

Brightness temperature histograms observed 50-191 GHz by the Advanced Microwave Sounding Unit (AMSU) on operational NOAA satellites are shown to be consistent with predictions made using a mesoscale NWP model (MM5) and a radiative transfer model (TBSCAT/F(λ)) for a global set of 122 storms coincident with the AMSU observations. Observable discrepancies between the observed and modeled histograms occurred when: 1) snow and graupel mixing ratios were increased more than 15 and 25 percent, respectively, or their altitudes increased more than ~25 mb, 2) the density, F(λ), of equivalent Mie-scattering ice spheres increased more than 0.03 g/cm^3, and 3) the two-stream ice scattering increased more than ~1 percent. Using the same MM5/TBSCAT/F(λ) model, neural networks were developed to retrieve from AMSU and geostationary microwave satellites: hydrometeor water paths, 15-minute average surface precipitation rates, and cell-top altitudes, all with 15-km resolution. Simulated AMSU rms precipitation-rate retrieval accuracies ranged from 0.4 to 21 mm/h when grouped by octaves of MM5 precipitation rate between 0.1 and 64 mm/h, and were ~3.8 mm/h for the octave 4-8 mm/h. AMSU and GEM precipitation rate retrieval accuracies for random 50-50 mixtures of profiles simulated with either the baseline or a modified-physics model were largely insensitive to changes in model physics that would be clearly evident in AMSU observations if real. This insensitivity of retrieval accuracies to model assumptions implies that MM5/TBSCAT/F(λ) simulations offer a useful testbed for evaluating alternative millimeter-wave satellite designs and methods for retrieval and assimilation, to the extent that surface effects are limited.

5.2 Introduction

In order to assimilate passive microwave precipitation observations or retrievals into numerical weather prediction (NWP) models, the modeled radiances must be consistent with those observed. This chapter tests the sensitivity of that consistency to assumptions in a particular radiative transfer model (RTM), and in a cloud-resolving numerical weather prediction (NWP) model that predicts hydrometeor habits and profiles. The precipitation and water path retrieval accuracies are shown to be less sensitive to the physical models than are the radiances, provided that the retrieval method is tuned to reality.

These model-sensitivity results are most relevant to imaging microwave spectrometers such as the Advanced Microwave Sounding Unit (AMSU) flying on the National Ocean and Atmospheric Administration (NOAA) polar orbiting satellites NOAA-15, -16, -17, and -18 [23], [24], [34], [52], and its planned successor, the Advanced Technology Microwave Sounder (ATMS) [26]. These instruments observe frequencies above 23 GHz with spatial resolution of ~15-50 km. Retrieval accuracies at nadir are also predicted for proposed geosynchronous microwave sounders that could monitor precipitation at intervals as short as ~5-15 minutes [53]-[54]. Development and analysis of AMSU precipitation retrieval algorithms for use at all angles is presented to in Chapters 7 and 8.

The use of cloud-resolving NWP model-based simulations for developing and evaluating microwave precipitation retrieval methods is motivated by the lack of trustworthy ground truth coincident with microwave observations. For example, there is no practical method for accurately observing the three-dimensional density, size, and habit distributions of various hydrometeor species at the same time their microwave emission spectrum is being continuously mapped from above. Although multi-frequency Doppler radar systems offer some hope for accurate three-dimensional imaging of hydrometeors, such studies are rare and require simultaneous microwave spectrometers operating overhead to complete the experiment. Even rain gauge measurements of surface rainfall are suspect because of the influence of local winds and because arrays of gauges are seldom sufficiently extensive to compensate for the non-uniformity of rain, particularly convective rain. Moreover, since the character of precipitation varies substantially over the globe, high quality ground-truth instrumentation must be mobile or replicated.

One way to obtain more precise precipitation retrieval training data is to use cloud-resolving NWP models in combination with radiative transfer models (RTM) that together match satellite observations with acceptable fidelity over a global set of co-located test cases. For example, simulated cloud radiation databases linking meteorological parameters to emergent microwave spectra have long been used to train "physically based" retrieval algorithms designed for TRMM data (e.g., [55]-[56]). Another model-based approach to precipitation retrievals involves Bayesian schemes based on Gaussian assumptions, as demonstrated by Bauer et al. [57] for a hypothetical sensor with five window channels 18-150 GHz plus 8 channels in the 54- and 118-GHz oxygen absorption bands

A simpler approach is to evaluate the separate impacts of various modifications to the NWP and RTM models. This was done, for example, for TRMM frequencies by Tassa et al. [58], and for AMSU frequencies 23-191 GHz in a limited way by Surussavadee and Staelin [1]. In the latter work, observed AMSU radiance histograms agreed within ~±10K at all frequencies with those predicted by the NWP model

NCEP/MM5 followed by the RTM model TBSCAT/F(λ), not only for global averages over 122 diverse storms observed between 83N and 73S over a year, but also for subsets of convective, stratiform, snowy, and other types of precipitation. This chapter extends this initial sensitivity analysis to several additional model assumptions and to their impact upon predicted retrieval accuracies.

Section 5.3 reviews briefly the physical basis for the link between millimeter-wave spectra and surface precipitation rates. Section 5.4 explores the sensitivity of the brightness temperature histograms to various assumptions in the radiative transfer model and MM5. Section 5.5 then presents analyses of: 1) precipitation retrieval accuracies for AMSU and a proposed geostationary microwave sounder using frequencies 150-430 GHz, and 2) the sensitivity of those predicted accuracies to model assumptions and meteorological conditions. Section 5.6 summarizes the prospects for assimilation of millimeter-wave precipitation-sensitive radiances and retrievals into numerical models, and the conclusions to be drawn from these studies. MM5 domain configurations, AMSU observations over 122 global storms, and computation of MM5/TBSCAT predicted radiances used in this chapter are described in Sections 3.1, 3.2, and 4.4, respectively.

5.3 Physical Basis

Most prior centimeter-wave precipitation observations from satellites have used dual-polarized window channels below 90 GHz viewed at large constant zenith angles that permit surface emissivity and temperature to be partially distinguished, thus permitting atmospheric absorption and water paths to be estimated [59]. In contrast, millimeter-wave spectrometers rely more on scattering signatures deduced as a function of altitude and wavelength for wavelengths that span the transition between Rayleigh and geometric scattering for typical hydrometeors. Thus millimeter-wave spectra reveal information about hydrometeor size and altitude distributions, both of which are correlated with precipitation intensity. Millimeter-wave observations in window channels over ocean also yield water path information, but multiple channels are required to help distinguish the effects of water vapor and ocean roughness from absorption by water droplets. The instrument of primary interest in this chapter (AMSU) scans cross-track with only a single angle-dependent polarization.

The altitude distributions of hydrometeors can be inferred, for example, using the opaque oxygen band channels near 54, 118, and 425 GHz. Only frequencies penetrating down to cell-top levels can sense their scattering signature [60]-[61], and these penetration depths are frequency dependent, ranging from the surface to the mesosphere. The observable cell tops are defined by hydrometeors of ~1-5 mm diameter, which generally dominate millimeter-wave scattering, and these tops can lie well below the visible cloud top. The signature of an icy cell top can be strong because its albedo can exceed 50 percent and yield local perturbations over 100 K, large compared to nominal satellite receiver sensitivities of ~0.2 K. This "altitude slicing" phenomenon associated with frequency-dependent penetration depths is also evident in 183-GHz water vapor observations because, for example, only the highest cell tops rise to the dry altitudes observable from space near 183.7±1 GHz [34], [62].

Hydrometeor size distributions are revealed by the frequency dependence of scattering signatures 50-200 GHz because the transition between Rayleigh and geometric scattering for most hydrometeors lies within this band. The larger hydrometeors are more evident in the 50-100 GHz region, while smaller ones dominate above 100 GHz [60], [62], [63]. Because hydrometeor size and weight are related to the vertical wind necessary to maintain them aloft, there is significant correlation between the presence of larger hydrometeors, higher vertical winds, and stronger convective rain.

The information content in the millimeter-wave brightness temperature spectrum relevant to icy hydrometeor distributions can be estimated from the variances of the eigenvectors characterizing the millimeter-wave spectral difference between atmospheric columns with and without such icy hydrometeors. Studies of ~1.6 million 15-km resolution differential microwave emission spectra 21-190 GHz computed for 122 storms distributed over the globe and year, as described in more detail in section 3.2, yielded normalized variances for the first three differential spectral eigenvectors of 95.7, 3.2, and 0.7 percent. Millimeter-wave aircraft and satellite data have shown that both cell-top altitudes and particle-size distributions are separately revealed by such spectra [61]-[63]. These parameters are correlated to some degree, however, and are also correlated with precipitation rate.

5.4 Sensitivity of Radiance Histograms

5.4.1 Sensitivity to the radiative transfer model

Successful assimilation of observed radiances into NWP models requires that simulated radiances match the observations, and therefore both the NWP and radiative transfer (RTM) models must be correct. The same is true if precipitation retrievals are assimilated instead of radiances because retrievals are trained and tested using such models.

This section characterizes the effects of radiative transfer assumptions on the quality of brightness-temperature-histogram matches between NWP models and AMSU observations for 122 global storms described in Section 3.2. Histograms are matched instead of values at individual pixels because the precise locations and strengths of simulated convective instabilities are partially determined by chaotic processes within MM5 that are not resolved or predicted by available NWP initialization fields. Even pixel-to-pixel radiance comparisons for stratiform systems would be problematic, as suggested in Fig. 3.3 where AMSU and NCEP/MM5/RTM radiances at 183±7 GHz are compared for two storms. Surussavadee and Staelin [1] demonstrated earlier that histogram comparisons are sensitive to modest changes in MM5 and AMSU radiative transfer models.

Modeling radiative transfer in precipitation at millimeter wavelengths is problematic because ice habits are diverse and have unknown three-dimensional distributions in form, size, and density, all of which affect microwave scattering and absorption. Both complex [37] and simpler approximations (e.g., [55]) have been used to model radiative transfer in these cases. The related simple radiative transfer model used here [1], [7] is generally consistent with AMSU observations, as demonstrated below, and is designated the TBSCAT/F(λ) model, which names its two most significant components.

The sensitivity of computed brightness temperature histograms to RTM assumptions was tested by comparing radiance histograms computing using: 1) a baseline RTM versus 2) RTM's with alternative ice factors, loss tangents, back-scattering fraction, and hydrometeor size distributions. Fig. 4.6(a) presents the brightness temperature histograms observed by AMSU at six frequencies for the 122 global storms characterized in Table 3.2, and the corresponding histograms for simulated NCEP/MM5/TBSCAT/F(λ) brightnesses for the same storms. The worst-case discrepancy in these histograms between observed and modeled brightness temperatures is roughly 10K, and this is used as the nominal threshold for detecting possible failures in the MM5 and RTM models as their parameters are varied. Because these observed and modeled storms overlap almost exactly in time and space for a very large number of pixels, these histogram comparisons are more sensitive to model deficiencies than are comparisons lacking concurrence or scale.

Fig. 5.1 presents the same data as in Fig. 4.6(a), but subdivided by precipitation type; only those three frequencies most sensitive to icy hydrometeors are illustrated, i.e., 89, 150, and 183±7 GHz. The six types include convective, stratiform, snow-only, rain-only, tropical ($|lat| \leq 25$), and non-glaciated (warm) rain, as classified for each pixel using its observed or simulated brightness spectrum [1]. The baseline RTM generally matches the AMSU brightness temperature histograms for these diverse types of precipitation, suggesting its ability to match reality despite its simplicity. The strong exception is snow-only pixels, for which the window channels at 89 and 150 GHz respond to the frozen surface and possible deep snow, which is not consistent with the current assumption of 0.91-0.97 surface emissivity. Although existing frozen-surface emissivity models could be used, these two window channels would remain problematic for hydrometeor retrievals over ice or snow fields. Fortunately the more opaque bands near 183 GHz are insensitive to the surface, but are sensitive to snow and graupel, as suggested here and later in Fig. 5.5. The next largest type of discrepancy in Fig. 5.1 involves a few of the very coldest pixels observed by AMSU, but some of these are located over water misclassified as land.

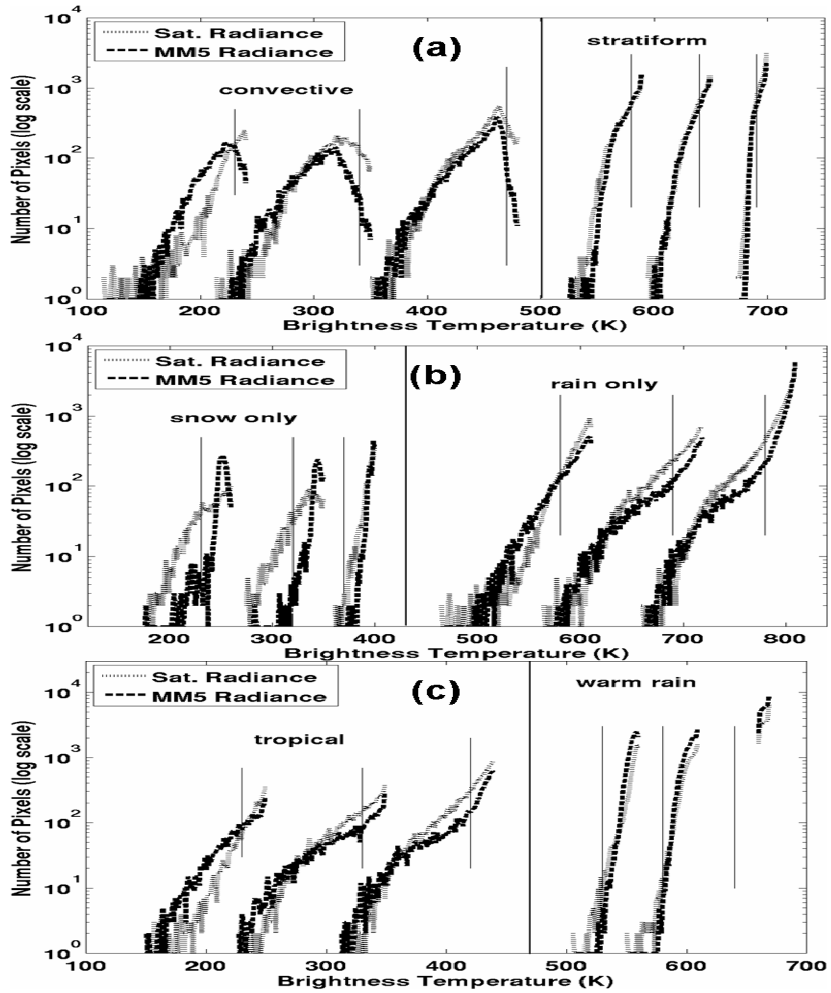

Fig. 5.1. Brightness temperature histograms (pixels per degree K) for channels near 89, 150, and 183±7 GHz, for each precipitation type in order of increasing opacity from left to right, for 122 storms using F(λ) from Table 4.2. (a) Convective vs. stratiform where only T_B's below 240 K are plotted and the absolute T_B's were shifted to the right by 0, 110, 240, 350, 410, and 460 K, respectively; (b) snow-only vs. rain-only where only T_B's below 260 K are plotted and the absolute T_B's were shifted to the right by 0, 90, 140, 350, 460, and 550 K, respectively; (c) |lat| ≤ 25 with T_B's <250K, vs. warm rain with T_B's < 260K, where the absolute T_B's were shifted to the right by 0, 100, 190, 300, 350, and 410 K, respectively. The vertical bar for each histogram represents 230K.

The first change made to the RTM was an arbitrary increase in the ice factor F by 0.1 for snow alone and graupel alone, as shown in Figs. 5.2(a) and 5.2(b), respectively. These perturbations to F(λ) are generally small compared to its possible range between 0 and 1, but nonetheless produce a noticeable change in the MM5/TBSCAT/F(λ) brightness temperature distributions. This sensitivity of radiance to F(λ) is consistent with the difficulty encountered in some earlier studies that effectively used larger values, leading to conjectures that modeled ice densities should be lowered [58]. Note that 183±3 GHz responds more strongly to graupel than to snow, and therefore senses strong convection. Fig. 5.2(c) compares the histograms for all 122 storms for the case where the ice loss tangent has been decreased by reducing the imaginary part of the permittivity ε" by a non-physical factor of ten. Fig. 5.2 implies that only reasonably apt RTM's will produce agreement across all precipitation types. Changes of ~0.1 in F(λ) for snow and graupel produce worst-case discrepancies of ~40K in the Fig. 5.2 histograms, suggesting that changes or errors in F(λ) of ~0.025 might be detectable, and certainly changes of ~0.05, which are small fractions of the possible range from 0 to 1. It should be noted that the baseline MM5 and RTM models incorporated no tuning other than the model architecture itself, and they nonetheless yield few discrepancies in Fig. 4.6(a) beyond 10K for the benchmark 122 storms.

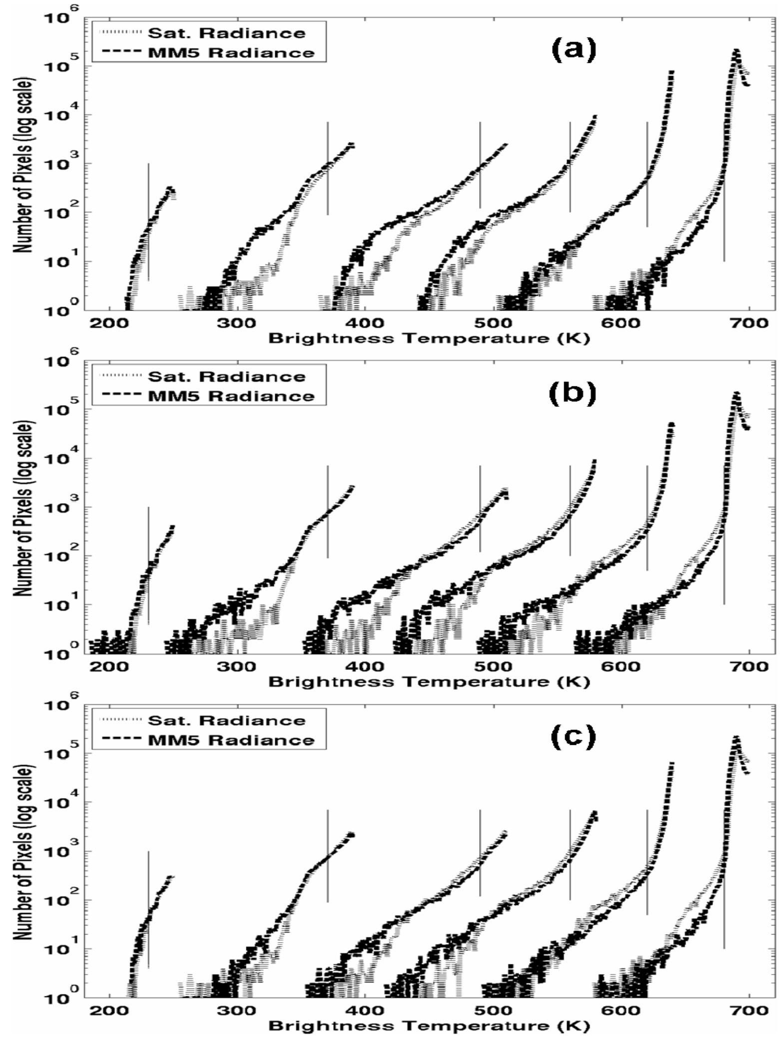

Fig. 5.2. Brightness temperature histograms for AMSU and MM5 for channels near 50.3, 89, 150, 183±7, 183±3, and 183±1 GHz, from left to right, for: (a) F(λ) increased by 0.1 for snow, (b) F(λ) increased by 0.1 for graupel, (c) imaginary part of ice permittivity, ε'', decreased by 10 times. Only T_B's below 250 K are plotted. The absolute T_B's were shifted to the right by 0, 140, 260, 330, 390, and 450 K, respectively. The vertical bar for each histogram represents 230K.

This conclusion is reinforced by Figs. 5.3(a) and 5.3(b), which respectively illustrate for 122 storms the effects of increasing the backward scattering slightly, and the particle size distribution by a significant factor. The Mie back-scattering fraction was increased by 0.02. The Mie back-scattering fraction is the fraction of radiance scattering backward and equals (1-G)/2, where G is the scattering asymmetry factor from the Mie calculation for the assumed particle size distribution, which is defined by (3.1). The worst-case brightness discrepancies for a 0.02 increase in BS ratio in the two-stream Mie scattering model are ~30K in Fig. 5.3(a), so a change of ~0.01 would produce a noticeable discrepancy with the AMSU histograms. This sensitivity is high because it is ~10-20 percent of the nominal BS ratio for typical particle sizes (~0.05 – 0.1), and is therefore equivalent to ~10-20 percent change in scattering cross-section in the two-stream radiative transfer limit. Since scattering can cool brightness temperatures ~50 – 100K, this high sensitivity is not unexpected.

The exponentially distributed particle sizes assumed in (3.1) were decreased by increasing the zero-diameter intercept N_o for snow (N_s) and graupel (N_g) from 0.04 to 3; this increases the numbers of particles because the mass mixing ratio was held constant. Because the volume of a sphere varies as D^3 and its scattering cross-section in the Rayleigh and geometric limits varies as D^4 and D^2, respectively, scattering for constant mass will decrease in the Rayleigh limit and increase in the geometric limit as a result of increasing N_o, depending on wavelength λ and the initial value of N_o. The warmer MM5/TBSCAT brightness temperatures in Fig. 5.3(b) are generally increased for a given histogram pixel count, consistent with reduced scattering by smaller hydrometeors in the Rayleigh limit. The colder temperatures remain unchanged, however, which is consistent with the coldest pixels scattering more strongly and being characterized by hydrometeors somewhat closer to the geometric scattering limit. The worst-case brightness discrepancies are no more than 10K, however, so the histogram comparisons do not strongly constrain N_o.

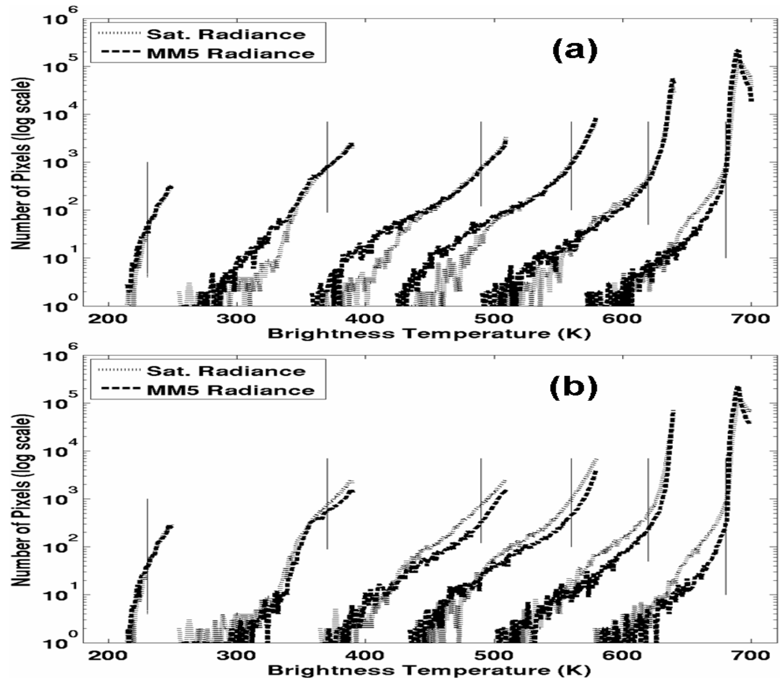

Fig. 5.3. AMSU and MM5 brightness temperature histograms for 122 global storms for channels near 50.3, 89, 150, 183±7, 183±3, and 183±1 GHz, from left to right, for: (a) Mie back-scattering fraction increased by 0.02, and (b) the intercepts, both N_s and N_g, for snow and graupel exponential hydrometeor size distributions increased from 0.04 to 3, respectively. Only T_B's below 250 K are plotted. The absolute T_B's were shifted to the right by 0, 140, 260, 330, 390, and 450 K, respectively. The vertical bar for each histogram represents 230K.

5.4.2 Sensitivity to MM5/RTM model assumptions

Successful assimilation of observed radiances into NWP models also requires that the NWP model produce hydrometeor profiles faithful to the true atmosphere. The potential NWP benefits from assimilated radiance information increases with the sensitivity of radiances and their histograms to hydrometeor profiles. Figs. 5.4(a) and 5.4(b) illustrate for 122 storms the sensitivity of radiance histograms to increases in MM5 predicted mass profiles of snow and graupel. The worst-case brightness discrepancies resulting when snow and graupel mass distributions are increased by 50 and 75 percent, respectively, are both ~25K, corresponding to detectable 10K excursions of ~20 and ~30 percent in MM5 snow and graupel production, respectively. Only snow and graupel significantly affect these millimeter wavelengths, while the impacts of cloud ice and liquid water were usually found to be negligible in comparison.

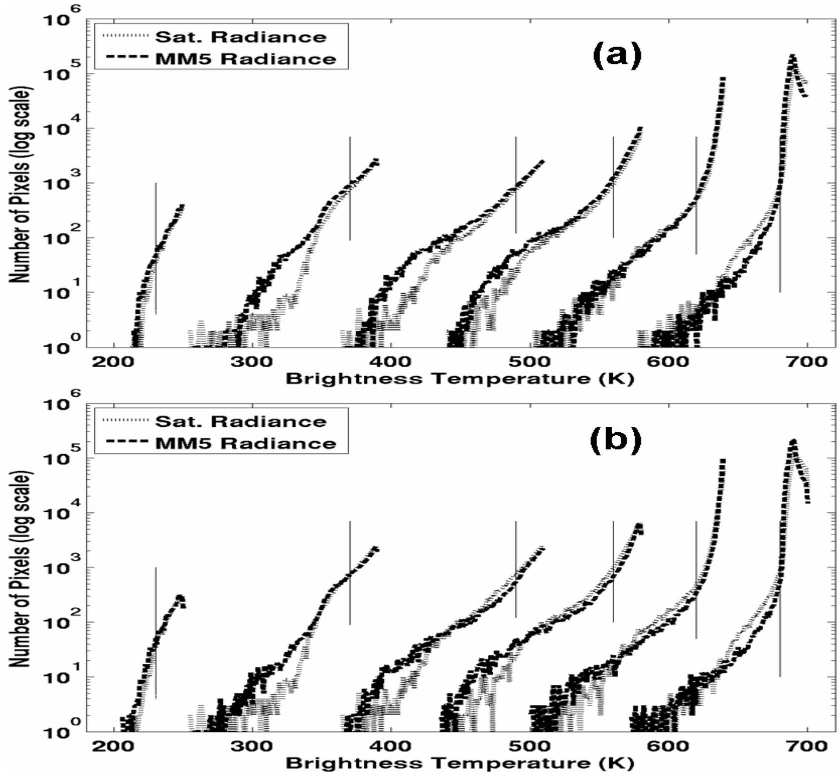

Fig. 5.4. Sensitivity of radiances near 50.3, 89, 150, 183±7, 183±3, and 183±1 GHz, from left to right, to increases in MM5-predicted: (a) snow ×1.5, (b) graupel ×1.75. Only T_B's below 250 K are plotted. The absolute T_B's were shifted to the right by 0, 140, 260, 330, 390, and 450 K, respectively. The vertical bar for each histogram represents 230K.

Fig. 5.5 shows that increasing and decreasing the MM5-predicted altitudes of snow and graupel by 75 and 50 mb, respectively, does not always produce comparable histogram effects, where the MM5 pressure levels are equally spaced at 25 mb. This figure also indicates the substantial sensitivity of the 183-GHz band to the altitudes of icy hydrometeors as a result of the water vapor altitude-slicing effect. The worst-case brightness discrepancies shown in Fig. 5.5 are ~35K for 75-mb altitude changes, so systematic errors in MM5 snow/graupel altitudes of ~20 mb would be marginally detectable using the AMSU brightness histograms.

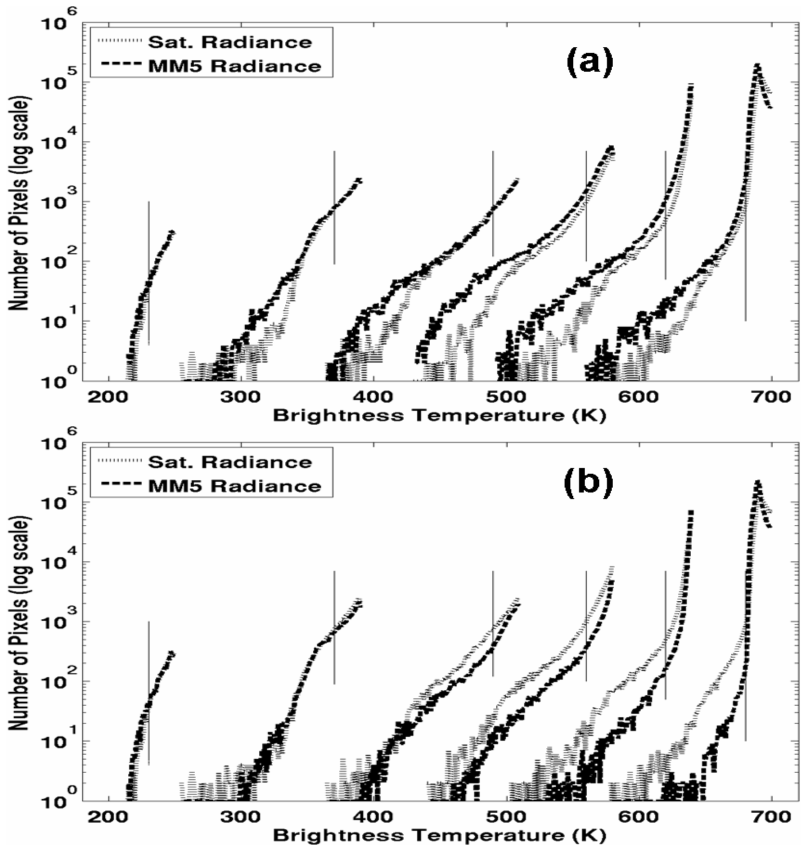

Fig. 5.5. Sensitivity of radiances to: (a) increases of snow and graupel altitudes by 75 mbar, and (b) decreases of snow and graupel altitudes by 50 mbar. Only T_B's below 250 K are plotted. The absolute T_B's for channels near 50.3, 89, 150, 183±7, 183±3, and 183±1 GHz, from left to right, were shifted to the right by 0, 140, 260, 330, 390, and 450 K, respectively. The vertical bar for each histogram represents 230K.

The sensitivity of radiance histograms to MM5 and the RTM was also evaluated by computing the rms difference between simulated radiances for the baseline case and the same radiances computed using different MM5/RTM variations. The measure for the difference is defined as:

$$\Delta T_B = \sqrt{\frac{1}{Q}\sum_{i=1}^{Q}\sigma_i^2} \qquad [\mathrm{K}] \tag{5.1}$$

$$\sigma_i^2 = \frac{1}{N_i}\sum_{j=1}^{N_i}\left(y_j - \bar{x}\right)^2 \tag{5.2}$$

where Q is the number of brightness-temperature histogram bins, N_i is the number of baseline pixels that fall in brightness bin i, x_j and y_j are brightness temperatures from the baseline case and the perturbed case, respectively, for a given pixel j and bin i, $\bar{x}$ is the sample mean of x_j for bin i, and the variance within bin i is σ_i^2. This rms ΔT_B sensitivity metric is presented in Table 5.1 for the same 122 storms and the six AMSU frequencies 50.3-183±1 GHz used before: AMSU-A channel 3 (A3) at 50.3 GHz, and AMSU-B channels 1-5 (B1-B5) at the frequencies 89, 150, and 183±1, ±3, and ±7 GHz, respectively.

TABLE 5.1
ΔT_B [K] (RMS) FOR DIFFERENT VARIANTS OF RTM AND MM5

Variations	A3	B1	B2	B3	B4	B5
$F_S + 0.1$	1.57	9.82	11.86	2.28	6.54	10.16
$F_G + 0.1$	2.76	16.24	11.81	15.36	15.18	13.05
$F_I = 0.1$	0.50	2.12	1.27	0.36	0.28	0.87
BS + 0.02	0.75	6.53	10.92	10.39	12.61	13.41
$\varepsilon''_{ice} \times 6$	0.67	12.74	22.43	8.80	16.80	21.46
$\varepsilon''_{water} \times 2$	0.84	2.18	1.39	0.47	0.46	0.73
$N_s = N_g = 3$	2.58	12.68	7.25	2.99	4.22	4.72
S × 1.5	1.48	7.44	9.61	2.33	6.15	9.30
G × 1.75	1.20	6.85	5.70	11.31	10.16	8.13
I × 20	0.51	6.24	14.13	6.17	11.66	14.70
W × 20	5.69	14.94	15.99	3.54	9.04	11.84
S/G ↓ 50 mb	0.72	6.62	9.75	18.47	17.68	13.00

A3 signifies AMSU-A ch. 3 (50.3 GHz). B1-B5 signify AMSU-B chs. 1-5 (89, 150, 183±1, 183±3, and 183±7 GHz). F_S, F_G, and F_I indicate F(λ) for snow, graupel, and cloud ice, respectively. S, G, I, and W signify snow, graupel, cloud ice, and rain and cloud liquid water, respectively. BS signifies Mie back-scattering fraction. ε''_{ice} and ε''_{water} signify imaginary parts of ice and water permittivity, respectively. N_s and N_g characterize the exponential size distributions (3.1) for snow and graupel, respectively, where nominal $N_s = N_g = 0.04$ and larger values imply smaller hydrometeors. ↓ signifies movement to lower altitude.

The model-sensitivity results presented in Table 5.1 are generally consistent with those inferred from Figs. 5.2-5.5, but also reveal the insensitivity of the brightness temperature histograms to three parameters: F(λ) for cloud ice, ε" for water (related to the loss tangent for water), and the abundances of cloud ice and rain water. The table suggests a modest sensitivity to ε" for ice, however, to within a factor of ~3, where ε" is highly sensitive to ice temperature, particularly near the melting point. The table also shows that AMSU-B channels are usually at least three times more sensitive than the 50.3-GHz window channel to changes in hydrometeor distributions or propagation physics. Thus with respect to snow and graupel mixing ratios and altitudes, F(λ), and ice scattering, the baseline MM5/RTM model cannot depart from physical truth very far before yielding clearly observable differences of ~10K between simulated and observed brightness temperatures.

5.5 Retrievals of Hydrometeor Profiles and Precipitation Rates

5.5.1 Retrieval accuracies

Retrievals of precipitation rates and hydrometeor profiles can also be assimilated into NWP models. Two different instruments are analyzed here: the operational instrument AMSU, characterized in Table 5.2, and a proposed GEostationary Microwave (GEM) spectrometer, also characterized in Table 5.2, that could map and assimilate precipitation for important storms at ~15-minute intervals with ~15-km resolution. The GEM frequencies were selected to be consistent with a practical instrument employing a 2-meter diameter filled-aperture antenna that could readily be integrated on geostationary satellites such as GOES [53]. In particular, the 380-GHz water vapor resonance and the 425-GHz oxygen resonance were selected for their abilities to sense individual convective cells larger than ~10 km, and the 183-GHz water vapor band was selected because it can sense to the surface except in the tropics. For simplicity the sensitivity of all channels is assumed to be 0.2K rms, although for precipitation retrievals this specification is not critical because hydrometeor perturbations can exceed 100K.

Fig. 5.6 shows that F(λ) providing matches between Mie spheres with hexagonal plates at 424.763 ± 4.0 GHz or rosettes at 380.197 ± 4.0 GHz are size-dependent when the particle size is large. This makes electromagnetic models for snow and graupel more complicated. Fortunately, since Section 5.5.2 later demonstrates that estimated retrieval accuracies are reasonably insensitive to errors in F(λ) even when random F(λ) were used for both snow and graupel, the size-dependent characteristics for F(λ) at large particle size should not affect predicted precipitation retrieval accuracies. For simplicity, F(λ) for frequency higher than 200 GHz used in Chapters 5 and 6 in this thesis was defined as the average of the values given by Table 4.2 and F(200 GHz), which was generally consistent with preliminary DDSCAT calculations at these higher frequencies, for GEM simulations. The assumed zenith angle was 40 degrees.

TABLE 5.2
FREQUENCIES AND WEIGHTING FUNCTION PEAK HEIGHTS FOR AMSU-A/B AND GEM, AS COMPUTED USING THE 1976 US STANDARD ATMOSPHERE VIEWED AT NADIR OVER A NONREFLECTIVE SURFACE

AMSU-A/B			GEM		
Ch.	Center frequency (GHz)	Weighting function peak height (km)	Ch.	Center frequency (GHz)	Weighting function peak height (km)
A1	23.8 ± 0.07	0	A1	150 ± 0.9	0
A2	31.4 ± 0.05	0	A2	183.31 ± 1	6.1
A3	50.3 ± 0.05	0	A3	183.31 ± 3	4.0
A4	52.8 ± 0.11	0	A4	183.31 ± 7	1.8

A5	53.6 ± 0.12	4	B1	380.197 ± 1.5	8.5
A6	54.4 ± 0.11	8	B2	380.197 ± 4.0	6.6
A7	54.9 ± 0.11	9.5	B3	380.197 ± 9.0	4.6
A8	55.5 ± 0.09	12.5	B4	380.197 ± 18.0	3.1
B1	89 ± 0.9	0	C1	424.763 ± 0.6	14.5
B2	150 ± 0.9	0	C2	424.763 ± 1.0	11.5
B3	183.31 ± 1	6.1	C3	424.763 ± 1.5	7.5
B4	183.31 ± 3	4.0	C4	424.763 ± 4.0	4
B5	183.31 ± 7	1.8			

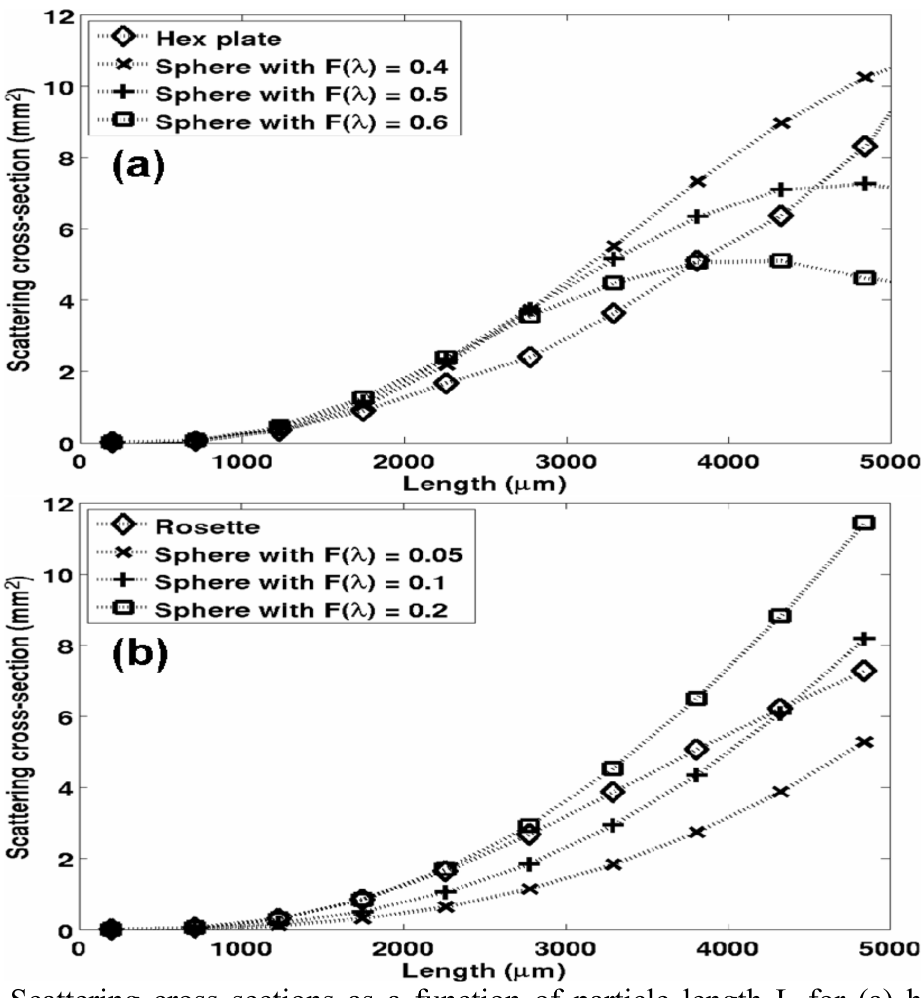

Fig. 5.6. Scattering cross sections as a function of particle length L for (a) hexagonal plates at 424.763 ± 4.0 GHz and (b) rosettes at 380.197 ± 4.0 GHz, both compared with those of equal-mass spheres having three different values for F(λ).

Because the RTM is non-linear and the statistics of precipitation are non-Gaussian, the optimum estimator is non-linear. For that reason neural networks were used to estimate for both AMSU and GEM the 15-minute average surface precipitation rates for rain and snow, and also the water paths for graupel, snow, cloud ice, rain water, and the sum of graupel, snow, and rain water. The neural networks were trained using 5-km resolution MM5/RTM brightness temperatures blurred to 15-km resolution. The pixels used for training were distributed uniformly over the blurred 4.4 million 5-km pixels in the 122 globally distributed MM5/TBSCAT/F(λ) storms that were selected from a larger set of 255 storms to best match concurrent AMSU observations [1]. Only large sets of representative cloud-resolved physical model data permit neural networks to yield realistic retrievals in the absence of precise *in situ* ground truth. It is reassuring that this MM5/TBSCAT/F(λ) physical model data yields brightness temperature distributions that reasonably match those observed by AMSU over the same set of storms (see Figs. 4.6(a) and 5.1).

All neural networks had three layers with 10, 5, and 1 neurons, respectively, where the first two layers employed tangent sigmoid operators, and the final layer was linear. Limited experimentation with network architectures did not reveal significant opportunities for improvement, probably because the 10-5-1 networks were more complex than needed, but were sufficiently simple that the extensive training data was adequate. These networks were trained using MM5/TBSCAT/F(λ) simulations of nadir radiances for 122 globally representative storms, and have three layers with 10, 5, and 1 neurons, respectively. The first two layers employed tangent sigmoid operators, and the final layer was linear. Other network architectures did not offer noticeable improvement. The Levenberg-Marquardt [49] training algorithm was used and the net weights were initialized using the Nguyen-Widrow method [50]. Each of the 122 MM5 storms has 190×190 15-km pixels, and altogether 293 thousand pixels were used for training and validating, and all 4.4 million were used for testing. The same neural network was used for both land and sea without introducing significant coastal artifacts, as illustrated later in Fig. 5.11(a).

The retrieval architectures used for AMSU and GEM are illustrated in Figs. 5.7(a) and 5.7(b), respectively. The simulated AMSU data included 18 numbers: the brightness temperatures for channels 1-8 of AMSU-A and all AMSU-B channels, plus the five estimated brightness perturbations due to icy hydrometeors for AMSU-A channels 4-8. The perturbations were estimated using the method described by Chen and Staelin [34], but were left at 50-km resolution. Such perturbations are the difference between simulated AMSU-A icy signatures at locations detected using 183±7 GHz data, and brightness temperatures determined by Laplacian interpolation of AMSU-A brightness temperatures surrounding the icy patch.

The architecture for estimating surface precipitation rates using GEM has two stages, the first of which merely determines which of the following two neural networks should be used. This two-stage complexity was not necessary for the water path estimates, which were extracted at point A in Fig. 5.7(b). Each estimated parameter was produced by its own neural network, independent of others. The input data for GEM simulations included only the 15-km and 33-km resolution brightness temperatures at the frequencies listed in Table 5.2; no perturbations were estimated.

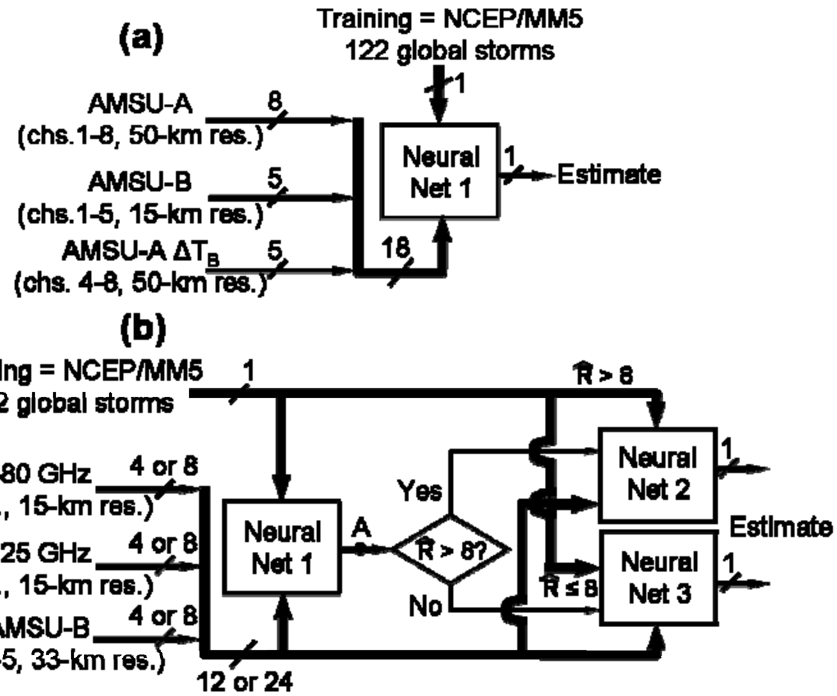

Fig. 5.7. Architectures of neural networks used to retrieve surface precipitation rate $\hat{R}$ and water paths for various hydrometeor species for (a) AMSU and (b) GEM; GEM water path estimates appear at port A.

Since millions of globally and seasonally representative pixels were used in this study, the size of the data set is believed to be adequate for the purposes of this chapter. The simulated radiances are believed to be relevant and adequate because MM5 models the altitude distributions of snow, ice, rainwater, graupel, and cloud ice, all of which are uniquely handled by the radiative transfer model with 5-km resolution. Any residual biases relative to reality are believed to have minor consequences in view of: 1) the similarity between observed and simulated radiance histograms despite the sensitivity of these histograms to several critical assumptions, as demonstrated in this chapter, 2) the agreement shown in Fig. 5.1 between observed and simulated radiance histograms for five precipitation types (convective, stratiform, tropical, rain only, and warm rain), and in similar comparisons for three latitude bands (tropical, mid-latitude, and beyond ±55 degrees) [1], and 3) the insensitivity of the predicted rms retrieval accuracies to changes in many key model parameters, as demonstrated later in Section 5.5.2 and Tables 5.3 and 5.4.

Scatter plots characterizing retrieval accuracies are presented for AMSU and GEM in Figs. 5.8(a) and 5.8(b), respectively; water paths of snow, graupel, other ice, and rain water (mm) are evaluated. Because surface precipitation is shielded by overlying opacity at most millimeter wavelengths and because precipitation that evaporates before reaching the ground (virga) is difficult to detect, better retrieval accuracies are obtained for ice water paths near the cell tops than for rain water at lower altitudes.

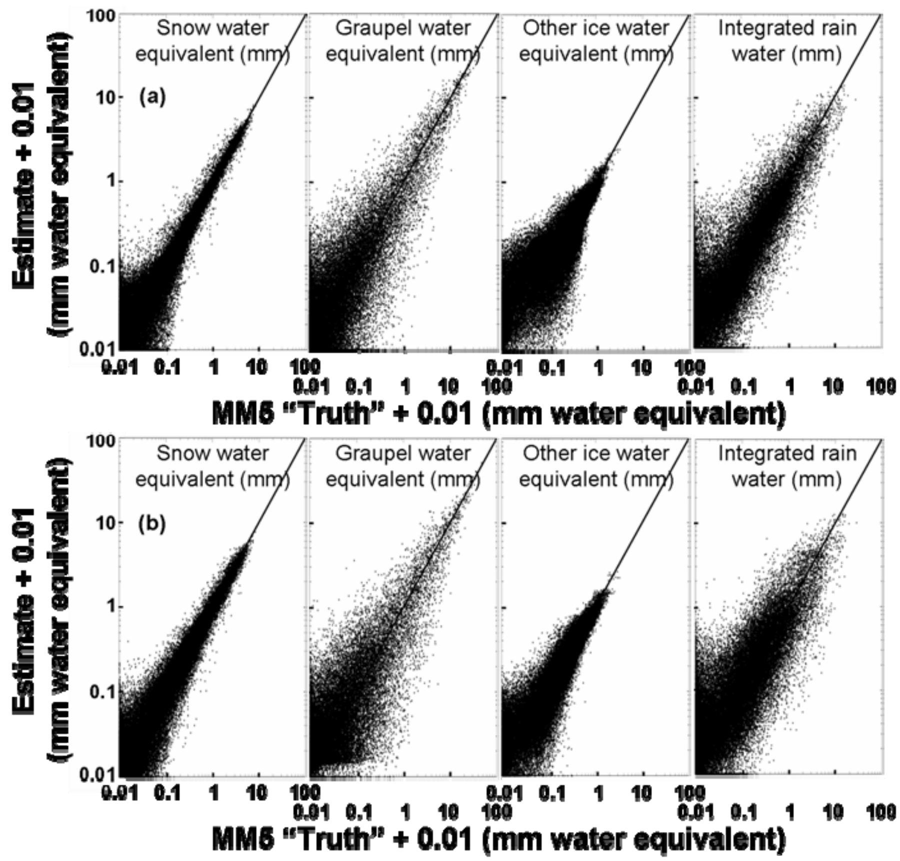

Fig. 5.8. Scatter diagrams for simulated water-path retrievals for snow, graupel, other ice, and rain water for (a) AMSU and (b) GEM, based on 122 global atmospheres over both land and sea.

Fig. 5.9 illustrates the simulated 15-minute surface precipitation-rate retrieval accuracy of AMSU and GEM relative to MM5 truth for 15-km resolution. AMSU estimates are based on one look at the end of the 15-minute averaging period. It was found that a small improvement was obtained when the GEM estimates were based on two looks 15-minutes apart (before and after), partially accounting for the effect of virga; this doubled the number of inputs to the GEM neural network from 12 to 24. The scatter plots suggest useful accuracy for precipitation rates above ~1 mm/h.

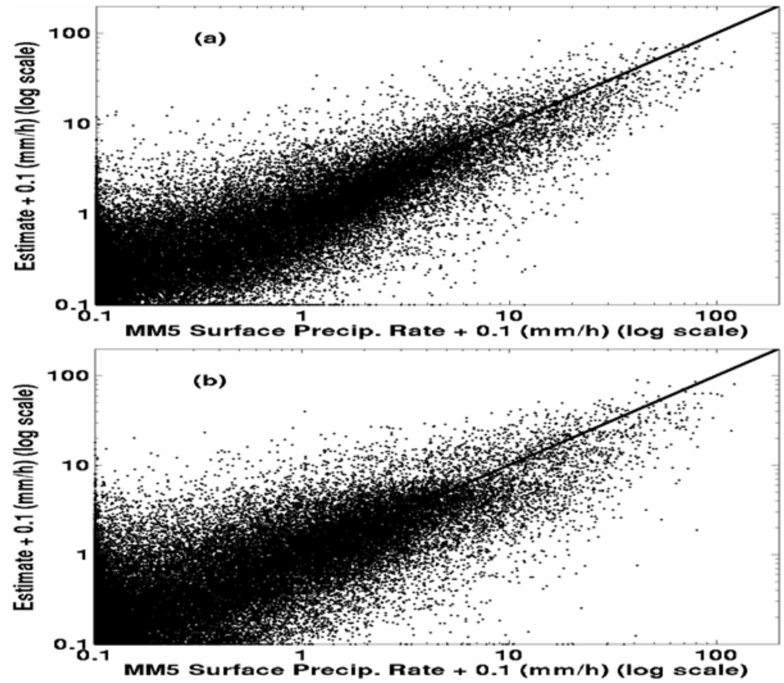

Fig. 5.9. Scatter diagrams for retrieved surface precipitation rates (mm/h, 15-minute averages) for (a) AMSU and (b) GEM based on 122 global atmospheres over both land and sea.

Fig. 5.10 presents the accuracy with which cell-top altitudes can be estimated using GEM, where cloud-top altitude is defined as the highest altitude for which the summed rain, snow and graupel water paths to space exceeds 0.05 mm. The mean and rms altitude errors above 5-km for GEM are approximately zero and 0.7 km, respectively, and ±0.5 km and ~0.9-1.2 km below 5-km altitude. The accuracy degradation in the low troposphere is consistent with the limited penetration depths above 140 GHz for tropical humidity. Similar simulations of cell-top altitude retrievals using AMSU yielded mean errors near zero at all altitudes and rms errors of ~0.9-1.2 km, consistent with the results from earlier airborne 118-GHz spectrometers observing oxygen absorption bands [61].

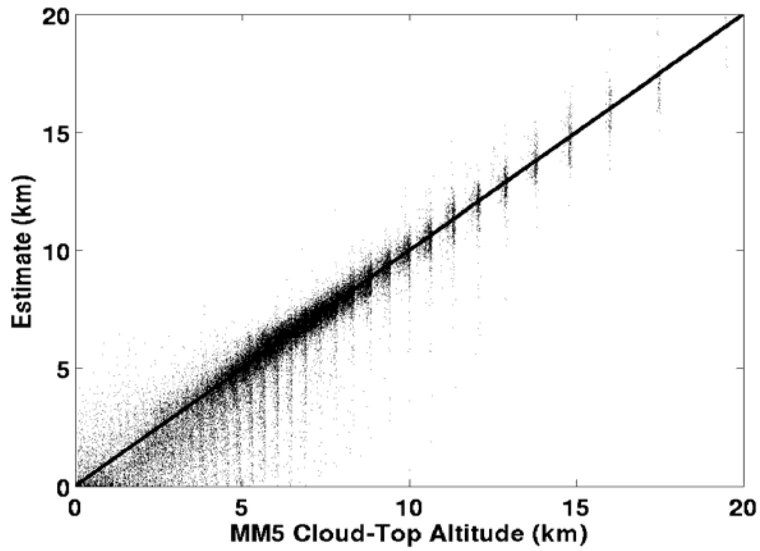

Fig. 5.10. Scatter diagram for simulated cloud-top altitudes (km) retrieved using GEM based on 122 global atmospheres over both land and sea.

The accuracies for surface rain and snowfall rates are determined largely by their statistical correlation with the abundance and altitudes of snow and graupel, which at millimeter wavelengths can be estimated more accurately than precipitation rates. Although this statistical relationship is climate-dependent, climate information is provided by the temperature and humidity profiles sensed by the same millimeter-wave sounding channels. The accuracy of the resulting surface precipitation retrievals is suggested in Fig. 5.11, which presents MM5 ground-truth precipitation rates and the corresponding rates derived for simulated AMSU and GEM observations of: a) a mid-latitude front over France at 1003 UTC 2 January 2003, b) the ITCZ at 0553 UTC 15 April 2003, c) snow (top half) plus rain (bottom half) over the western U.S. observed at 0423 UTC 10 November 2002, and d) a non-glaciated front observed at 0503 UTC 16 November 2002. The boundaries of raining regions are generally retrieved reasonably well with a 1-mm/h threshold, and only a few smaller convective cells located within stratiform zones are missed. The snow events (c) are better bounded with a 0.25-mm/h threshold. The largest errors occur when warm rain is observed by GEM, which usually cannot penetrate well the lowest 1-2 kilometers of the atmosphere where warm rain may reside, and therefore may fail to register some or all of it.

It is interesting to note that it took ~22 minutes to train a neural network to retrieve precipitation using AMSU data and 2.9×10^5 MM5 training pixels. Once trained, it retrieved ~2×10^5 pixels per second with a conventional 2.8-GHz PC and the MATLAB neural network toolbox operating in its computationally inefficient interpretive mode; it could therefore reduce one satellite year of data in a couple of hours. The most time consuming step was generation of the 2.9×10^5 brightness temperature and MM5 training pixels. To predict a single storm for 1 hr using the MM5 configurations shown in Table 3.1 took ~254 minutes using a conventional 2.4-GHz PC. To simulate AMSU-A and –B brightness temperatures for a single MM5 output with 190×190 pixels in the inner domain required ~1 hour with a 2.4 GHz PC. Clusters of 20 PC's were typically used for the 255 storms analyzed.

One important metric involves the ability of retrieval algorithms to distinguish precipitating from non-precipitating pixels. Such errors commonly occur near true precipitation, as suggested in Fig. 5.11, and depend upon the threshold definition for precipitation. For example, MM5 pixels with surface precipitation rates above 0.3 mm/h and retrievals less than 0.3 mm/h contribute ~3.2 and 3.0 percent of MM5 total surface precipitation rates for AMSU and GEM, respectively. On the other hand, MM5 pixels with surface precipitation rates below 0.3 mm/h and retrievals above 0.3 mm/h contribute ~7.9 and 11.8 percent of AMSU and GEM total surface precipitation rates, respectively. Both AMSU and GEM retrieve some excess precipitation when heavy cirrus spreads beyond convective cores.

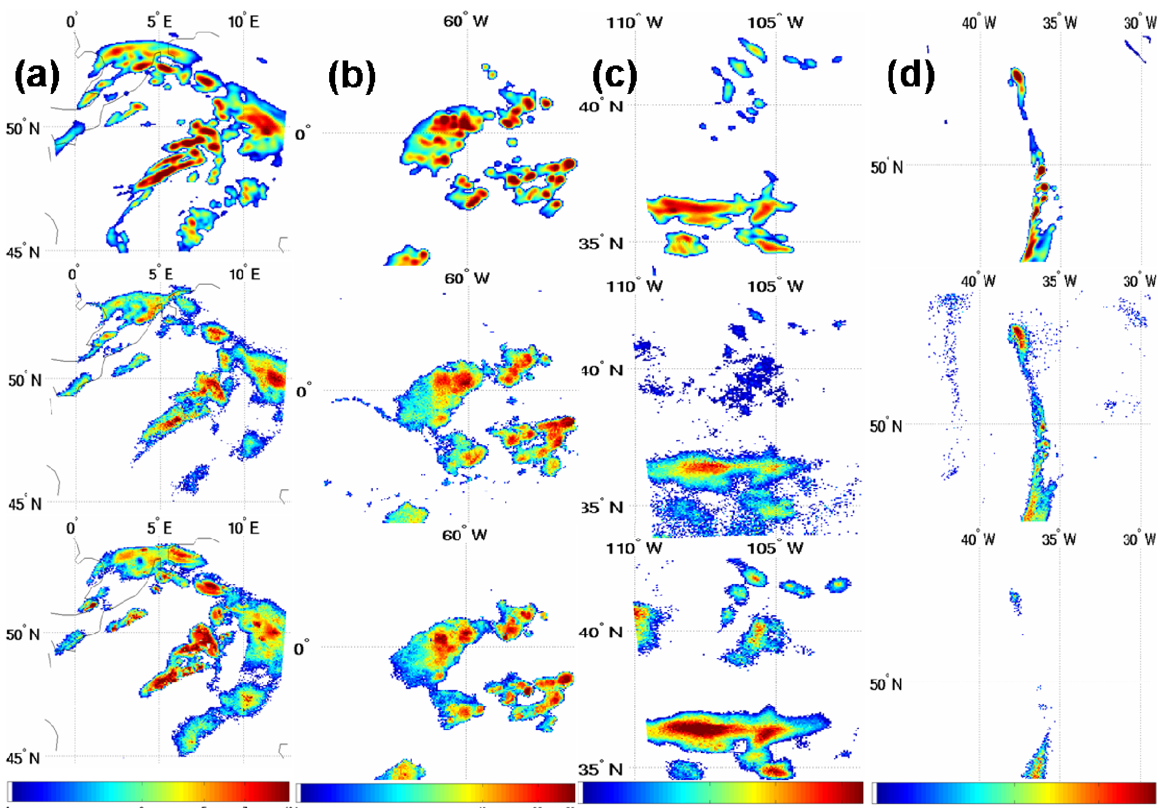

Fig. 5.11. Surface precipitation rates (mm/h; 15-minute integration) for: (a) summer frontal system over France at 1003 UTC 2 January 2003, (b) ITCZ at 0553 UTC 15 April 2003, (c) snow (top half) plus rain (bottom half) over land at 0423 UTC 10 November 2002; the threshold is 0.25 mm/h, and (d) non-glaciated system over ocean at 0503 UTC 16 November 2002. From top to bottom are displayed the MM5 simulated values, the instantaneous AMSU retrieval, and the two-sample 15-minute GEM retrieval.

5.5.2 Sensitivity of predicted accuracies to model imperfections

Retrieval accuracies determined using only simulations rather than field observations are suspect because they depend on how well the simulations model reality, which is often unknown. This section examines the degree to which the deduced retrieval accuracy depends upon the fidelity of the simulated world, designated "planet MM5", to Earth. The approach involves computation of retrieval accuracies for an ensemble of planets MM5 for which the physics has been varied over a dynamic range that arguably approximates or exceeds the unknown true differences between planet MM5 and Earth. Since the deduced retrieval accuracies are surprisingly independent of these large simulated physical variations, it can be inferred that the retrieval accuracies deduced from these simulations are reasonably reliable and probably would be achievable in practice.

Table 5.3 presents MM5-simulated AMSU rms surface-precipitation-rate retrieval accuracies for the baseline NCEP/MM5/TBSCAT/F(λ) model discussed in Chapter 4, and for a variety of altered physical assumptions involving the ice factors, abundances, altitudes, backscattering, loss tangent, and size distributions for snow and graupel. The table also presents the rms water-path accuracies derived for snow S, graupel G, cloud ice I, rain water R, and summed snow/graupel/rain (S+G+R) for the same baseline model. Blank entries in the table indicate that too few examples were available to compute reliable statistics. The same neural network architecture and strategy described in section 5.5.1 were used for all retrievals in Table 5.3; each estimated parameter utilized a different network trained on 293 thousand pixels selected uniformly from the same set of 122 storms; all 4.4 million pixels were used for testing.

The water path accuracies listed for AMSU in Table 5.3 correspond to the scatter plots presented in Fig. 5.8(a). The derived rms accuracies are less than the corresponding mean values in any octave range of interest, suggesting that all water path retrievals are useful, although rain-water path estimates are less accurate than those for icy hydrometeors. They also suggest that retrievals of the total water path for S+G+R are more accurate than are sums of the estimated components, and sometimes more accurate than single contributors (S, G, or R).

The baseline AMSU surface precipitation rate accuracies tabulated in Table 5.3 correspond to the scatter plot in Fig. 5.9(a), and suggest that surface precipitation rate retrievals are useful primarily above 1 mm/h. The baseline case, however, assumed a fixed: 1) set of F(λ)'s, 2) mixing-ratio-dependent hydrometeor size distribution function N(D) given by (3.1), 3) MM5 strategy for determining hydrometeor altitudes and abundances, 4) backscattering dependence on particle diameter, permittivity, and wavelength, and 5) temperature-dependent ice loss tangent. In fact, these assumptions represent averages of behaviors that vary, even within a single storm. For example: 1) hydrometeor habits and F values vary far more than assumed here in the DDSCAT computations for simple hexagonal plates, 6-pointed rosettes, and spheres, 2) the back-scattering ratio depends on those ice shapes, 3) the size distribution N(D) can vary with electrification, storm age, turbulence, and other variables, and 4) hydrometeor loss tangents and ε''_{ice} can depend on temperature and impurities. Therefore it is not sufficient simply to evaluate rms retrieval accuracies under different fixed sets of assumptions. Instead the simulated retrievals must reflect uncertainties and variations that can occur within a single test ensemble of storms. How best to accomplish this is the "randomization problem".

The retrieval system was randomized here by assuming that half the time MM5/RTM physics was governed by the baseline assumptions, and half the time by a relatively extreme modification of one of those assumptions. For example, the third column in Table 5.3 corresponds to a Planet MM5 for which, at random, half the time the physics is that of the baseline, and half the time the ice factors F_S and F_G for snow and graupel are both increased by 0.1, a change that produced clear disagreement with AMSU observations in Figs. 5.2(a) and 5.2(b). The neural network retrieval system was both trained and tested with the same fifty-percent ratio. The fourth column of the table similarly mixes the baseline with cases for which all ice is doubled, while columns 5, 6, and 7 present the rms retrievals errors for which the non-baseline cases involve lifting the snow and graupel by 100 mbar in altitude, increasing the back-scattering ratio by 0.1, and increasing ε''_{ice} by a factor of six, respectively.

Table 5.4 corresponds to Table 5.3, but for the geostationary sounder GEM. The results are similar, although the rms retrieval accuracies for GEM are ~20 percent worse than for AMSU due to the lack of GEM observations below ~140 GHz. Random doubling of snow and graupel abundances degrades the rms retrieval accuracy only 11 percent. For all physical assumptions, all estimated retrieval accuracies for each octave range are below the octave maximum for rain rates above 1 mm/h, and below the octave minimum for AMSU rates above 4 mm/h, and for GEM rates above 8 mm/h.

The important result derived from Tables 5.3 and 5.4 is that the predicted rms retrieval accuracies for all surface precipitation rates are surprisingly independent of the changes in physical assumptions, provided the statistics of the randomization are known. For example, for MM5 precipitation rates of 2-4 mm/h, the rms retrieval error varied no more than ±7 percent over all assumptions tested, the worst case being a reduction when the snow-to-graupel ratio increased an average of 50 percent. For rates of 32-64 mm/h the maximum departure from baseline was only ±4 percent in predicted rms retrieval errors. When the percentage increases in predicted rms retrieval errors are averaged over all rain-rate octaves, they increased ~1.3, 9.0, 4.6, 2.2, -1.0, and 0.8 percent for detectably different $F(\lambda)$, snow/graupel abundances, snow/graupel altitudes, backscattering, ice loss tangents, and snow/graupel size distributions, respectively. The largest increase in simulated retrieval errors is only 9 percent and corresponds to an average increase in snow and graupel mixing ratios of 50 percent, approximately twice the increase that would make the modeled brightness temperature histograms inconsistent with those observed by AMSU. The second largest increase, 4.6 percent, corresponds to increases in snow/graupel altitudes averaging 50 mb, also approximately twice the changes that could be detected using AMSU brightness histograms. That is, the retrieval accuracies estimated using MM5 vary less than a few percent for changes in the tested assumptions that would produce noticeable degradation in the demonstrated agreement (Fig. 4.6(a)) between MM5 and observed AMSU brightness temperature distributions for 122 storms.

The reason for this surprising insensitivity of predicted retrieval accuracies to physical uncertainties is still unclear.

As a result of this insensitivity to physical model uncertainties, quantified in Table 5.3, NCEP/MM5/TBSCAT/F(λ) simulations should yield reasonably reliable predictions of precipitation rate retrieval performance for a variety of millimeter-wave instruments and algorithms, and these accuracies should be reasonably achievable in practice.

TABLE 5.3
RMS ERRORS FOR 15-KM RESOLUTION AMSU RETRIEVALS UNDER VARIOUS PHYSICAL ASSUMPTIONS

MM5 Range (mm/h or mm)	Precipitation Rate Retrieval Accuracies (mm/h, rms)							Hydrometeor Water-path Retrievals (mm, rms) for Baseline Case				
	Baseline	$F_{S,G}$ + 0.1*	(S/G) × 2*	S/G ↑100 mb*	BS + 0.1*	ε''_{ice} × 6*	N_s, N_g = 3	S	G	I	R	RSG
0 – 0.125	*0.39*	*0.37*	*0.43*	*0.45*	*0.39*	*0.39*	*0.41*	0.02	0.04	0.06	0.06	*0.07*
0.125 – 0.25	*0.68*	*0.69*	*0.83*	*0.76*	*0.73*	*0.70*	*0.74*	**0.05**	0.19	**0.10**	0.16	**0.08**
0.25 – 0.5	*0.84*	*0.84*	*0.96*	*0.87*	*0.88*	*0.83*	*0.87*	**0.07**	0.30	**0.12**	**0.25**	**0.11**
0.5 – 1	*1.09*	*1.11*	*1.24*	*1.10*	*1.14*	*1.05*	*1.08*	**0.10**	0.52	**0.11**	**0.40**	**0.18**
1 – 2	1.44	1.45	1.60	1.44	1.46	1.36	1.38	**0.18**	**0.93**	**0.41**	**0.78**	**0.35**
2 – 4	2.27	2.21	2.36	2.26	2.21	2.15	2.11	**0.35**	**1.56**	-	**1.34**	**0.70**
4 – 8	**3.84**	4.01	4.09	**3.99**	**3.78**	**3.78**	**3.78**	**0.59**	**2.24**	-	**2.23**	**1.54**
8 – 16	**6.97**	**7.37**	**7.25**	**7.07**	**7.06**	**7.08**	**7.25**	**1.62**	**3.31**	-	**4.58**	**3.17**
16 – 32	**11.8**	**12.0**	**11.5**	**11.8**	**12.1**	**12.2**	**11.9**	-	**3.91**	-	**9.98**	**5.19**
32 - 64	**20.8**	**21.2**	**20.6**	**21.7**	**21.2**	**20.4**	**20.1**	-	-	-	**18.7**	**8.03**
64-174	**38.8**	**40.4**	**45.4**	**42.7**	**40.7**	**38.8**	**40.2**	-	-	-	-	-

S, G, I, R, and RSG signify the water paths for snow, graupel, cloud ice, rain water, and the sum of rain, snow, and graupel, respectively. BS is the Mie back-scattering fraction. ε''_{ice} is the imaginary part of ice permittivity. ↑ signifies movement to higher altitude. * indicates that baseline and modified pixels were mixed 50/50 for training and testing. Italics: rms errors that exceed the maximum value bounding the octave. Boldface: rms errors less than the minimum for the octave.

TABLE 5.4
RMS ERRORS FOR 15-KM RESOLUTION GEM RETRIEVALS UNDER VARIOUS PHYSICAL ASSUMPTIONS

MM5 Range (mm/h or mm)	Precipitation Rate Retrieval Accuracies (mm/h, rms)							Hydrometeor Water-path Retrievals (mm, rms) for Baseline Case				
	Baseline	$F_{S,G}$ + 0.1*	(S/G) × 2*	S/G ↑100 mb*	BS + 0.1*	ε''_{ice} × 6*	N_s, N_g = 3	S	G	I	R	RSG

0 – 0.125	*0.53*	*0.57*	*0.60*	*0.54*	*0.53*	*0.56*	*0.55*	0.03	0.05	0.04	0.07	*0.07*
0.125 – 0.25	*0.93*	*1.04*	*1.10*	*0.88*	*0.95*	*0.96*	*0.97*	**0.07**	0.22	**0.08**	0.21	**0.11**
0.25 – 0.5	*1.13*	*1.28*	*1.32*	*1.03*	*1.12*	*1.12*	*1.14*	**0.09**	0.35	**0.09**	0.34	**0.17**
0.5 – 1	*1.42*	*1.54*	*1.61*	*1.30*	*1.42*	*1.42*	*1.42*	**0.14**	0.59	**0.10**	0.52	**0.28**
1 – 2	1.72	1.84	1.89	1.65	1.68	1.76	1.73	**0.24**	0.98	**0.22**	**0.93**	**0.47**
2 – 4	2.42	2.55	2.67	2.55	2.41	2.47	2.52	**0.45**	**1.75**	**0.58**	**1.61**	**0.91**
4 – 8	4.11	4.08	4.59	4.24	4.21	3.99	4.13	**0.79**	**2.60**	**-**	**2.82**	**2.02**
8 – 16	**7.5**	**7.20**	8.30	**7.41**	8.06	**7.36**	**7.52**	**1.90**	**3.39**	**-**	**5.45**	**3.81**
16 – 32	**13.0**	**12.8**	**13.6**	**13.4**	**14.4**	**13.5**	**13.7**	**-**	**4.29**	**-**	**11.3**	**6.20**
32 - 64	**23.5**	**25.1**	**24.1**	**24.1**	**25.6**	**25.2**	**24.5**	**-**	**-**	**-**	**20.1**	**9.10**
64-174	**43.9**	**53.3**	**46.5**	**43.2**	**46.1**	**44.3**	**45.1**	-	-	-	-	-

S, G, I, R, and RSG signify the water paths for snow, graupel, cloud ice, rain water, and the sum of rain, snow, and graupel, respectively. BS is the Mie back-scattering fraction. ε''_{ice} is the imaginary part of ice permittivity. ↑ signifies movement to higher altitude. * indicates that baseline and modified pixels were mixed 50/50 for training and testing. Italics: rms errors that exceed the maximum value bounding the octave. Boldface: rms errors less than the minimum for the octave.

5.5.3 Characterization of Retrieval Errors

Improved understanding of the origins of retrieval errors can facilitate future retrieval improvements and understanding of limits to performance potentially available from cloud-scale precipitation assimilation methods. This understanding was sought by computing correlation coefficients between various storm-characterization parameters and "fractional surface-precipitation-rate error" Δ, where for each 15-km pixel Δ is defined as: $\Delta = (\hat{R} - R)/(R+1)$, where $\hat{R}$ and R are the estimated and MM5 true surface precipitation rates, respectively. The additive constant 1 mm/h in the denominator of the Δ definition was empirically selected to yield reasonable results; values much less than ~1 unduly exaggerated the error contributions of low rain rates, while much larger values excessively muted them.

The single most highly correlated explanatory variable for fractional error Δ is the dimensionless "virga parameter", which is defined here for each 15-km pixel as: $V = (\rho_{max} + 0.2)/(\rho_{ground} + 0.2)$. In this expression ρ_{max} is the maximum sum of rain, snow, and graupel densities (g m^{-3}) for any MM5 level, and ρ_{ground} is the corresponding summed density at 1000 mb. The correlation coefficient between virga V and fractional error Δ over 122 storms was found to be 34 percent for AMSU and 50 percent for GEM, as listed in Table 5.5. The additive constant 0.2 in the expression for V was empirically found to yield a reasonable compromise between excessive emphasis of low surface densities and excessive muting of low precipitation rates. Another way to characterize typical values of virga is by the ratios: $\langle \rho_{max} \rangle / \langle \rho_{ground} \rangle = 2.54$ and $\langle (\rho_{max} + 0.05)/(\rho_{ground} + 0.05) \rangle = 1.79$, where <x> is the sample mean for x. Thus, very roughly, only half of all MM5 precipitation reaches the surface, and most microwave sensors have difficulty detecting the virga phenomenon. The standard deviation associated with the second ratio is 1.35 for 15-km pixels. Corrections for descent velocity would refine these ratios. GEM retrievals are more sensitive to virga than are AMSU retrievals because AMSU has window, water vapor, and temperature-sounding channels that penetrate to the surface, whereas GEM usually does not.

TABLE 5.5
CORRELATION COEFFICIENTS, CORRCOEF(X,Y), BETWEEN MM5 PARAMETERS AND SURFACE-PRECIPITATION-RATE FRACTIONAL ERRORS

MM5 parameter	AMSU fractional error Δ	GEM fractional error Δ
Virga	0.34	0.50
Cloud-top altitude	0.13	0.21
Snow/graupel ratio	-0.04	0.005
Precipitation rate R	-0.12	-0.13

On the other hand, by assimilating GEM data directly into cloud-scale convective models at ~15-minute intervals there is hope that virga might be predicted by MM5 with sufficient fidelity that GEM-assimilated retrievals of surface precipitation rates could be noticeably improved. In addition, such assimilation success would also more properly account for the tendency of snow to spread laterally away from strong convective regions, mimicking stronger rain in millimeter-wave spectra. Thus there is substantial opportunity for improvement in the retrieval accuracies presented in Table 5.4. Success with precipitation assimilation on such spatial and time scales remains a grand challenge, however. Table 5.5 also presents correlation coefficients between fractional error Δ and the MM5 snow/graupel integrated mass ratio, cell-top altitude, and surface precipitation rate, none of which are strongly correlated.

5.6 Summary and Conclusions to Chapter 5

This chapter makes four technical points. First, there is an observable increase in the differences between NCEP/MM5/TBSCAT/F(λ) simulated radiance histograms and those observed by AMSU over coincident storm systems as certain properties of MM5 and the RTM are varied modestly. That is, changes in the equivalent Mie ice sphere density [F(λ)] of more than ~0.03 produced observable discrepancies with observations, as did increases in: two-stream ice scattering of more than ~1 percent, snow production more than ~15 percent, graupel production more than 25 percent, and the altitudes of snow and graupel more than ~25 mb. Less sensitive were ice loss tangents characterized by ε" and particle size distributions characterized by their zero intercept N_o; increases in ε" and N_o by factors of 4 and 7, respectively, were detectable. However physically plausible changes in cloud ice and rain water mixing ratios and water loss tangents were largely undetectable.

The second point is that the rms retrieval accuracies inferred from MM5 simulations are relatively insensitive to MM5 and RTM model variations that are sufficient to cause the MM5 simulations to differ from the AMSU radiance-histogram observations. When the model changes were randomly inserted half the time, and the changes were at least twice those detectable by the observed AMSU radiance histograms for 122 storms, the predicted rms retrieval errors for surface precipitation rate typically increased less than five percent, and sometimes declined. This result suggests that retrieval accuracies predicted using physical models comparable to MM5/TBSCAT/F(λ) should be achievable by satellites in orbit once the model physics is tuned to the actual observations. The AMSU retrievals tested here emphasized opaque frequencies and therefore these conclusions may not apply to retrievals for sensors relying more on surface channels since variations of the sea and land models described earlier were not tested.

Thirdly, the simulated retrieved precipitation-rate images (Fig. 5.11), scatter plots for surface precipitation rate and water paths versus model truth (Figs. 5.8 and 5.9), and predicted rms retrieval errors for each rate and water-path octave (Tables 5.3 and 5.4) suggest the utility of operational NOAA satellites carrying AMSU and successor instruments such as ATMS. The 2-3 such satellites now typically in orbit each map most of the earth in wide swaths twice daily, yielding repeat sampling by the constellation every ~4-8 hours.

Finally, it was shown in Table 5.4 that geostationary satellites could approach AMSU precipitation retrieval performance with a two-meter diameter filled-aperture antenna that could be integrated on current operational polar satellites. Such geostationary microwave precipitation sounders could observe significant storms on the spatial and time scales at which they evolve by making ~15-minute repeat observations with ~15-km resolution.

One implication of these results is that simulated assimilation experiments using appropriate NWP/RTM models should predict with reasonable accuracy the performance of actual systems for which the NWP and RT models are fine-tuned before operational use. Therefore it may not be necessary to place more experimental millimeter-wave systems in orbit before estimating their potential retrieval performance and contributions to NWP; rather accurate performance predictions can arguably now be made using proper simulations alone.

Chapter 6

Precipitation Retrieval Accuracies for Geo-Microwave Sounders

All results presented in this chapter are from [3].

6.1 Abstract

Only instruments on geostationary or comparable platforms can view global precipitation at the ~15-minute intervals necessary to monitor rapidly evolving convective events. This chapter compares the abilities of eleven such alternative passive microwave sensors to retrieve surface precipitation rates and hydrometeor water paths--five instruments observe selected frequencies from 116 GHz to 429 GHz with a filled-aperture antenna, and six observe from 52 to 191 GHz with a U-shaped aperture synthesis array. The analysis is based on neural network retrieval methods and 122 global MM5-simulated storms that are generally consistent with simultaneous AMSU observations. Several instruments show considerable promise for retrieving hydrometeor water paths and 15-minute average precipitation rates ~1-100 mm/h with spatial resolutions that vary from ~15 km to ~50 km. This space/time resolution is potentially adequate to support assimilation of precipitation information into cloud-resolving numerical weather prediction models

6.2 Introduction

One major current remote sensing challenge is to monitor global precipitation accurately on the time and spatial scales at which it evolves--e.g., ~10-30 km and ~10-30 minutes. Such a system could not only provide better nowcasting, but may also permit cloud-scale assimilation of precipitation into numerical weather prediction (NWP) models so as to improve both precipitation retrievals and weather forecasts.

Current geostationary (GEO) satellites permit better than 15-minute and 10-km resolution at infrared wavelengths, but cannot penetrate overlying clouds, while the more accurate low-earth-orbit (LEO) satellites with cloud-penetrating ~15-km microwave resolution generally repeat their observations only at intervals of hours or more. Although dense radar and rain gauge networks provide good local coverage, they are too costly and land-bound to cover most nations and their surrounding waters. Even the NEXRAD 158-radar system covers only ~20 percent of the continental United States within its best-performance 110-km range, and less than 60 percent within 220-km range.

Geo-microwave systems that resolve important storms in both time and space have been proposed for many years [53], [64], but generally without analysis of their precipitation and hydrometeor retrieval performance, which is the focus of this chapter. The main conclusion is that most precipitation can be retrieved at ~15-60 minute intervals from geosynchronous orbit, and that at least one relatively inexpensive approach exists--use of a micro-scanned aperture antenna ~1.2 meters in diameter.

6.3 Filled Aperture Antennas

6.3.1 Spatial Resolution

Approaches to achieving the required high angular resolution include a single mechanically steered filled-aperture antenna of ~1-3 meter diameter D operating at frequencies up to 425 GHz, designated here as GEM [53], and aperture synthesis systems incorporating hundreds of antenna feeds and amplifiers, designated GeoSTAR [65]. A uniformly-illuminated circular aperture yields 3-dB beamwidths $\theta_B \cong 1.2\ \lambda/D$ radians, where λ is wavelength, while reasonable illumination tapering yields $\theta_B \cong 1.3\lambda/D$. Nyquist sampling and image sharpening can yield $\theta_B \cong 0.95\lambda/D$, as discussed later. Aperture synthesis systems yield, for example, beamwidths of ~$0.7\lambda/D$, where D is the diagonal length of a square U-shaped antenna array. The spatial resolution of GEM at nadir ranges from 12 km for an image-sharpened 2-m antenna operating near 425 GHz, to values over 45 km below 118 GHz. For a single-band aperture synthesis system the resolution ranges from 25 km for a 600-receiver system to 50 km for 300 receivers, independent of wavelength, as discussed further in Section 6.4.1.

6.3.2 Image Sharpening

From Section 2.4, Nyquist sampling and image sharpening can yield $\theta_B \cong 0.95\lambda/D$, as illustrated in Fig. 6.1 for reasonable assumptions about receiver sensitivity. Image sharpening involves deconvolving the antenna pattern $G(\theta,\phi)$ from the antenna temperature observations $T_A(\theta,\phi)$ to yield the estimated angular brightness temperature distribution $\hat{T}_B(\theta,\phi)$ with improved spatial resolution:

$$\hat{T}_B(\theta,\phi) = F^{-1}\{W \cdot F[T_A(\theta,\phi)] / F[G(\theta,\phi)]\} \quad [\mathrm{K}] \tag{6.1}$$

where F and F^{-1} are the angular Fourier- and inverse-Fourier-transform operators, respectively, and W is a weighting function in angular frequency space (cycles/radian) that maximizes the signal-to-noise ratio, partly by canceling nulls in $F[G(\theta,\phi)]$. It can be shown by differentiating the total mean-square error with respect to W(f), and assuming the noise is uncorrelated with the image, that W(f) at any two-dimensional angular frequency f is:

$$W(f) = \left[1 + \frac{\left\langle \left| \underline{N}(f) \right|^2 \right\rangle}{\left\langle \left| \underline{T}_A(f) \right|^2 \right\rangle} \right]^{-1} \tag{6.2}$$

where $\langle A \rangle$ is the expected value of A, $\underline{N}(f)$ is the complex two-dimensional angular Fourier transform of the additive thermal noise, and $\underline{T}_A(f)$ is the same for the antenna temperature. $\underline{F}[G] = G(f)$ is purely real when $G(\theta,\phi)$ is an even function, as assumed here.

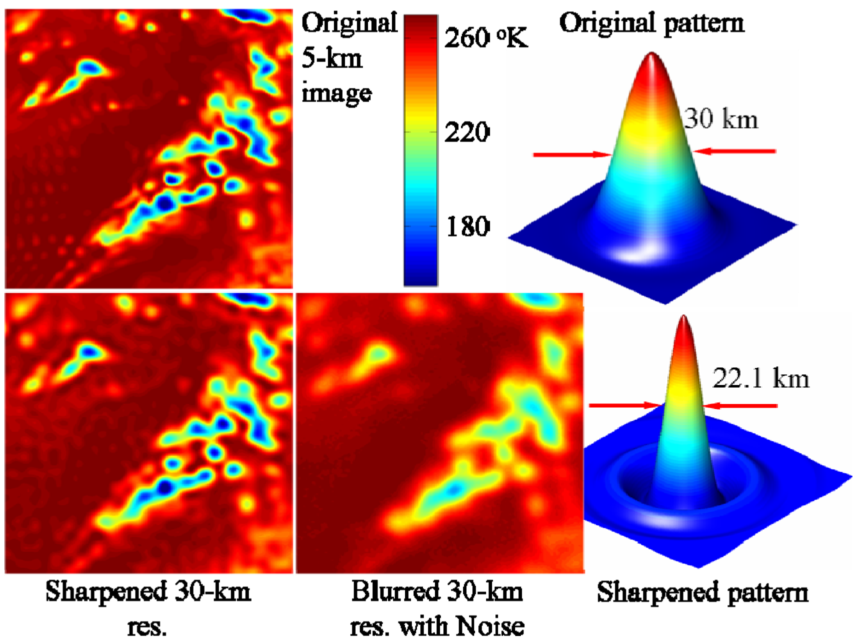

Fig. 6.1. Original, blurred, and sharpened images using Nyquist sampling and assuming $\Delta T_{rms} = 0.5K$ for 30-km steps, which is equivalent to $\Delta T_{rms} = 3K$ for 5-km steps.

Fig. 6.1 (top left) shows a rainstorm 555-km square viewed at 183±7 GHz with 5-km resolution, as simulated using the numerical weather prediction and radiative transfer models NCEP/MM5/TBSCAT/F(λ) described in Section 6.6.1. This was then blurred with the illustrated original antenna pattern, which is 30-km wide at half-power. The image was then sharpened using (6.1) and (6.2). It was assumed in (6.2) that the signal-to-noise ratio $|\underline{T}_A|^2/|\underline{N}|^2 = 20 \bullet G(f)$, where $G(0) = 1$, and that the receiver sensitivity for independent 30-km pixels was 0.5K rms, which corresponds to 3K rms when the integration time is shortened to permit 5-km sample spacing. The sharpened image is shown at the lower left, and the synthesized antenna pattern $G_s(\theta,\phi)$ with its 22.1-km half-power width is at the lower right, where it can be seen from (6.1) that:

$$G_s(\theta,\phi) = F^{-1}\{W(f)\} \tag{6.3}$$

Any image to be sharpened must be sampled above its Nyquist rate to avoid aliasing. For aperture antennas of maximum aperture width D the Nyquist angle of maximum sample separation is $\lambda/2D$. Such frequent sampling reduces the integration time and sensitivity per spot, but this loss is partially recovered by the averaging that occurs in image reconstruction. Sharpening increases the high-angular-frequency noise, which is evident in the non-precipitating areas of the illustrated sharpened image. The resulting rms noise in the quiet portions of the sharpened image is ~2K. Since the dynamic range of precipitation signatures is generally large compared to noise of less than a few degrees, sharpening often exacts little penalty. This penalty was incorporated in the retrieval analyses presented in Section 6.6.

6.3.3 Micro-Scanned Filled-Aperture Antennas

The principal advantage of filled-aperture microwave systems is their simplicity and low cost even when observing many frequency bands and channels within bands. Their principal disadvantage is that they must be scanned mechanically, which may affect the pointing of other instruments on the same satellite. Fortunately, the momentum impact of scanning can be significantly reduced by using a small rapidly tilting/translating subreflector in a Cassegrain configuration, as suggested in Fig. 6.2. The large primary reflector can then be scanned very slowly without disturbing other instruments.

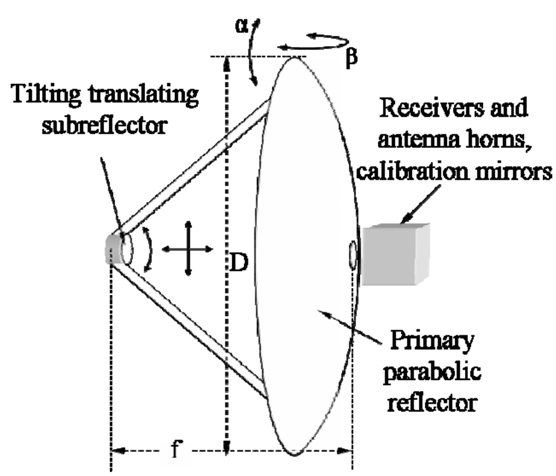

Fig. 6.2. Microscanned aperture antenna.

The main beam efficiencies of 425-GHz beams scanned ten 3-dB beamwidths (0.3 degrees) off axis by a 15-cm diameter tilted and translated subreflector are not significantly degraded for a 2-m aperture with a 1-meter focal length f. Tilting the subreflector without translating it produces higher sidelobes [66]. If adjacent scan lines are separated by 10 km, which is Nyquist spacing at 425 GHz, then 20 or more beamwidths can be "microscanned" cross-track each second as the main reflector scans orthogonally down-track at only ~0.016 degree per second, approximately one-sixth the angular speed of the minute hand on a watch. With such slow scan rates open-loop momentum compensation can readily handle the residual momentum transfer to the satellite due to the scanning. Also, the required scan power is less than a watt for both the subreflector and main reflector, neglecting bearing friction. Even when slewing from one storm to another the average scan rate could still be less than 0.2 degrees per second, twice the angular speed of a minute hand. For nominal total-power receiver noise temperatures near 400 GHz of 3000K, and a scan retrace time of 0.2 seconds, the integration time would be 40 ms per 425-GHz beamwidth of 17 km; the receiver sensitivity ΔT_{rms} would then be ~0.47K for a 1-GHz bandwidth, generally consistent with the retrieval studies presented in Section 6.6.

Although the entire earth cannot readily be scanned rapidly with a 2-meter antenna, most or all economically significant precipitation could be scanned at ~15-minute intervals with ~20-km resolution, sufficient to resolve most storm evolution. For example, if each 20-km grid point were observed for ~0.04 seconds, consistent with one 20-beam microscan line being scanned per second with ~0.2-second retrace time, then in 15 minutes approximately 7.2×10^6 km^2 could be surveyed. This compares to the ~2.3×10^6 km^2 and ~0.4×10^6 km^2 typically observed by AMSU to be precipitating above 1 and 5 mm/h, respectively, within a circular geostationary field of view bounded by ±50-degree latitude. If the precipitating areas are surveyed inefficiently with swaths ~200 km wide rather than pixel by pixel, the required survey areas increase very approximately to ~13.5×10^6 km^2 for the 1-mm/h rate, deduced by dilating three days of AMSU data using an annulus of 75 km about each precipitating pixel.

Based on this example, a 2-meter GEM could survey 10 storms of size 600×600 km every 15 minutes, plus all other 1-mm precipitation every hour. More could be surveyed with smaller GEM antennas, or by using only frequencies below 200 GHz, with the attendant loss in spatial resolution. Conversely, if image sharpening is used when surveying severe storms every 15 minutes, then only five such storms could be studied at once. The areas to be surveyed could be selected in real time by computer algorithms using a combination of prior microwave images, current GOES infrared data showing new cloud growth, and numerical model output.

The technical risks below 500 GHz are low because a mechanically scanned 1.6-meter parabolic reflector with a 640-GHz sub-millimeter spectrometer has already flown on the Microwave Limb Sounder (MLS) on the NASA Aura satellite [67] and is working successfully more than two years after launch. Moreover, studies have shown that such 2-m micro-scanned instruments could be integrated and launched on GOES platforms and vehicles used in the 1990's [68], and more capable geostationary platforms are available today.

6.4 Aperture Synthesis Systems

6.4.1 Complexity versus Resolution

An alternate approach to achieving high spatial resolution involves aperture synthesis techniques long used in radio astronomy [69]. One advantage of this approach is that it yields beamwidths $\theta_B \cong 0.7\lambda/D$ instead of $0.95\lambda/D$ or even $1.3\lambda/D$, where D is the diagonal length of a square U-shaped antenna array. However the practical cost limit in this case is not posed by the aperture size D but rather by the very large numbers of RF receivers and correlators required to avoid aliasing of the earth within the field of view of interest. That is, the synthesized image of the earth contains duplicate overlapped images spaced at $\theta_I = \lambda/L$ radians, where L is the distance between adjacent antennas, and the desired image width $\theta_I = M\theta_B \cong 0.3$ radians in order to avoid earth aliasing; M is the number of independent pixels across the image. If the antenna array is U-shaped and comprises three equal length arms of length A that each have N antennas equally spaced L apart in a straight line, then $A \cong NL$ and $\theta_B = \lambda/2A = \lambda/2NL$. It follows that $M = 2N$ since $M = \theta_I/\theta_B = (\lambda/L)/(\lambda/2NL)$. For resolution near nadir of S km, $\theta_B \cong S/35{,}000$, and the required number of antennas and RF units for each spectral line or broad band observed is:

$$3N = 1.5\theta_I/\theta_B \cong 16{,}000/S \tag{6.4}$$

System cost, power, and complexity all increase with N, and therefore N rather than aperture length would generally limit system size.

For the choices of N analyzed in this chapter, the resolution θ_B available from aperture synthesis systems is either 25 or 50 km. The assumed antenna array configuration is always a U-shaped square with a smaller maximum dimension than Y-configurations offering equivalent resolution [65]. A U-shaped array could also be wrapped around a rectangular spacecraft, simplifying and perhaps even avoiding deployment. If the length of each of the three connected arms is A = 2 meters, then near 53-GHz the synthesized antenna beamwidth $\theta_B \cong \lambda/2A$ radians, peak-to-first-null. This corresponds to 50-km nadir resolution and a U-array hypotenuse of ~2.8 m, larger than the 2-meter filled-aperture antenna diameter assumed here. If 100 equally spaced antennas and receivers are used in each arm (300 units total), the recovered image would exhibit aliased images of the earth in a square grid at angles of $100\lambda/A \cong 16.2$ degrees, and provide a non-aliased square clear zone of ~200 50-km pixels that measures ~10,000 km across. Thus 50-km resolution requires ~300 receivers per band, and 25-km resolution requires ~600. Slightly more non-aliased area per antenna can be obtained with the Y-configuration, although its maximum dimension also increases.

Since the bandwidths of millimeter-wave receivers are much less than an octave, separate antenna arrays are required for each observed band. However several channels within each band can be observed sequentially by repeatedly retuning the local oscillators. The principal advantage of synthesis systems is lack of mechanical scanning and large area coverage, and their principal disadvantages are their relatively high power, weight, and cost, in addition to their current unproven laboratory performance at scale or above 60 GHz.

6.4.2 Receiver Sensitivity

The sensitivity of an aperture synthesis system can be estimated by noting that its effective area is ~$3NA_e$, where 3N is the number of antennas and A_e is the effective area of each [69]. The effective area A_e is governed by the beam solid angle that embraces the earth, and is only ~$10\lambda^2$. This disadvantage relative to a filled aperture is almost perfectly compensated by the fact that all $4N^2$ pixels on the earth are viewed simultaneously, increasing the available integration time correspondingly. Thus synthetic and unsharpened filled apertures yield comparable image noise levels for comparable receivers and total integration times, provided that both systems survey the entire visible earth and have the same bandwidth and receiver noise temperature. Since GEM could image critical precipitating regions arbitrarily frequently by narrowing the survey area, its integration time per pixel and its sensitivity could be correspondingly greater. In addition the bandwidth for most GEM channels is ~1 GHz instead of the 100 MHz reported for GeoSTAR [70], which offers an opportunity to reduce GEM integration times another factor of ten, making it feasible for GEM to view storms with 0.5K rms sensitivity and 20-km resolution at 425 GHz and 15-minute intervals rather than the 30-minute or longer intervals required by comparably sensitive aperture synthesis systems, even with receiver noise temperatures of 1000K.

6.5 Physical Basis for Frequency Selection

6.5.1 Introduction

The principal historical barrier to placing microwave systems in geostationary orbit has been the high projected costs resulting from the large antenna diameters D required to achieve a useful angular resolution $\theta_B \cong 1.3\lambda/D$, where λ is the wavelength and the 3-dB antenna beamwidth θ_B is diffraction limited. The recent successful measurement of precipitation by the Advanced Microwave Sounding Unit (AMSU) on NOAA-15 and successor instruments has motivated renewed exploration of microwave frequencies above 120 GHz for this purpose, permitting use of smaller practical antennas. Such microwave systems can also help cloud-clear geostationary hyperspectral infrared imagery, as demonstrated for the infrared and microwave sensors on the NASA Aqua satellite by Cho and Staelin [71] and others. This section reviews the key features of the candidate millimeter-wave bands.

The four most important microwave signatures of precipitation arise from: 1) emission over cold reflective oceanic backgrounds, 2) scattering by ice aloft at altitudes revealed by comparing observations at nearby frequencies that penetrate to different known altitudes in oxygen absorption bands, 3) scattering by ice aloft observed at different frequency- and humidity-dependent altitudes within water vapor absorption bands, and 4) diameter-dependent scattering from icy hydrometeors observed at well-spaced frequencies sounding comparable altitudes. The use of these signatures is discussed below.

6.5.2 Emission over Cold Backgrounds

Global vapor and liquid water emission is routinely measured by the U.S. Department of Defense Special Sensor Microwave/Imager (SSM/I) and similar sensors [59] by using cross-polarized antennas in "window" bands below 90 GHz to help separate the effects of surface temperature from surface emissivity. Although dual polarization does not work well for equatorial regions viewed from geostationary orbit because of the small zenith angles there, good performance can be achieved with a single polarization because equatorial oceanic emissivity is reasonably predictable. Geosynchronous dual polarization will work at mid-latitudes and above over both land and sea because of the large zenith angles. Separation of humidity and rain water effects is straightforward for SSM/I because most hydrometeors are in the linear Rayleigh scattering regime, and the water vapor band near 22 GHz is sufficiently transparent to both water vapor and liquid water that spectral observations respond almost linearly to their superposition with known frequency-dependent coefficients. The resulting equations can be solved to retrieve both constituents. Unfortunately geosynchronous antennas systems that resolve convective precipitation cells near 22 GHz could be prohibitively large

6.5.3 Sensing of Cell-Top Altitudes

The use of adjacent frequencies in opaque oxygen bands to infer the altitudes of icy cell tops was first demonstrated using aircraft observations near the 118-GHz oxygen resonance [60]-[61]. Discrepancies between retrieved cell-top altitudes and those inferred from optical parallax observations were estimated to be ~1-km rms due to microwave uncertainties. The same technique can also be used in the 54-GHz oxygen band. Since icy cloud tops lie above most humidity, even the 425-GHz oxygen band can be used for this purpose, although it usually cannot penetrate atmospheric humidity to reach the tops of warm rain cells below ~3-5 km altitude.

The altitudes of icy cell tops relative to the humidity profile can be determined from observations in opaque water vapor bands such as those near 183 and 380 GHz. That is, strong convection can carry hydrometeors higher into dryer layers of the atmosphere so they become more visible in the most opaque water vapor channels. This is evident, for example, in typhoons where only the most intense convection produces strong signatures in the 183±1 GHz band [72].

6.5.4 Hydrometeor Size Distribution

Finally, the size distributions of icy hydrometeors can be inferred from the relative scattering signatures at frequencies located an octave or more apart in the 50 - 200 GHz region. Most snow and graupel has diameter d of 1-5 mm, so this spectral region includes the transition from Rayleigh to geometric scattering where scattering cross-sections are proportional to d^6 and d^2, respectively. Thus comparable scattering near 50 and 150 GHz implies large hydrometeors, while strong scattering above 150 GHz and very little near 50 GHz indicates smaller ones. This ability to sense variations in d below the visible cloud tops has been demonstrated using aircraft observations over convective cells at frequencies from 50 to 430 GHz [60], [62], [63]. These ice scattering signatures include albedos that can exceed 50 percent and yield perturbations over 100K, which is substantially greater than nominal rms receiver sensitivities <1K. Because large hydrometeors require higher vertical winds to create and hold them aloft, d is positively correlated with higher vertical wind speeds and stronger convective rain.

6.5.5 Frequencies Selected for Study

The altitude h_λ to which any wavelength λ penetrates is suggested by its weighting function $W(h,\lambda)$, where temperature weighting functions at opaque oxygen band wavelengths are given by:

$$T_B(\lambda) \cong \int_0^\infty T(h)\alpha(h,\lambda) e^{-\int_h^\infty \alpha(h,\lambda)dh} dh \tag{6.5}$$

$$= \int_0^\infty T(h) W(h,\lambda) dh \tag{6.6}$$

where T_B is brightness temperature (K), T(h) is the atmospheric temperature profile, and $\alpha(h,\lambda)$ is the absorption coefficient at wavelength λ and altitude h. The temperature weighting function peak height h_λ is defined as the altitude where $W(h,\lambda)$ peaks. Similar weighting functions can be defined for water vapor sounding channels.

Table 6.1 indicates the frequencies of interest in this study and the altitudes h_λ at which their temperature weighting functions peak for the U.S. standard atmosphere. For simplicity, only four observing frequencies are listed for each band, although optimum sensors might reasonably incorporate more. However, as suggested by the retrieval results reported later in Table 6.3, the additional retrieval performance enabled by including more frequencies is believed to be modest.

TABLE 6.1
INSTRUMENT FREQUENCIES AND WEIGHTING FUNCTION PEAK HEIGHTS FOR THE 1976 U.S. STANDARD ATMOSPHERE VIEWED AT NADIR OVER A NONREFLECTIVE SURFACE

Center frequencies (GHz)	Weighting function peak height (km)	Center frequencies (GHz)	Weighting function peak height (km)
52.8	0	183.31 ± 3	4.0
53.6	4	183.31 ± 7	1.8
54.4	8	380.197 ± 1.5	8.5
55.5	12.5	380.197 ± 4.0	6.6
118.75 ± 0.5	12.5	380.197 ± 9.0	4.6
118.75 ± 1.15	7.5	380.197 ± 18.0	3.1
118.75 ± 1.5	4.5	424.763 ± 0.6	14.5
118.75 ± 2.05	0	424.763 ± 1.0	11.5
166	0	424.763 ± 1.5	7.5
183.31 ± 1	6.1	424.763 ± 4.0	4

6.6 Retrieval Method

6.6.1 Simulation of Brightness Temperatures

The brightness temperature spectra used for training the retrieval algorithm were based on NCEP-initialized MM5 forecasts computed for 122 global storms in all seasons described in Section 3.2. The NCEP analyses had 1-degree resolution at 0Z, 6Z, 12Z, and 18Z for pressure levels extending to 10 mbar. MM5 was then run with 5-km resolution for 4-6 hours after initialization so as to coincide with simultaneous observations by AMSU on NOAA-15, -16, and -17. These 122 storms represent about half the original set of 255 storms that were evaluated, the remainder typically having been discarded because the NCEP initialization fields were not sufficiently accurate, as determined using concurrent AMSU observations [1].

The brightness temperatures were computed using: 1) domain 3 of MM5 at 5-km resolution, 2) radiative transfer computations using TBSCAT in its two-stream formulation, together with Mie scattering from spheres of density $F(\lambda)$ defined as the average of the values given by Table 4.2 and F(200 GHz) as discussed in Section 5.5.1, which was generally consistent with preliminary DDSCAT calculations at these higher frequencies where Section 5.5.2 demonstrates that estimated retrieval accuracies are reasonably insensitive to errors in $F(\lambda)$, and then 3) Gaussian blurring of the brightness temperatures with the spatial resolution indicated in Table 6.2; the resolutions shown for options B and D are sharpened beamwidths.

Since uncertainties in surface emissivity and brightness can significantly affect retrieval accuracies, the emissivity of land was assumed to be random and uniformly distributed between 0.91 and 0.97. Ocean emissivity was modeled using FASTEM [47]. Only 12 percent of the 1.5 million available pixels were used for training; these were arranged in a rectangular grid that was maximally offset from the validation pixel grid.

6.6.2 Neural Network Design and Training

Because the retrieval problem is nonlinear and non-Gaussian, neural networks trained with the Levenberg-Marquardt training algorithm [49] were used. All sensors were compared using the same method, which utilizes three feed-forward neural networks [2]. If the first network estimated over 8 mm/h, then the second neural network was used to estimate the 15-minute average precipitation rate; otherwise the third network was used. The networks were trained with MM5 precipitation rates blurred to 25 km, a land/sea flag, and the channel brightness temperatures.

Each neuron in the first layer of the network utilized two inputs per channel, i.e., the current brightness temperatures and those observed 15 minutes earlier. The three layers of each network with more than 9 inputs had 10, 5, and 1 neuron, respectively, and 5, 5, and 1 neuron otherwise. The first two layers used a $\tanh(\theta)$ sigmoid function. For each network and task the best of 100 tested networks was used. For hydrometeor water path retrievals one feed-forward neural network and one observation time were used for each hydrometeor species. The precipitation retrieval accuracy predicted using these techniques is relatively insensitive to modest errors in MM5 and in the radiative transfer model [2].

6.6.3 Instrument Options Analyzed

Table 6.2 lists the sets of frequencies and nadir spatial resolutions for each instrument type and frequency band for which performance was evaluated; these include five filled-aperture options (A-E), and six aperture-synthesis options (F-K). Four channels are observed in each band, each channel having assumed sensitivities ΔT_{rms} of 0.5K for 40-ms integration times. When image sharpening is used the integration time per sample is reduced a factor of 8, increasing the rms noise to 1.41K. Simulations indicate that rms sensitivities as poor as 1K do not significantly degrade most precipitation retrievals because millimeter-wave precipitation signatures are so strong.

TABLE 6.2
FREQUENCIES AND NADIR RESOLUTION (KM) FOR 11 INSTRUMENT OPTIONS

Approximate Frequencies (GHz)	A (1.2m)	B (2m,S)	C (2m)	D (1.2m,S)	E (1.2m)	F (1200)	G (600)	H (900)	I (600)	J (300)	K (300)
52.8, 53.6, 54.4, 55.5						25	50	50	25	50	
118.75±0.5, ±1.15, ±1.5, ±2.05	97	38	58	62	97	25	50				50
166	69	28	42	44	69			25			
183.31±1, ±3, ±7	63	26	38	42	63			25			
380.2±1.5, ±4, ±9, ±18		14	18	22	30						
424.76±0.6, ±1, ±1.5, ±4		12	17	20	27						

Two of the filled-aperture options (B-C) employ a Cassegrain antenna 2 meters in diameter, small enough to be readily integrated on an operational GOES satellite, and three employ an even smaller and more practical one of diameter 1.2 m (A, D, E). Options B and D employ image sharpening with full-width-half-power (FWHP) beamwidths of 0.95λ/D resolution, while the other options have FWHP beamwidths of 1.3λ/D.

The largest aperture synthesis systems (F and I) measure ~5.6 meters on the diagonal for a U-shaped configuration operating near 53 GHz with 4-m arms; the corresponding Y configuration with 25-km resolution would be even larger [65]. Options G, H, and J measure 2.8 meters, and K measures only ~1.2 meters. The nominal set of 300 antenna/amplifier/mixer assemblies assumed for options J and K may already stress feasible cost, weight, and power limits while yielding a synthesized resolution of ~50 km at nadir in any 10-percent spectral band if we accept some aliasing near the limb. Use of 600 RF assemblies permits spectral observations in two bands (option G), or ~25-km resolution in one band (option I), while 900 RF assemblies permit AMSU-like 50- and 25-km resolution near 53 and 183 GHz (H), respectively, and 1200 yield 25-km resolution at both 53 and 118 GHz (F).

6.6.4 Precipitation Rate Retrieval Results

Precipitation-rate retrieval images (mm/h) for four representative precipitation types are presented in Fig. 6.3 for instrument configurations C, D, E, F, G, and H, arranged left to right. The left-most image in each row is the corresponding MM5 simulation. From top to bottom the precipitation corresponds to a typhoon (12/8/02; ~15N/145E), stratiform rain (12/14/02; ~40N/125W), a strong front over France (1/2/03; ~50N/5E), and oceanic warm rain (11/16/02; ~50N/35W). The images suggest that even the 1200-receiver 5.6-m aperture synthesis system F cannot always surpass the performance of the inexpensive 1.2-meter diameter GEM option E, particularly for the typhoon. Comparison of systems F and G show the image degradation when the resolution grows to 50 km, and comparison of systems D and E show that the benefits of image sharpening are restricted primarily to relatively rare isolated storms such as the ones in the upper left and lower right of the French frontal system, and within the warm rain event, and that the noise introduced by sharpening is otherwise unwelcome. Comparison of the images for the unsharpened 2- and 1.2-meter GEM systems (C and E) does not suggest a major advantage for the 2-meter option except for its important ability to retrieve the warm rain event. The demonstration that such a small simple and relatively inexpensive system E rivals larger more expensive alternatives is one of the key contributions of this chapter.

Table 6.3 presents the rms errors in retrieved 15-minute, 25-km surface precipitation rates averaged over the same 122 storms, but for an offset grid of pixels, 1369 pixels per storm and 167,018 total. The 25-km resolution MM5 rates were determined by convolving the 5-km rates with a 25-km gaussian, which is the resolution for which all neural network estimators were trained. Training and evaluating retrievals with better resolution should favor the sharpened results more. The error statistics are computed for each octave (factor of two) of surface precipitation rate, as defined by MM5. The table also presents rms retrieval errors for instantaneous graupel, snow, and rain water paths, and for the sum of these three paths.

Table 6.3 suggests that surface precipitation rates and rain water paths are estimated most accurately by the 5.6-meter 1200-receiver 25-km resolution 54/118-GHz aperture synthesis system (F), and that the rms errors for the 1.2-meter antenna without image sharpening (E) are only ~16 percent worse. However, this comparison assumes both instruments have comparable sensitivity, which implies much longer integration times (less frequent repeat visits) for system F, as discussed in Section 6.4.2. When retrieving snow water paths the 54/183-GHz AMSU-like aperture synthesis system (H) performs best, while systems E and F are each about 20 percent worse. These results reflect the fact that higher rain rates are most evident between 54 and 118 GHz because it is in this frequency range that hydrometeors aloft transition from Rayleigh to geometric scattering with an observable microwave signature. Snow particles in the upper troposphere are smaller, however, which favors the more sensitive 183-GHz band relative to 54 GHz

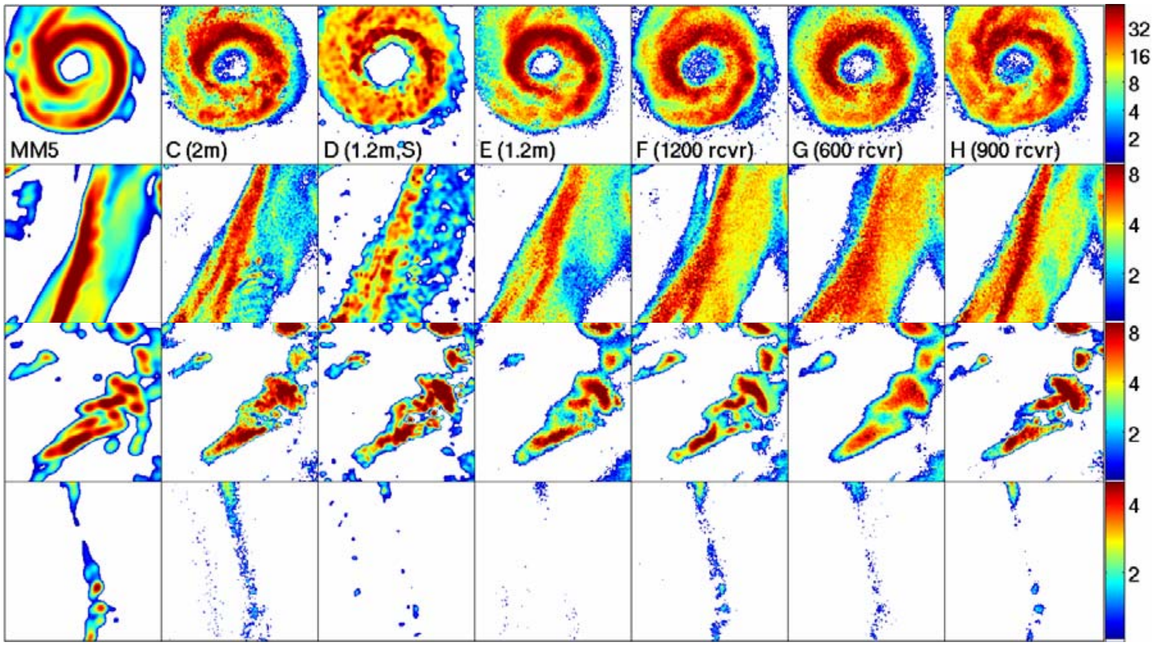

Fig. 6.3. Comparisons of MM5-simulated surface precipitation rates (left-most image) with 555-km images retrieved by four-band GEM's: (C) 2-m without image sharpening, (D) 1.2-m with image sharpening, and (E) 1.2-m without image sharpening. Also images retrieved by GeoStar systems with: (F) 1200 receivers at 54/118 GHz with 25-km resolution, (G) 600 receivers at 54/118 GHz with 50-km resolution, and (H) 900 receivers at 54/166/183 GHz with 50-km resolution. From top to bottom the images correspond to a typhoon (12/8/02; ~15N/145E), stratiform rain (12/14/02; ~40N/125W), a strong front over France (1/2/03; ~50N/5E), and oceanic warm rain (11/16/02; ~50N/35W); the units are mm/h.

The table also shows that image sharpening generally increases average errors (compare B to C, and D to E for the 2-m and 1.2-m antennas, respectively). Fortunately the precipitation-rate retrieval images of Fig. 6.3 reveal more clearly the benefits and liabilities of image sharpening. The MM5 truth is on the left of the figure, and instrument options C, D, E, F, G, and H appear in order to the right. The benefit is evident in the comparison of D and E, where the sharpened images capture better small convective events that would otherwise be blurred and lost, such as in the northwest and southeast of the French front, and in the warm rain event. The decision to employ image sharpening can be made on a case-by-case basis during ground processing if the scan lines are 10-km apart. More generally, the unsharpened 1.2-m antenna (E) appears to capture the typhoon and stratiform images best, while the 5.6-m 1200-receiver 54/118-GHz system (F) and the 2-m unsharpened GEM (C) capture the warm rain best. For the French front, all systems are roughly comparable except for the inferior 50-km resolution 54/118-GHz system (G), which is blurred. In general the 1200-receiver 54/118-GHz system F senses the typhoon and warm rain better than the 900-receiver 54/183-GHz system H.

The apparent rankings of systems for the illustrated storms can also vary depending on weather; for example, the strong convective events and warm rain illustrated here tend to favor higher resolution data and use of lower frequencies such as 54/118 GHz. The apparent differences in system ranking by rms errors versus imagery can be due in part to the choice of error metric (25-km smoothed MM5 data), and the preference of the eye for low noise and underlying features in the correct position, even if the values are biased.

TABLE 6.3
RMS RAIN AND HYDROMETEOR RETRIEVAL ERRORS

MM5 Octave Range: Rate (mm/h) or Path (mm)	Instrument Configuration										
	A (1.2m)	B (2m,S)	C (2m)	D (1.2m,S)	E (1.2m)	F (1200)	G (600)	H (900)	I (600)	J (300)	K (300)
Precipitation											
1-2 mm/h	1.6	1.6	1.5	1.6	1.5	1.1	1.3	1.5	1.5	1.5	1.6
4-8 mm/h	3.8	4.2	3.9	4.2	3.8	3.3	3.4	3.7	4.1	4.3	4.1
32-64 mm/h	19.7	23.0	18.2	23.2	17.5	16.1	17.3	20.5	20.7	21.7	24.6
Rain water RW											
0.25-0.5 mm	0.33	0.32	0.30	0.33	0.30	0.24	0.25	0.29	0.27	0.27	0.34
2-4 mm	1.58	1.64	1.49	1.58	1.55	1.32	1.45	1.48	1.47	1.62	1.63
8-16 mm	5.11	5.68	4.36	5.87	4.51	4.23	4.46	4.97	5.22	5.52	6.26
Snow path S											
0.25-0.5 mm	0.14	0.12	0.08	0.12	0.11	0.13	0.16	0.09	0.24	0.25	0.20
1-2 mm	0.33	0.28	0.20	0.27	0.25	0.25	0.34	0.20	0.64	0.67	0.42
2-4 mm	0.59	0.48	0.38	0.48	0.43	0.45	0.58	0.38	0.88	1.04	0.61
Graupel path G											
0.25-0.5 mm	0.38	0.36	0.31	0.35	0.31	0.35	0.35	0.30	0.46	0.47	0.39
2-4 mm	1.75	1.54	1.44	1.56	1.58	1.48	1.71	1.59	1.90	2.01	1.83
8-16 mm	4.09	3.49	2.80	3.48	3.06	2.73	3.61	2.88	3.42	4.91	4.21
RW+S+G path											
0.125-0.25 mm	0.15	0.16	0.10	0.15	0.13	0.13	0.13	0.11	0.37	0.39	0.23
2-4 mm	1.11	0.98	0.85	0.94	0.96	0.73	0.92	0.81	1.24	1.39	1.06
16-32 mm	7.32	6.12	4.72	6.28	5.43	4.32	5.99	5.26	5.22	7.59	7.13

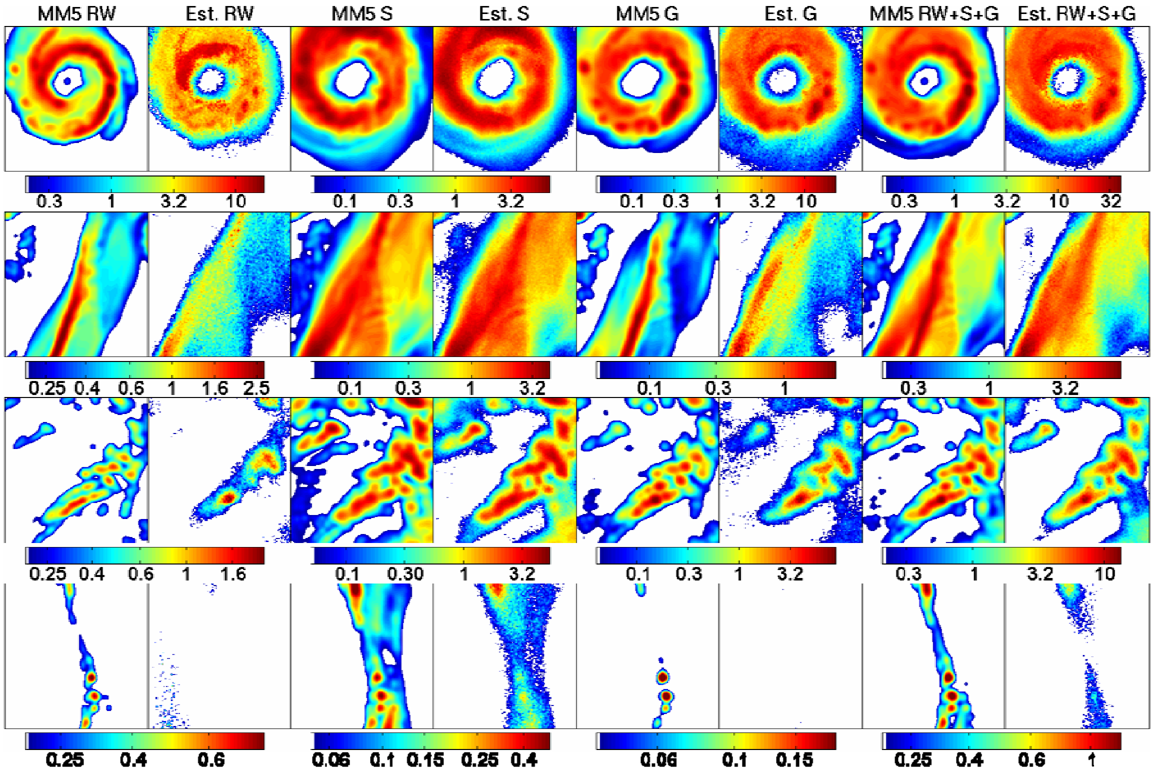

Fig. 6.4. MM5-simulated and retrieved water-paths for rain water (RW), snow (S), graupel (G), and rain water + snow + graupel (RW+S+G) (left-to-right in pairs) by a four-band GEM with a 1.2-m Cassegrain antenna without image sharpening (E). From top to bottom the images correspond to a typhoon (12/8/02; ~15N/145E), stratiform rain (12/14/02; ~40N/125W), a strong front over France (1/2/03; ~50N/5E), and oceanic warm rain (11/16/02; ~50N/35W); the units are mm. Each image is 555-km square.

6.6.5 Hydrometeor Water Path Retrievals

The same neural network architecture can be used to estimate water paths for snow, graupel, and rain water, as presented in Fig. 6.4 for four storms along with the MM5 ground truth used for these simulations. The retrievals of snow water path, and the sum of rain water, snow, and graupel water paths are most accurate, followed closely by graupel and then rain water. Rain water scatters less and is located at lower altitudes so it is retrieved with less precision than are hydrometeors aloft. Such retrievals of rain water paths by neural networks are based primarily upon multivariate statistical relationships among channels rather than upon the direct detection of rain water itself. This was shown by the very small change in the brightness temperature spectrum that resulted when rain water was artificially increased in MM5 without changing any other parameters [2].

The various instrument precipitation-rate retrieval performances shown in Table 6.3 are surprisingly indifferent to instrument frequencies or spatial resolution. Examination of the images suggests that most differences above ~1 mm/h arise because the boundaries of precipitation features and intensity levels are often misplaced, typically within ~30km of the correct location. For example, snow at 10-km altitude can take more than 30 minutes to reach the ground, during which time the ice aloft can increase, decrease, or translate ~20 km. One expected result of such space/time offsets would be that slightly blurry observations of convective events would be nearly as accurate numerically as perfect ones suffering the same offsets. Although higher spatial resolution sensors see smaller isolated cells, such cells with microwave signatures less than ~10 km in diameter generally contribute little to overall error statistics or rainfall. In contrast, the snow water path retrieval accuracies presented in Table 6.3 vary more than a factor of two from instrument to instrument. Snow retrievals are more sensitive to instrument configuration because snow resides at altitudes more readily sensed by satellite, particularly by instruments with high spatial resolution above 150 GHz

6.6 Discussion

Perhaps the most surprising result of this study is that a filled-aperture antenna of only 1.2-meter diameter on a geostationary satellite can produce revealing images of most significant precipitation with ~20-km resolution at 425 GHz every ~15 minutes. The decision of how much image sharpening to employ, if any, can be made in real time, depending on the type of weather system being imaged. The small size, weight, complexity, momentum impact, and nominal cost of such a system make it much more practical for use in geostationary orbit than were earlier proposed systems using longer wavelengths and larger antennas. The simulated precipitation retrieval performances of the more expensive 2-meter filled-aperture antenna system and the 1200-receiver aperture synthesis system were slightly better than the 1.2-meter system, but probably not enough to warrant their use in an economically constrained global system. The better 5.6-m aperture synthesis systems suffer from large size and complexity, and from higher noise levels when revisiting storms frequently, while the more practical 50-km resolution systems suffer from excessive blur.

Although the tested systems span a wide range of practical possibilities, many others also exist and should be evaluated before any final design is selected. For example, at the economically important mid-latitudes cross-polarization can be used to help reduce the unknown effects of surface emissivity and temperature at window channels such as 50, 90, and 150 GHz. Also, only four channels were used in each band, and not all combinations of bands were explored. Finally and most important, these simulated retrievals were based on data from single pixels and no use was made of storm morphology or prior information to improve results. The opportunity here involves replacement of single-pixel retrievals with assimilation methods at cloud convective scales. For example, such retrievals could better use the knowledge within convective-scale numerical weather prediction models to account for precipitation that evaporates before reaching the ground (virga) and overspreading of cirrus anvils beyond their convective cores.

Although possibilities exist for further improvement in expected system performance, the abilities of a 1.2-meter geosynchronous sounder to map precipitation at ~15-minute intervals would represent a major improvement over current capabilities to monitor economically and socially important global precipitation events on the time and spatial scales at which they evolve.

Chapter 7

AMSU Precipitation Retrieval Algorithm Trained with a NWP Model

All results in this chapter are from [4].

7.1 Abstract

This chapter develops a global precipitation rate retrieval algorithm for the Advanced Microwave Sounding Unit (AMSU). The algorithm was trained using a numerical weather prediction model (MM5) for 106 globally distributed storms that predicted brightness temperatures consistent with those observed simultaneously by AMSU. Neural networks were trained to retrieve hydrometeor water-paths and 15-minute average surface precipitation rates for rain and snow at 15-km resolution for land and sea at all viewing angles. Different estimators were trained for land and sea, where surfaces classed as snow or ice were generally excluded from this study. Surface-sensitive channels were incorporated by using linear combinations (principal components) of their brightness temperatures that were observed to be relatively insensitive to the surface, as determined by visual examination of global images of each brightness-temperature-spectrum principal component.

Predicted rms errors for retrieved precipitation rates segmented by octaves from 0.5 to 64 mm/h, were 1.29-23 and 0.96-26 mm/h over land and sea, respectively, as evaluated using independent samples of MM5 truth. When MM5 indicated rain-free snowfall and no significant accumulated precipitation on the ground, the rms precipitation rate accuracy per AMSU octave ranged from 0.21 to 2.3 mm/h for octaves covering 0.25-8 mm/h. The range of rms retrieval accuracies by octaves for hydrometeor water paths between 0.125 and 4 mm for rainwater, snow, graupel, cloud liquid water, cloud ice, and the sum of rainwater, snow, and graupel were 0.19-1.64, 0.10-0.57, 0.22-1.69, 0.11-1.48, 0.11-0.47, and 0.10-0.94 mm, respectively. The range of rms retrieval accuracies by octaves for the peak vertical wind 0.125-8 m/s was 0.08-2.54 m/s. These results are averages for all viewing angles and precipitation types, although precipitation retrievals for convective precipitation are generally less accurate than for stratiform precipitation, snow, and warm rain. Biases are small for cumulative precipitation estimates, and a small correction is derived for estimated convective surface precipitation rate probability distributions. The chapter also demonstrates that multiple scattering in high microwave albedo clouds may help explain the observed consistency between AMSU-observed 50-191 GHz brightness temperature distributions for a global set of 122 storms and corresponding distributions predicted using a cloud-resolving mesoscale numerical weather prediction (NWP) model (MM5) and a two-stream radiative transfer model that models icy hydrometeors as low-density spheres.

7.2 Introduction

Development of accurate methods for global observation of precipitation using satellites has been impeded by lack of reliable global ground truth. For example, rain gauges, ground-based and satellite-borne radars, visible and infrared sensors, and various passive microwave sensors all have deficiencies as sources of that ground truth. For example, rain inhomogeneity, wind, and the lack of good global coverage significantly degrade rain gauge measurements. Infrared satellite observations only see the tops of most clouds, and almost all remote sensors respond to precipitation aloft, not that reaching the ground. Radar is expensive and global coverage is sparse, particularly for the better multi-frequency doppler systems.

In recent decades the best global coverage of precipitation has been provided by passive-microwave spectrometers such as the Special Sensor Microwave/Imager (SSM/I) [73] aboard the Defense Meteorological Satellite Program (DMSP) satellites and the passive Tropical Rainfall Measuring Mission (TRMM) Microwave Imager (TMI) [74] aboard the TRMM satellite. They and similar instruments use the cross-polarized conical scanning configuration first demonstrated by the Scanning Multichannel Microwave Radiometer (SSMR) [75]. Since 1998 these conically scanned sensors have been supplemented by the cross-track scanning Advanced Microwave Sounding Unit (AMSU-A and AMSU-B) [23]-[24] aboard the United States National Ocean and Atmospheric Administration NOAA-15, -16, -17, and -18 satellites, which fly in additional orbits and view the earth with swaths ~2200 km wide (NOAA-18 replaced AMSU-B with the similar microwave humidity sounder MHS).

An early AMSU-based surface precipitation rate retrieval algorithm used neural networks trained with the National Weather Service's Next Generation Weather Radar (NEXRAD) for 38 coincident rainy orbits of NOAA-15 obtained over the eastern United States and coastal waters during a full year [34]; this was an improved version of a still earlier AMSU algorithm [72]. The algorithm first detected precipitation based on ice-scattering signatures at 183±3 and 183±7 GHz, and then retrieved surface precipitation rates only where those brightness temperatures were colder than some threshold. Precipitation was not detected when there was not enough ice aloft to be flagged, thereby excluding warm rain. This initial algorithm also was less accurate in regions more polar than $\sim\pm50^{o}$ latitude because of the limited NEXRAD training regime. An alternate physics-based approach relying primarily on window channels has also been developed for AMSU [52].

To overcome the geographic limitations imposed by training with NEXRAD, subsequent retrieval algorithms were trained and tested instead using physical models based on MM5, but only for a constant viewing angle in order to evaluate the sensitivity of predicted retrieval accuracies to assumptions in the radiative transfer model and MM5 [2], and to predict precipitation retrieval accuracies for Geo-Microwave sounders [3]. These earlier algorithms are extended here to all AMSU incidence angles and to realistic surface emissivities and temperatures. The surface effects are accommodated in three ways, by: relying primarily on the more nearly opaque frequencies, using MM5 in combination with land and sea surface models, and empirically attenuating surface effects before the final retrieval step. Even with these precautions, retrievals over snow and ice surfaces remain problematic. Retrieval performance for convective and stratiform rain, warm rain, and snow is evaluated separately.

The validity of these retrievals depends on the fidelity with which the brightness temperatures predicted by MM5 and the radiative transfer model match the full range of behavior observed by AMSU around the globe. Fortunately previous studies [1]-[2] have shown that a physics-based combination of a cloud-resolving version of MM5 followed by a two-stream radiative transfer model (TBSCAT) [7] using ice-scattering models ($F(\lambda)$) for ice habits yields NCEP-initialized simulated brightness temperature histograms and morphologies that generally agree with those coincidentally observed by AMSU over 122 global storms, even when the precipitating pixels are segregated by precipitation type or latitude. An example of such a comparison, discussed later, appears in Fig. 7.2.

Section 7.3 of this chapter reviews: 1) the physical basis for the link between millimeter-wave spectra and surface precipitation rates, 2) the MM5 configuration, 3) the characteristics of the storms studied, 4) the radiative transfer model and degree of scattering, and 5) the effects of changing the ratio of MM5-produced snow to graupel to compensate an alternative scattering paradigm. Section 7.4 describes the AMSU/MM5 algorithms for retrieving surface precipitation rate, hydrometeor water-paths, and the peak vertical wind, while Section 7.5 analyzes the predicted retrieval performance and presents comparisons with real AMSU data for selected storms coincident with MM5 predictions. Section 7.6 compares simultaneous AMSU and AMSR-E retrievals, and Section 7.7 concludes the chapter and discusses possible future retrieval improvements. MATLAB codes for these new AMSU precipitation rate and hydrometeor water-path retrievals are available from the authors upon request.

7.3 Approach to Deriving the Precipitation Retrieval Method

7.3.1 Physical Basis for Millimeter-Wave Precipitation Retrievals

Both scattering and absorption signatures of precipitation can be observed at millimeter wavelengths. Absorption in the more transparent window channels is generally evident as a warm signature over ocean, and as a cold signature over warm land. The absorption spectrum of water droplets smaller than a millimeter is generally in the Rayleigh regime and roughly proportional to the square of frequency for AMSU. For larger droplets the absorption spectrum flattens as their diameters approach a half a wavelength. Absorption by ice is generally negligible in comparison. These absorption signatures are usually less than a few tens of degrees and are generally unambiguous over ocean; over land they are confounded with frequency-dependent variations in surface emissivity. Over ocean absorption by water vapor can be distinguished from precipitation by use of AMSU channels near the 22.2 and 183-GHz water vapor resonances and adjacent spectral windows.

In contrast to absorption, the scattering signatures of larger icy hydrometeors (snow and graupel) can approach 200K. Scattering by water droplets has much less effect on brightness temperatures because water has a higher loss tangent. The primary advantage of AMSU relative to sensors at longer wavelengths is that scattering in the 50-200 GHz band is highly dependent on ice particle size distribution and abundance. Only larger hydrometeors characteristic of strong vertical wind and heavy precipitation scatter strongly in the 54-GHz band, while smaller hydrometeors characteristic of light precipitation still have strong signatures near 150-200 GHz; ordinary cloud ice is too small to have much effect. Most snow and ice aloft is in the Rayleigh scattering regime where their scattering cross-sections are proportional to d^6/λ^4, where d is ice diameter and λ is wavelength. Since AMSU also senses humidity, precipitation rates can be surmised by combining estimates of humidity and vertical wind within neural network estimators.

AMSU-A channels sense the temperature profile by measuring thermal emission from oxygen at frequency-dependent altitudes. For example, the more opaque frequencies sense temperatures near the top of the atmosphere while the more transparent frequencies sound atmospheric temperatures closer to the surface. The altitudes where scattering occurs can also be estimated by observing the strength of the scattering signature as a function of frequency and atmospheric transparency--microwave cell tops deep in the atmosphere can be observed only with the most transparent channels. Cell top altitude is also correlated with precipitation intensity.

In combination with AMSU-A temperature profile information, the AMSU-B channels are sensitive to the middle and lower tropospheric humidity profile. AMSU-B channels are also sensitive to strong scattering signals from hydrometeors aloft larger than ~1 mm in diameter [62], and to their relative altitudes. Thus most particles affecting AMSU channels are large enough to fall. AMSU-A channels 1-5 (below 54 GHz) and AMSU-B channels 1-2 (89 and 150 GHz) are affected by the surface and are called window channels.

Despite the utility of AMSU-sensed information about atmospheric absorption and the altitude and size distributions of hydrometeors, retrieval of surface precipitation rates remains difficult because precipitation rates are inferred primarily from the radiometric signatures of hydrometeors aloft that may evaporate or significantly shift location before reaching the surface, perhaps 5-20 minutes later. These problems are more severe for convective precipitation than for stratiform, which is more stable.

7.3.2 Mesoscale Model

The mesoscale model MM5 and domain configurations are described in Section 3.1. To minimize computer time the brightness temperatures analyzed in Section 7.3 were based on the 15-km resolution MM5 domain2 output, whereas the brightness temperatures and MM5 predictions used in the retrieval studies discussed in Sections 7.4-7.6 were based on the 5-km resolution domain3 MM5/RTM output. Surface precipitation rates and hydrometeor water-paths at resolutions other than 5 km were similarly generated by convolving the 5-km retrievals with Gaussian functions having the desired full width at half maximum (FWHM). Surface precipitation rates (mm/h) were defined as four times the difference between total accumulated surface precipitation (mm) at the time of interest and that at 15 minutes earlier. Hydrometeor water-paths were defined as the total instantaneous water-equivalent mass in a column at an instant of time, in units of millimeters. Both retrieval errors and precipitation type were determined in this chapter using MM5 truth.

7.3.3 Globally representative storms

The 106 global storms analyzed for this chapter are a random subset of the 122 MM5 storms that were earlier shown to have simulated brightness temperatures statistically consistent with coincident observations by AMSU instruments aboard NOAA-15, -16, and -17 satellites [1]; the reduction from 122 to 106 was necessary due to lack of data storage capacity. Fig. 7.1 shows the locations and month/season for these 106 storms. Each has 190×190 picture elements (pixels) spaced on a rectangular 5-km grid. The total number of 5-km pixels is 106×190×190 > 3.8M, of which over 1.75M pixels were found to be precipitating; a pixel was designated as precipitating if either the MM5 rain water or snow at 1000 mbar were non-zero.

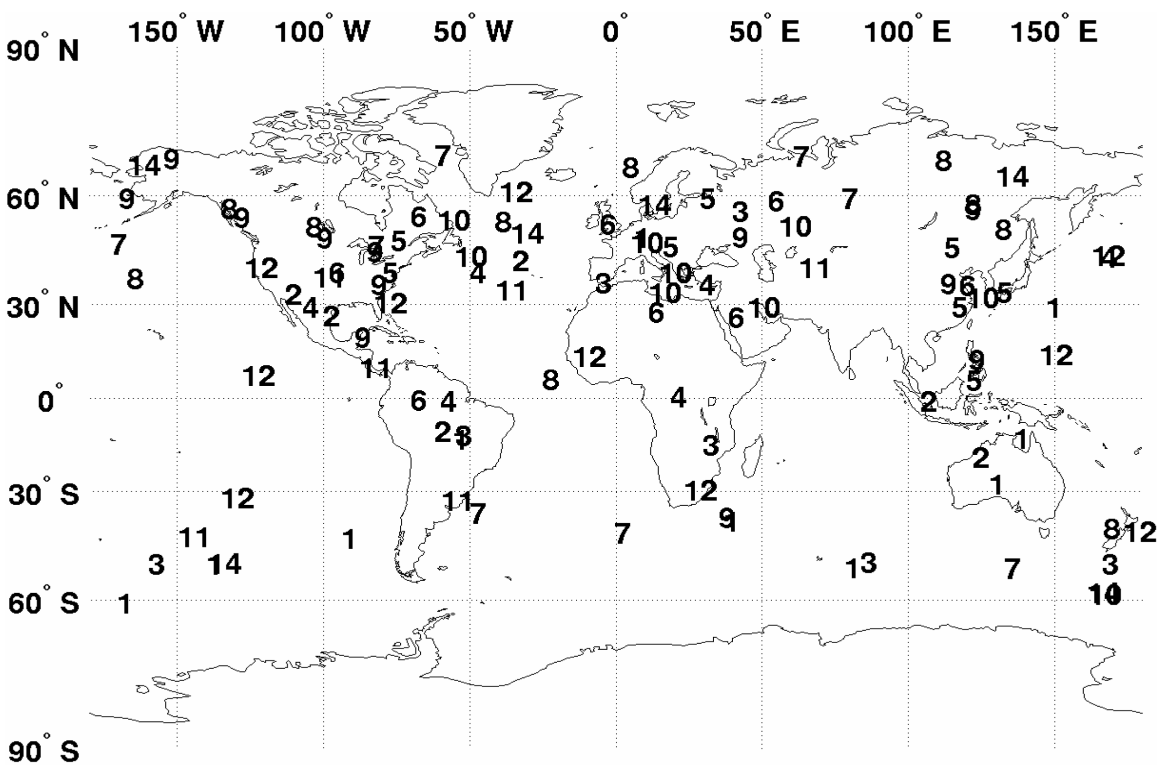

Fig. 7.1. 106 global representative storms; the numbers 1-12 stand for January-December, and 14 indicates largely unglaciated cases.

Table 7.1 presents the numbers of precipitating 5-km MM5 pixels in various categories for the 106 storms. Pure snow is the only category with marginal representation (34,000 pixels). Based on empirical examination of representative MM5 storms, a pixel was defined as convective if the 15-km MM5 vertical wind peak exceeded 0.45 m/s; otherwise, the pixel was defined as stratiform. MM5 5-km pixels having only rain and no snow at 1000 mbar were defined as rain-only pixels. Similarly, pixels having only snow and no rain at 1000 mbar were defined as snow-only pixels. Pixels having both MM5 rain and snow at 1000 mbar were called mixed rain and snow. For 15-km pixels the same definitions were used, where all nine 5-km pixels were considered. A 15-km pixel was classified as non-glaciated rain if its MM5 integrated rain water were over 0.1 mm and $T_B(183\pm7 \text{ GHz}) \geq 250$ K, which was found to indicate that very little ice was aloft. These criteria used to classify precipitation types were described more thoroughly earlier and differ from those used when comparing brightness temperature histograms, as required when AMSU data is analyzed [1].

TABLE 7.1
NUMBERS OF 5-KM MM5 PRECIPITATING PIXELS (IN THOUSANDS) BY CATEGORY

Category	Pixels (000)	Category	Pixels (000)
$\lvert lat \rvert \leq 25$	241	Winter	516
$25 < \lvert lat \rvert \leq 55$	1112	Spring	506
$55 < \lvert lat \rvert \leq 90$	398	Summer	347
Convective	198	Autumn	382
Stratiform	1552	Rain only	1664
Non-glaciated (Land)	231	Mixed rain and snow	52
Non-glaciated (Ocean)	337	Snow only	34

7.3.4 Radiative Transfer and Simulation of Brightness Temperatures

A two-stream Mie-scattering variant of P. W. Rosenkranz's efficient radiative transfer algorithm TBSCAT [7] was used to compute AMSU brightness temperatures based on MM5 profiles. The radiative transfer model TBSCAT and the $F(\lambda)$ model for icy hydrometeors are described in details in Sections 4.3 and 4.4.

The assumption of two-stream Mie scattering deserves discussion. First, the MM5 and AMSU radiance histograms match well when two-stream Mie scattering [1]-[2] is assumed, as shown by Figs 7.2(a) and 7.2(b), which present for 122 global storms MM5 vs. AMSU brightness temperature histograms for incidence angles less than 40 degrees, and for 40-59.2 degrees, respectively. The discrepancies between the AMSU and MM5 histograms are small compared to those caused by small changes in assumptions in MM5 or radiative transfer model [2], and can be reduced further by assuming that the NCEP initializations overestimated humidity below 260K, as shown later in Fig. 7.3. One possible partial explanation for reasonable agreement at all viewing angles despite the two-stream approximation is that even at extreme satellite scan angles those convective cells that scatter most strongly are viewed roughly normal to their tall puffy cloud surface, which is consistent with the agreement in Fig. 7.2(b) for opaque channels. Another partial explanation for good agreement using the two-stream approximation, defended later in this chapter, is that strongly scattering clouds scatter each microwave photon several times in random directions, reducing the importance of direction for the scattering component. High-order scattering also makes the angular distribution (phase function) of Mie scattering less important than the total scattering cross-section, which was matched here to DDSCAT calculations for each frequency and hydrometeor shape by defining $F(\lambda)$ appropriately.

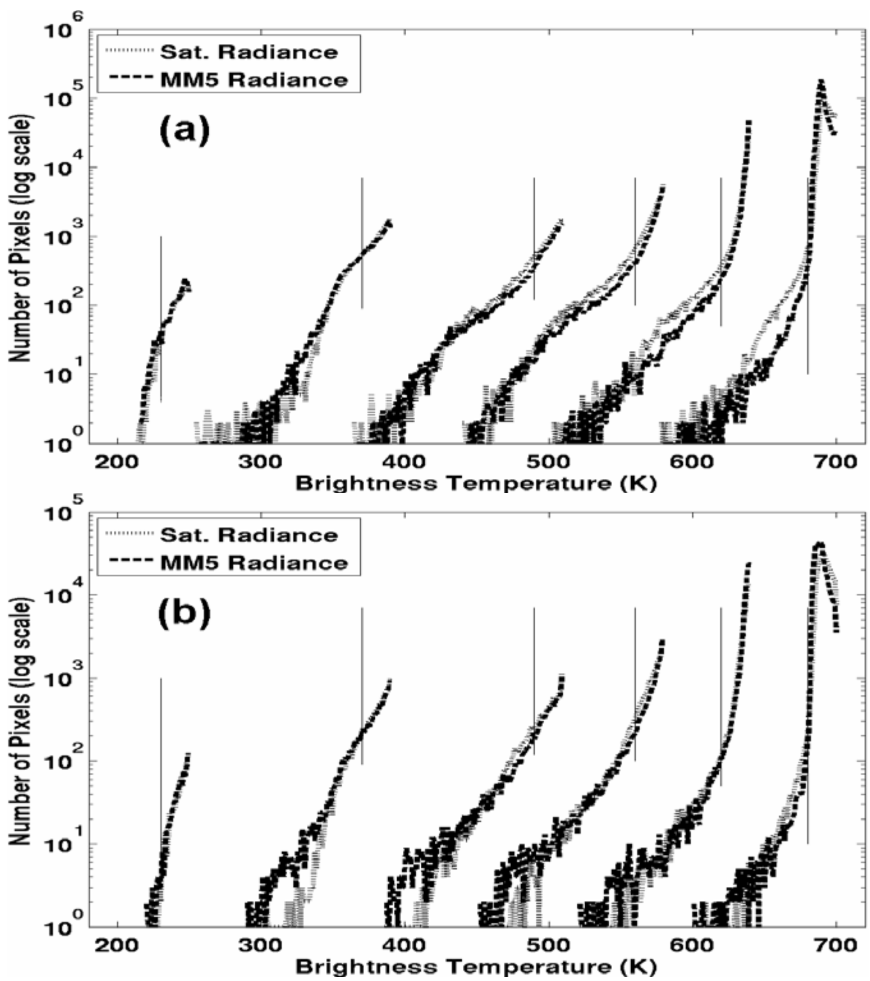

Fig. 7.2. Brightness temperature histograms (pixels per degree K) for channels near 50.3, 89, 150, 183±7, 183±3, and 183±1 GHz, in order of increasing opacity from left to right, for 122 storms using $F(\lambda)$ from [1] when (a) incidence angles less than 40 degrees, and (b) incidence angles greater than or equal to 40 degrees, are plotted. Only T_B's below 250 K are plotted. For clarity, the absolute T_B's were shifted to the right by 0, 140, 260, 330, 390, and 450 K, respectively, and the vertical lines indicate 230K.

The small gaps in Fig. 7.2(a) near 210K in these histograms are most likely due to excessive upper tropospheric humidity in the NCEP initializations. Fig. 7.3 shows that decreasing MM5 water vapor by 40 percent when the local temperature is less than 260K helps close these gaps. The small gaps near 150K for 89 and 150 GHz at angles beyond 40 degrees could be due in part to the two-stream approximation, for no other obvious explanation has yet been found.

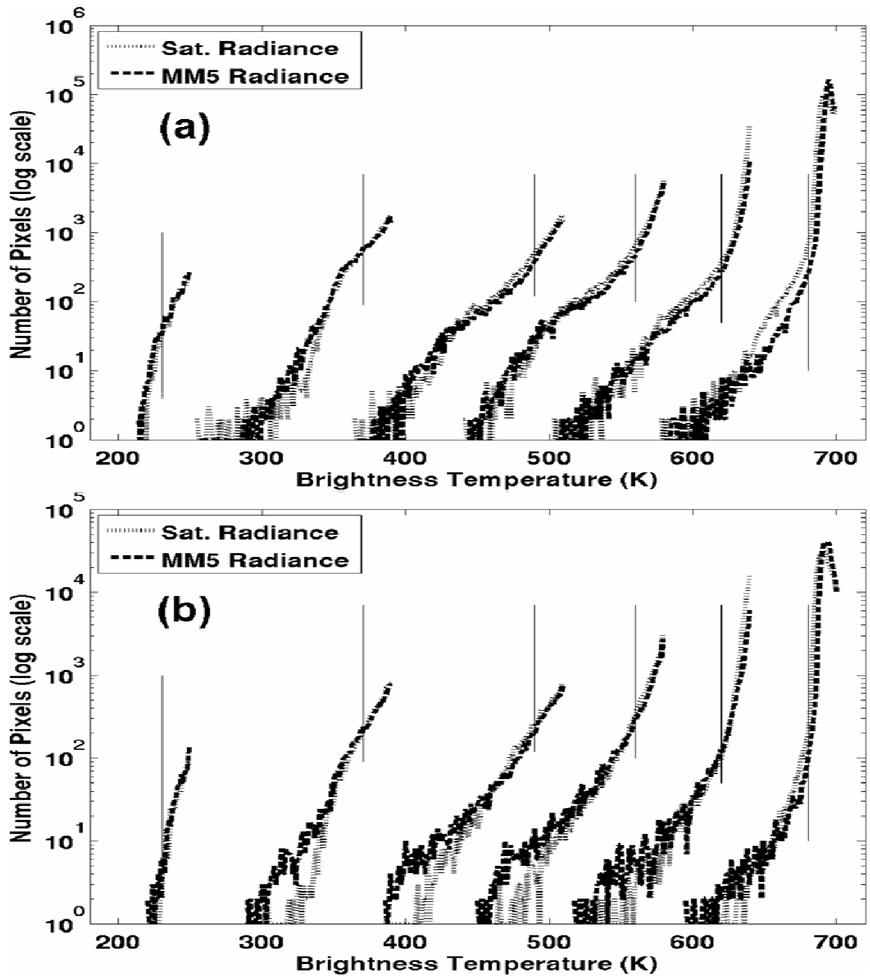

Fig. 7.3. Brightness temperature histograms (pixels per degree K) after reducing MM5 water vapor by 40 percent when temperatures are below 260K for channels near 50.3, 89, 150, 183±7, 183±3, and 183±1 GHz, in order of increasing opacity from left to right, for 122 storms using F(λ) from [1] when (a) incidence angles less than 40 degrees, and (b) incidence angles greater than or equal to 40 degrees, are plotted. Only T_B's below 250 K are plotted. For clarity, the absolute T_B's were shifted to the right by 0, 140, 260, 330, 390, and 450 K, respectively, and the vertical lines indicate 230K.

The simulated radiance data used to develop these precipitation retrievals were based on MM5 domain-3 data on a square 5-km grid. These brightness temperatures computed at appropriate zenith angles were convolved with Gaussian functions having full width at half maximum (FWHM) of 15 and 50 km for AMSU-B and AMSU-A observations, respectively. This yields simulated brightness temperatures for AMSU-A and AMSU-B at appropriate resolutions on the 5-km grid. Blurring to 15-km resolution was postponed until the final radiances were computed because brightness temperatures computed for nadir using a 15-km blurred version of the MM5 fields were found to differ from these results up to 10 K at 89.9 GHz for one representative storm.

Gaussian random noise of 0.4 and 1.0 K rms was added to simulated brightness temperatures for all AMSU-A and AMSU-B channels, respectively, to simulate AMSU instrument noise in a simple manner generally consistent with the radiometric sensitivity values presented in Tables 2.1 and 2.2. Small biases of 0.71, 0.63, -3.25, and -0.65 K were found on average over 122 representative storms described in Section 3.2 between coincident simulated and observed brightness temperatures for AMSU-A channels 5-8, respectively, on NOAA-15, -16, and -17 satellites. These biases could be partly due to AMSU calibration errors, MM5 initialization errors, or MM5 prediction errors; for example, AMSU channel 7 is known to suffer radio frequency interference. Biases for other channels are minimal. AMSU-A channels 9-14 have little information about precipitation and were not used. At 89-GHz only the 15-km resolution AMSU-B channel 1 was used. More accurate biases, which vary among instruments on different satellites and depend on time of operation, could be found by comparing simulated and observed brightness temperatures. However, these more detailed bias corrections are negligible compared to signals from precipitation.

7.3.5 MM5 snow/graupel adjustment

It was found in [1] that the DDSCAT and AMSU brightness-temperature histograms match well for 122 global storms, even though we assumed Mie scattering from spheres having the same total scattering cross-sections as those computed by DDSCAT for rosette-shaped graupel and planar hexagonal snow. However, the back-scattering fractions of the resulting Mie spheres are typically half those of graupel having a rosette shape, as computed using DDSCAT6.1 and shown in Fig. 7.4 as a function of rosette length. The back-scattering fraction is defined as that fraction of single-scattered energy that is scattered rearward into 2π steradians. This difference in backscattering raises the question of whether the density of icy Mie spheres, i.e., $F(\lambda)$, should be adjusted so that their total scattering cross-sections (left scale and dashed lines in Fig. 7.4) or their back-scattering fractions match those determined using DDSCAT (right scale and solid lines in Fig. 7.4).

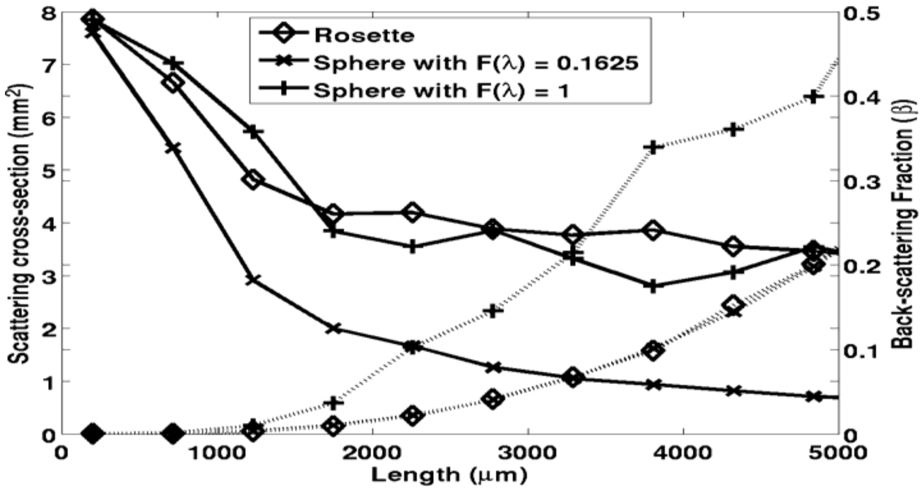

Fig. 7.4. Comparison of scattering cross-sections (left scale) and back-scattering fractions (right scale) for rosettes and equal-mass spheres at 183±7 GHz, where solid lines are back-scattering fractions.

If the backscattering fractions rather than the total scattering cross-sections of Mie spheres must match DDSCAT computations, then MM5 might be generating too much graupel instead of snow, which back-scatters less per gram. This hypothesis is tested in the brightness temperature histograms of Fig. 7.5, for which the densities of icy Mie spheres, i.e. F(λ), were increased to 0.125, 0.4, 1, 1, 1, and 1 at 50.3, 89, 150, 183±7, 183±3, and 183±1 GHz, respectively so that their back-scattering fractions match those for rosettes determined using DDSCAT. Snow of equivalent mass was substituted for half the MM5 graupel to reduce some of the resulting increase in backscattering. That is, with these increased values of F(λ) the total scattering cross-sections of Mie spheres are roughly double those of rosettes, as shown in Fig. 7.4, and so graupel must be reduced by at least half. Snow can be substituted for graupel to maintain constant surface precipitation rates because the back-scattering ratio of snow approximates that for Mie spheres [1]. The agreement in Fig. 7.5 for 122 global storms is so degraded by the increased backscattering by graupel, despite the substitution of snow for half of it, that clearly the total scattering cross-section is most relevant here, and the present MM5 production ratios of snow to graupel are probably correct. If corrections were made for the fact that snow usually falls more slowly than graupel, backscattering and the Fig. 7.5 histogram discrepancies would only increase further.

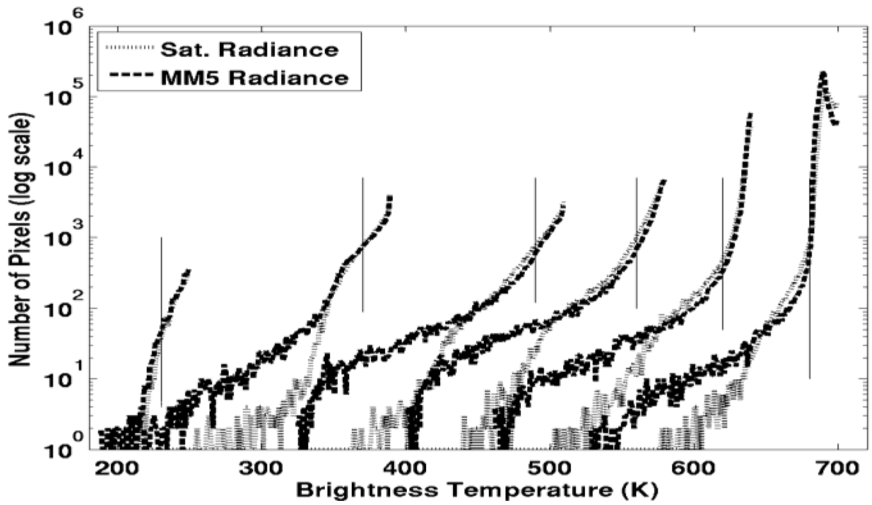

Fig. 7.5. Brightness temperature histograms (pixels per degree K) if F(λ) is increased for graupel so that it matches DDSCAT back-scattering fractions, and if half of all graupel is replaced by snow to partly compensate. Brightness temperatures below 250K are plotted for 50.3, 89, 150, 183±7, 183±3, and 183±1 GHz in order of increasing opacity from left to right, and are shifted to the right by 0, 140, 260, 330, 390, and 450 K, respectively; the vertical lines indicate 230K.

An alternative explanation for why the total scattering cross-section controls brightness more than the back-scattering ratio is that millimeter-wave photons scatter many times in many directions before exiting those low-brightness regions where scattering is important, and therefore the "backwards" direction becomes increasingly isotropic. This hypothesis can be tested in part by computing the degree of multiple scattering in each pixel using the successive-order radiative transfer method [20], which explicitly accounts for each scattering event. Fig. 7.6 plots for each pixel as a function of its 183±7 GHz brightness temperature the fraction of the scattered radiation (B/(A+B)) emerging from the top of the atmosphere that was scattered more than once, where A is the single-scattered energy and B is the higher-order scattered energy, for a summer frontal system over France at 1003 UTC 2 January 2003, which is shown later in Figs. 7.15 and 7.16. At brightness temperatures below ~240K over half of all scattered energy was scattered more than once, and below ~220K most photons scatter several times. It is these pixels below 220K that dominate the brightness histogram matches. Only pixels for which more than one percent of the radiation was scattered are plotted. The peak discrepancy in brightness temperature between this two-stream successive-order scattering algorithm and TBSCAT is 1.3K at 183±7 GHz over the summer frontal system. The successive-order method involves much more computation than TBSCAT, however.

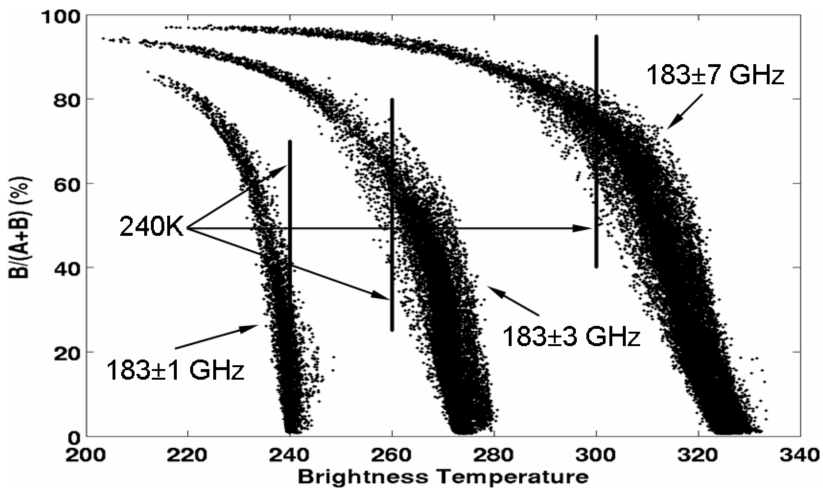

Fig. 7.6. B/(A+B) (percent) as a function of simulated brightness temperatures, where A is the fraction of scattered photons that scatter only once and B is the fraction that scatters more than once. Data at 183±3 and 183±7 GHz were shifted right by 20 and 60 K, respectively, where vertical lines indicate 240 K. Only pixels for which more than one percent of the radiation was scattered are plotted.

7.4 Retrieval Algorithms

7.4.1 General approach

Since the relationship between precipitation and satellite brightness temperatures is nonlinear and imperfectly known, the retrievals here employ neural networks trained with tested physical models. The estimates for surface precipitation rates and hydrometeor water-paths were trained using NCEP-initialized MM5 simulations of 106 representative storms and their corresponding brightness temperatures simulated using TBSCAT and the F(λ) approximation at AMSU frequencies. Only storms with simulated morphologies that match simultaneous AMSU observations near 183±7 GHz were used. The global nature of these storms used for training addresses the principal weakness in statistical methods trained with radar or other non-global data. The validity of these simulated storms is supported by their general agreement with histograms of concurrent AMSU observations [1].

Precipitation retrievals over sea ice or snow-covered land are difficult because those channels penetrating to the surface have difficulty distinguishing snow or ice on the ground from icy hydrometeors aloft. Even the normally opaque channel near 183±1 GHz can sense the surface when the air is sufficiently dry. Furthermore, the microwave emissivity of snow and ice on the ground exhibits many degrees of freedom that overlap those degrees exhibited by precipitation. To explore this issue, brightness temperatures were simulated using emissivity spectra retrieved from AMSU/HSB aboard the Aqua satellite for 7 full days between Aug 30, 2002 and February 4, 2003, one day per month

[76]. Principal component analysis of the brightness temperature perturbations induced by precipitation over these surfaces revealed that the scores of most perturbation principal components (PC's) were contaminated by contributions from snow or ice on the ground that could sometimes create false detections. The score of a PC is the vector dot product of that PC and the data for a particular pixel. Because of such difficulties with surface complexity and the possibility of undetected atmospheric transparency that could produce false snowfall detections, this chapter focuses only on precipitation retrievals over snow-free land and ice-free sea, although precipitation retrievals over land with snow and sea ice can reveal snowstorms, as shown later in Fig. 7.15.

The AMSU/MM5 retrieval algorithm first checks whether the data is valid. An AMSU footprint will be flagged as invalid if 1) any brightness temperature for that pixel is less than 50K or greater than 400K, 2) AMSU-A channel 5 (53.6 GHz) senses less than 242 K, implying that the atmosphere is so dry that precipitation is unlikely (even 183±1 GHz can then sometimes sense the surface and yield false detections of precipitation), 3) the surface altitude is above 2 km for $|\theta_{lat}|<60$ degree or above 1.5 km for $60\leq|\theta_{lat}|<70$ degree, or above 0.5 km otherwise [34]; these high altitude surfaces can be snow covered and are sensed more strongly. These three cases (bad data, too dry, and too high) are identified with flag values of 1, 2, and 4, respectively, where each case has its own flag, which is zero otherwise. If any of these flags is nonzero, retrievals were not performed for that AMSU footprint.

The surface classification algorithm [77], a modified version of [78], was used to separate AMSU-observed pixels into four surface classes: snow-free land, land with snow, seawater, and sea ice. A fourth flag assumes a value of 8 for land with snow or sea ice, and is zero otherwise. The sum of these four flag values is designated the "return code". Fig. 7.7(a) shows a map of surface class for five ascending orbits of AMSU aboard NOAA-16 on July 26, 2002. White areas signify gaps between satellite orbits or locations where retrievals were not performed. Fig. 7.7(b) shows a corresponding map of the algorithm's return code, which is the sum of all four flags described.

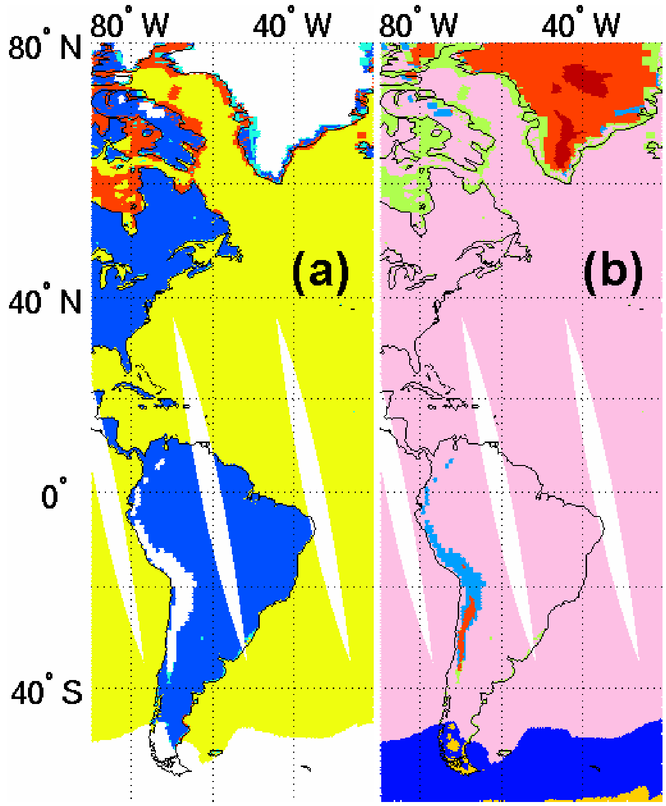

Fig. 7.7. Global maps of 5 ascending orbits of AMSU aboard NOAA-16 on July 26, 2002 for: (a) surface class; blue is snow-free land, cyan is land with snow, yellow is seawater, orange is sea ice, and white indicates no retrieval; and (b) return code; pink signifies a good retrieval, blue is a dry atmosphere, cyan mean high altitude, green is snow or ice, yellow is dry air over snow or ice surfaces, orange is snow at high altitude, red is dry air over high altitude snow, and white is a gap between satellite orbits.

The first retrieval step, illustrated in Fig. 7.8(a), is to correct small biases, typically less than 1K, in a few temperature channels, and then to correct the brightness temperatures to values that would have been seen at nadir. Next principal components of the window channel brightness temperatures that were found to be insensitive to surface and view-angle effects are computed, as are brightness perturbations due to icy hydrometeors. Finally, these values are input to neural networks that estimate a single output parameter such as surface precipitation rate for either land or sea. This architecture is diagrammed in Fig. 7.8 and elaborated in the following sections.

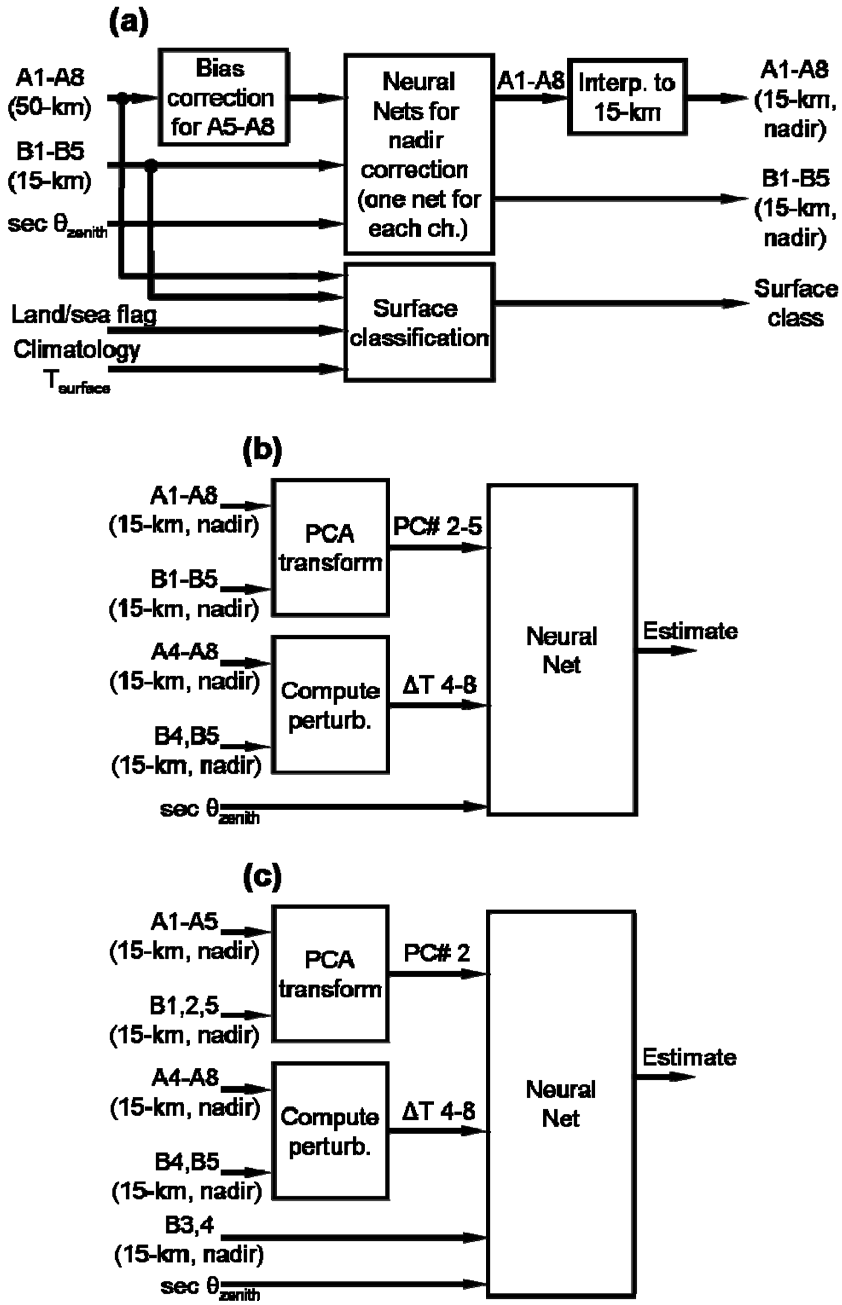

Fig. 7.8. (a) Architecture for surface classification and for estimation of brightness temperatures that would have been seen at nadir. Block diagrams for retrieval algorithms for (b) ocean and (c) land. A1 and B1 signify channel 1 for AMSU A and AMSU B, respectively. $\Delta T4$ is the spatially local perturbation in AMSU-A channel 4 brightness due to precipitation. PC's are principal components, θ_{zenith} is the zenith angle, and $T_{surface}$ is the climatology surface temperature [79].

Separate neural networks are used over land and over sea because the window-channel brightness temperatures observed over land and sea respond very differently to atmospheric absorbers like water vapor and hydrometeors. It is difficult for a single estimator to do well in both cases because land surface brightness temperatures are generally warm, so absorbers aloft typically appear colder, whereas over ocean the same absorbers typically appear warmer. The observation-based surface classification [77] determined which estimator to use. The algorithm also executes over snow or sea ice, but with a strong risk of false alarms. The same neural network architecture was used for surface precipitation rate and hydrometeor water-path retrievals.

All neural networks have three layers with 10, 5, and 1 neuron, respectively, where the first two layers employ tangent sigmoid operators, and the final layer is linear. Limited experimentation with network architectures did not reveal significant opportunities for improvement, probably because the 10-5-1 networks were slightly more complex than needed, but simple relative to the information available in the extensive training data. The Levenberg-Marquardt [49] training algorithm was used and the net weights were initialized using the Nguyen-Widrow method [50]. For each network and task, the best of 10 networks was used.

Each neural network was trained using 244,224 5-km MM5 pixels (half for training, and one quarter for each of testing and validation), and separately evaluated using 234,154 other pixels, where the closest distance between any training and final evaluating pixel was ~14 km. These were subsamples taken from the set of 106 MM5 storms, each of which has 190×190 5-km pixels. Of the total set of 3.8M 5-km pixels, ~1.75M were precipitating.

7.4.2 Corrections of angle-dependent brightness temperatures to nadir

Brightness temperatures over ocean at large zenith angles are typically warmer for window channels and cooler for opaque channels. Such differences in angular dependence can confuse simple estimators. To permit simpler estimators to be used, the first step in the AMSU retrieval algorithm employs neural-network estimators that correct these angle-dependent brightness temperatures to nadir using one estimator per channel. The training data included brightness temperatures simulated for 106 MM5 storms at nadir and at all satellite zenith angles. To estimate brightness temperatures at nadir for AMSU-A, the inputs to the neural networks were the secant of the satellite zenith angle and the MM5-simulated brightness temperatures for AMSU-A channels 1-8 (50.2 - 55.5 GHz). To estimate brightness temperatures at nadir for AMSU-B, the inputs to the neural networks were MM5-simulated brightness temperatures for AMSU-B channels 1-5, and the secant of the satellite zenith angle. In both cases, the target was the MM5-simulated brightness temperature at nadir for the same pixel. The same diverse surface models were used as described in Section 4.4.

The MM5-simulated performance shown in Table 7.2 validates this approach, for the rms discrepancy for the worst channel other than 89 GHz is only 1 K for zenith angles less than 50°, and 1.57 K for zenith angles greater than or equal to 50°, probably because the large number of neural network inputs captures atmospheric profiles quite well, simplifying angle correction. Also, the relationship between brightness temperature and the secant of zenith angle is approximately linear. Because most precipitation signatures exceed ten degrees and are large compared to these residual nadir correction errors, the retrieval performance evaluated using those pixels having zenith angles greater than 50° was found to be comparable to that averaged over all angles.

TABLE 7.2

RMS ERRORS IN NADIR-CORRECTED BRIGHTNESS TEMPERATURES EVALUATED USING MM5 SIMULATED BRIGHTNESS TEMPERATURES FOR ZENITH ANGLES < 50° AND ≥ 50°

AMSU-A Channel	RMS Error for angles < 50° (K)	RMS Error for angles ≥ 50° (K)	AMSU-B Channel	RMS Error for angles < 50° (K)	RMS Error for angles ≥ 50° (K)
1	0.84	1.46	1	1.59	3.56
2	0.83	1.57	2	1.00	1.43
3	0.43	0.56	3	0.71	0.69
4	0.33	0.42	4	0.67	0.68
5	0.31	0.37	5	0.84	1.02
6	0.33	0.38	-	-	-
7	0.31	0.36	-	-	-
8	0.34	0.33	-	-	-

7.4.3 Precipitation retrieval algorithm for ocean

Fig. 7.8(b) diagrams the precipitation retrieval algorithm used over ocean. To reduce any residual dependence of brightness temperatures upon viewing angle, and dependence upon surface properties, only those principal components of the brightness temperature spectrum that exhibited the least dependence were preserved. The principal components were computed for the estimated nadir brightness temperature spectra of all AMSU-B channels and AMSU-A channels 1-8 that were classified as ice-free ocean and have no low-quality flags (out-of-range, too dry, too high, or snow/ice surface, as described in Section 7.4.1) for 122 satellite orbits spanning a year. The resulting first principal component was strongly affected by surface roughness, the second to the fifth principal components exhibited little surface sensitivity, and the rest exhibited either residual angle-dependent brightness temperatures or were noisy, as illustrated in Fig. 7.9 where only footprints classified as ice-free ocean and having no low-quality flags are plotted. The second to the fifth principal components, designated SEA PC# 2-5, and their eigenvectors are listed in Table 7.3; an interpretation follows the table.

The inputs to the precipitation-retrieval neural networks included: SEA PC# 2-5, five estimated brightness perturbations due to icy hydrometeors for AMSU-A channels 4-8 computed from estimated nadir brightness temperatures, and the secant of the zenith angle. The perturbations were estimated using the spatial filtering method described by [34]; they are the difference between simulated AMSU-A icy signatures at locations detected using 183±7 GHz data, and brightness temperatures determined by Laplacian interpolation of AMSU-A brightness temperatures surrounding the icy patch. 183±3 GHz data are used in place of 183±7 GHz data when the atmosphere is very cold and dry, as inferred when AMSU-A channel 5 (53.6 GHz) registers less than 248 K. These perturbations could be sharpened to 15-km resolution using the technique described by [34], but the original 50-km perturbations were found in this chapter to be slightly better correlated with 15-km surface precipitation rates than were the 15-km sharpened perturbations, presumably due to mismatches between locations of icy hydrometeors aloft and precipitation near the surface. This result contrasts with that of [34] because their estimator was trained with NEXRAD, which responds to hydrometeors more nearly co-located with those sensed radiometrically. The neural network estimates of AMSU-A nadir brightness temperatures at 50-km resolution were interpolated to AMSU-B footprints.

7.4.4 Precipitation retrieval algorithm for land

Fig. 7.8(c) diagrams the precipitation retrieval algorithm used over land. Since window channels, including AMSU-A channels 1-5 and AMSU-B channels 1, 2, and 5, are strongly affected by land surfaces in complex ways, it is beneficial to attenuate these effects before providing the data to the neural network. Principal components for AMSU-A channels 1-5 and AMSU-B channels 1, 2, and 5 were computed for estimated nadir brightness temperature spectra classified as snow-free land and that had no low-quality flags (described in Section 7.4.1), the test ensemble was 122 satellite orbits spanning a year. Only the second principal component was reasonably insensitive to the surface whereas the others exhibited residual angle-dependent brightness temperatures or were surface sensitive or noisy, as illustrated in Fig. 7.10 which plots only footprints classified as snow-free land without low-quality flags are plotted. The second principal component is designated LAND PC# 2. The eigenvector for this surface-insensitive principal component is also listed in Table 7.3 and interpreted in the text following the table. The inputs used to train the neural networks include: LAND PC# 2, estimated nadir brightness temperatures for AMSU-B channels 3 and 4, and five estimated brightness perturbations due to icy hydrometeors for AMSU-A channels 4-8 computed from estimated nadir brightness temperatures.

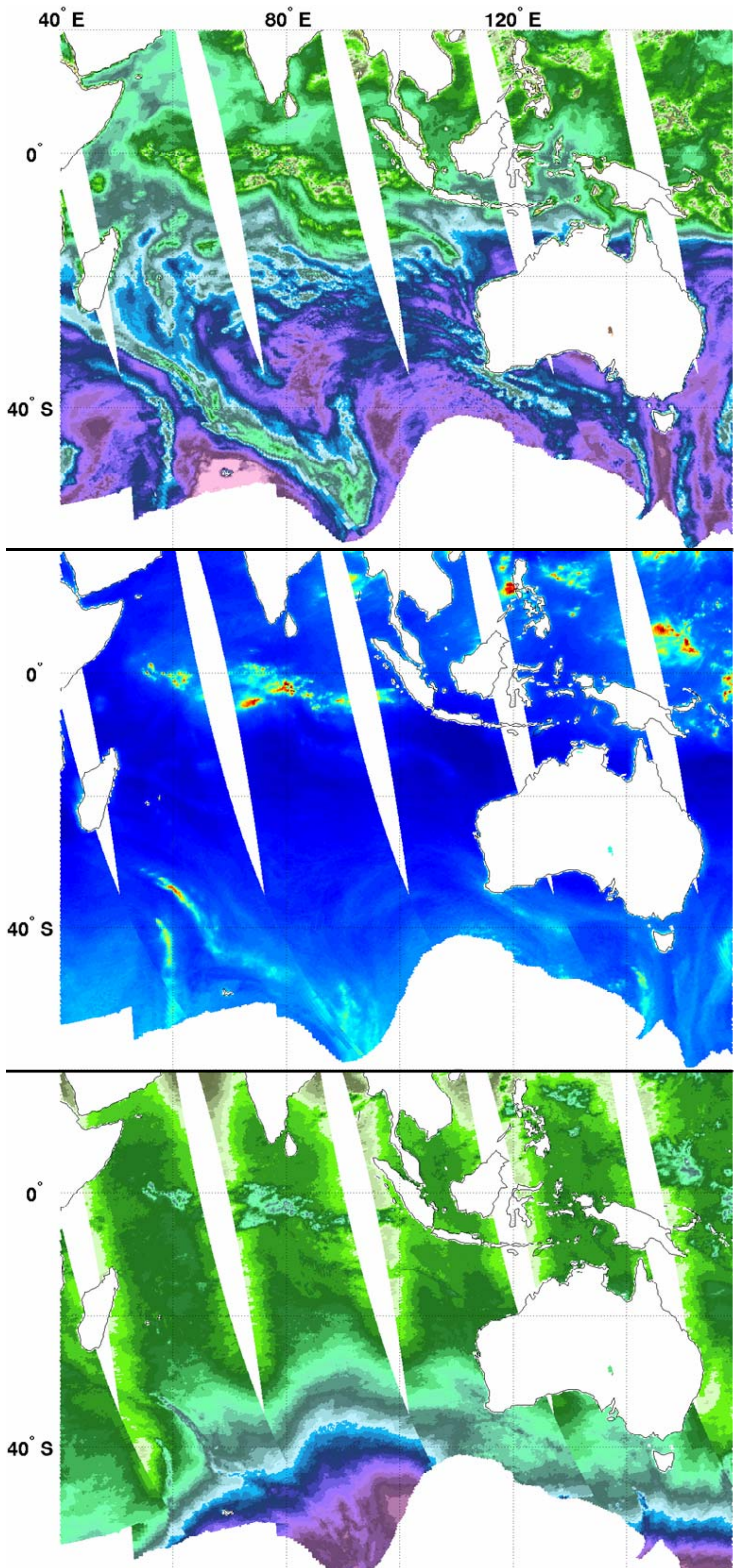

Fig. 7.9. Ocean principal components for ascending orbits of AMSU aboard NOAA-16 on July 26, 2002. Top to bottom are SEA PC# 1, SEA PC# 2, SEA PC# 6, respectively.

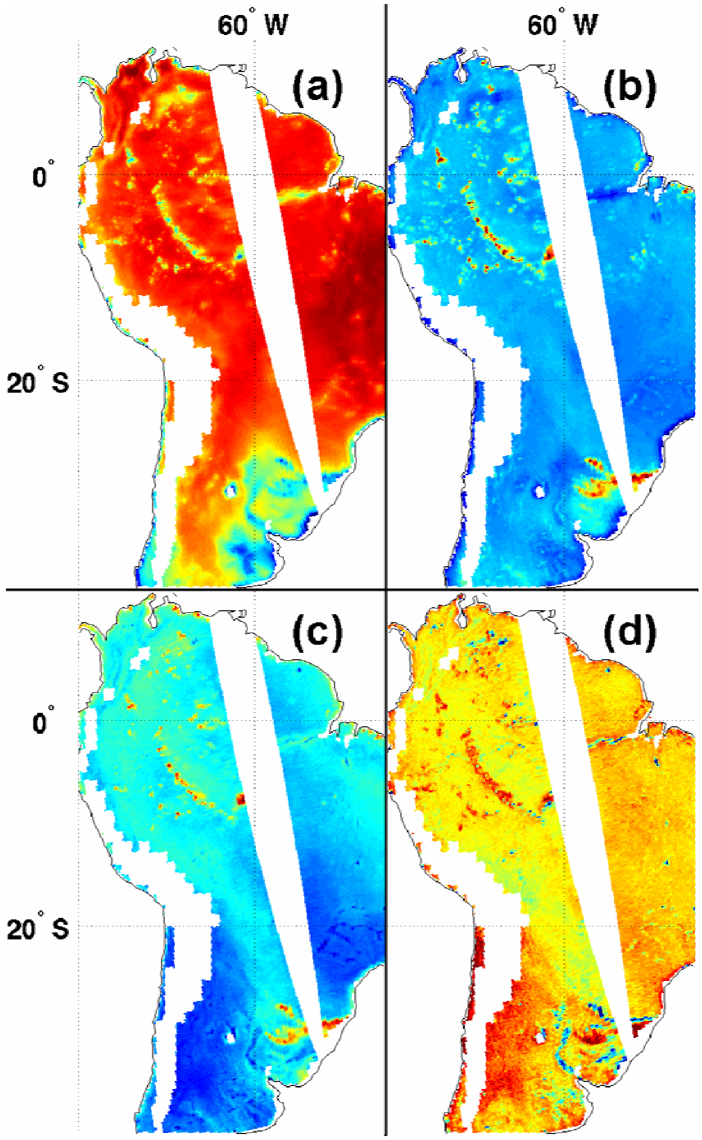

Fig. 7.10. Land principal components for ascending orbits of AMSU aboard NOAA-16 on July 26, 2002. (a) LAND PC# 1, (b) LAND PC# 2, (c) LAND PC# 3, and (d) LAND PC# 5.

TABLE 7.3

NORMALIZED SURFACE-INSENSITIVE EIGENVECTORS REPRESENTING AMSU-A CHANNELS 1-8 AND AMSU-B CHANNELS 1-5 OVER SEAWATER, AND AMSU-A CHANNELS 1-5 AND AMSU-B CHANNELS 1, 2, AND 5 OVER LAND WITHOUT SNOW (XI SIGNIFIES AMSU-X CHANNEL I)

Input	SEA PC#2	SEA PC#3	SEA PC#4	SEA PC#5	LAND PC#2
A1	**-16.58**	19.44	**-47.09**	-18.13	**33.69**
A2	**-38.83**	**49.16**	18.68	**45.26**	**42.19**
A3	-14.00	15.55	11.29	7.47	4.15
A4	14.15	5.09	-25.02	-28.29	-12.60

A5	14.97	2.47	-26.72	-29.90	-12.11
A6	6.59	1.14	-13.28	-17.44	-
A7	1.78	0.21	-5.41	-10.28	-
A8	-7.60	-1.37	11.69	9.07	-
B1	-0.95	**-37.68**	**64.73**	-29.96	-31.29
B2	**48.78**	**-37.72**	-10.66	**47.38**	**-55.38**
B3	32.90	**45.51**	31.95	-30.85	-
B4	**42.66**	**40.67**	16.99	-8.29	-
B5	**47.02**	18.99	-3.21	34.89	**-52.11**

The physical significance of the principal components can be partly surmised from their dominant entries, listed in bold font. The first principal component SEA PC#2 primarily cancels the surface effects observed by AMSU-A, channels 1 and 2 (23.8 and 31.4 GHz), against those evident in AMSU-B, channels 2 and 5, while responding strongly to water vapor; water vapor warms A1 and A2 while cooling B2-B5, consistent with their opposite signs. SEA PC#3 also cancels AMSU-A and AMSU-B window channels while responding to a different combination of water vapor and rainwater. SEA PC#4 cancels the water vapor and surface effects in AMSU-A and AMSU-B channel 1, and SEA PC#5 responds strongly to liquid water while canceling surface effects in channel 1 against channel 2 for both AMSU-A and B. LAND PC#2 also cancels the surface effects seen by AMSU-A against those seen in AMSU-B while reinforcing sensitivity to both rainwater and humidity. Although it is difficult to surmise exactly what information survives the cancellations, these independent sources of nearly-surface-blind information clearly facilitate precipitation estimates.

The nature of the neural network estimator can also be determined by correlating each network input channel with the output. This revealed that all input channels sounding below 15-km altitude were utilized in estimating surface precipitation rates, but that AMSU-A channels 4-8 (52.8-55.5 GHz) were generally the most important below 60 GHz, and AMSU-B channel 5 (183±7 GHz) was generally the most important above 60 GHz. Moreover, the relative importance and use of the channels by the network shifts from one precipitation type to another. The apparent complexity of these minimum-rms neural network estimators suggests that alternative estimators based on physical models requiring specific knowledge of atmospheric profiles may be challenged unless those profiles are known reasonably well. Future study of such issues may be rewarding.

It is interesting to see how each input to the precipitation neural networks shown in Fig. 7.8 is correlated with the estimated precipitation parameters, and how well these precipitation parameters are correlated with themselves. Tables 7.4, 7.5, and 7.6 show for the 106 storms described in Section 7.3.3 these correlation coefficients between: 1) simulated land and sea brightness temperatures at 50-km resolution for AMSU-A and 15-km resolution for AMSU-B, and 2) MM5 truth at 15-km resolution. Note that a correlation coefficient only tells statistical relationship between a pair of parameters in the linear sense whereas the algorithms used in this chapter employ a nonlinear neural network method, which captures both linear and nonlinear statistics. Since the parameters for which correlation coefficients are computed span up to three orders of magnitude, two types of correlation coefficient are given; the first correlates the two parameters of interest and the second correlates their logarithms, $\log_{10}[X + 0.01]$. Whereas the former better indicates the correlation for large parameter values, the later better indicates the overall correlation, including small values. Boldface indicates correlation coefficients greater than or equal to 0.5.

Table 7.4 shows that SEA PC# 2, LAND PC# 2, and AMSU-B channel 4 are strongly correlated with all MM5 precipitation parameters except for cloud water. Correlation coefficients between other SEA PC's and MM5 parameters are generally smaller. Brightness perturbations, ΔT, for AMSU-A channels 4-7 are strongly correlated with all MM5 precipitation parameters, except for cloud water over both land and sea, and cloud ice over sea. AMSU-B channel 3 (183±1 GHz) is strongly correlated with graupel, the sum R+S+G, cloud ice, and peak vertical updraft wind because it sounds humidity and ice at high altitudes. Zenith angle has no significant linear relationship with any MM5 precipitation parameter, and therefore these entries suggest the precision of such correlations.

TABLE 7.4

CORRELATION COEFFICIENTS, CORRCOEF(X,Y), BETWEEN INPUTS TO PRECIPITATION NEURAL NETWORKS AND MM5 PRECIPITATION PARAMETERS

X/Y	RR	R	S	G	RSG	C	I	W_p
Sea								
SEA PC#2	**0.61**	**0.65**	**0.79**	**0.55**	**0.77**	0.48	**0.68**	**0.65**
SEA PC#3	0.44	0.47	0.49	0.24	0.45	0.48	0.29	0.40
SEA PC#4	0.21	0.25	0.20	0.37	0.34	0.44	0.12	0.30
SEA PC#5	0.22	0.24	**0.60**	0.33	0.45	0.23	0.49	0.32
$\Delta T4$	**0.58**	**0.66**	**0.65**	**0.69**	**0.79**	0.20	0.43	**0.67**
$\Delta T5$	**0.60**	**0.69**	**0.64**	**0.71**	**0.81**	0.23	0.44	**0.68**
$\Delta T6$	**0.58**	**0.66**	**0.59**	**0.71**	**0.78**	0.23	0.43	**0.68**
$\Delta T7$	**0.53**	**0.62**	**0.53**	**0.68**	**0.73**	0.22	0.42	**0.65**
$\Delta T8$	0.31	0.36	0.42	0.35	0.44	0.17	0.41	0.38
θ_{zenith}	0.02	0.02	0.01	0.01	0.02	0.03	0.01	0.01
Land								
LAND PC#2	**0.58**	**0.64**	**0.89**	**0.55**	**0.78**	0.31	**0.71**	**0.61**
B3	0.43	0.47	0.49	**0.58**	**0.61**	0.19	**0.64**	**0.50**
B4	**0.59**	**0.64**	**0.75**	**0.71**	**0.82**	0.28	**0.74**	**0.66**
$\Delta T4$	**0.65**	**0.71**	**0.74**	**0.67**	**0.82**	0.29	**0.54**	**0.63**
$\Delta T5$	**0.65**	**0.72**	**0.70**	**0.71**	**0.83**	0.29	**0.53**	**0.65**
$\Delta T6$	**0.61**	**0.68**	**0.59**	**0.75**	**0.80**	0.28	**0.50**	**0.65**
$\Delta T7$	**0.55**	**0.61**	**0.50**	**0.72**	**0.74**	0.26	0.48	**0.62**
$\Delta T8$	0.28	0.31	0.38	0.32	0.39	0.16	0.41	0.32
θ_{zenith}	0.02	0.02	0.03	0.01	0.01	0.04	0.04	0.02

A1 and B1 signify channel 1 for AMSU A and AMSU B, respectively. $\Delta T4$ is the spatially local perturbation in AMSU-A channel 4 brightness due to precipitation. SEA

PC's and LAND PC's are principal components for sea and land, respectively. θ_{zenith} is the zenith angle. Boldface: correlation coefficient is greater than or equal to 0.5. RR, R, S, G, RSG, C, I, and W_p signify surface precipitation rate, rainwater, snow, graupel, sum of rain, snow, and graupel, cloud liquid water, cloud ice, and peak vertical wind, respectively.

Table 7.5 shows that SEA PC# 2 is better correlated with MM5 rain rate, rainwater, and graupel than it was in Table 7.4, presumably due to the somewhat greater accuracies for stratiform precipitation at lower rates. SEA PC# 3 is strongly correlated with surface precipitation rate, rainwater, graupel, and the sum of rainwater, snow, and graupel. LAND PC# 2 is strongly correlated with all MM5 precipitation parameters except for cloud water and peak vertical wind. In contrast to the results in Table 7.4, Table 7.5 shows much lower correlations between MM5 and the AMSU-A brightness perturbations, ΔT, except for graupel, which is expected since stratiform precipitation is prominent in Table 7.5 and often produces little or no ΔT response.

TABLE 7.5

CORRELATION COEFFICIENTS, CORRCOEF($\log_{10}$(X+0.01),$\log_{10}$(Y+0.01)), BETWEEN LOGARITHMS OF INPUTS TO PRECIPITATION NEURAL NETWORKS AND LOGARITHMS OF MM5 PRECIPITATION PARAMETERS

X/Y	RR	R	S	G	RSG	C	I	W_p
Sea								
SEA PC#2	**0.66**	**0.73**	**0.65**	**0.83**	**0.71**	0.41	0.47	**0.62**
SEA PC#3	**0.60**	**0.63**	0.41	**0.57**	**0.50**	0.44	0.13	0.45
SEA PC#4	0.32	0.24	0.03	0.16	0.08	**0.59**	0.09	0.11
SEA PC#5	0.15	0.21	0.46	0.45	0.41	0.18	0.34	0.29
ΔT4	0.28	0.35	0.29	**0.54**	0.33	0.11	0.20	0.38
ΔT5	0.29	0.37	0.28	**0.55**	0.33	0.13	0.19	0.38
ΔT6	0.28	0.36	0.28	**0.54**	0.33	0.13	0.20	0.38
ΔT7	0.27	0.35	0.29	**0.52**	0.33	0.13	0.21	0.37
ΔT8	0.29	0.35	0.36	0.42	0.37	0.15	0.27	0.32
θ_{zenith}	0.02	0.03	0.03	0.01	0.03	0	0.04	0.03
Land								
LAND PC#2	**0.65**	**0.73**	**0.76**	**0.76**	**0.78**	0.32	**0.54**	0.49
B3	0.32	0.36	0.47	0.47	0.48	0.14	**0.57**	0.32
B4	0.45	**0.51**	**0.56**	**0.66**	**0.59**	0.22	**0.50**	0.44
ΔT4	0.43	**0.50**	0.39	**0.64**	0.44	0.22	0.27	0.40
ΔT5	0.37	0.44	0.34	**0.58**	0.39	0.19	0.24	0.37
ΔT6	0.31	0.37	0.30	**0.51**	0.34	0.16	0.22	0.33
ΔT7	0.28	0.34	0.29	0.46	0.33	0.15	0.22	0.31
ΔT8	0.27	0.32	0.36	0.36	0.37	0.14	0.28	0.25
θ_{zenith}	0.08	0.08	0.08	0.05	0.09	0.05	0.06	0.06

A1 and B1 signify channel 1 for AMSU A and AMSU B, respectively. ΔT4 is the spatially local perturbation in AMSU-A channel 4 brightness due to precipitation. SEA

PC's and LAND PC's are principal components for sea and land, respectively. θ_{zenith} is the zenith angle. Boldface: correlation coefficient is greater than or equal to 0.5. RR, R, S, G, RSG, C, I, and W_p signify surface precipitation rate, rainwater, snow, graupel, sum of rain, snow, and graupel, cloud liquid water, cloud ice, and peak vertical wind, respectively.

The correlations shown in Tables 7.4 and 7.5 arise partly from direct physical relationships between hydrometeors and brightness temperatures, and partly from correlations between types of hydrometeors, some of which cannot be sensed well directly and therefore must be inferred from estimates of observable types. Table 7.6 shows the correlations between various hydrometeor types and other parameters for this same MM5 data set. AMSU retrievals of surface precipitation rate rely on correlations between that rate and three hydrometeor species more directly sensed by AMSU: graupel, snow, and rainwater. Table 7.6 shows that these linear correlations with surface precipitation rate (upper triangle of the table) are greatest for rainwater and graupel, whereas snow, graupel, and rainwater contribute importantly to the logarithmic correlations (lower triangle) that are more indicative of lower rain rates. Estimates of cloud ice, for example, rely on its correlation with observable hydrometeor species since cloud ice has little effect on millimeter-wave emissions.

TABLE 7.6

LINEAR AND LOGARITHMIC CORRELATION COEFFICIENTS BETWEEN PAIRS OF MM5 PRECIPITATION PARAMETERS; THE UPPER AND LOWER TRIANGLES PRESENT THE COEFFICIENTS FOR (X,Y) AND ($\log_{10}$(X+0.01),$\log_{10}$(Y+0.01)), RESPECTIVELY

X/Y	RR	R	S	G	RSG	C	I	W_p
RR	-	**0.93**	0.46	**0.72**	**0.84**	**0.53**	0.37	**0.75**
R	**0.90**	-	0.49	**0.78**	**0.90**	**0.56**	0.40	**0.82**
S	**0.68**	**0.72**	-	0.41	**0.70**	0.18	**0.67**	**0.50**
G	**0.71**	**0.81**	**0.67**	-	**0.91**	0.29	0.35	**0.75**
RSG	**0.78**	**0.83**	**0.97**	**0.74**	-	0.40	**0.53**	**0.83**
C	**0.64**	**0.63**	0.31	0.41	0.44	-	0.19	0.46
I	0.40	0.43	**0.77**	0.41	**0.72**	0.16	-	0.44
W_p	0.46	**0.53**	0.49	**0.63**	**0.56**	0.27	0.41	-

Boldface: correlation coefficient is greater than or equal to 0.5. RR, R, S, G, RSG, C, I, and W_p signify surface precipitation rate; water paths for rainwater, snow, graupel, R+S+G, cloud liquid water, and cloud ice; and peak vertical wind, respectively.

7.5 Results

The simulated retrieval performances of estimators for surface precipitation rate, hydrometeor water-paths, and peak vertical wind were evaluated against MM5 ground-truth using pixels that were not used for neural network training, as described in Section 7.4.1. The neural network inputs were MM5-simulated AMSU T_B's. The inferred retrieval accuracies were largely independent of zenith angle and are presented here as averages over all possible angles. Surface precipitation includes both water and the water equivalent for any icy components. Tables 7.7 and 7.8 show good 15-km resolution surface precipitation rate retrieval performance per octave of rain rate (RR, mm/h), where the octaves are determined using MM5 and AMSU, respectively. Estimates over land are usually slightly less accurate than those over sea, as expected, particularly at the lower rain rates where the surface remains visible. A rough measure of retrieval utility is the ratio of the rms error relative to the rates defining each octave; in the tables, italics highlights cases where the rms errors exceed the upper bound for the octave, indicating low utility, and boldface highlights cases where the rms errors are less than the lower bound, which suggests good performance. Based on rms errors in Table 7.7, AMSU surface precipitation rate retrievals appear to be generally useful above ~1 mm/h over ocean and above ~2 mm/h over land. Fig. 7.11 shows scatter plots between MM5 truth and AMSU/MM5 surface precipitation rate estimate over land and sea for 106 storms, where the test pixels are uniformly subsampled. The correlation coefficient ρ is computed using $\log_{10}(X + 0.01)$, where X is any variable of interest.

TABLE 7.7

RMS, MEAN, AND STANDARD ERRORS FOR (MM5 – ESTIMATE) FOR 15-KM RESOLUTION MM5-SIMULATED SURFACE PRECIPITATION RATE RETRIEVALS (MM/H, RMS), WHERE THE RR RANGE IS DEFINED BY MM5

RR Range (mm/h)	RMS Error			Mean Error			Standard Error		
	Land	Sea	All	Land	Sea	All	Land	Sea	All
0-0.125	*0.45*	*0.42*	*0.43*	*-0.15*	*-0.14*	*-0.15*	*0.43*	*0.39*	*0.40*
0.125-0.25	*0.94*	*0.78*	*0.86*	*-0.33*	*-0.30*	*-0.31*	*0.89*	*0.72*	*0.81*
0.25-0.5	*1.13*	*0.83*	*0.98*	-0.29	-0.25	-0.28	*1.09*	*0.79*	*0.94*
0.5-1	*1.29*	0.96	*1.18*	**-0.29**	**-0.23**	**-0.26**	*1.26*	0.93	*1.15*
1-2	1.62	1.30	1.47	**-0.28**	**-0.13**	**-0.19**	1.60	1.30	1.46
2-4	2.35	2.02	2.20	**0.23**	**-0.09**	**0.05**	2.34	2.02	2.20
4-8	**3.98**	**3.94**	**3.96**	**1.58**	**0.01**	**0.81**	**3.65**	**3.94**	**3.87**
8-16	**7.59**	**7.30**	**7.55**	**4.09**	**2.00**	**3.22**	**6.40**	**7.03**	**6.83**
16-32	**13.81**	**13.48**	**13.55**	**9.95**	**8.88**	**9.52**	**9.58**	**10.16**	**9.64**
32-64	**23.04**	**26.19**	**25.01**	**18.62**	**21.93**	**20.68**	**13.60**	**14.34**	**14.07**
>64	**49.19**	**50.68**	**49.43**	**43.38**	**47.31**	**45.21**	**23.65**	**18.34**	**20.00**

Italics: rms errors that exceed the maximum value bounding the octave. Boldface: rms errors less than the minimum for the octave

TABLE 7.8

RMS, MEAN, AND STANDARD ERRORS (MM5 – ESTIMATE) FOR 15-KM RESOLUTION MM5-SIMULATED SURFACE PRECIPITATION RATE RETRIEVALS (MM/H, RMS), WHERE THE RR RANGE IS DEFINED BY THE ESTIMATE

RR Range	RMS Error	Mean Error	Standard Error

(mm/h)	Land	Sea	All	Land	Sea	All	Land	Sea	All
0-0.125	*0.28*	*0.14*	*0.30*	-0.00	-0.02	0.00	*0.28*	*0.14*	*0.30*
0.125-0.25	*0.42*	*0.37*	*0.48*	-0.07	-0.03	-0.04	*0.41*	*0.36*	*0.47*
0.25-0.5	*0.81*	*0.72*	*0.78*	-0.04	0.02	-0.02	*0.81*	*0.72*	*0.78*
0.5-1	*1.46*	*1.15*	*1.15*	0.03	0.08	-0.01	*1.46*	*1.14*	*1.15*
1-2	*2.11*	1.34	1.77	-0.04	0.01	0.03	*2.11*	1.34	1.77
2-4	3.59	2.97	3.26	-0.01	0.03	0.05	3.59	2.97	3.26
4-8	6.45	5.72	6.23	-0.09	0.16	0.24	6.45	5.71	6.22
8-16	9.30	12.31	10.61	-0.05	1.11	0.37	9.30	12.27	10.60
16-32	16.90	18.81	16.05	-0.50	0.89	0.88	16.91	18.80	16.02
32-64	**25.30**	**24.32**	**23.23**	4.77	2.90	-0.99	**25.03**	**24.27**	**23.22**
64	**-**	**-**	**-**	-	-	-	-	-	-

Italics: rms errors that exceed the maximum value bounding the octave. Boldface: rms errors less than the minimum for the octave.

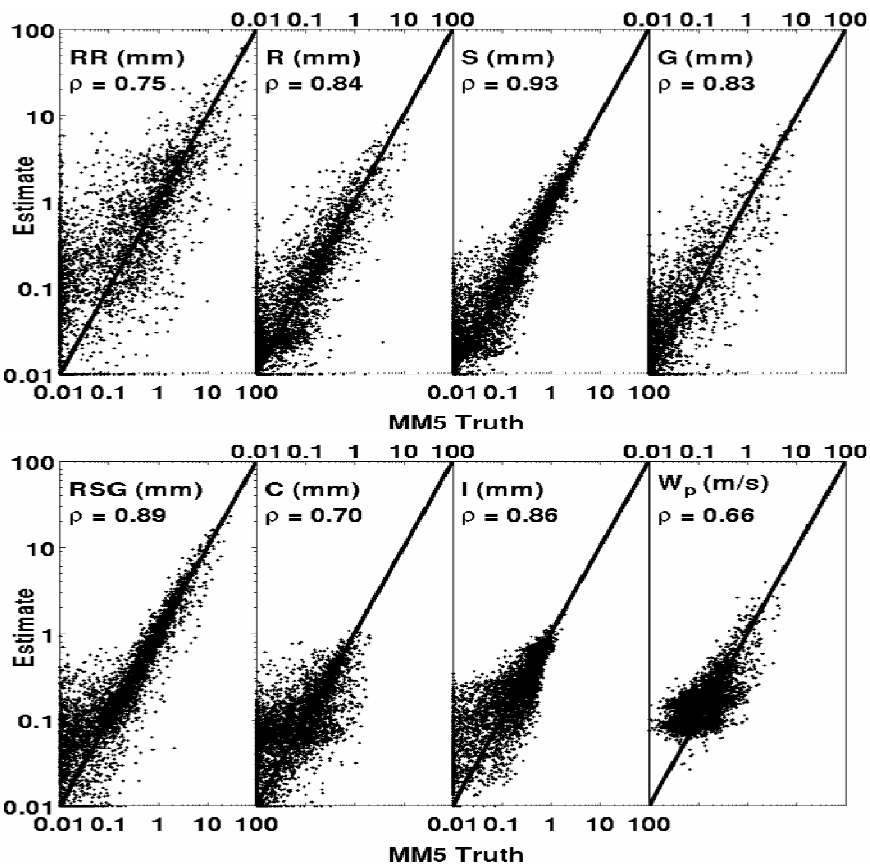

Fig. 7.11. Scatter plots between MM5 truth and AMSU/MM5 estimates for surface precipitation rate (RR); water-paths for rain water (R), snow (S), graupel (G), the sum R+S+G (RSG), cloud liquid water (C), and cloud ice (I); and peak vertical wind (W_p).

The mean errors shown in Table 7.8 are approximately zero except for sampling noise due to the limited number of pixels observed at the very highest rain rates. As a result of these small mean errors, AMSU surface precipitation rate estimates can be summed to yield nearly unbiased estimates of the total precipitation that fell within any AMSU-defined time-space box. However, estimates of the distribution of precipitation rates within any space-time box would be biased as indicated in Table 7.7, and this bias can be corrected as discussed later. The underestimates at higher rain rates occur partly because strong convection is often topped with icy shields overhanging narrower columns of intense precipitation. In this case zero mean error per octave requires peak rates to be underestimated to compensate for anvil spreading so that when the estimates are averaged over both central and neighboring areas the typical mean error per storm is zero. In Table 7.7, for rates above 4 mm/h the fractional mean error is approximately one-third of the mean rate, suggesting typical overhang areas are ~25 percent of the indicated precipitation zone. This small enlargement should not be confused with the larger overhang ratio for visible cirrus or for the raw microwave response; it corresponds instead to the residual overhang ratio after the neural network has extracted all available information about precipitation extent from the microwave spectrum.

Of particular interest is the sensitivity of retrieval algorithms at the lowest precipitation rates. To help address this question Fig. 7.12 shows for land and sea the derived probability density functions (PDF) of the "true" MM5 surface precipitation rate for pixels for which the simulated AMSU estimate was below 0.1, 0.3, and 1 mm/h, where the total number of pixels per PDF has been normalized to unity. The figure suggests that, averaged over all precipitation types, the rms sensitivity over land is roughly 1 mm/h, and over sea it is roughly 0.5 mm/h. These sensitivities are shown later to be even better for stratiform and snow, and worse for convective precipitation.

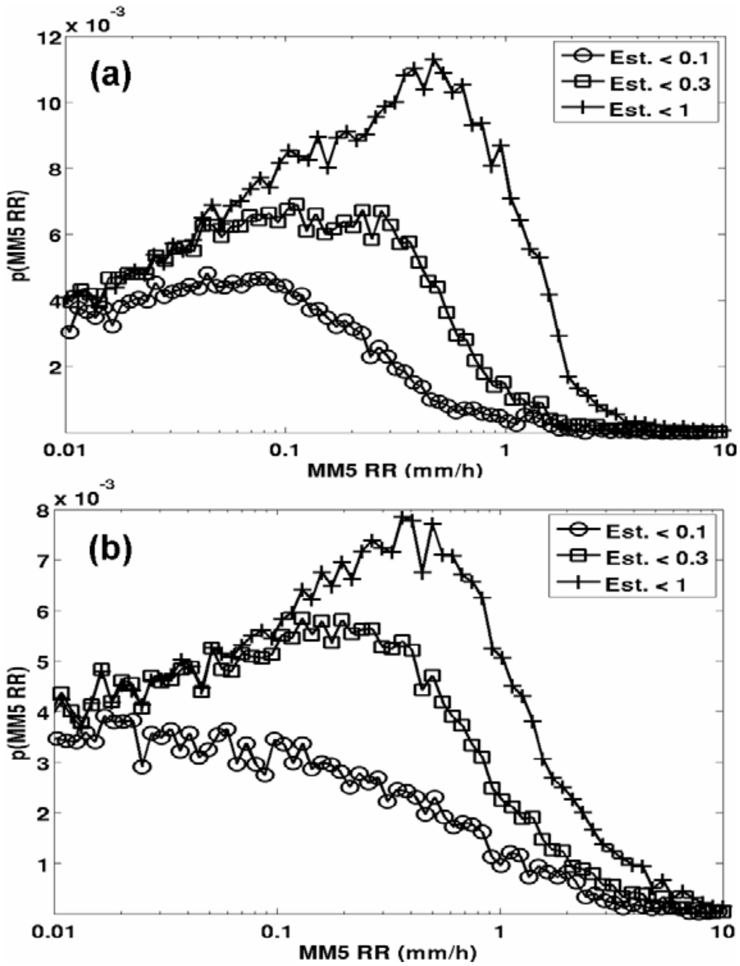

Fig. 7.12. Probability density function of MM5 surface precipitation rate for pixels with estimates below 0.1, 0.3, and 1 mm/h, for (a) sea and (b) land.

Fig. 7.13 presents histograms of estimation errors (MM5 truth – estimate) for different ranges of estimated surface precipitation rate for land and sea, where the histograms were normalized so they peak at unity. For clarity the histograms for estimates 8-16 mm/h were shifted to the right by 4 mm/h for both land and sea. The results in Fig. 7.13 are consistent with the rms and mean errors listed in Table 7.8. The figure shows that the errors are roughly symmetric and Gaussian, and are biased relative to the estimate, as expected, but are nearly unbiased relative to the MM5 truth for which the estimates were trained (with independent samples).

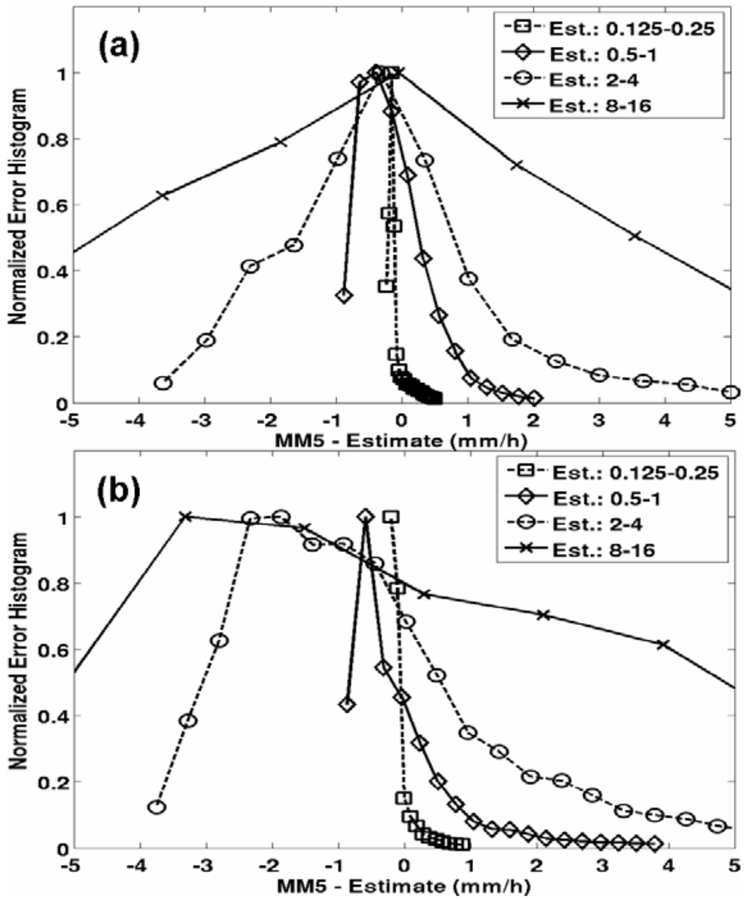

Fig. 7.13. Normalized error (MM5 truth – estimate) histograms for different surface precipitation rate ranges defined by the estimate for (a) sea and (b) land. Histograms for estimates 8-16 mm/h were shifted to the right by 4 mm/h for both land and sea

For different MM5 precipitation-rate thresholds over land and sea, Table 7.9 shows the percentages of AMSU precipitating pixels due to false detection, the percentages of total AMSU precipitating surface precipitation rate due to false detection, the percentages of MM5 precipitating pixels that were missed, and the percentages of to MM5 precipitating surface precipitation rate that was missed. For a given MM5 threshold, x [mm/h], and a given AMSU threshold, y [mm/h], a false detection occurs when the MM5 truth is less than the threshold x and the AMSU estimate equals or exceeds the threshold y. AMSU precipitating pixels are those pixels with surface precipitation rate equals or exceeds the threshold y. A missed detection occurs when the MM5 truth equals or exceeds x, and the AMSU estimate is less than y. MM5 precipitating pixels are those pixels with surface precipitation rate equals or exceeds the threshold x. The level of false detection over land is reasonable if AMSU retrievals below 1 mm/h are treated as zero. The false detection is less over sea. The percentages of missed detection are small for both land and sea.

TABLE 7.9

FREQUENCY AND AMOUNT OF FALSE DETECTION AND MISSED DETECTION FOR DIFFERENT MM5 AND AMSU THRESHOLDS

MM5 threshold (mm/h)	AMSU threshold (mm/h)	Percentage of AMSU precipitating pixels due to false detection		Percentage of AMSU precipitating RR due to false detection	
		Land	Sea	Land	Sea
0.01	0.1	36.75	26.45	9.18	5.10
0.01	0.3	16.33	9.21	6.13	2.98
0.01	1	7.05	2.51	3.99	1.44
0.1	0.1	47.80	37.64	13.37	8.81
0.3	0.3	33.21	28.25	14.06	10.24
1	1	34.35	24.61	20.35	12.90
MM5 threshold (mm/h)	AMSU threshold (mm/h)	Percentage of MM5 precipitating pixels that were missed		Percentage of MM5 precipitating RR that was missed	
		Land	Sea	Land	Sea
0.1	0.1	11.38	5.56	2.81	0.80
0.3	0.1	7.52	2.04	2.44	0.50
1	0.1	3.75	0.57	1.64	0.22
0.3	0.3	21.46	9.83	6.88	2.32
1	1	25.46	16.89	12.16	6.73

When AMSU observations are used to estimate precipitation-rate distributions the biases evident in Table 7.9 and Fig. 7.13(b) should be corrected. Because these biases are different for convective and stratiform precipitation, pixels were defined as stratiform if their maximum updraft MM5 layer vertical velocity (w_p) was less than 0.45 m/s; this threshold was chosen empirically using representative global classification images. The stratiform and convective precipitation-rate distributions are plotted in Fig. 7.14(a) for the set of 106 storms using MM5 data, and for the corresponding AMSU retrievals. Note that there is no evident bias for the pixels classed as stratiform ($w_p \leq 0.45$ m/s), although there is a tendancy for the AMSU retrieval algorithm to favor precipitation rates near 2 mm/h. Fig. 7.14(a) also compares the MM5 and AMSU precipitation-rate distributions for the pixels classed as convective ($w_p > 0.45$ m/s); AMSU is biased toward lower values as expected. Empirical matching of these two histograms suggests that AMSU convection rates should be biased toward higher rates by ~37 percent to yield nominal agreement with true distribution functions. Such corrections produce a bias in total rainfall, however, so they should only be applied to distribution functions.

In real applications where truth is unavailable the estimated peak vertical updraft wind can be used to classify precipitation. Fig. 7.14(b) shows the same plots as Fig. 7.14(a) except that the estimated AMSU/MM5 peak vertical updraft wind was used instead to classify footprints as convective or stratiform, which slightly blurs the distributions in the transition zone 4-20 mm/h and effectively biases the detected convective pixels slightly toward higher rates. In this case AMSU is biased a bit lower than MM5 for stratiform pixels because some convective pixels have been added at the higher rates. Bias correction improves the agreement between AMSU and MM5 for detected convective pixels, but AMSU is still biased lower due to errors in the AMSU/MM5 peak vertical wind estimates and misclassification (to the stratiform set) of convective pixels at lower rates.

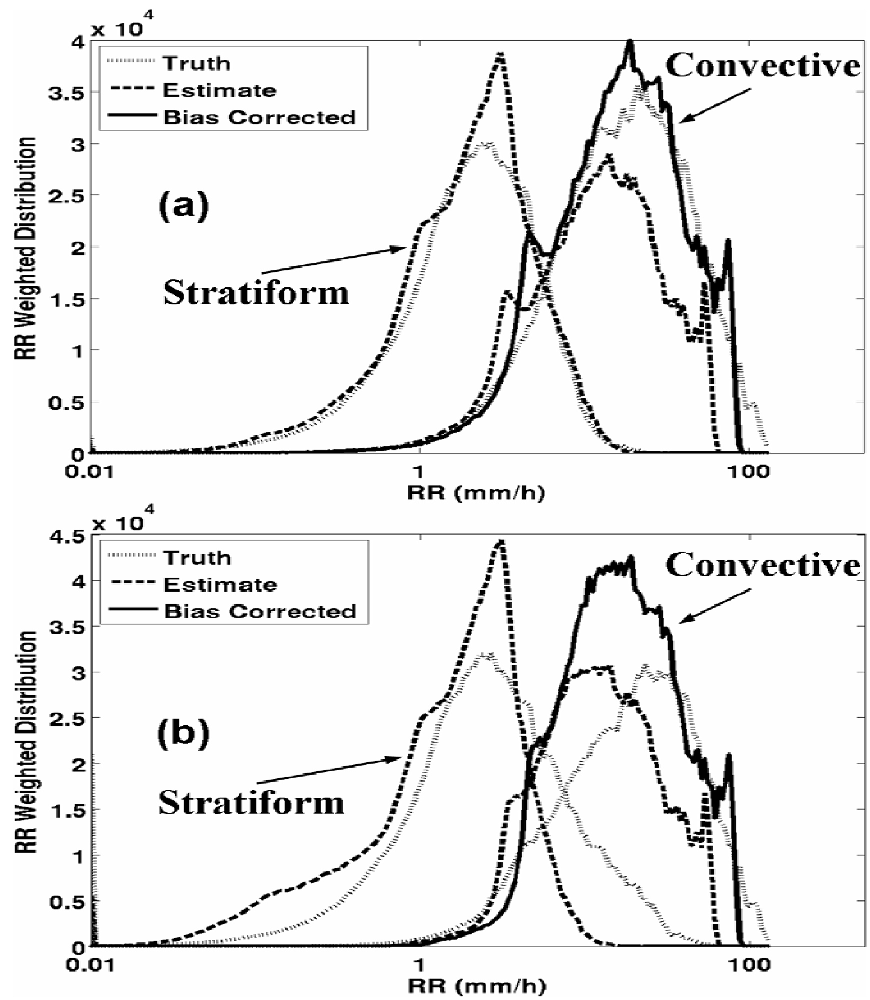

Fig. 7.14. MM5-simulated convective and stratiform rainfall per unit of $\log_{10}$(precipitation rate); pixel counts are weighted by the surface precipitation rate per pixel. The solid line is the distribution function for convective precipitation after a multiplicative bias correction of 1.37. Pixels are classified as convective or stratiform using (a) MM5 peak vertical wind, (b) AMSU/MM5 estimate of peak vertical wind.

Further understanding of the origins of retrieval errors was sought by computing the correlation coefficient between "fractional surface-precipitation-rate error" Δ and a "virga parameter" V for different types of precipitation. For each 15-km resolution pixel Δ is defined as $\Delta = (\hat{R} - R)/(R + 1)$, where $\hat{R}$ and R are the estimated and true surface precipitation rates, respectively [2]. The additive constant 1 mm/h in the denominator of the Δ definition was empirically selected to yield reasonable results; values much less than ~1 unduly exaggerated the error contributions of low rain rates, while much larger values excessively muted them. V for each 15-km pixel is defined as $V = (\rho_{max} + 0.2)/(\rho_{ground} + 0.2)$, where ρ_{max} is the maximum sum of rain, snow, and graupel densities (g/m^3) for any MM5 level, and ρ_{ground} is the corresponding summed density at 1000 mb [2]. Virga is precipitation that evaporates before reaching the ground. The additive constant 0.2 avoids excessive emphasis of low surface densities, while not being so large as to under-represent low precipitation rates. The correlation coefficients between Δ and V for convective, stratiform, snow only, rain only, warm rain, and all precipitation were found to be 0.64, 0.38, 0.28, 0.49, 0.44, and 0.51, respectively. This virga parameter is most highly correlated with Δ for convective rain. These results suggest that virga contributes additional errors beyond the overhang bias noted above. The errors introduced by overhang and virga could probably be reduced further if NWP data were used in the retrieval or, equivalently, if such microwave precipitation data were successfully assimilated into cloud-resolving numerical weather models.

Comparisons of retrieved precipitation rate images with truth can also be revealing, as shown for 6 storm systems in Fig. 7.15. From top to bottom the illustrated storms include an intense frontal system over France at 1003 UTC 2 January 2003 for which some footprints are classified as land with snow cover (light blue), a Typhoon over Guam at 1625 UTC 8 December 2002, an system over Florida at 2344 UTC 31 December 2002, an ITCZ system over Indonesia at 1210 UTC 15 February 2003, a system having some precipitating footprints north of Siberia classified as sea ice (red) at 1731 UTC 9 July 2002, and a non-glaciated system over the North Atlantic Ocean at 0503 UTC 16 November 2002. Fig. 7.15 first compares AMSU-B 183±7 GHz channel-5 observations (first column) with coincident MM5-simulated brightness temperatures (second column), showing that the storm morphologies and brightness distributions are generally similar although the details differ. Initializing MM5 typhoon predictions is difficult because the initialization data is not sufficiently fine-grained and accurate; thus the MM5 typhoon does not have the long spiral arms of the real typhoon and is more intense.

The next three columns compare AMSU retrievals (third column) with MM5 ground-truth (fourth column) and simulated MM5-based surface precipitation rate retrievals (fifth column). The last column characterizes the surface based on the actual AMSU observations (land, sea, snow over land, or sea ice). Surface precipitation rate retrievals using MM5/TBSCAT-simulated T_B's agree reasonably well with MM5 ground-truth for all types of precipitation, although in each storm the retrieved AMSU/MM5 precipitation zone typically extends slightly beyond that of the MM5 truth, but with generally lower peak values, which illustrates the "overhang" retrieval phenomenon noted earlier that results in lower estimated peak values, thereby minimizing rms errors. The extended area of retrieved precipitation is primarily due to the overspreading of snow and graupel aloft, beyond the borders of the updrafts that created them and slightly beyond the true surface precipitation. The retrieved non-glaciated precipitation over the North Atlantic, which has no significant ice-scattering signature and therefore could not be retrieved using 183±7 GHz as a flag [34], agrees reasonably well with the associated MM5 ground-truth. Fig. 7.15 also shows that AMSU/MM5 retrievals over footprints classified as land with snow and sea ice match MM5 truth if retrieved rates below ~0.3 mm/h are presumed to be zero. Unfortunately, the universal ability to retrieve precipitation over snow and sea ice is compromised by occasional false alarms in dry air.

AMSU can also retrieve hydrometeor water paths and peak vertical wind, as suggested in Fig. 7.16 for the strong French frontal system. The figure compares MM5 truth (mm, 15-km resolution) with retrieved images of the water paths for rainwater, snow, graupel, rainwater + snow + graupel, and cloud water, and also peak vertical wind. MM5 truth is presented in the middle row, while the top row presents retrievals using the corresponding AMSU data, and the bottom row present retrievals based on MM5 simulated brightness temperatures. The MM5 simulated retrievals show the greatest fidelity for snow, graupel, and rainwater, and their sum, while the cloud water retrieval is underestimated because cloud water has a weak signature below 200 GHz. The AMSU/MM5 retrievals are roughly consistent in probability distribution and morphology with the MM5 simulation, but suggest a less severe storm. For both AMSU/MM5 and MM5 truth, snow is most pervasive, rainwater less so, and significant graupel is restricted primarily to the strongest convective cells. The vertical wind retrievals tend to be concentrated closer to the convective cores than in MM5, and the retrievals largely miss the orographically induced wind. This suggests that inclusion of model winds and surface elevations could improve precipitation retrievals.

Fig. 7.17 is the same as Fig. 7.16 except that the comparison is for a system over Florida on December 31. Again all simulated retrievals reasonably agree with MM5 truth except for cloud water. Although estimates for cloud water appears to be underestimated compared to the truth, rms accuracies appear to be quite good, as Table 7.13 later shows.

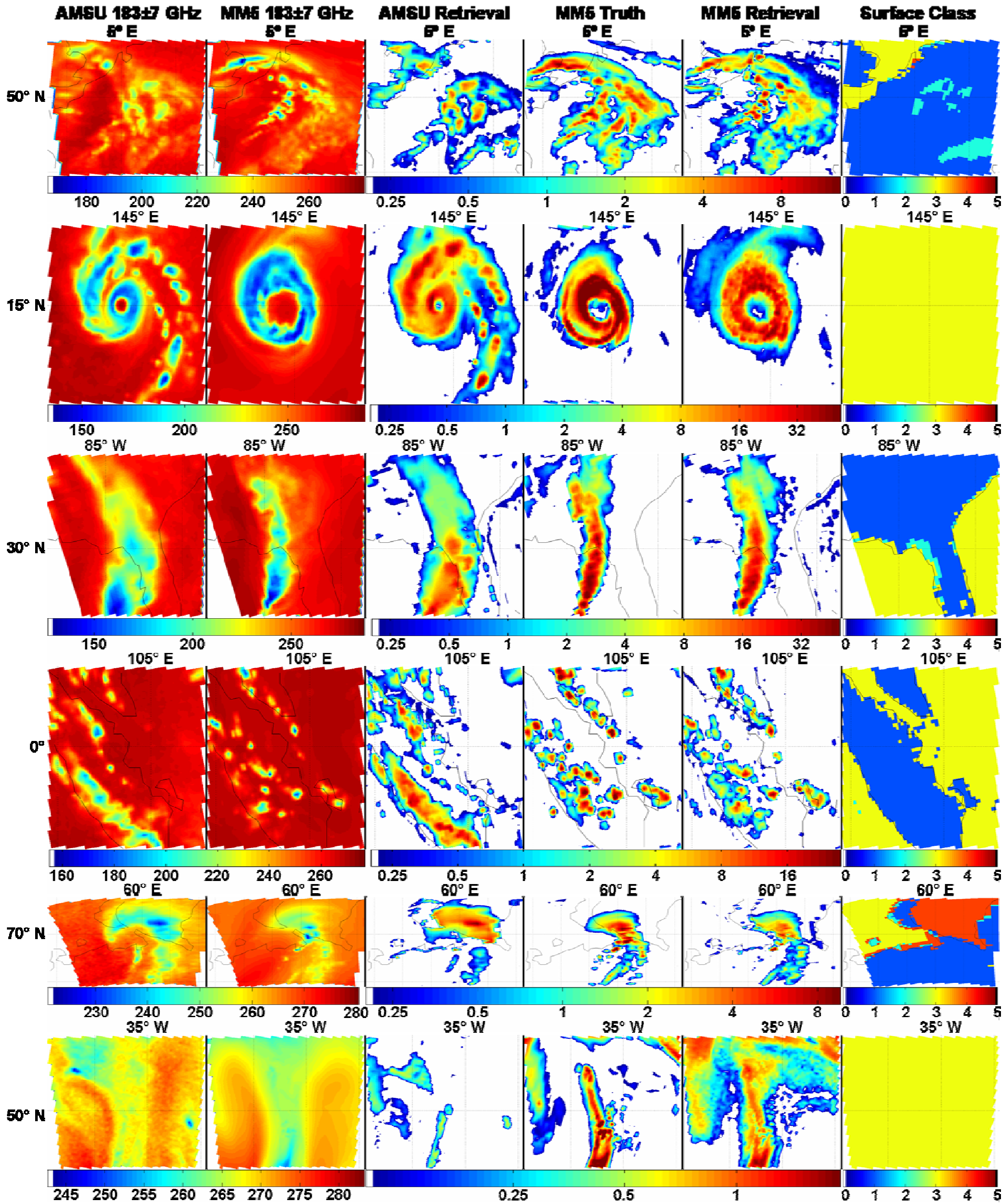

Fig. 7.15. Columns, from left to right: 1) brightness temperatures (T_B) at 183±7 GHz, 2) the corresponding MM5-simulated T_B, 3) AMSU surface precipitation rate (RR) retrievals (mm/h for 15-minute integration; 15-km resolution), 4) MM5 RR truth, 5) retrieved MM5-simulated RR, and 6) AMSU surface classification. From top to bottom: frontal system over France at 1003 UTC 2 January 2003 (some footprints are snow covered (light blue); a Typhoon over Guam at 1625 UTC 8 December 2002; a system over Florida at 2344 UTC 31 December 2002; an ITCZ system over Indonesia at 1210 UTC 15 February 2003; and a system north of Siberia over sea ice at 1731 UTC 9 July

2002; and a non-glaciated system over ocean at 0503 UTC 16 November 2002. For surface class, blue: snow-free land, cyan: land with snow, yellow: seawater, orange: sea ice.

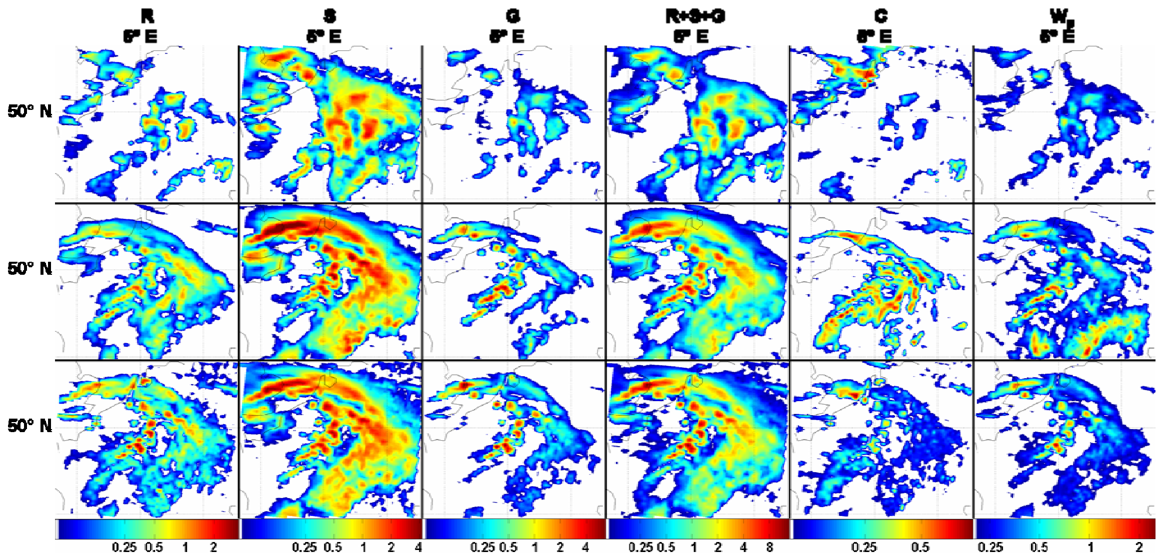

Fig. 7.16. Columns, left to right: water path retrievals (mm) for rainwater (R), snow (S), graupel (G), rainwater + snow + graupel (R+S+G), and cloud liquid water (C); peak vertical wind (W_p, m/s) for a strong frontal system over France at 1003 UTC 2 January 2003. Rows, top to bottom: AMSU/MM5 retrievals, MM5 ground truth, and MM5 simulated retrievals.

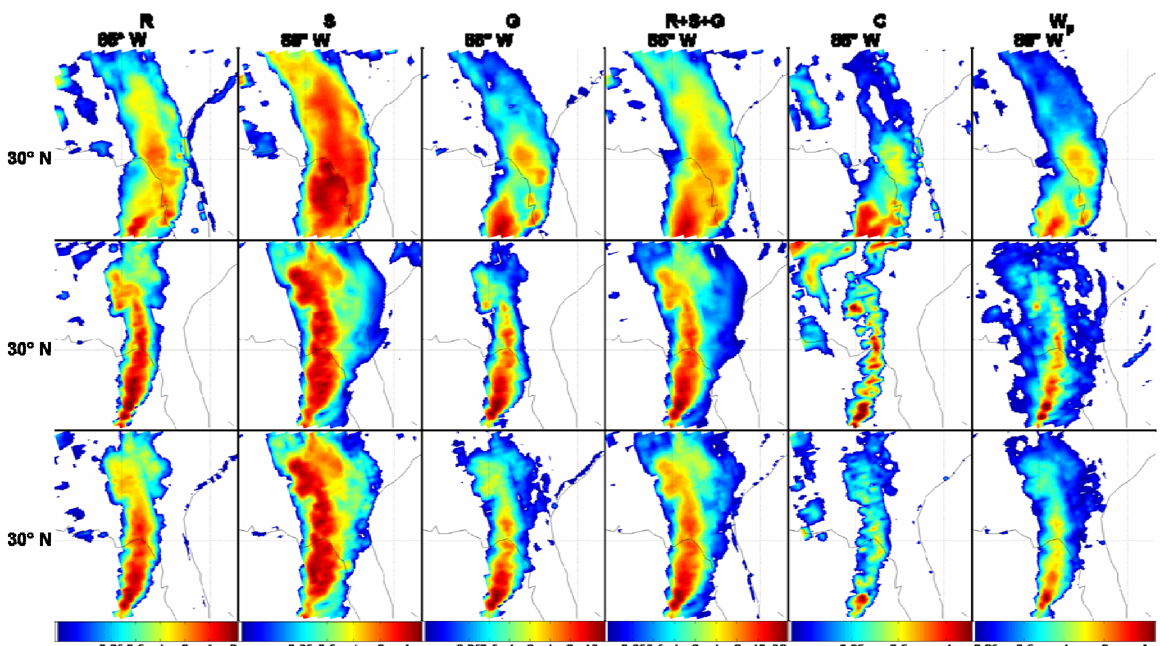

Fig. 7.17. Columns, left to right: water path retrievals (mm) for rainwater (R), snow (S), graupel (G), rainwater + snow + graupel (R+S+G), and cloud liquid water (C); peak

vertical wind (W_p, m/s) for a system over Florida at 2344 UTC 31 December 2002. Rows, top to bottom: AMSU retrievals, MM5 ground truth, and MM5-simulated retrievals.

The simulated retrieval errors can also be characterized in terms of precipitation type, where precipitation type can readily be determined from MM5, as discussed in Section 7.3.3. The rms and mean retrieval errors for 15-km surface precipitation rates are presented in Tables 7.10 and 7.11 for each octave of rate (RR), where only precipitating pixels, defined in Section 7.3.3, are evaluated and the octaves are defined using MM5 and AMSU, respectively, for convective, stratiform, snow only, rain only, and non-glaciated (warm) rain. A pixel was designated as precipitating if either the MM5 rainwater or snow at 1000 mbar were non-zero. When the range boundaries are defined by MM5 truth (Table 7.10) the rms retrieval errors are less than the upper bound for each octave of precipitation rate above ~0.25, ~0.5, 1, and 2 mm/h for pure snow, stratiform and non-glaciated precipitation (warm rain), pure rain, and convective precipitation, respectively; these are the nominal detection thresholds for these four precipitation categories. Similar results are obtained in Table 7.11 where the rms retrieval errors are less than the upper bound for each octave of precipitation rate above ~0.125, ~0.5, ~1, and ~8 mm/h for pure snow, stratiform, rain and warm rain, and convective precipitation, respectively, when the range boundaries are defined by the AMSU estimates.

TABLE 7.10

RMS AND MEAN ERRORS (TRUTH – ESTIMATE) FOR 15-KM RESOLUTION SURFACE PRECIPITATION RATE RETRIEVALS (RR, MM/H) USING MM5-SIMULATED T_B'S FOR AMSU, AND MM5 FOR GROUND-TRUTH AND FOR DEFINING THE RR RANGE BOUNDARIES

RR Range (mm/h)	Convective		Stratiform		Snow Only		Rain Only		Warm rain	
	RMS Error	Mean Error	RMS Error	Mean Error	RMS Error	Mean Error	RMS Error	Mean Error	RMS Error	Mean Error
0-0.125	*1.87*	*-0.99*	*0.51*	*-0.22*	*0.28*	*-0.21*	*0.59*	*-0.24*	*1.30*	*-0.92*
0.125-0.25	*2.57*	*-1.36*	*0.69*	*-0.28*	*0.33*	-0.17	*0.87*	*-0.33*	*1.07*	*-0.68*
0.25-0.5	*2.76*	*-1.35*	*0.75*	**-0.22**	0.35	**-0.09**	*0.97*	-0.29	*0.91*	**-0.47**
0.5-1	*3.04*	*-1.66*	0.88	**-0.20**	**0.42**	**-0.04**	*1.13*	**-0.29**	0.83	**-0.23**
1-2	*3.54*	-1.77	1.07	**-0.09**	**0.57**	**0.15**	1.45	**-0.25**	**0.92**	**0.04**
2-4	3.96	**-1.26**	**1.47**	**0.29**	**1.23**	**0.69**	2.16	**-0.02**	**1.45**	**0.63**
4-8	4.93	**-0.03**	**2.75**	**1.36**	**3.31**	**3.18**	**3.93**	**0.68**	**3.39**	**2.44**
8-16	**7.59**	**2.89**	**5.74**	**4.61**	-	-	**7.40**	**3.08**	8.18	**7.57**
16-32	**13.63**	**9.41**	-	-	-	-	**13.63**	**9.43**	17.21	16.68
32-64	**24.90**	**20.55**	-	-	-	-	**24.90**	**20.55**	38.28	37.31
64	-	-	-	-	-	-	-	-	-	-

Italics: rms or mean errors that exceed the maximum value bounding the octave. Boldface: rms or mean errors less than the minimum bounding the octave. *Retrievals were convolved with 30-km Gaussian functions before the differences were computed.

TABLE 7.11

RMS AND MEAN ERRORS (TRUTH – ESTIMATE) FOR 15-KM RESOLUTION SURFACE PRECIPITATION RATE RETRIEVALS (MM/H) USING MM5-SIMULATED T_B'S FOR AMSU, MM5 FOR GROUND-TRUTH, AND THE ESTIMATE ITSELF FOR DEFINING THE RR RANGE BOUNDARIES

RR Range (mm/h)	Convective		Stratiform		Snow Only		Rain Only		Warm rain	
	RMS Error	Mean Error	RMS Error	Mean Error	RMS Error	Mean Error	RMS Error	Mean Error	RMS Error	Mean Error
0-0.125	*2.51*	*0.91*	*0.37*	0.08	*0.33*	0.10	*0.53*	0.10	*1.95*	1.18
0.125-0.25	*2.98*	*1.10*	*0.52*	**0.09**	0.21	**-0.07**	*0.75*	0.13	*1.95*	0.89
0.25-0.5	*3.34*	*1.48*	*0.56*	**0.06**	0.32	**-0.12**	*0.88*	**0.11**	*1.48*	0.57
0.5-1	*3.74*	*1.76*	0.73	**-0.02**	0.54	**-0.02**	*1.09*	**0.06**	*1.32*	**0.32**
1-2	*5.28*	*2.42*	1.03	**-0.05**	1.00	**0.23**	1.80	**0.14**	1.74	**0.23**
2-4	*6.37*	2.45	**1.69**	**-0.47**	**1.58**	**0.17**	3.35	**0.16**	2.88	**0.13**
4-8	*8.46*	**2.67**	**2.81**	**-1.67**	**2.34**	**-2.19**	6.26	**0.46**	5.16	**0.15**
8-16	11.10	**1.44**	**5.52**	**-4.63**	-	-	10.49	**0.57**	8.76	**-1.98**
16-32	16.74	**1.26**	**-**	-	-	-	16.73	**1.20**	**-**	-
32-64	**23.17**	**-0.01**	-	-	-	-	**23.17**	**-0.01**	-	-
64	-	-	-	-	-	-	-	-	-	-

Italics: rms and mean errors that exceed the maximum value bounding the octave. Boldface: rms and mean errors less than the minimum for the octave. *Retrievals were convolved with 30-km Gaussian functions before the differences were computed.

In both tables the retrievals of convective precipitation were noticeably less accurate, perhaps because the precipitation reaches the surface at locations displaced from the hydrometeors observed aloft. To partially test this hypothesis, the rms errors for convective precipitation after Gaussian smoothing to 30-km resolution were evaluated. It was found that the improvement was modest (~0-30 percent) suggesting that simple spatial displacements alone are not the main reason convective retrievals are less accurate. Alternate explanations include evaporation of hydrometeors, high time variability coupled with delays in reaching the ground, and the shielding effects of heavy cirrus spreading outward from strong convective cores. Since the snowfall retrievals evaluated in Table 7.10 and 7.11 assumed snow-free land surfaces, they would be achievable only if the surface effects are minimal due to atmospheric water vapor or opaque precipitation.

Table 7.12 is the same as Table 7.11, except that the classification of precipitation type is based on both the AMSU and MM5 data, as discussed in [1]. That is, pixels were classified as: 1) convective when the estimated 15-km resolution peak vertical wind exceeds 0.45 m/s and 2) stratiform when the wind is less than 0.45 m/s, 3) snow when the MM5 surface temperatures were below 266 K, 4) rain, when the MM5 surface temperature was above 294 K, or 5) warm rain when (a) T_B (183±7 GHz) ≥ 250 K, and (b) over 0.1-mm integrated rainwater was retrieved. Since convection is defined to have a strong vertical wind that is generally associated with large ice aloft and hence high surface precipitation rates, few convective pixels have estimated surface precipitation rates below 0.5 mm/h.

TABLE 7.12
RMS AND MEAN ERRORS (TRUTH – ESTIMATE) FOR 15-KM RESOLUTION SURFACE PRECIPITATION RATE RETRIEVALS (MM/H) USING MM5-SIMULATED T_B'S FOR AMSU, MM5 FOR GROUND-TRUTH, AND THE ESTIMATE ITSELF FOR DETERMINING THE RR RANGE, WHERE PRECIPITATION TYPE IS CLASSIFIED USING BOTH THE AMSU AND MM5 DATA AS IN [1], AND ONLY PRECIPITATING PIXELS ARE EVALUATED

RR Range (mm/h)	Convective		Stratiform		Snow Only		Rain Only		Warm rain	
	RMS Error	Mean Error	RMS Error	Mean Error	RMS Error	Mean Error	RMS Error	Mean Error	RMS Error	Mean Error
0-0.125	-	-	*0.52*	**0.10**	-	-	*0.79*	0.11	*1.56*	*0.80*
0.125-0.25	-	-	*0.73*	**0.12**	0.22	**-0.08**	*1.60*	*0.27*	*1.93*	*0.51*
0.25-0.5	-	-	*0.85*	**0.11**	0.30	-0.27	*1.51*	0.17	*1.18*	0.32
0.5-1	*2.33*	0.67	*1.06*	**0.06**	**0.41**	**-0.36**	*2.13*	**0.21**	*1.19*	**0.16**
1-2	*4.56*	**0.97**	1.65	**0.12**	-	-	*3.85*	**0.55**	1.68	**0.11**
2-4	*5.37*	**0.87**	2.81	**0.04**	-	-	*5.90*	**0.39**	2.87	**0.07**
4-8	7.24	**0.81**	4.43	**-0.06**	-	-	*8.39*	**0.97**	5.16	**0.09**
8-16	10.67	**0.77**	**6.24**	**-3.22**	-	-	12.17	**1.40**	8.77	**-2.05**
16-32	16.73	**1.22**	-	-	-	-	17.63	**1.49**	-	-
32-64	**23.17**	**-0.01**	-	-	-	-	**23.66**	**-0.19**	-	-
64	-	-	-	-	-	-	-	-	-	-

Italics: rms and mean errors that exceed the maximum value bounding the octave. Boldface: rms and mean errors less than the minimum for the octave.

Simulated 15-km resolution retrievals of hydrometeor water paths (mm) and peak vertical wind (m/s) are evaluated in Table 7.13 and illustrated in Figs. 7.11, 7.16, and 7.17. These multi-angle simulations generally exhibit accuracy comparable to earlier predictions for observations at nadir [2]. The indicated threshold of detectability is ~0.1 mm for all types of hydrometeors, and ~0.1 m/s for peak vertical wind. The slightly lower water path accuracies in any octave for rainwater (R) and cloud water (C) estimates are probably due to the generally lower altitudes and scattering signatures of liquid water.

Vertical wind retrievals have simulated rms accuracies σ as low as ~0.1 m/s for peak winds W_p less than ~0.25 m/s, and this sensitivity ratio $\sigma/W \cong 0.4$ is approximately preserved at all higher peak vertical wind speeds. This sensitivity is probably due to the responsiveness of AMSU to the size distributions of icy hydrometeors.

TABLE 7.13

RMS ERRORS FOR 15-KM RESOLUTION MM5-SIMULATED AMSU HYDROMETEOR WATER-PATH RETRIEVALS (MM) AND PEAK VERTICAL WIND (M/S) FOR BOTH LAND AND SEA; THE OCTAVE RANGES ARE BASED ON MM5

Range (mm)	R	S	G	RSG	C	I	W_p
0-0.125	0.07	0.05	0.05	0.09	0.07	0.09	0.07
0.125-0.25	0.19	**0.10**	0.22	**0.10**	**0.11**	**0.11**	**0.08**
0.25-0.5	0.29	**0.14**	0.33	**0.15**	**0.17**	**0.14**	**0.17**
0.5-1	**0.44**	**0.20**	0.59	**0.26**	**0.34**	**0.14**	**0.39**
1-2	**0.85**	**0.32**	1.01	**0.48**	**0.85**	**0.27**	**0.75**
2-4	**1.64**	**0.57**	**1.69**	**0.94**	**1.48**	**0.47**	**1.2**
4-8	**2.84**	**0.79**	**2.49**	**1.99**	-	**-**	**2.54**
8-16	**5.04**	**-**	**3.61**	**3.71**	-	**-**	**6.40**
16-32	**10.22**	**-**	**3.39**	**6.33**	-	-	
32-64	**-**	**-**	**5.68**	**7.61**	-	-	
64	-	-	-	-	-	-	

R, S, G, RSG, C, I, and W_p signify rainwater, snow, graupel, sum of rain, snow, and graupel, cloud liquid water, cloud ice, and peak vertical wind, respectively. Italics: rms errors exceed the maximum value bounding the octave. Boldface: rms errors less than the minimum for the octave

7.6 Comparison of precipitation rate retrievals from AMSU and AMSR-E

These retrieval algorithms were further tested by comparing their results for AMSU on NOAA-16 with retrievals obtained using the Advanced Microwave Scanning Radiometer for the Earth Observing System (AMSR-E) aboard the Aqua satellite. Two separate AMSR-E precipitation rate products were compared. One retrieval product is available over both land and sea and is based on the GSFC profiling algorithm [9]; it has 5.4-km spatial resolution and is designated AMSR-E#1. The other is available only over ocean [8], has 0.25-degree spatial resolution, and is designated AMSR-E#2. Neither product includes retrievals over snow or ice. The comparison was performed over all satellite orbits occurring on 36 different days from July 2002 to June 2003. These days include the 5th, 15th, and 25th of most months, where August 9th, September 21st, and November 14th replaced August 5th, September 5th, and November 15th, respectively, due to lack of AMSR-E data.

Fig. 7.18 exhibits good agreement between surface precipitation rate images retrieved from AMSU and AMSR-E for both land and sea, where AMSU observed the scene almost simultaneously with AMSR-E for Figs. 7.18(a) and 7.18(b), and roughly one hour after AMSR-E for Figs. 7.18(c)- 7.18(g). Fig. 7.18(a) and 7.18(b) were over Africa, 7.18(c) and 7.18(d) were over North America, and 7.18(e)-7.18(g) portray a typhoon over the western Pacific Ocean. In general AMSU/MM5 agrees better with AMSR-E#2 than with AMSR-E#1 because AMSR-E#1 tends to restrict the geographic extent of the precipitation to smaller cells.

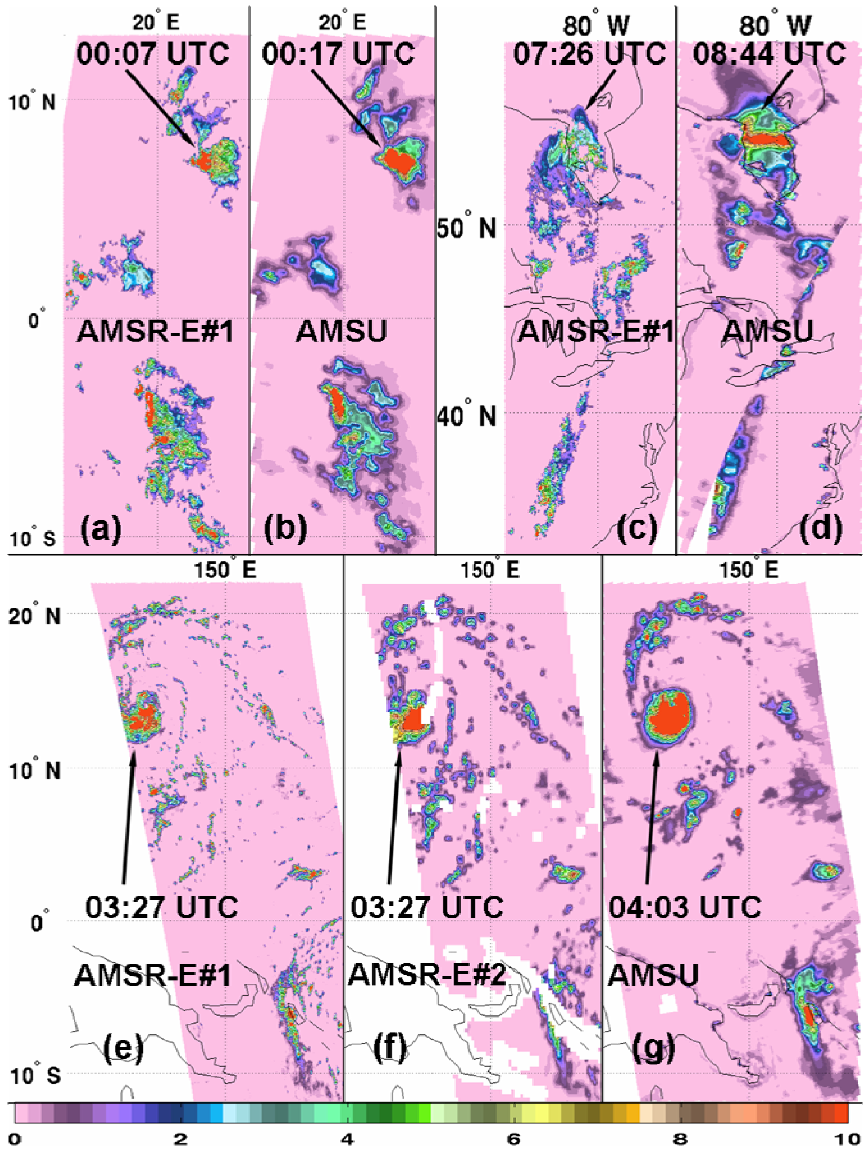

Fig. 7.18. Surface precipitation rates retrieved using: (a) AMSR-E#1 on September 22, 2002, (b) AMSU/MM5 on September 22, 2002, (c) AMSR-E#1 on September 21, 2002, (d) AMSU/MM5 on September 21, 2002, (e) AMSR-E#1 on July 5, 2002, (f) AMSR-E#2 on July 5, 2002, and (g) AMSU/MM5 on July 5, 2002. (a)-(d) are mostly over land and (e)-(g) are mostly over ocean.

Another comparison is illustrated in Fig. 7.19, which shows the cumulative distributions of surface precipitation rates estimated by AMSU/MM5 and AMSR-E over land and sea for the 36 days previously described. Since surface precipitation rates below 1 mm/h contribute very little to total surface AMSR-E#1 precipitation, the illustrated cumulative distributions for AMSU/MM5 and AMSR-E over land shown in Fig. 7.19(b) were computed using only pixels having estimated surface precipitation rates above 1 mm/h. For the comparison over ocean shown in Fig. 7.19(a), estimated surface precipitation rates lower than 0.3 were set to zero for AMSU/MM5, AMSR-E#1, and AMSR-E#2. The agreement between AMSU and AMSR-E is reasonably good over land, while the differences over ocean are more substantial. AMSU suggests perhaps ten percent of the total oceanic precipitation falls at rates above ~15 mm/h, while AMSR-E suggests almost none falls above that threshold despite its higher spatial resolution. Although AMSU further suggests that a much larger fraction of the precipitation falls at rates below 1 or 2 mm/h than does AMSR-E, this ratio could readily be altered by assuming all AMSU detections below some threshold, like 0.4 mm/h, are probably false detections that should be set to zero. An additional curve designated AMSU/MM5* is plotted under this assumption which results in better agreement for the 0.4-5 mm/h range.

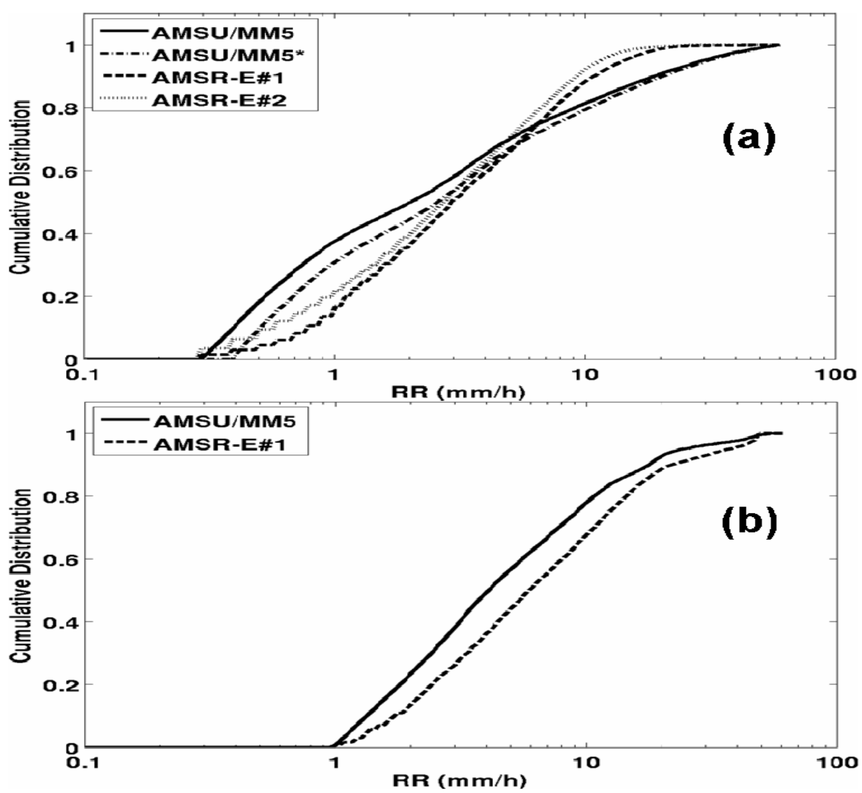

Fig. 7.19. Cumulative distributions of estimated surface precipitation rate as a function of surface precipitation rate: (a) over ocean, and (b) over land. Rates below 0.3 were set to zero for AMSU/MM5, AMSR-E#1, and AMSR-E#2 over ocean. Rates below 0.4 mm/h were set to zero for AMSU/MM5* over ocean. Rates below 1 mm/h were set to zero for AMSU/MM5 and AMSR-E#1 over land.

7.7 Summary and Conclusions

The MM5-based AMSU algorithms, AMSU/MM5, generally retrieved surface precipitation rates and hydrometeor water paths over both land and sea for most types of precipitation encountered globally. Both the AMSU land and sea algorithms first corrected the angle-dependent brightness temperatures to nadir. Then the less surface-dependent information in window channels was extracted using principal component analysis, and was found to be well correlated with surface precipitation rates. The final retrieval step used a neural network trained using 106 MM5 global storms distributed over a year, where each storm was consistent with simultaneously observed AMSU data. The same architecture was also used to retrieve peak vertical updraft wind and hydrometeor water paths for snow, graupel, rain water, cloud ice, and cloud water.

The AMSU-retrieved surface precipitation generally extends over a slightly larger area than does the MM5 ground-truth. This is consistent with heavy overhanging cirrus that extends beyond its convective core, and with hydrometeor evaporation that often appears to reduce surface precipitation rates by 30 percent or more. The AMSU estimates of precipitation-rate weighted distribution functions appear to be largely unbiased for stratiform precipitation, but to be biased about 20 percent low for convective systems. AMSU/MM5 and AMSR-E surface precipitation rate estimates were found to agree reasonably both over land and sea.

These AMSU-based algorithms could be extended to surfaces covered with snow or sea ice, and to high mountains. These cases are problematic, however, because the atmosphere is sometimes so dry that all or almost all microwave water vapor channels see the icy surface, which can scatter strongly and mimic the microwave spectrum of precipitation sufficiently that the retrieval algorithm can be confused. Snowfall rates over snow and ice are retrieved, however, if the atmosphere is sufficiently humid (see Fig. 7.15 AMSU retrievals over the Alps (top row) and over sea ice (fifth row). Another retrieval challenge involves better prediction of hydrometeor evaporation, which could be improved by assimilation schemes that utilize model data to predict such effects. Cloud resolving assimilation models might also predict to some degree the presence of cirrus overspreading, and thus reduce that significant source of error.

Chapter 8

Comparison of AMSU Surface Precipitation Rate Retrieval with Others over Land

All results in this chapter are from [5].

8.1 Abstract

This chapter compares surface precipitation rates retrieved using the Advanced Microwave Sounding Unit (AMSU) aboard the United States National Ocean and Atmospheric Administration NOAA-15 and -16 satellites with four similar products derived from other systems that also observed the United States Great Plains (USGP) during the summer of 2004. These systems include the Advanced Microwave Scanning Radiometer for the Earth Observing System (AMSR-E) aboard the Aqua satellite, the Special Sensor Microwave/Imager (SSM/I) aboard the Defense Meteorological Satellite Program (DMSP) F-13, -14, and -15 satellites, the passive Tropical Rainfall Measuring Mission (TRMM) Microwave Imager (TMI) aboard the TRMM satellite, and a surface precipitation rate product (NOWRAD), produced and marketed by Weather Services International Corporation (WSI) using observations from the Weather Surveillance Radar-1988 Doppler (WSR-88D) systems of the Next-Generation Weather Radar (NEXRAD) program.

AMSU surface precipitation rates were retrieved using the same neural network algorithm that was developed in Chapter 7 and was trained in two different ways, by using the MM5 physical model or NEXRAD radar data. Specifically, one set of neural networks, designated AMSU/MM5, was trained using precipitation predicted by a cloud-resolving version of the numerical weather prediction model MM5 for a global set of 106 storms, and the corresponding simulated AMSU radiances. The other set of neural networks, designated AMSU/NR, was trained using NOWRAD surface precipitation rate estimates and radiances observed within the same 15-minute period by AMSU for storms over the United States Great Plains during the summer of 2004. The least represented sensor, TMI, observed 1.6 million precipitating 5-km grid points, while the two AMSU sensors yielded over 15 million points. Observed correlation coefficients between $\log_{10}(X + 0.01)$ for NOWRAD surface precipitation rates X (mm/h) at 0.25-degree resolution and those for other sensors were, in declining order, 0.82, 0.79, 0.78, 0.71, and 0.68 for TMI, SSM/I, AMSU/NR, AMSR-E, and AMSU/MM5, respectively. Higher correlation coefficients were obtained when TMI was regarded as truth. In declining order they were 0.86, 0.83, 0.82, 0.80, and 0.78 for SSM/I, AMSU/NR, NOWRAD, AMSU/MM5, and AMSR-E, respectively. Other comparisons include false detection

statistics, rms and mean differences with respect to NOWRAD, precipitation rate distributions, and AMSU precipitation, snow, graupel, and water path retrievals relative to NOWRAD.

8.2 Introduction

Many polar orbiting passive microwave sensors observe global precipitation. One group is conically scanned with dual polarization and concentrates on "window" channels 6 - 90 GHz where the atmosphere is approximately transparent except for precipitation. Among these sensors are the Defense Meteorological System Program (DMSP) Special Sensor Microwave/Imager (SSM/I) [73], the National Aeronautics and Space Administration (NASA) Tropical Rainfall Measuring Mission (TRMM) Microwave Imager (TMI) [74], the NASA Advanced Microwave Scanning Radiometer-EOS (AMSR-E) [80], and the DMSP imaging sounder (SSM/IS). The principal parameter physically sensed at the longer wavelengths is the water path (mm) from which precipitation rates (mm/h) can be inferred; icy hydrometeors become more evident at frequencies above ~70 GHz and have a different precipitation signature.

A second group of microwave instruments also senses precipitation, although they were designed primarily for sounding atmospheric temperature and humidity profiles. These "sounding" sensors include, for example, the Advanced Microwave Sounding Unit (AMSU) flying on the National Ocean and Atmospheric Administration (NOAA) polar orbiting satellites NOAA-15, -16, -17, and -18 [23]-[24], and the planned successor to AMSU, the Advanced Technology Microwave Sounder (ATMS) [26]. Microwave sounders have also been proposed for use in geosynchronous orbit, permitting precipitation to be monitored at intervals as short as ~5-15 minutes [3].

This chapter compares surface precipitation rates retrieved from various microwave sensors, including AMSU [4], TMI [11], SSM/I [11], and AMSR-E [9], with a surface precipitation rate product, called NOWRAD [10], that is produced and marketed by Weather Services International Corporation (WSI) using observations from the Weather Surveillance Radar-1988 Doppler (WSR-88D) systems of the Next-Generation Weather Radar (NEXRAD) program. The comparison is performed in summer for land surfaces within the United States Great Plains (USGP) between 0000 UTC June 1 2004 and 2300 UTC August 31 2004, and within each distinct 15-minute period.

AMSU surface precipitation rates were retrieved using a neural network algorithm that was developed in Chapter 7 and was trained using either the MM5 physical model or NEXRAD radar data. As discussed later, the first set of neural networks, designated AMSU/MM5, was trained using precipitation predicted by a cloud-resolving version of the numerical weather prediction model MM5 for a global set of 106 storms, and the corresponding AMSU radiances computed using a variation of the radiative transfer model TBSCAT and a wavelength-dependent model for scattering by icy hydrometeors characterized by $F(\lambda)$. The second set of neural networks, designated AMSU/NR, was trained using NOWRAD surface precipitation rate estimates and radiances observed within the same 15-minute period by AMSU for storms over the United States Great Plains during the summer of 2004.

Section 8.3 describes the data sets used in the chapter, including: NOWRAD, AMSU/MM5, AMSU/NR, TMI, SSM/I, and AMSR-E. Section 8.4 defines the experiments, and Section 8.5 presents the comparisons, analyzes and discusses the results, and Section 8.6 summarizes and concludes the chapter.

8.3 Data Sets Used for Comparison

The microwave surface precipitation rate products compared in this chapter are based on two sets of algorithms. The TMI, SSM/I, AMSR-E surface precipitation rate products compared in this chapter utilize nearly the same algorithm, where the relations between surface precipitation rate and brightness temperatures at various window frequencies below 90 GHz were calibrated using co-located TRMM precipitation radar and TMI observations. The AMSU/MM5 and AMSU/NR products are based on a neural network method utilizing both window and opaque frequencies between 23 and 190 GHz. Both the opaque 54-GHz oxygen band and 183-GHz water vapor band frequencies were included.

8.3.1 NOWRAD

NOWRAD is a radar image product generated by Weather Services International (WSI) Corporation, Andover, Massachusetts, using observations from the United States Weather Surveillance Radar-1988 Doppler (WSR-88D) systems of the Next-Generation Weather Radar (NEXRAD) program [10]. This continuously available data set provides 15-minute cumulative rainfall estimates over the continental United States on a 2-km grid with a precision of 0.254 mm; the maximum allowed 15-minute cumulative rainfall is ~20 mm. The NOWRAD algorithm removes ground clutter, anomalous propagation, and other radar-induced artifacts to estimate the radar reflectivity (Z), which is then converted to instantaneous rain rate estimates and 15-minute precipitation accumulation estimates using proprietary Z-R relationships that depend on the season and NEXRAD site. The NOWRAD data used in this chapter was obtained from Atmospheric and Environmental Research (AER), Inc., of Lexington, Massachusetts.

For all analyses in this chapter the NOWRAD data was convolved with a Gaussian having full width at half maximum of 0.25 degrees in order to maximize the correlation between NOWRAD and all other sensors. Although a wide variety of other resolution assumptions could have been used, to provide consistency between all results presented here only one was employed, as discussed further in Section 8.4.

8.3.2 AMSU/MM5

AMSU is described in Section 2.8. The data used in this chapter were from NOAA-15 and -16. The AMSU/MM5 retrievals used the AMSU/MM5 algorithm developed in Chapter 7. Since the relationship between precipitation and observations is complex and nonlinear, this algorithm employs neural networks that were trained using a statistical ensemble of global precipitation and simulated observations for 106 global storms predicted by the MM5/TBSCAT/F(λ) model.

8.3.3 AMSU/NR

The AMSU/NR data set was retrieved from AMSU observations using the same AMSU/MM5 algorithm, except that the neural network shown in Fig. 7.8(b) was trained instead with AMSU observations and coincident NOWRAD surface precipitation rates observed over USGP from 0000 UTC June 1 2004 to 2300 UTC August 31 2004, as described in Section 8.3.1. The radar estimates were first convolved with a Gaussian having a FWHP width of 0.15 degrees, as discussed in Section 8.4. The training was based on a subsampled grid representing 17 percent of all USGP summer AMSU data. The AMSU brightness temperatures were generally matched to the nearest NOWRAD data field within ~±7 minutes. Since the training data was limited to the Midwestern United States, the conclusions could be regionally limited.

8.3.4 SSM/I

SSM/I is a conically scanning passive microwave radiometer aboard United States DMSP satellites. Table 8.1 lists the frequencies, polarizations, intermediate frequency (IF) passbands, and effective fields of view (EFOV) for SSM/I [73]. The retrieved data set used in this study is the Goddard Profiling Algorithm (GPROF) 6.0 Quarter-Degree Gridded Orbit-by-Orbit Precipitation Data Set. It currently contains most of the SSM/I data from November 1, 2001 through the present for SSM/I instruments aboard the DMSP F-13, -14, and -15 satellites. It presents the real-time orbit-by-orbit instantaneous rain rate on a 0.25×0.25 degree latitude/longitude grid and is available from NASA GSFC DAAC at: http://disc.gsfc.nasa.gov/data/datapool/TRMM_DP/01_Data_Products/06_Ancillary/02_GPROF6/index.html. The land portion of the algorithm was upgraded in February 2004 to SSM/I version 7. This algorithm is equivalent to the TMI profiling algorithm version 6 [11] with some modification to account for the lack of the lowest TMI frequency and the substantially reduced spatial resolution. As in the case of TMI, the algorithm estimates only liquid precipitation over unfrozen surfaces.

TABLE 8.1
CHARACTERISTICS OF SSM/I

Center Frequency (GHz)	Polarization	IF Passband (MHz)	EFOV (km × km) Cross-track × along-track
19.35	Dual	10-250	43×69
22.235	Vertical	10-250	40×60
37.0	Dual	100-1000	37×29
85.5	Dual	100-1500	15×13

8.3.5 TMI

TMI is aboard the TRMM satellite, and differs from SSM/I in four main ways: 1) a pair of 10.7-GHz channels with horizontal and vertical polarization was added to TMI, 2) the water vapor channel was moved from 22.235 to 21.3 GHz in order to reduce saturation in the tropics and provide more uniform sensitivity to water vapor with respect to altitude, 3) a larger antenna and the lower orbit of the TRMM satellite provides more than twice the spatial resolution of SSM/I, and 4) the concurrent flight of the TRMM Precipitation Radar (PR) permits direct calibration of TMI. The TRMM satellite observes latitudes between 38°S and 38°N. Table 8.2 lists the frequencies, polarizations, bandwidths, and effective fields of view (EFOV) for TMI [74]. The data set used in this study is the TMI Level-2 Hydrometeor Profile Product (2A12 product in TRMM nomenclature), which provides rainfall rates, the vertical structure of hydrometeors, and the latent heating based upon the nine channels of TMI. It has a grid spacing of 5.1 km with a precision of 0.1 mm/hr, and is available from NASA GSFC DAAC at: http://disc.sci.gsfc.nasa.gov/data/datapool/TRMM/01_Data_Products/01_Orbital/05_Tmi_Prof_2A_12/. The land portion of this data set is produced using the version-6 TMI profiling algorithm [11], which supersedes version 5 [81]. The algorithm was calibrated using co-located TMI and TRMM PR observations over Africa and South America during October and November, 2000. The algorithm estimates only liquid precipitation over unfrozen surfaces.

TABLE 8.2
CHARACTERISTICS OF TMI

Center Frequency (GHz)	Polarization	Bandwidth (MHz)	EFOV (km × km) Cross-track × along-track
10.65	Dual	100	63×37
19.35	Dual	500	30×18
21.3	Vertical	200	23×18
37.0	Dual	2000	16×9
85.5	Dual	3000	7×5

8.3.6 AMSR-E

AMSR-E is a conically scanning passive microwave radiometer aboard the NASA Aqua satellite. Table 8.3 lists its frequencies, bandwidths, and instantaneous fields of view (IFOV) [80]. The AMSR-E surface precipitation rate product used in this chapter is the AMSR-E/Aqua L2B Global Swath RainRate/Type Goddard Space Flight Center (GSFC) Profiling Algorithm V001 [9]. This data set covers all ice-free and snow-free land and ocean between 70°N and 70°S at 5.4-km gridded resolution. The data set is available at: http://nsidc.org/data/amsre/order.html. The architecture of the land portion of the algorithm is nearly identical to that of the TMI profiling algorithm, version 6 [9]. As in the cases of TMI and SSM/I, the algorithm estimates only liquid precipitation over unfrozen surfaces.

TABLE 8.3
CHARACTERISTICS OF AMSR-E

Center Frequency (GHz)	Polarization	Bandwidth (MHz)	IFOV (km × km) Cross-track × along-track
6.925	Dual	350	43×75
10.65	Dual	100	29×51
18.7	Dual	200	16×27
23.8	Dual	400	18×32
36.5	Dual	1000	8.2×14
89.0(A)	Dual	3000	3.7×6.5
89.0(B)	Dual	3000	3.5×5.9

8.4 Experiment Definition

The surface precipitation rate estimates of NOWRAD, AMSU/MM5, AMSU/NOWRAD, AMSR-E, SSM/I, and TMI were made over the United States Great Plains (USGP), which follows United States Geological Survey hydrological unit boundaries and is the region in Fig. 8.1 bounded by the solid line. This region is located between 25.85°N-49.01°N and 114.07°W-90.12°W. The comparison was performed only over land. Since none of the precipitation rate retrieval algorithms compared here work over snow or ice covered surfaces, the time interval used for comparison was from 0000 UTC June 1, 2004 to 2300 UTC August 31, 2004, which typically has no snow on the ground. All data were interpolated to the same 0.05° latitude/longitude grid and binned into 15-minute intervals bounded by 00, 15, 30, and 45 minutes. For example, all data observed between 08:15 and 08:30 were binned to 08:30. Although NOWRAD data is continuous, its overlap with microwave satellites is intermittent and depends on their orbits. Table 8.4 lists the numbers of 15-minute periods and precipitating 0.05° pixels for which NOWRAD overlaps the various types of microwave data, where a pixel is defined as precipitating if any instrument estimates a surface precipitation rate greater than 0.01 mm/h. Note that the overlap is extensive except for SSM/I vs. AMSR-E, which were never simultaneous.

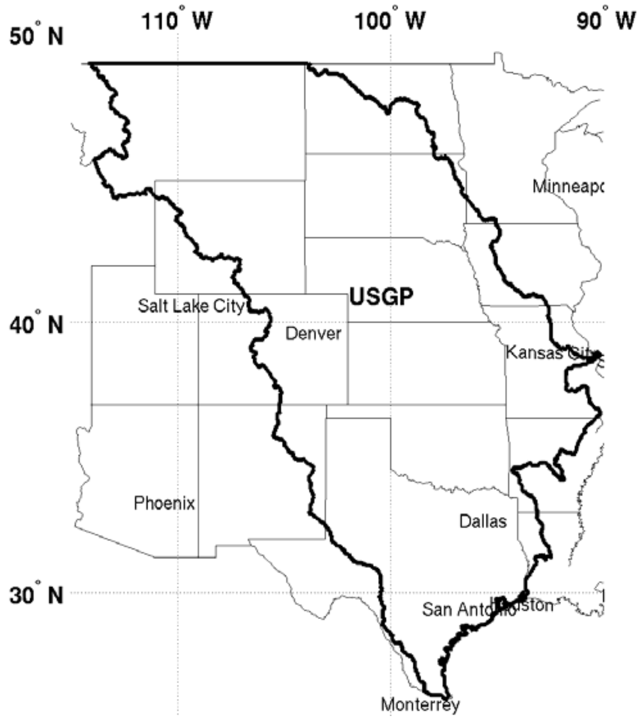

Fig. 8.1. The United States Great Plains (USGP), which is the region inside the solid line.

TABLE 8.4

NUMBERS OF OVERLAPPING VIEWS AND PRECIPITATING 0.05° PIXELS

Data set	Number of overlapping 15-minute periods	Number of precipitating 5-km pixels (millions)
AMSU/MM5 & NOWRAD	672	22.9
AMSU/NOWRAD & NOWRAD	668	15.3
AMSR-E & NOWRAD	384	2.3
SSM/I & NOWRAD	900	5.1
TMI & NOWRAD	425	1.6
AMSU & AMSR-E & NOWRAD	35	0.64
AMSU & SSM/I & NOWRAD	86	1.7
AMSU & TMI & NOWRAD	22	0.24
AMSR-E & SSM/I & NOWRAD	0	0
AMSR-E & TMI & NOWRAD	10	0.017
SSM/I & TMI & NOWRAD	23	0.041

Since different channels and instruments have different antenna beamwidths, the effective spatial resolution of the instruments varies. It was found that blurring the 0.05°

NOWRAD retrievals with Gaussian filters improves its correlation with the various precipitation rate retrievals. The optimum filter Full Width at Half Maximum (FWHM) depends on the retrieval algorithm and whether the correlation coefficient is computed directly between the surface precipitation rates, which emphasizes the higher rates and convective events, or between the logarithms of those rates so that accuracies at all rates are treated more equally. Overemphasis of low rates is limited by adding 0.01 mm/h before computing the logarithm. Both types of correlation coefficients are listed in Table 8.5 as a function of NOWRAD spatial resolution. For all algorithms the precipitation rate correlation coefficient exhibits a broad maximum for Gaussian FWHM blurring between 0.15 and 0.4 degrees, with a maximum near 0.35 degrees, whereas using the logarithm yields an even higher correlation coefficient that generally peaks near 0.3 degrees for SSM/I and 0.15 degrees for the other algorithms. To simplify all further comparisons in this chapter only one NOWRAD resolution is employed, 0.25 degrees, which is a compromise across all cases evaluated in Table 8.5. Similar tables could be constructed using blurred data from other instruments as the baseline. Comparisons of retrievals using other possible combinations of blurring are left to future papers.

TABLE 8.5
CORRELATION COEFFICIENTS BETWEEN SATELLITE AND NOWRAD PRECIPITATION RATE ESTIMATES AS A FUNCTION OF NOWRAD SPATIAL RESOLUTION, WHERE THE SECOND ENTRY IS THE CORRELATION COEFFICIENT FOR $\mathrm{LOG}_{10}(\mathrm{Y}+0.01)$

NOWRAD Resolution	TMI	SSM/I	AMSR-E	AMSU/NR	AMSU/MM5
0.05°	0.64; 0.78	0.56; 0.66	0.51; 0.67	0.60; 0.67	0.51; 0.64
0.1°	0.69; 0.83	0.62; 0.74	0.58; 0.72	0.66; 0.75	0.57; 0.68
0.15°	0.76; 0.84	0.68; 0.77	0.62; 0.72	0.72; 0.78	0.63; 0.69
0.20°	0.75; 0.82	0.70; 0.77	0.64; 0.71	0.74; 0.78	0.64; 0.68
0.25°	0.79; 0.82	0.74; 0.79	0.66; 0.71	0.78; 0.78	0.68; 0.68
0.3°	0.77; 0.80	0.75; 0.78	0.67; 0.69	0.78; 0.77	0.68; 0.67
0.35°	0.79; 0.79	0.78; 0.79	0.67; 0.68	0.81; 0.77	0.70; 0.67
0.4°	0.76; 0.77	0.77; 0.78	0.66; 0.67	0.81; 0.76	0.70; 0.65

8.5 Results

Fig. 8.2 illustrates the generally good agreement between NOWRAD, AMSR-E, and TMI precipitation imagery on two occasions, each of 15-minute duration. The few discrepancies result from the 0.25-degree blurring of the NOWRAD data and the tendency of the AMSR-E and TMI retrievals to miss some smaller cells in the second storm. There is also a factor-of-two discrepancy in the northern half of the northern event in the first storm, and similar factor-of-two discrepancies can be found elsewhere in small features that may be due to time-offset or resolution differences.

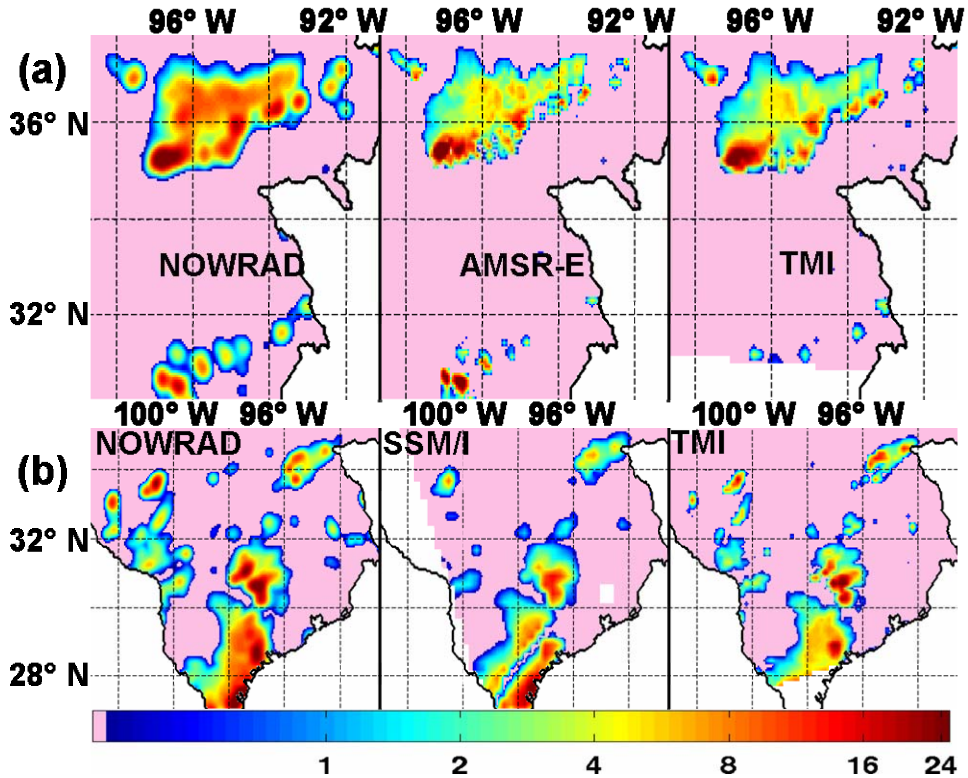

Fig. 8.2. Comparison of retrieved surface precipitation rates: (a) 1930 UTC 9 July 2004, (b) 0030 UTC 26 June 2004. White areas are either outside the USGP or indicate unavailable retrievals. Latitude and longitude are plotted every two degrees.

Fig. 8.3 illustrates similar comparisons between NOWRAD and AMSU for three other storms for which AMSR-E, SSM/I, or TMI data were also available. The agreement within all sets of four retrievals is again quite good, with the main discrepancies being due to the reduced spatial resolution of AMSU, and the occasional tendency of the conical scanners to miss some of the smallest precipitation events. There is also the tendency of AMSR-E and TMI to exhibit slightly smaller areas of precipitation relative to NOWRAD, even after allowance for differences in spatial resolution. A possible explanation for this is offered later in the context of Table XII. The reduced resolution of AMSU in Fig. 8.3(a) and (b) is partly due to the location of the storms near the edge of the swath. Better resolution is exhibited in Fig. 8.3(c), which lies closer to nadir. AMSU resolution can be significantly improved by sharpening to ~15-km resolution the graupel-sensitive 50-km resolution 50-GHz band data using methods demonstrated successfully earlier in other comparisons of AMSU precipitation retrievals with NEXRAD data [34]. This step was not employed in this chapter because slightly larger correlation coefficients between MM5 truth and simulated retrievals were obtained by not sharpening the brightness temperature images; numerical metrics are the main focus of this chapter.

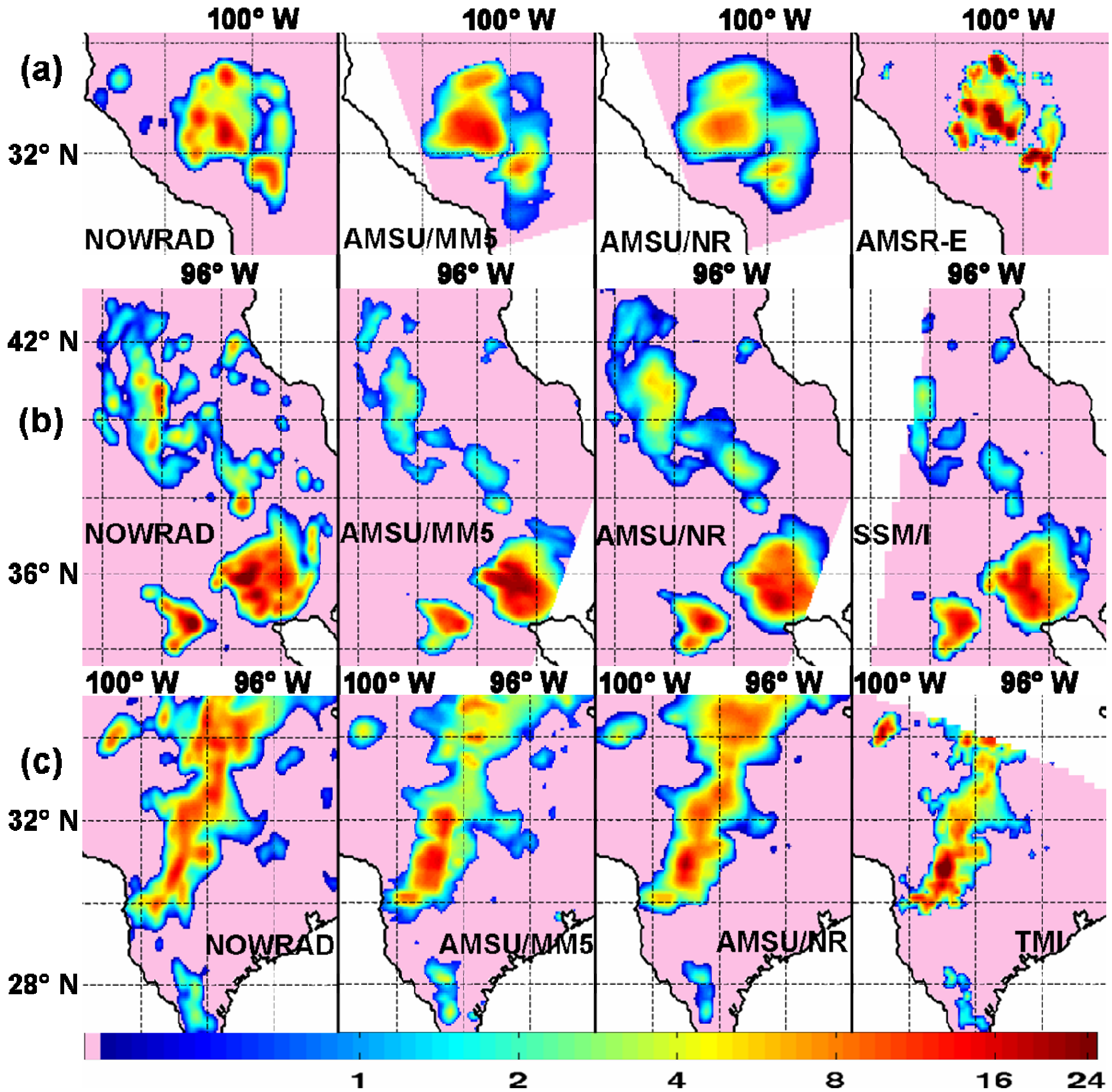

Fig. 8.3. Comparison of retrieved surface precipitation rates over USGP: (a) 2015 UTC 18 August 2004; (b) 1400 UTC 2 July 2004; and (c) 1300 UTC 9 June 2004. White areas are either outside the USGP or indicate unavailable retrievals. Latitude and longitude are plotted every two degrees.

Table 8.6 presents the surface-precipitation-rate-retrieval correlation coefficients for all pairs of retrieval algorithms. In order to avoid overemphasis of the highest precipitation rates, the correlation coefficients are computed for the logarithms of the precipitation rates (base 10); 0.01 mm/h is added before computing the logarithm to avoid overemphasis of the smallest rates. All AMSU/MM5 retrievals below 0.5 mm/h, and all AMSU/NR retrievals below 0.3 mm/h were set to zero in order to maximize these correlation coefficients. The upper and lower triangles in Table 8.6 present the correlation coefficients for $\log_{10}(0.01 + X)$ and X, respectively, where the latter corresponds more to the heavier rain.

In the upper triangle, representing all precipitation rates, the three strongest correlation coefficients involve TMI versus SSM/I, AMSU/NR, and NOWRAD, in that declining order. At the higher precipitation rates (lower triangle) the three highest correlation coefficients link AMSU and SSM/I. The lowest correlation coefficients link AMSR-E and AMSU for all precipitation rates. Since correlation coefficients do not unambiguously reveal absolute or relative performance of sensors in the absence of a calibration standard, the coefficients in Table 8.6 merely indicate in a more quantitative way that the precipitation retrievals for all algorithms are in reasonable agreement, as was evident in Figs. 8.2 and 8.3. If one regards TMI as an approximate calibration standard, then the log metrics for all other instruments are correlated with it at levels above 0.78 in the declining sequence: SSM/I, AMSU/NR, NOWRAD, AMSU/MM5, and AMSR-E. No other algorithm used as a calibration standard yields such a high minimum correlation coefficient. Since the algorithms for all instruments continue to evolve and improve, these results should be encouraging.

TABLE 8.6

CORRELATION COEFFICIENTS BETWEEN ALTERNATIVE PRECIPITATION RATE RETRIEVALS

Instrument	TMI	SSM/I	NOWRAD	AMSR-E	AMSU/NR	AMSU/MM5
TMI	-	0.86	0.82	0.78	0.83	0.80
SSM/I	0.82	-	0.79	-	0.83	0.76
NOWRAD	0.79	0.74	-	0.71	0.78	0.68
AMSR-E	0.64	-	0.66	-	0.68	0.67
AMSU/NR	0.78	0.88	0.78	0.62	-	0.73
AMSU/MM5	0.77	0.83	0.68	0.60	0.85	-

The upper triangle is the correlation coefficient for the metric $\log_{10}(x+0.01)$ and the lower triangle is the correlation coefficient for x (mm/h).

Another metric of interest is the frequency of false precipitation detection for all pairs of retrieval algorithms, which is presented in Table 8.7. False detection is defined here as occurring when the reference estimate (indicated by row headings) is less than 0.3 mm/h while the other estimate (indicated by column headings) is more. Thus for each pair of instruments there are two false detection rates, depending on which instrument is the reference. For this metric, no lower thresholds were used for AMSU retrievals. The inter-comparisons of the algorithms for the conically scanning TMI, SSM/I, and AMSR-E generally exhibit false detection percentages below one percent, except for AMSR-E, which exhibits 1.59 percent relative to TMI truth. When TMI is the reference, the false detection rates are 2.63, 3.33, and 3.73 percent for AMSU/NR, NOWRAD, and AMSU/MM5, respectively. The images in Figs. 8.2 and 8.3, and other images, suggest that the great majority of these "false detections" are contiguous with legitimate precipitation and presumably correspond either to drizzle that the reference missed, or to evaporating precipitation or heavy cirrus aloft that resembles surface precipitation. If we weight these false detections by their associated precipitation rates, they contribute even less to the total precipitation budget. No study has yet been made of false detections that are not contiguous with legitimate precipitation or in its immediate vicinity.

TABLE 8.7

PERCENTAGES OF FALSE DETECTIONS BETWEEN PAIRS OF PRECIPITATION RATE RETRIEVAL ALGORITHMS

Instrument	TMI	SSM/I	NOWRAD	AMSR-E	AMSU/NR	AMSU/MM5
TMI	-	0.81	3.33	0.63	2.63	3.73
SSM/I	0.56	-	2.43	-	3.54	7.70
NOWRAD	0.44	1.53	-	0.77	3.29	6.11
AMSR-E	1.59	-	3.70	-	6.30	7.16
AMSU/NR	0.53	0.56	1.77	0.37	-	4.06
AMSU/MM5	0.63	0.60	2.04	0.61	1.56	-

The percentages of false detections over 0.3 mm/h are for the algorithms heading the columns when the algorithms heading the rows are regarded as truth and yield less than 0.3 mm/h.

Another common performance metric for algorithms involves comparison with doppler radar data. Table 8.8 presents the rms deviation, mean, and standard deviation between the 0.25-degree NOWRAD data (mm/h) and each algorithm output Y as a function of NOWRAD precipitation rate, divided into octaves, and Table 8.9 presents the same statistical parameters for octaves of the precipitation rate Y.

TABLE 8.8

RMS, MEAN, AND STANDARD DIFFERENCES BETWEEN 0.25-DEGREE BLURRED NOWRAD PRECIPITATION RATE RETRIEVALS AND ALGORITHM X, FOR OCTAVES OF NOWRAD PRECIPITATION RATES

Range (mm/h)		0.125-0.25	0.25-0.5	0.5-1	1-2	2-4	4-8	8-16	16-32	32-64
	A/M	*1.19*	*1.46*	*1.83*	*2.50*	3.51	4.96	**7.12**	**10.9**	**17.3**
	A/N	*0.68*	*0.85*	*1.12*	1.54	2.14	**3.19**	**5.80**	**12.0**	**21.4**
RMS	A-E	*0.69*	*1.03*	*1.53*	*2.27*	3.37	5.01	8.11	**13.9**	**26.8**
	SMMI	*0.75*	*0.97*	*1.32*	1.92	2.71	**3.70**	**5.74**	**11.2**	**24.9**
	TMI	*0.44*	*0.68*	*1.07*	1.76	2.79	4.23	**6.83**	**10.3**	**18.6**
	A/M	-0.10	-0.07	-0.04	0.01	0.32	1.17	3.13	6.29	13.8
	A/N	-0.16	-0.17	-0.17	-0.10	0.32	1.43	4.38	10.8	20.7
Mean	A-E	-0.01	0.01	0.04	0.12	0.41	1.26	2.96	6.56	20.3
	SSMI	-0.10	-0.07	-0.01	0.06	0.34	1.36	3.91	9.67	24.0
	TMI	0.07	0.14	0.23	0.31	0.48	0.98	1.82	2.69	13.2
	A/M	*1.19*	*1.46*	*1.83*	*2.50*	3.50	4.82	**6.40**	**8.90**	**10.6**
	A/N	*0.66*	*0.83*	*1.11*	1.53	2.12	**2.85**	**3.80**	**5.27**	**5.50**
SDev	A-E	*0.69*	*1.03*	*1.53*	*2.27*	3.35	4.84	**7.54**	**12.3**	**17.6**
	SMMI	*0.74*	*0.96*	*1.32*	1.92	2.68	**3.45**	**4.21**	**5.67**	**6.74**
	TMI	*0.44*	*0.66*	*1.05*	1.73	2.74	4.11	**6.59**	**9.94**	**13.0**

Abbreviations: Mean is E[X - NOWRAD], SDev is the standard deviation of [X - NOWRAD], A/M is AMSU/MM5, A/N is AMSU/NR, and A-E is AMSR-E

TABLE 8.9

RMS, MEAN, AND STANDARD DIFFERENCES BETWEEN 0.25-DEGREE BLURRED NOWRAD PRECIPITATION RATE RETRIEVALS AND ALGORITHM X, FOR OCTAVES OF X PRECIPITATION RATES

Range (mm)		0.125-0.25	0.25-0.5	0.5-1	1-2	2-4	4-8	8-16	16-32	32-64
	A/M	-	-	*1.32*	*2.19*	3.28	4.47	**7.16**	**12.4**	**28.7**
	A/N	-	*0.78*	*1.15*	1.78	2.81	4.31	**6.22**	**9.40**	-
RMS	A-E	*1.23*	*1.50*	*1.79*	*2.08*	2.94	4.22	**6.84**	**13.5**	**26.7**
	SMMI	*0.77*	*1.07*	*1.46*	*2.10*	3.15	4.34	**6.59**	**9.65**	**13.2**
	TMI	*1.19*	*1.53*	*1.84*	*2.19*	2.95	**3.83**	**5.64**	**11.0**	**20.9**
	A/M	-	-	0.03	0.34	0.63	-0.49	-3.51	-9.11	-26.1
	A/N	-	-0.02	0.02	0.02	0.07	0.29	-0.02	-1.29	-
Mean	A-E	0.47	0.55	0.51	0.32	0.13	-0.24	-3.32	-10.6	-24.8
	SMMI	0.18	0.25	0.33	0.48	0.48	-0.38	-2.07	-5.79	-11.9
	TMI	0.62	0.79	0.87	0.88	1.05	0.60	-1.81	-8.09	-19.2
	A/M	-	-	*1.32*	*2.16*	3.21	4.45	**6.24**	**8.34**	**12.0**
	A/N	-	*0.78*	*1.15*	1.78	2.81	4.30	**6.22**	**9.31**	-
SDev	A-E	*1.13*	*1.40*	*1.71*	*2.05*	2.94	4.21	**5.99**	**8.36**	**9.93**
	SMMI	*0.75*	*1.04*	*1.42*	*2.05*	3.11	4.33	**6.25**	**7.72**	**5.72**
	TMI	*1.01*	*1.31*	*1.62*	*2.01*	2.76	**3.78**	**5.34**	**7.46**	**8.17**

Abbreviations: Mean is E[X - NOWRAD], SDev is the standard deviation of [X - NOWRAD], A/M is AMSU/MM5, A/N is AMSU/NR, and A-E is AMSR-E

The sensitivities of these methods to low precipitation rates can be very roughly estimated using the smallest standard deviation, which is 0.44 mm/h for TMI vs. NOWRAD in Table 8.8. These standard deviations would equal the geometric sum of the standard deviations associated with each instrument separately if those deviations were uncorrelated. High correlation is not expected since the TMI retrievals are sensitive primarily to absorption by hydrometeors, and NOWRAD is sensitive instead to scattering. It is therefore reasonable to suppose that random surface and humidity effects probably contribute less than ~0.4 mm/h rms to TMI retrievals. The corresponding upper bounds deduced from the table for other retrieval methods are larger but potentially too pessimistic if those other methods are merely more sensitive to light precipitation than is NOWRAD, which is entirely possible for AMSU retrievals utilizing frequencies above 140 GHz.

Table 8.8 also suggests that, relative to NOWRAD, TMI offers the most accurate retrieval algorithm for NOWRAD rates below 1 mm/h and 16-32 mm/h, and that AMSU/NR is slightly superior between 1 and 16 mm/h. The mean errors in the table are less than 10-15 percent of the rms errors for rates below ~4 mm/h, but rise to approximate the standard deviation for rates of 8-12 mm/h. The standard deviation is least for AMSU/NR for all rates above 1 mm/h. The results in Table 8.9 are somewhat different, for AMSU/NR provides the lowest rms errors below 4 mm/h and at 16-32 mm/h, whereas TMI is superior 3-16 mm/h, approximately the reverse of the ranking obtained from Table 8.8. Also, when the octaves are defined by the sensor of interest rather than by NOWRAD, the mean errors remain less than ~ten percent for rates below ~8 mm/h. As expected, AMSU/NR offers the smallest mean errors in Table 8.9 because its neural networks were trained against a portion of the same USGP data set. These mean errors at the higher precipitation rates are all highly negative because the strong convective cores of storms can yield surface precipitation at times and places removed from the peaks in graupel and snow aloft that mark the tops of strong cells. To minimize rms error the estimators therefore tend to bias their estimates low in regions where such strong cores could be easily missed due to time and/or spatial offsets.

Yet another way to characterize retrieval algorithms is by their precipitation-rate distribution functions for a standard set of storms. Although not all instruments in this experiment viewed the same pixels simultaneously, all observed many summer storms (see Table 8.4) under sufficiently similar geographic and meteorological conditions that the comparison should be informative. Fig. 8.4 presents as a function of the surface precipitation rate estimate (RR) the weighted histograms of RR for the various retrieval algorithms. The histogram employs rain rate bins of equal size in the logarithm of RR, and therefore even though the logarithmic scale shrinks the width of the bin, its height is correspondingly increased, so equal areas of the histogram correspond to equal numbers of events. This histogram is then weighted by the corresponding RR, yielding a precipitation rate distribution function where equal areas correspond to equal precipitation, as shown in Fig. 8.4. Thus Fig. 8.4 suggests that for all algorithms about half of all precipitation falls at rates below ~8 mm/h, and half above. The final step is to normalize the areas of all weighted histograms so they are equal; this helps compensate for the different numbers of pixels viewed by each sensor.

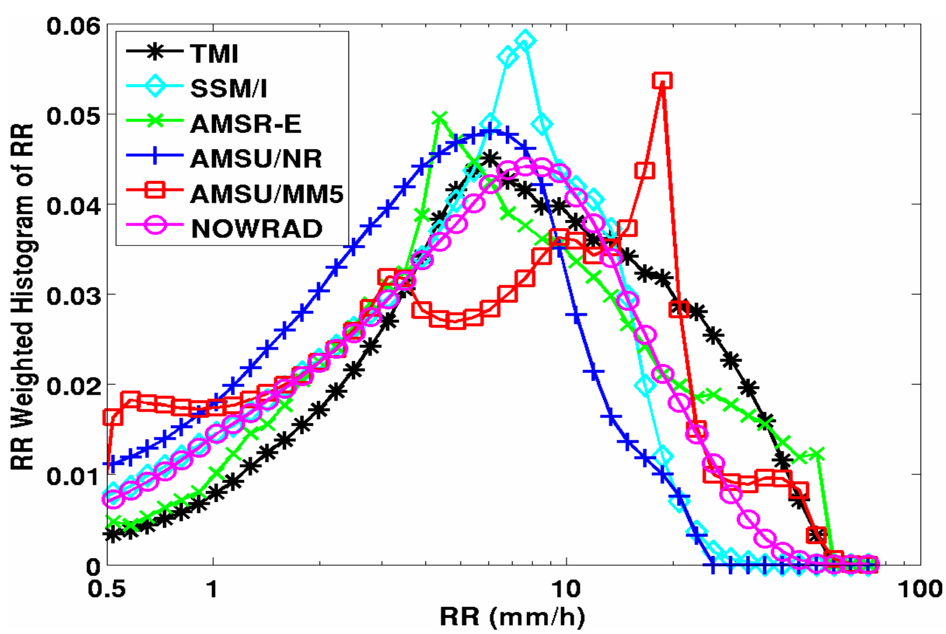

Fig. 8.4. Surface precipitation rate (RR) distributions for six retrieval algorithms. The RR histograms were weighted by RR so that total precipitation falling at various rates is proportional to the associated area under the curve.

It is not surprising that the two high-spatial-resolution instruments, TMI and AMSR-E, are the only ones in Fig. 8.4 with more than one percent of the precipitation falling at rates above ~40 mm/h, and that SSM/I with its poorer spatial resolution reports little precipitation above 20 mm/h. It is currently unclear, however, why the two AMSU algorithms respond differently to precipitation above 20 mm/h, and why NOWRAD with 0.25-degree blurring responds more strongly to high rates than does AMSU/NR, which was trained using NOWRAD data. One contributing possibility is that since the highest NOWRAD precipitation rates are not perfectly concurrent with peaks sensed by AMSU, AMSU retrievals should be biased lower. Also, the two AMSU algorithms report the most precipitation at rates below 1 mm/h, presumably because they utilize frequencies above 140 GHz that are sensitive to the smallest icy hydrometeors. Whether this difference below one mm/h corresponds to actual precipitation reaching the ground or merely to hydrometeors aloft cannot be determined here.

The steep character of the SSM/I distribution near 15 mm/h, of the AMSU/NR distribution near 12 mm/h, and the AMSU/MM5 distribution near 30 mm/h are apparently due largely to the loss of sensitivity at higher precipitation rates because of limited spatial resolution. This steepness is enhanced when these potentially higher estimates are shifted to lower estimates by being blurred across a larger set of adjacent pixels, thus also producing the observed excesses relative to NOWRAD, TMI, and AMSR-E in the 5-30 mm/h range. Similarly, the increased sensitivity of AMSU/MM5 to rates below 3 mm/h is balanced by decreased rates 3-10 mm/h. The somewhat reduced sensitivity of AMSU to high precipitation rates can be largely remedied by sharpening the 50-GHz band AMSU data, as demonstrated relative to NEXRAD in [34].

Tests were performed to determine the origins of the fluctuations in the AMSU/MM5 distribution. By using not just the best set of neural networks relative to the training data, but the best three sets in parallel and averaging the resulting estimates, the distribution curve was smoothed somewhat, suggesting that these neural networks are operating near their stability limit. Each set of neural networks yielded slightly different small uncorrelated fluctuations in the distribution curve, and therefore such distribution functions provide sensitive detectors for neural network anomalies.

Finally, it is interesting to see the relationship between retrieved hydrometeor water-paths and surface precipitation rates. Fig. 8.5 for two storms shows images of water paths for snow (S), graupel (G), rainwater (R), and the sum (S + G + R) retrieved using the same AMSU/MM5 algorithm used here, but trained using MM5 to estimate water paths instead [4]. The distinction between the spatial distributions of graupel and other hydrometeors is evident in both storms. Rainwater distributions generally resemble the surface precipitation rate, while graupel covers the smallest areas at locations of higher rain rate, and snow generally extends beyond the rainwater zone. Although the distinction between snow and rainwater morphology is not strong for these cases, it is sometimes more so in other images [4].

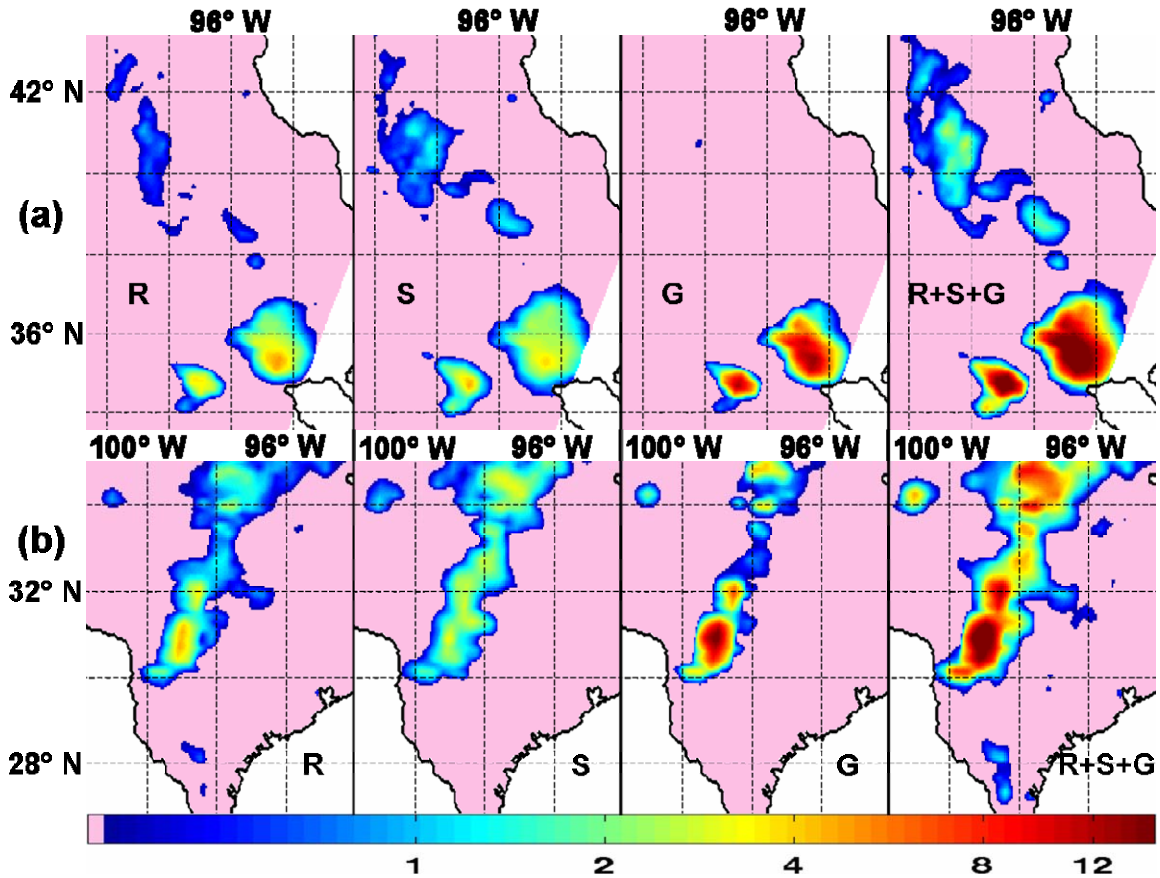

Fig. 8.5. Retrieved AMSU/MM5 water-paths for rain water (R), snow (S), graupel (G), and the sum of rain water, snow, and graupel (R+S+G) over USGP: (a) 1400 UTC 2 July 2004; and (b) 1300 UTC 9 June 2004, corresponding to Figs. 8.3(b) and 8.3(c), respectively. Latitude and longitude are plotted every two degrees.

A more quantitative analysis of water path retrievals and their relation to NOWRAD USGP precipitation estimates is presented in Table 8.10 where the first column lists the MM5-simulated correlation coefficients between surface precipitation rate and the water paths for rainwater R, snow S, graupel G, and the sum R + S + G. These simulations were computed for the same set of 122 storms cited earlier. Two types of correlation coefficient are given; the first listed in each box correlates the two parameters of interest and the second correlates their logarithms, $\log_{10}[X(\mathrm{mm}) + 0.01]$, which better indicates the correlation for smaller water paths. These correlation coefficients are greatest for rainwater and graupel, and least for snow. The correlation coefficient for snow is only 0.46 for stronger precipitation, but 0.68 when the logarithm increases the role of lighter precipitation. The AMSU/MM5 surface precipitation rate estimates respond most strongly to the AMSU/MM5 estimates of rainwater and graupel, as shown by the high correlation coefficients in the second column, but also fairly strongly to snow. The third column of the table shows that NOWRAD surface precipitation estimates rely even more heavily upon snow than does AMSU/MM5, and in fact the observed NOWRAD logarithmic correlation coefficients over USGP are higher for AMSU/MM5 snow than for either graupel or rainwater. The wider separation of NEXRAD stations over the

USGP than in the eastern United States encourages increased reliance upon hydrometeors at higher altitudes, and therefore upon snow, as suggested by Table 8.10.

TABLE 8.10
CORRELATION COEFFICIENTS BETWEEN AMSU/MM5 OR MM5 HYDROMETEOR WATER-PATH FOR X AND NOWRAD OR AMSU/MM5 SURFACE PRECIPITATION RATE RETRIEVALS OR MM5 SURFACE PRECIPITATION RATES, WHERE THE 1ST NUMBER IS CORRCOEF(X,Y) AND THE 2ND NUMBER IS CORRCOEF(LOG_{10}(X+0.01), LOG_{10}(Y+0.01))

X	MM5 X and MM5 RR	AMSU/MM5 X and AMSU/MM5 RR	AMSU/MM5 X and NOWRAD
R	0.93; 0.90	0.91; 0.84	0.72; 0.67
S	0.46; 0.68	0.72; 0.75	0.71; 0.72
G	0.72; 0.71	0.88; 0.78	0.60; 0.61
R+S+G	0.84; 0.78	0.92; 0.85	0.69; 0.74

R: rain water, S: snow, and G: graupel water paths, respectively.

8.6 Summary and Conclusions

The USGP is an important well monitored hydrological area, and studies of its hydrological behavior are useful for agriculture and as a testbed for hydrological models. This chapter compares several microwave systems for remotely sensing precipitation and finds sufficient agreement in Figs. 8.2 and 8.3 and Tables 8.5 – 8.9 that their precipitation data can be combined over the summertime USGP with modest adjustments, particularly if ~25-km spatial resolution suffices.

Improving the spatial resolution to ~15 km (e.g., TMI and AMSR-E) was found in Fig. 8.4 to be very helpful in detecting precipitation rates 20-60 mm/h. It was also found in Table 8.5 that precipitation-rate correlation coefficients between NOWRAD and other sensors were improved by blurring NOWRAD data to at least 10-15 km, and that further blurring to 25-40 km increased the correlation coefficients for the higher more convective rain rates. The reason correlations are increased by blurring small intense precipitation peaks is unclear, although such an effect is reasonable to the extent NEXRAD and the other sensors sound different altitudes or forms of precipitation at different times. The correlation coefficients for the logarithms of precipitation retrievals are more sensitive to NOWRAD spatial resolution, however, and Table 8.5 shows correlation maxima near 15, 30, 15, 20, and 15 km for TMI, SSM/I, AMSR-E, AMSU/NR, and AMSU/MM5, respectively. Thus spatial structure can be significant at those light rain rates probed by the logarithmic metric.

Besides spatial resolution, the main difference between the various sensors is that AMSU seems to respond more strongly than the others to rates below 1 mm, presumably because of the increased sensitivity to hydrometeors near 1-mm diameter provided by the four AMSU-B channels in the 150-190 GHz band. Since most such detections lie adjacent to pixels found by other sensors to be precipitating, the net effect on imagery is modest. It is unknown what fraction of the time AMSU detections below 1 mm/h are false and due merely to evaporating precipitation or heavy, non-precipitating cirrus. The statistics in Table 8.7 suggest an upper bound to false detections by AMSU of ~4 percent of all detections, if we regard TMI as truth.

Tables 8.8 and 8.9 show that the various precipitation rate estimates agree with NOWRAD principally above 1 mm/h, and that the agreement improves further above ~8 mm/h. TMI and AMSU/NR agree with NOWRAD the best, depending on precipitation rate and whether NOWRAD or the other instrument defines the octaves for which comparisons are made. To the extent that NOWRAD is deficient below 1 mm/h, particularly in drizzle, these discrepancies leave open the possibility that TMI and AMSU could provide useful retrievals in the 0.3-1 mm/h range, as hinted by the standard deviations in Table 8.8 which, at the lowest rain rates, reach 0.44 mm/h for TMI and 0.66 mm/h for AMSU/NR.

Chapter 9

Preliminary Study of Assimilating Millimeter-Wave Radiances into MM5

9.1 Introduction

Assimilation of real-time precipitation data from radar networks or satellites into cloud-resolving NWP models is a "grand challenge" motivated by the tremendous significance of being able to model and predict the course of severe storms such as Katrina on the scale of individual convective elements. Kalnay [82] has reviewed conventional 3DVAR and related techniques for assimilating data into models, but these currently have difficulties at cloud-resolving scales. For example, MM5 mesoscale simulations of marine cyclones consistently exhibit position errors [83] of the sort that significantly degrade forecasts [84]. Also, the "bogusing" of assumed cyclones into models, and the removal of incorrectly located cyclones, must be very precise to avoid shocks and "ghosts" that can severely degrade forecasts [85]; such precision is not assured. Manual "warping" of microwave humidity fields to match locations of detected features [83] may prove useful, but has not been automated. Use of a displacement-based cost function has been tested with thunderstorms [86], and a variational minimization of forecast/observation discrepancies in displacement space has been proposed as an alignment preprocessor for 3DVAR and other assimilation approaches [87].

Since microwave spectrometers viewing precipitation primarily sense hydrometeor distributions, a method for relating those hydrometeor distributions to cloud-resolved wind and humidity distributions is required. Fortunately geostationary microwave satellites can extract approximately 3 degrees of freedom (DoF) from the hydrometeor signature, and additional DoF from the temperature and humidity profiles. This set of several independent parameters offers geostationary microwave spectrometers a significant potential assimilation advantage over ground-based radar networks limited by hilly terrain and yielding only a single output backscattering parameter, Z.

9.2 Preliminary Results

Due to time limits, assimilation work presented in this thesis is preliminary. This section reports the proposed idea, important issues, difficulty, and preliminary results. Fig. 9.1 illustrates the idea of using a feedback system for assimilating precipitation information from observed radiances into MM5 model to improve MM5 predictions. The goal is to observe brightness temperatures at time t, compare with those predicted by MM5, derive appropriate adjustment for MM5 parameters at time t - τ, make the adjustment in MM5 at time t - τ, and run MM5 forward to get better agreement with satellite observation at time t. This closed-loop process might have to be repeated until achieving good results.

The feedback system has three aspects: displacement estimation, dimensionality reduction, and amplitude adjustment. First, it is essential to ensure that observations made at time t influence the model at the correct location at time t - τ, allowing for storm translation during the time offset τ. The MM5 winds at appropriate altitudes were used to make a first-order correction for translational movements; perfection is not necessary and this step may not be required. Fig. 9.2 shows the differences in 183±7 GHz radiances over a 15-minute period before (left side) and after (right side) positional corrections are made using smoothed 500-mbar winds for the intense French front illustrated here in Figs. 3.3, 5.11, and 6.1, for example. Note that the velocities associated with advance of the main front toward the northeast and those associated with the more stationary orographic precipitation pinned to the Alps are different, and therefore motion correction of orographic precipitation is to be avoided. Although the displacement estimation is not perfect, it clearly helps reduce errors in displacement. It is important to note that assimilating microwave spectral observations at the 15-60 minute intervals appropriate to geostationary satellites and cloud-resolving models is easier than doing so at the longer intervals typically addressed by most prior research. The reason is that it is more difficult to make good displacement estimates for longer time interval.

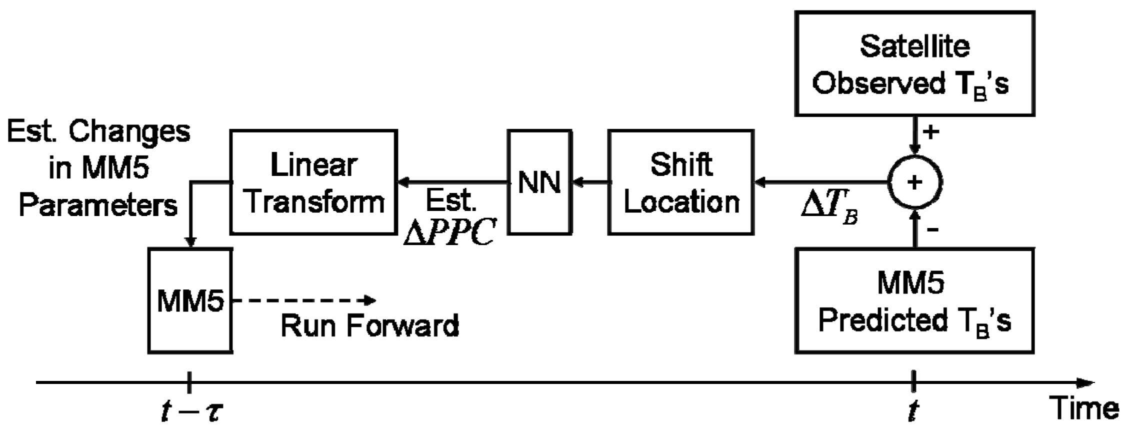

Fig. 9.1. A feedback system to assimilate radiances into MM5, where Est. ΔPPC is the estimated change in projected principal component and NN is a neural network.

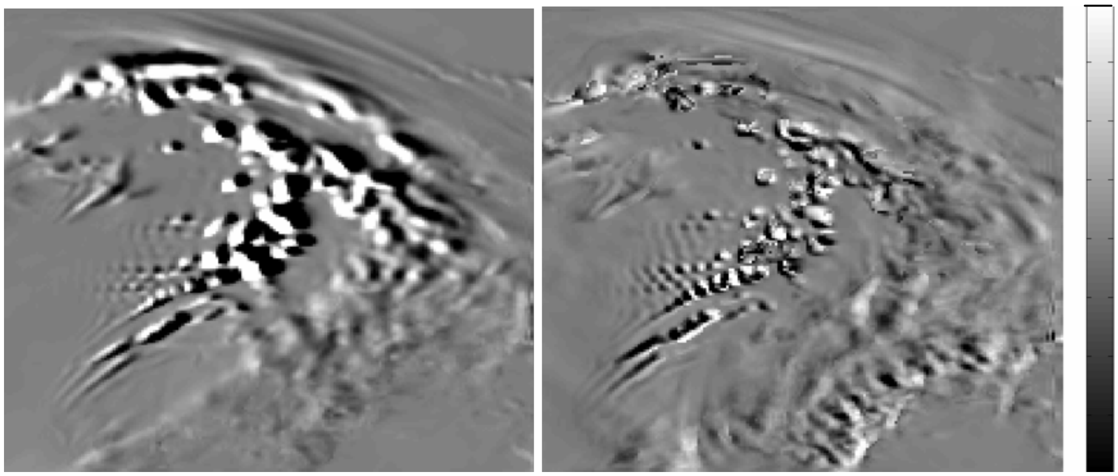

Fig. 9.2. Brightness temperature difference, $T_B(t = 0)$ - $T_B(t = -15\text{ min})$, at 183±7 GHz, before (left image) and after (right image) preliminary wind correction for radiance position. The brightness temperature scale extends from +20K (white) to -20K (black). The image is ~900 km wide.

The second assimilation issue is that cloud-resolving NWP models have too many important degrees of freedom (DoF) relative to the number found in the microwave data, and therefore realistic cloud-resolved wind and humidity fields in storms cannot be retrieved directly from satellites; the DoF of the model itself must be utilized in the retrieval process too. This part of the effort involves identifying those DoF in the model that most influence those future wind and humidity fields that in turn generate the observed hydrometeor distributions. It is these most critical DoF that should be iteratively perturbed at times $t - \tau_i$ with the position-corrected transformed differential radiance data (observation minus model). Projected Principal Component (PPC) technique discussed in Section 2.6.2 is suitable for identification of such key DoF. PPC's are those functions of an input space that most efficiently characterize any associated output space after linear transformation.

The third assimilation issue involves optimization of the amplitude adjustment step at times $t - \tau_i$. Since the model must be allowed to evolve so the wind, temperature, humidity, and hydrometeor fields become consistent with the observed radiances, and the required evolution time depends the features that are evolving, both the perturbation estimator and the time intervals τ_i (typically more than one would be used) must be chosen. The estimator could be neural network trained on large ensembles of storms. An alternative approach to be explored or merged is the combined field and amplitude adjustment method of Ravela et al. [87].

It is difficult to be more precise about methods at this point because several important experiments with MM5 must be performed sequentially in order to identify the most efficient and effective research path. It is left here as suggested future study.

Chapter 10

Conclusions

10.1 Summary of the Thesis

The thesis starts with validation of a model composed of a numerical weather prediction model MM5, a radiative transfer model TBSCAT, and electromagnetic models for icy hydrometeors aloft (F(λ)) to be used as global statistical ground-truth for microwave precipitation retrieval development. The model was validated by comparing its predicted millimeter-wave radiances with those coincidentally observed by the Advanced Microwave Sounding Unit (AMSU) aboard the operational satellites NOAA-15, -16, and -17. Predicted and observed brightness temperatures reasonably agree over 122 global storms spanning a year and including different types of precipitation. Sensitivity of predicted radiances to assumptions in MM5 and the radiative transfer model, and the robustness of predicted retrieval accuracies of millimeter-wave instruments were studied. It was found that whereas predicted radiances are fairly sensitive to assumptions in MM5 and the radiative transfer model, predicted retrieval accuracies of millimeter-wave instruments are robust to these assumptions. Once validated, MM5/TBSCAT/ F(λ) model was then used for real applications. Appropriate specifications for geostationary microwave sounders and their retrieval accuracies were studied and it was found that a 1.2-m micro-scanned filled-aperture antenna operating at 118/166/183/380/425 GHz, which is relatively inexpensive, technologically mature, simple to build, and readily installed on a geostationary satellite, provides useful observations of important global precipitation with 20-km resolution every 15 minutes. A new global precipitation retrieval algorithm over non-icy surfaces was developed for AMSU by using information from the MM5/TBSCAT/ F(λ) model. This algorithm was shown to have good retrieval accuracies for different types of precipitation. AMSU surface precipitation rates retrieved using this algorithm reasonably agree with those retrieved for AMSR-E over both land and sea, and with those retrieved for SSM/I, TMI, and NEXRAD over land, where comparison over sea with SSM/I, TMI, and NEXRAD retrievals was not performed. The proposed idea, important issues, difficulty, and preliminary results for assimilation of satellite precipitation data into MM5 with the objective of improving the model forecasts so that they are as close to satellite observations as possible were also presented.

10.2 Contributions

Contributions of this thesis are listed here for each chapter.

10.2.1 Contributions from Chapter 4

- This chapter is the first to develop electromagnetic models, Mie spheres with ice densities F(λ) found using DDSCAT, for icy hydrometeors and to show that such models in combination with a numerical weather prediction model, MM5, and a two-stream radiative transfer model, TBSCAT, provide reasonable agreement between predicted brightness temperatures and AMSU observations over 122 global representative storm systems for all precipitation types evaluated, including convective, stratiform, snow, and unglaciated precipitation.

10.2.2 Contributions from Chapter 5

- This chapter shows that assumptions in MM5 and the radiative transfer model have to be very close to reality to get reasonable agreement between predicted brightness temperatures and AMSU observations over 122 global representative storm systems.
- This chapter shows that predicted precipitation retrieval accuracies are not very sensitive to assumptions in MM5 and the radiative transfer model.
- This chapter shows that the MM5/TBSCAT/F(λ) model could be used to develop microwave precipitation retrieval algorithms and to predict precipitation retrieval accuracy of microwave instruments before launch.

10.2.3 Contributions from Chapter 6

- This chapter suggests appropriate configurations for geostationary microwave sounders for precipitation observation.
- This chapter is the first to evaluate and compare precipitation retrieval accuracies for different configurations of geostationary microwave sounders including aperture synthesis systems.
- This chapter shows that the image sharpening technique could be used to increase resolution for filled-aperture antenna and can help capture small and isolated precipitation.
- This chapter shows that a 1.2-m micro-scanned filled-aperture antenna operating at 118/166/183/380/425 GHz, which is relatively inexpensive, technologically mature, simple to build, and readily installed on a geostationary satellite, could provide useful observation of global precipitation with 20-km resolution and every 15 minutes.

10.2.4 Contributions from Chapter 7

- This chapter develops a new global precipitation retrieval algorithm, called AMSU/MM5, that works over non-icy surface for AMSU by using the MM5/TBSCAT/F(λ) ground-truth and shows that AMSU/MM5 has good retrieval

accuracy for all types of precipitation evaluated, including convective, stratiform, snow, and unglaciated precipitation.
- This chapter shows that AMSU/MM5 reasonably agrees with AMSR-E over both land and sea.

10.2.5 Contributions from Chapter 8

- This chapter compares precipitation rate retrievals from NOWRAD, AMSU, AMSR-E, SSMI, and TMI over land and shows that all reasonably agree.
- This chapter reemphasizes that AMSU/MM5 algorithm could be used operationally with reasonable accuracy.

10.2.6 Contributions from Chapter 9

- This chapter presents the idea of how to assimilate satellite brightness temperatures into a numerical weather prediction model to improve forecasts.
- This chapter points out important issues and difficulty to assimilate radiance information successfully.
- This chapter shows a technique to estimate storm translation in time.

10.3 Suggestions for Future Work

10.3.1 Radiative transfer Model

The radiative transfer model TBSCAT in its two-stream variant and the Mie sphere model with density $F(\lambda)$ for icy hydrometeors were validated in this thesis against observations at 50-200 GHz. Interesting future work would be validation using a multi-stream radiative transfer against observations at 50-200 GHz and/or the extension to frequencies above 200 GHz once observations at this frequency range become available. Since surface has a strong impact to window channels and even opaque channels if the atmosphere is dry, realistic models for different types of surface, i.e., sea ice, snow on the ground, wet soil, etc., could help improve precipitation retrieval algorithms.

10.3.2 Improvements for Microwave Precipitation Retrieval Algorithm

It is very difficult to distinguish signals from ice or snow on the surface from those from icy hydrometeors. This leads to false alarms when precipitation estimation is performed over such surfaces. Observations in infrared frequency and information from numerical weather prediction model could help detect such false alarms.

10.3.3 Data Assimilation

The proposed “precipitation locking” idea in Chapter 9 could be carried further. If successful, this will improve both precipitation retrieval accuracies and weather forecasts.

One might also be interested in assimilating the different surface precipitation rate products presented in Chapter 8 to have better estimates of surface precipitation rate for a given area in a time period for hydrological or climatological studies. This thesis has shown that MM5 could serve as ground-truth. Biases and error variances for these surface precipitation rate products could be found using MM5 simulations as demonstrated in Section 7.5, and could also be compared to those computed from retrievals themselves, as demonstrated in Section 8.5. Hence, these surface precipitation rate products can then be combined according to their MM5-derived error statistics to minimize a defined error function. Chapter 8 also suggests that blurring can help reduce the effect of positional errors among these products.

Appendix A

Assumptions and Details for Experiments

A.1 List of 270 Globally Representative Storms

Table A.1 lists 255 globally representative storms July 2002 – June 2003 selected by examining AMSU data and described in Chapter 3. These storms included 20 for each month plus 15 that were not glaciated (~warm rain). In addition, Table A.1 also shows 15 candidate storms over the North Pole that were simulated but not used in this thesis because it is very difficult to model icy surface correctly to be able to validate against AMSU observations. The satellite passes typically overlap with MM5 storm systems over an area ~ 2200 km × 2200 km. Obvious morphological discrepancies between AMSU observations and MM5 predictions, as well as storms embracing either pole or very high mountains, led to deletion of approximately half the initial set of 255 storms, leaving 122 storms for studies in Chapters 4-9 and are marked with stars next to case numbers in Table A.1. In Table A.1, # is the case number, date is the calendar date, date# is the date number for that year, orbit# is the NOAA satellite orbit number, scan# is the AMSU scan number, lat and lon are latitude and longitude of the center of the storm, time is the observation time in UTC at latitude/longitude, sat. tells the storm was observed by which NOAA satellite, where NK, NL, and NM are NOAA-15, -16, and -17, respectively. Storm type in Table A.1 tells roughly how the storm looks like. S or C is used when surface precipitation rate estimate for that storm is only $<$ or $\geq$ 10 mm/h, respectively. SC is used when surface precipitation rate estimate for that storm are both $<$ and $\geq$ 10 mm/h. TP, H, and WR are typhoon, hurricane, and warm rain, respectively.

These storms were simulated for 6 hours after MM5 initialization. MM5 outputs were saved every 15 minutes between the 3rd and the 6th hours for all 3 MM5 domains. These 270 storms are in /net/ds-0a/raid1/STORM270/ on the ACESGRID cluster at MIT. A simple naming system was used. For example, all MM5 outputs for case# 3 of July 2002 are in /net/ds-0a/raid1/STORM270/July/July_3/. Each storm directory has the size of 7.7 GB.

TABLE A.1
LIST OF 270 GLOBAL REPRESENTATIVE STORMS

July 2002

#	Date	Date#	Orbit#	Scan#	Time	Lat	Lon	Type	Sat.
1	2	183	2	2100	04:38:46	19.86	129.31	TP	NL
2	2	183	6	650	10:28:12	9.81	-131.48	SC	NL

3*	6	187	2	2250	03:59:02	40.04	138.56	SC	NL
4*	9	190	10	2320	17:40:22	69.97	-62.14	SC	NL
5*	9	190	10	2110	17:31:02	69.77	60.67	C	NL
6*	11	192	3	620	05:11:45	60.02	77.24	S	NM
7*	11	192	4	190	05:55:05	48.22	-172.85	SC	NK
8*	15	196	6	600	09:56:38	-35.5	-119.95	S	NL
9	15	196	4	250	06:10:25	38.42	-60.04	SC	NL
10*	17	198	14	1100	23:44:49	-51.06	133.00	SC	NM
11	17	198	6	2450	11:05:37	57.27	156.23	S	NM
12	17	198	9	1450	15:43:50	-29.91	108.25	SC	NM
13*	19	200	14	1600	23:21:42	-41.29	-0.59	S	NM
14	19	200	7	1300	11:15:18	-65.65	-57.93	S	NM
15*	22	203	10	1700	17:39:23	-35.5	-49.85	SC	NL
16*	22	203	13	610	21:47:29	50.09	85.13	SC	NL
17*	29	210	11	200	17:02:41	47.54	-84.61	SC	NM
18	29	210	2	1000	03:39:56	15.91	100.29	SC	NM
19	29	210	3	100	04:48:06	34.40	-101.46	SC	NM
20	31	212	3	1180	04:43:21	0.00	80.00	SC	NM

August 2002

#	Date	Date#	Orbit#	Scan#	Time	Lat	Lon	Type	Sat.
1*	2	214	7	2300	11:48:01	52.00	130.00	SC	NM
2*	6	218	6	300	10:32:22	52.66	-105.76	C	NL
3*	12	224	6	500	10:04:33	50.89	17.91	SC	NM
4	12	224	9	1800	16:19:08	20.00	85.31	SC	NM
5	12	224	6	2000	11:11:13	10.51	159.98	SC	NM
6*	12	224	7	600	11:57:48	6.78	-24.75	SC	NM
7	12	224	10	380	16:56:49	26.67	-92.51	SC	NM
8	14	226	3	2010	05:12:38	36.79	129.49	SC	NL
9	16	228	11	100	17:03:34	40.00	-90.00	SC	NM
10*	16	228	14	300	22:08:28	38.42	-167.23	SC	NM
11*	16	228	4	850	05:18:46	68.74	109.65	SC	NM
12	16	228	10	900	17:50:22	-34.58	-166.06	SC	NK
13	18	230	3	1820	06:07:07	19.96	109.83	SC	NL
14*	21	233	3	210	04:15:02	67.28	2.28	S	NL
15*	21	233	7	330	11:07:50	57.42	-134.81	SC	NL
16*	23	235	7	1700	11:53:21	-40.00	167.23	SC	NM
17	23	235	3	2400	05:23:40	10.91	-109.65	SC	NM
18	26	238	13	820	22:14:57	20.55	64.19	SC	NL
19*	26	238	9	2080	16:41:05	54.17	-41.25	SC	NL
20*	29	241	3	2190	05:56:22	58.43	119.66	SC	NL

September 2002

#	Date	Date#	Orbit#	Scan#	Time	Lat	Lon	Type	Sat.
1*	1	244	3	300	03:57:10	59.89	-20.48	S	NL

2*	1	244	11	810	17:36:38	49.06	140.96	SC	NL
3*	4	247	4	300	06:11:40	69.15	-154.59	S	NM
4*	7	250	3	200	04:59:29	49.65	-102.46	SC	NM
5	9	252	7	1840	12:06:24	5.57	26.51	SC	NL
6*	9	252	6	2300	11:10:11	57.16	119.48	SC	NK
7*	9	252	6	1850	10:50:11	13.45	120.83	SC	NK
8*	11	254	6	1600	11:34:24	-36.97	35.22	S	NL
9*	11	254	14	220	23:54:40	59.88	-169.86	SC	NL
10*	15	258	6	1880	11:14:19	50.06	39.96	SC	NL
11	18	261	4	550	06:11:28	-6.17	-72.26	SC	NL
12*	18	261	7	350	11:01:15	55.22	-130.66	SC	NL
13*	20	263	14	350	23:32:51	46.00	-85.08	SC	NK
14*	22	265	10	400	16:42:14	20.55	-89.46	IH	NM
15	22	265	14	150	23:06:52	73.43	-90.46	S	NM
16	23	266	3	1350	05:45:42	-67.77	170.04	SC	NL
17*	26	269	6	1980	10:59:41	36.79	111.06	SC	NK
18*	26	269	10	300	16:49:00	36.61	-83.91	SC	NM
19	30	273	10	1400	17:45:22	17.10	9.95	SC	NK
20	30	273	4	650	05:05:05	57.89	81.92	S	NM

October 2002

#	Date	Date#	Orbit#	Scan#	Time	Lat	Lon	Type	Sat.
1*	2	275	14	650	23:42:51	52.87	55.88	S	NL
2*	5	278	7	180	11:16:13	54.55	-61.15	SC	NK
3	7	280	11	1000	17:49:20	29.91	130.07	SC	NL
4*	7	280	2	2300	03:41:31	43.31	149.03	SC	NL
5	7	280	3	1100	04:20:33	9.30	89.94	SC	NM
6	7	280	11	2050	21:48:08	21.04	-54.89	SC	NK
7*	10	283	10	1580	17:20:18	40.22	14.86	SC	NK
8*	10	283	4	800	06:01:22	34.31	11.29	SC	NK
9	14	287	9	1640	17:16:27	-41.91	-45.00	S	NL
10	16	289	7	250	12:02:31	37.34	-70.10	SC	NK
11	17	290	3	650	05:56:11	-16.80	-53.31	SC	NL
12*	17	290	10	250	17:06:24	44.71	-55.00	SC	NL
13*	17	290	6	1900	11:07:51	32.73	119.95	SC	NK
14	24	297	3	1400	05:01:37	-56.48	43.42	S	NM
15	24	297	3	2220	05:38:04	13.92	-108.19	SC	NM
16*	24	297	7	1450	12:04:06	-57.79	161.85	S	NM
17	24	297	10	850	16:55:18	-72.83	-161.85	S	NM
18	25	298	11	100	17:11:28	9.71	-49.97	SC	NL
19*	25	298	7	2180	12:15:39	48.55	5.09	S	NL
20*	31	304	6	1700	11:00:59	29.91	45.11	SC	NL

November 2002

#	Date	Date#	Orbit#	Scan#	Time	Lat	Lon	Type	Sat.

1*	1	305	13	1580	21:52:50	-20.00	-40.00	SC	NK
2*	1	305	1	100	00:04:56	10.81	-87.83	SC	NK
3*	6	310	3	400	05:20:00	35.13	-41.25	SC	NL
4	6	310	6	1700	11:21:47	-20.25	35.34	SC	NL
5	7	311	10	1250	17:52:02	-9.50	21.06	SC	NK
6	8	312	3	2200	05:44:40	3.14	-161.85	SC	NK
7*	10	314	3	100	04:23:03	38.81	-103.51	SC	NM
8	11	315	3	850	04:26:31	50.00	100.00	S	NM
9	12	316	3	1580	05:03:07	-40.22	142.89	SC	NL
10	12	316	3	1200	04:18:36	0.00	86.95	SC	NM
11	12	316	3	1020	04:10:36	24.55	91.05	SC	NM
12*	13	317	13	700	22:41:36	41.64	62.61	S	NL
13*	15	319	6	900	10:48:08	-42.35	-149.91	S	NL
14	19	323	2	2050	03:57:04	8.60	156.29	SC	NL
15	19	323	10	900	16:47:17	-29.62	136.98	SC	NL
16	19	323	9	1700	16:01:21	0.00	94.44	SC	NM
17*	25	329	3	870	05:29:41	-31.79	-59.74	SC	NL
18	25	329	14	120	23:22:29	39.95	-148.27	S	NL
19	29	333	6	1750	10:41:52	29.91	36.86	SC	NL
20	29	333	10	1440	16:59:01	-68.60	3.39	S	NL

December 2002

#	Date	Date#	Orbit#	Scan#	Time	Lat	Lon	Type	Sat.
1	2	336	3	2100	06:19:41	-1.22	-178.47	SC	NK
2	2	336	6	1200	11:07:41	-65.22	118.08	S	NK
3*	2	336	10	1650	18:02:21	-28.58	23.41	SC	NK
4*	5	339	3	220	04:50:40	61.62	-39.96	S	NL
5	5	339	13	820	22:00:32	30.85	60.79	S	NL
6*	5	339	14	1900	23:27:35	14.52	-14.86	S	NM
7*	8	342	10	480	16:25:25	15.11	145.05	TP	NL
8*	8	342	14	1800	23:59:49	-30.94	-135.34	SC	NL
9	12	346	4	650	06:12:17	49.23	75.48	SC	NM
10*	12	346	6	1850	10:27:45	-40.93	173.55	SC	NM
11*	14	348	6	380	10:15:39	8.39	-128.09	SC	NL
12*	14	348	7	400	11:45:04	41.64	-126.97	S	NL
13	14	348	3	1850	04:29:21	-62.29	-51.84	SC	NM
14*	17	351	10	300	16:18:29	44.97	162.84	S	NL
15	17	351	11	380	17:38:50	55.93	-74.48	S	NL
16	21	355	14	1020	00:14:45	-6.48	19.95	SC	NL
17	25	359	3	2200	05:54:40	56.72	96.37	S	NL
18	25	359	14	250	22:45:11	36.24	-62.08	SC	NK
19	26	360	3	900	04:18:36	47.54	100.00	SC	NM
20*	31	365	14	1700	23:44:18	31.23	-82.97	SC	NK

January 2003

#	Date	Date#	Orbit#	Scan#	Time	Lat	Lon	Type	Sat.
1	2	002	13	900	22:23:56	-60.04	166.76	S	NM
2*	2	002	6	600	10:03:40	49.90	6.44	SC	NM
3*	5	005	10	850	16:22:39	-12.21	136.33	SC	NL
4*	7	007	6	1550	11:30:34	-37.97	36.92	SC	NL
5	10	010	9	2420	17:06:25	53.78	-105.44	SC	NM
6	10	010	9	2420	17:06:25	49.84	-81.22	S	NM
7*	10	010	10	1100	17:58:09	-50.84	78.29	S	NM
8*	10	010	6	1580	11:12:49	-60.04	-170.74	S	NM
9	10	010	7	200	11:59:45	67.82	1.52	S	NM
10*	13	013	10	600	16:28:12	-42.88	-93.97	SC	NM
11	13	013	7	500	11:04:49	21.04	-3.04	S	NM
12	13	013	7	620	11:10:09	2.43	-7.72	SC	NM
13*	16	016	6	1000	11:05:36	-50.06	-140.08	SC	NL
14*	16	016	3	600	05:47:33	-12.62	-55.94	SC	NL
15	19	019	14	350	23:22:34	68.60	-140.02	SC	NL
16	22	022	13	1950	22:13:00	19.67	1.29	S	NM
17	22	022	7	700	11:04:06	18.29	-3.16	S	NM
18	11	011	6	300	10:01:57	12.62	-111.29	SC	NL
19*	23	023	10	600	16:11:33	29.9	147.39	S	NL
20*	25	025	10	750	17:46:13	-26.57	127.55	SC	NL

February 2003

#	Date	Date#	Orbit#	Scan#	Time	Lat	Lon	Type	Sat.
1	2	033	10	2200	17:12:31	45.23	-65.00	S	NL
2	5	036	3	1750	06:11:27	-7.89	109.77	SC	NL
3	5	036	6	500	10:22:02	24.84	-114.98	S	NL
4*	7	038	10	400	16:47:34	27.24	-100.06	S	NM
5*	9	040	3	400	04:23:27	43.57	-35.40	S	NL
6*	9	040	4	580	06:20:48	-10.01	-61.97	SC	NL
7	11	042	13	2000	23:04:49	20.65	-11.23	S	NM
8	11	042	3	1100	05:21:53	-15.21	67.70	SC	NM
9	11	042	9	2000	16:28:33	53.51	70.10	C	NM
10	12	043	10	2000	17:48:33	51.55	44.35	C	NM
11	13	044	2	1000	04:04:16	-40.13	-40.00	SC	NL
12*	13	044	6	450	10:29:57	33.84	-112.93	S	NL
13*	15	046	7	1650	12:10:20	0.00	104.27	SC	NK
14	16	047	3	1400	05:21:53	-60.00	40.00	S	NM
15	18	049	2	2000	03:45:14	0.00	150.00	SC	NL
16	22	053	10	780	17:14:29	47.71	130.07	S	NL
17	25	056	3	180	04:23:56	45.49	-104.74	SC	NM
18	25	056	4	200	06:07:13	59.79	-124.75	SC	NM
19	25	056	10	1600	17:47:50	26.48	53.95	SC	NM
20*	27	058	11	1250	18:16:58	-18.28	122.11	SC	NL

March 2003

#	Date	Date#	Orbit#	Scan#	Time	Lat	Lon	Type	Sat.
1	2	061	3	400	04:13:58	56.06	-112.70	S	NM
2	2	061	7	1500	12:03:40	-66.64	-169.10	S	NM
3*	2	061	7	1600	12:08:06	-49.90	166.53	SC	NM
4	2	061	9	1950	15:59:08	44.22	92.80	S	NM
5	4	063	7	1550	11:19:29	-70.02	170.04	SC	NM
6	4	063	10	300	17:21:32	40.04	-102.46	S	NM
7	4	063	14	400	00:01:10	61.55	150.38	S	NM
8	7	066	3	700	04:13:58	74.60	150.50	S	NM
9	8	067	6	1300	10:22:55	-38.51	55.06	SC	NL
10*	8	067	14	1130	23:23:06	-14.51	29.90	SC	NL
11*	15	074	3	1850	05:56:17	-50.00	-160.00	SC	NK
12*	17	076	10	300	15:48:12	30.00	-81.33	SC	NM
13*	17	076	10	1400	16:37:05	-49.56	83.67	SC	NM
14*	17	076	7	600	10:44:44	37.15	-7.02	S	NM
15	20	079	4	700	06:11:18	46.09	60.50	S	NM
16	20	079	6	900	09:46:36	-2.84	8.54	SC	NM
17*	20	079	9	1600	16:04:54	20.55	46.40	SC	NK
18*	23	082	6	1850	11:22:34	56.68	39.87	S	NL
19*	25	084	3	800	04:51:54	-11.31	-54.71	SC	NL
20	29	088	6	350	10:35:06	54.89	-128.46	S	NL

April 2003

#	Date	Date#	Orbit#	Scan#	Time	Lat	Lon	Type	Sat.
1	2	092	3	1780	05:46:39	-11.91	119.46	SC	NL
2	4	094	8	350	12:13:21	65.65	-28.91	SC	NM
3*	6	096	6	2400	11:06:36	44.45	166.06	SC	NM
4	6	096	10	1000	17:09:26	-69.02	-101.70	SC	NM
5*	7	097	12	2450	22:04:10	44.97	-131.42	S	NL
6*	9	099	3	1000	05:32:23	1.22	18.61	SC	NK
7*	13	103	4	350	06:05:46	40.00	-50.00	S	NL
8	13	103	3	2100	05:34:13	27.82	120.00	SC	NL
9*	15	105	3	220	04:16:06	30.00	-107.26	S	NM
10	15	105	10	2150	18:08:01	69.98	-114.10	SC	NM
11*	15	105	4	600	05:53:25	0.00	-60.03	SC	NL
12	15	105	9	1550	15:51:29	10.00	43.07	SC	NK
13*	15	105	9	1650	15:55:56	35.51	40.14	S	NK
14	16	106	13	850	22:36:31	23.09	52.25	SC	NL
15	16	106	13	780	22:33:25	37.97	53.45	S	NL
16	18	108	14	200	23:10:41	23.19	-61.91	SC	NK
17*	18	108	3	800	05:12:49	36.61	28.44	S	NK
18	20	110	14	1050	23:40:52	25.32	48.77	SC	NL
19	23	113	10	1900	17:08:15	0.00	-43.71	SC	NL
20	25	115	10	1400	17:08:33	-1.62	73.61	SC	NM

May 2003

#	Date	Date#	Orbit#	Scan#	Time	Lat	Lon	Type	Sat.
1*	1	121	2	1100	03:52:49	20.00	93.50	SC	NM
2	3	123	3	920	04:18:50	-26.00	-36.60	SC	NL
3*	5	125	11	300	18:27:00	40.00	-80.00	SC	NL
4	9	129	11	710	18:01:29	71.12	127.50	S	NL
5	11	131	14	800	23:49:37	-21.44	157.64	SC	NM
6*	11	131	14	350	22:38:11	49.06	-76.89	SC	NK
7	12	132	9	1650	15:49:32	4.86	97.48	SC	NM
8	15	135	2	2200	04:37:51	34.58	141.19	SC	NL
9*	15	135	3	2000	06:18:17	29.90	115.03	SC	NL
10*	16	136	14	1100	22:54:59	6.68	120.01	SC	NK
11	16	136	3	550	04:02:48	68.33	91.63	S	NK
12*	16	136	4	600	05:48:30	60.04	28.67	SC	NK
13	18	138	10	800	16:39:38	1.82	146.69	SC	NL
14*	20	140	10	1600	17:21:28	47.29	16.21	SC	NK
15*	22	142	5	2100	09:50:06	52.04	131.66	SC	NK
16	27	147	2	2450	04:31:15	48.81	-168.64	SC	NK
17	27	147	3	2000	05:58:27	-1.01	-170.04	SC	NK
18*	27	147	6	2050	11:13:12	47.15	112.46	SC	NK
19*	30	150	3	2190	05:12:04	34.21	130.42	SC	NL
20	30	150	7	1900	11:51:59	8.69	22.38	SC	NL

June 2003

#	Date	Date#	Orbit#	Scan#	Time	Lat	Lon	Type	Sat.
1	1	152	7	800	10:40:49	7.39	1.58	SC	NM
2	1	152	10	1750	16:40:54	43.23	65.54	SC	NM
3	1	152	13	1900	21:43:34	9.50	0.82	SC	NM
4*	1	152	7	500	11:32:19	0.20	-70.00	SC	NK
5	1	152	14	850	00:03:59	18.78	30.08	SC	NL
6*	2	153	10	2000	17:10:59	28.20	11.23	SC	NK
7*	2	153	3	850	04:17:44	26.67	38.56	SC	NK
8*	2	153	3	100	04:37:26	40.00	-98.13	SC	NM
9	4	155	2	2210	04:13:13	33.00	139.90	SC	NL
10	4	155	10	1610	17:34:49	-18.98	-59.74	SC	NL
11	6	157	11	1000	18:01:35	25.61	121.83	SC	NL
12	9	160	14	980	00:20:58	4.66	25.16	SC	NL
13	9	160	14	605	00:04:17	62.59	35.22	SC	NL
14*	9	160	13	2150	22:16:01	53.35	-5.27	SC	NM
15	12	163	3	300	04:11:08	40.93	-95.85	SC	NM
16	12	163	10	500	16:36:33	7.69	-92.51	SC	NM
17	17	168	14	700	00:18:39	51.06	48.80	SC	NL
18*	22	173	3	2050	05:54:55	36.24	117.78	SC	NL
19*	25	176	14	500	22:46:02	59.28	52.08	SC	NL
20*	30	181	11	380	18:06:34	55.43	-70.00	SC	NL

Polar Storm

#	Month	Date	Date#	Orbit#	Scan#	Time	Lat	Lon	Type	Sat.
1	7	20	201	3	200	04:12:35	86.00	-131.03	S	NK
2	8	9	221	14	550	23:30:25	85.25	34.60	S	NL
3	8	14	226	3	2350	05:27:45	86.00	113.73	S	NL
4	8	23	235	3	600	04:03:40	86.00	90.00	S	NM
5	9	1	244	3	2400	05:30:30	86.00	-64.54	S	NL
6	9	4	247	14	500	23:42:35	85.27	28.44	S	NL
7	9	7	250	3	2400	06:05:42	86.00	-68.70	SC	NL
8	10	24	297	3	400	04:17:11	86.00	-89.15	S	NM
9	4	16	106	14	400	23:57:19	86.00	-144.06	S	NL
10	4	20	110	3	2400	06:13:41	86.00	-46.32	S	NL
11	4	25	115	14	150	22:39:40	86.00	-11.68	S	NM
12	4	29	119	11	550	18:07:11	86.00	-54.92	SC	NL
13	5	12	132	10	2250	17:55:24	86.00	-83.00	S	NM
14	5	18	138	7	200	11:11:06	86.00	-126.95	S	NL
15	6	17	168	13	300	22:25:24	86.00	-128.92	SC	NL

Warm rain

#	Month	Date	Date#	Orbit#	Scan#	Time	Lat	Lon	Type	Sat.
1*	9	6	249	13	100	23:10:40	67.77	-167.00	WR	NL
2*	9	6	249	6	240	10:21:36	-49.73	-139.38	WR	NL
3	9	6	249	7	510	12:25:36	-49.06	30.31	WR	NL
4*	9	6	249	2	800	04:28:00	65.22	130.02	WR	NL
5*	9	6	249	2	540	03:53:20	-54.74	166.53	WR	NL
6	9	6	249	2	850	04:34:40	75.11	64.48	WR	NL
7	9	6	249	3	100	04:44:00	49.76	-27.09	WR	NL
8	9	6	249	4	50	06:26:40	60.04	-58.86	WR	NL
9*	11	16	320	2	540	04:12:32	-57.27	161.26	WR	NL
10	11	16	320	2	400	03:53:52	-52.97	-38.97	WR	NL
11	11	16	320	10	340	17:29:52	-56.64	114.10	WR	NL
12*	11	16	320	3	100	05:03:44	51.17	-36.04	WR	NL
13	11	16	320	3	650	06:17:04	21.04	114.39	WR	NL
14*	11	16	320	5	680	09:49:44	53.99	49.03	WR	NL
15*	11	16	320	6	640	11:33:36	58.36	7.72	WR	NL

A.2 Assumptions used in MM5

This appendix provides more details for assumptions used in MM5, which are more complete than those given in Chapter 3. To get MM5 predictions of atmospheric profiles for pressure levels, five main MM5 submodels are required (see [6]). These include TERRAIN, REGRID, INTERPF, MM5, and INTERPB and are used in order. First, TERRAIN horizontally interpolates the regular latitude-longitude terrain elevation and vegetation (land use) onto the chosen mesoscale domains. Its options were shown in Table A.2. Second, REGRID reads archived gridded meteorological analyses and forecasts on pressure levels and interpolates those analyses from some native grid and map projection to the horizontal grid and map projection as defined by TERRAIN. One of parameters needed to be specified is a set of new pressure levels in units of Pascal and were chosen in this thesis to be from 1000 to 97500 Pascal with 2500 Pascal spacing. Third, INTERPF transforms data from the analysis programs to the mesoscale model. It takes output from REGRID or other programs as input to generate a model initial, lateral boundary condition and a lower boundary condition. One of parameters needed to be specified is a set of sigma levels between 0 and 1, and were chosen in this thesis to have 35 sigma levels including 1.00, 0.99, 0.98, 0.97, 0.96, 0.95, 0.94, 0.93, 0.92, 0.91, 0.90, 0.89, 0.88, 0.87, 0.85, 0.83, 0.80, 0.77, 0.74, 0.71, 0.67, 0.63, 0.59, 0.55, 0.50, 0.45, 0.40, 0.35, 0.30, 0.25, 0.20, 0.15, 0.10, 0.05, 0.00. Fourth, MM5 is the numerical weather prediction part of the modeling system. Its options were shown in Table A.2. Fifth, INTERPB transforms data required to go from the mesoscale model on sigma coordinates back to pressure levels. INTERPB interpolates MM5 predictions to pressure levels specified by the user. In this thesis, pressure levels were chosen to be from 1000 to 100000 Pascal with 2500 Pascal spacing.

TABLE A.2
OPTIONS USED IN TERRAIN AND MM5

Option	Domain 1	Domain 2	Domain 3
TERRAIN options			
Number of cells	100*100	190*190	190*190
Cell size (km)	45	15	5
Resolution of terrain height and landuse (km)	19	9	4
Landuse/vegetation/soil category	25-category USGS	25-category USGS	25-category USGS
Nest type	one way	two way	two way
Map projection	Polar stereographic if $\lvert lat_{center}\rvert \geq 60°$, Lambert conformal if $30° \leq \lvert lat_{center}\rvert < 60°$, and Mercator if $\lvert lat_{center}\rvert < 30°$	Polar stereographic if $\lvert lat_{center}\rvert \geq 60°$, Lambert conformal if $30° \leq \lvert lat_{center}\rvert < 60°$, and Mercator if $\lvert lat_{center}\rvert < 30°$	Polar stereographic if $\lvert lat_{center}\rvert \geq 60°$, Lambert conformal if $30° \leq \lvert lat_{center}\rvert < 60°$, and Mercator if $\lvert lat_{center}\rvert < 30°$
MM5 options			
Implicit scheme	Kain-Fritsch 2 [29]	Kain-Fritsch 2 [29]	None
Explicit scheme	Goddard [30]	Goddard [30]	Goddard [30]
Time step (sec)	40	13.33	4.44

Planetary boundary layer scheme	MRF [27]	MRF [27]	MRF [27]
Atmospheric radiation scheme	RRTM [88]	RRTM [88]	RRTM [88]
Surface scheme	Five-layer soil model [89]	Five-layer soil model [89]	Five-layer soil model [89]
Shallow convection	No	No	No

Appendix B

Computer Codes

All computer codes in this thesis are on the computer network of Remote Sensing and Estimation Group (RSEG) at MIT. Descriptions for important codes are given below.

B.1 Validation

B.1.1 Data Sets

Two important data sets used for validation study in this thesis include 1) MM5 domain-2 outputs with AMSU zenith angles, and 2) AMSU data that coincidently overlapped with MM5. MATLAB .mat files for MM5 domain-2 outputs with AMSU zenith angles are in /usr/amsu1/Validation/WORKSPACE/mm5pop/, where the naming system is such that mm5a_July_3.mat and mm5b_July_3.mat are MM5 outputs for case# 3 of July 2002 with AMSU-A and AMSU-B zenith angles, respectively. Each file has a size of 84 MB. AMSU data that coincidently overlapped with MM5 are in /usr/amsu1/Validation/WORKSPACE/precip_data/, where the naming system is such that precip_data_July.mat contains all AMSU data for all 20 cases in July 2002. Each file has a size of ~450MB.

B.1.2 Computer Scripts

There are 3 main scripts for simulating brightness temperatures from MM5 outputs, including tb_sim_11152006.m, superpop_scat_11152006.m, and tbscat.mexglx, which is a MATLAB compiled tbscat.f. All scripts are in /usr/barrett1/surusc/TBSCAT/. tb_sim_11152006.m reads in MM5 inputs described in Section B.1.1, computes F(λ), calls superpop_scat_11152006.m, then saves outputs. superpop_scat_11152006.m prepares all necessary inputs to tbscat.mexglx, i.e., surface emissivity (computed using FASTEM), size and density distributions, etc., and it then calls tbscat.mexglx. dilec5.for and dilec9.for are called by tbscat.mexglx to compute complex dielectric constants for fresh water and fresh-water ice, respectively. sedist.f is called by tbscat.mexglx to compute scattering and extinction from a distribution of spherical drops. These scripts are shown below.

B.1.2.1 tb_sim_11152006.m

```
% coded by Chinnawat Surussavadee on 11/15/2006
% this is to compute Tb's for AMSU using icefactors from DDSCAT

diary on;

addpath /net/ds-0a/raid1/Validation/SCRIPT9/

month{1} = 'July'; month{2} = 'August'; month{3} = 'September'; month{4} = 'October';
month{5} = 'November'; month{6} = 'December';
month{7} = 'January'; month{8} = 'February'; month{9} = 'March'; month{10} = 'April';
month{11} = 'May'; month{12} = 'June';
month{13} = 'Polar'; month{14} = 'Warmrain';

maindir_mm5pop = '/net/ds-01/scratch-0/surusc/Validation/WORKSPACE/mm5pop/';
maindir_tbsim = '/net/ds-01/scratch-0/surusc/Validation/WORKSPACE/tbsim9/';

freq_a=(1/1000)*[23800+72.5 31400+50 50300+50 52800+105 53596+115 54400+105
54940-105 ...
      55500-87.5 89000+1000]';
freq_b=[89.9 150.9 183.31+1 183.31+3 183.31+7]';

m = 1
i = 1

% AMSU-A
ices_amsua = 0.863*freq_a*1e-3 + 0.115;
iceg_amsua = 0.815*freq_a*1e-3 + 0.0112;

for ifreq = 1:9
   freq = freq_a(ifreq);
   icefacts = ices_amsua(ifreq);
   icefactg = iceg_amsua(ifreq);
   icefacti=.917;
   load([maindir_mm5pop 'mm5a_' month{m} '_' int2str(i) '.mat']);
   [tb(:,ifreq),status_o(:,ifreq)] =
superpop_scat_11152006(mm5pop,icefacts,icefactg,icefacti,freq);
end
save([maindir_tbsim 'tba_' month{m} '_' int2str(i) '.mat'],...
   'icefacts','icefactg','icefacti','tb','status_o');
clear mm5pop tb status_o

% AMSU-B
ices_amsub = 0.863*freq_b*1e-3 + 0.115;
iceg_amsub = 0.815*freq_b*1e-3 + 0.0112;

for ifreq = 1:5
```

```
    freq = freq_b(ifreq);
    icefacts = ices_amsub(ifreq);
    icefactg = iceg_amsub(ifreq);
    icefacti=.917;
    load([maindir_mm5pop 'mm5b_' month{m} '_' int2str(i) '.mat']);
    [tb(:,ifreq),status_o(:,ifreq)] =
superpop_scat_11152006(mm5pop,icefacts,icefactg,icefacti,freq);
end
save([maindir_tbsim 'tbb_' month{m} '_' int2str(i) '.mat'],...
    'icefacts','icefactg','icefacti','tb','status_o');
clear mm5pop tb status_o

quit
```

B.1.2.2 superpop_scat_11152006.m

```
% This script is to calculate Tb by using outputs from MM5 model
% as inputs to TBSCAT.
% Scripted by Chinnawat Surussavadee :- 05/24/2004
% Last modified by Chinnawat Surussavadee :- 08/05/2005
% grid points are in a column vector.
function                                   [tb,status_o]                                   =
superpop_scat_11152006(mm5pop,icefacts,icefactg,icefacti,freq);

temp=mm5pop.temp;
qvp=mm5pop.qvp;
clw=mm5pop.clw;
rnw=mm5pop.rnw;
ice=mm5pop.ice;
snow=mm5pop.snow;
graupel=mm5pop.graupel;
ground_t=mm5pop.ground_t;
tseasfc=mm5pop.tseasfc;
u10=mm5pop.u10;
v10=mm5pop.v10;
landuse=mm5pop.landuse;
pressure=mm5pop.pressure;

n_level = 42;
n_radii = 40;
n_point = size(rnw,1);

n_freq = length(freq);

propagate_zenith = mm5pop.zenith_angle;
```

```
ze_ang = mm5pop.zenith_angle;
n_angle = size(ze_ang,2);
[ze_ang,int] = sort(ze_ang,2);
zea = (pi/180)*ze_ang;
sec_ang = sec(zea);

% h=Planck's constant=6.626*10^-34 ; k=Boltzmann's constant=1.38*10^-23
% just use approximate values
tbc=2.736*ones(n_angle,n_freq);
rad=zeros(n_radii,1);

tb_1 = zeros(n_point,n_freq);
tb_2 = zeros(n_point,n_freq);
status_o = zeros(n_point,n_freq);

for yy = 1:n_point
   b = rnw(yy,:)+snow(yy,:)+graupel(yy,:);
   c = find(b~=0);
   i_bottom(yy) = 1;
   if sum(c)~=0
      i_top(yy) = max(c);
   else
      i_top(yy) = 1;
   end
end

% from p = RrT_v
% where T_v = T(1+0.61q_v), p = pressure(Pascal), R = constant = 286.9 (J/kg*K,
% r = density, and T = temperature(K), J = N*m
R = 286.9; % constant value for each gas, p = zeros(n_lat,n_lon);
pp = zeros(n_point,n_level); % initialize p
for i = 1:n_level
   pp(:,i) = 100*pressure(i);
end
T_v = temp.*(1+0.61*qvp/1000); % qvp is g/kg.
den_a = pp./(R*T_v); % air density (kg/m^3)
den_v = qvp.*den_a; % H2O vapor density (g/m^3) => from (g/kg)*(kg/m^3)
den_c = clw.*den_a; % H2O liquid density (g/m^3)
den_r = rnw.*den_a; % rain density (g/m^3)
den_s = snow.*den_a; % snow density (g/m^3)
den_g = graupel.*den_a; % graupel density (g/m^3)
den_i = ice.*den_a; % ice density (g/m^3)

% Use FASTEM to compute surface reflectivities.
bragg=1; % 1 = Calculate Bragg scattering
geom=1;  % 1 = Calculate geometric optics
```

```
foam=1;  % 1 = Calculate foam coverage
ev = zeros(n_point,n_angle,n_freq);
eh = zeros(n_point,n_angle,n_freq);
w10 = sqrt(u10.^2+v10.^2);
r1=zeros(n_point,n_angle,n_freq);
r2=zeros(n_point,n_angle,n_freq);

mask_land = find(landuse~=16)';
emiss_temp1 = rand(size(mask_land));
emiss_temp2 = 0.91+abs(emiss_temp1-.6)/10;
for ml = 1:length(mask_land)
   ev(mask_land(ml),:,:) = emiss_temp2(ml)*ones(1,n_angle,n_freq);
   eh(mask_land(ml),:,:) = emiss_temp2(ml)*ones(1,n_angle,n_freq);
end

mask_ocean = find(landuse==16)';
for i_emiss = 1:length(mask_ocean)
   pt = mask_ocean(i_emiss);
   ang = ze_ang(pt,:);
   Ts = tseasfc(pt);
   wind = w10(pt);
   for i_ang = 1:n_angle
      ang1 = ang(i_ang);
      for i_freq = 1:n_freq
         fq = freq(i_freq);
         [evv,ehh] = fastem(fq,ang1,Ts,wind,bragg,geom,foam);
         if evv<=1
            ev(pt,i_ang,i_freq) = evv;
         else
            ev(pt,i_ang,i_freq) = 1;
         end
         if ehh<=1
            eh(pt,i_ang,i_freq) = ehh;
         else
            eh(pt,i_ang,i_freq) = 1;
         end
      end
   end
end
rv = 1-ev;
rh = 1-eh;
% End FASTEM.

% tic

% Start the big loop for TBSCAT.
```

```
for y = 1:n_point
   sc = sec_ang(y,:)';
   p = pressure;
   ibot = i_bottom(y);
   itop = i_top(y);
   t=temp(y,:)';
   if landuse(y)==16
      ts = tseasfc(y);
   else
      ts = ground_t(y);
   end
   tss(y) = ts;
   v=den_v(y,:)';
   cld = den_c(y,:)';

% From Tao et. al. 1993, drop size distributions for GCE is
% N(D) = No * exp(-lamda*D)
% N(D):m^-4 ; No:m^-4 ; lamda:m^-1 ; D:m
% r_r(density):g*m^-3 ; q_r(mixing ratio):g/g
% qvp:g/kg, r_a = air density (kg/m^3)
%     Nr = 0.08*(10^8); Ns = 0.04*(10^8); Ng = 0.04*(10^8); Ni = 0.0004*(10^8);
   Nr = 0.08*(10^8); Ns = 0.04*(10^8); Ng = 0.04*(10^8); Ni = 0.0004*(10^8);
   r_r = 1*(10^6); r_s = icefacts*(10^6); r_g = icefactg*(10^6); r_i = 0.917*(10^6);

% TBSCAT requires drop dist. specified as mass densities vs. radius
% of the equivalent melted drop.
% from Density_r*Volume_r = Density_s*Volume_s =>  r_eq_s = (0.1^(1/3))*r_s
   rad = zeros(n_radii,1);
   dr = (log10(5*10^-3)-log10(10^-5))/39; % equivalent rain radius
   drr = [log10(10^-5):dr:log10(5*10^-3)]'; % radius is ranged from 10 micrometers to 5
mm.
   rad = (10.^drr)*1000; % radius is in the unit of mm.
   rad_s = rad/(icefacts^(1/3));
   rad_g = rad/(icefactg^(1/3));
   rad_ice = 0.02*ones(size(rad)); % cloud ice has a single size (mono- disperse)
   rad_i = (icefacti^(1/3))*rad_ice;

   n_level1 = itop-ibot+1;
   denr = zeros(n_radii,n_level1);
   dens = zeros(n_radii,n_level1);
   deng = zeros(n_radii,n_level1);
   deni = zeros(n_radii,n_level1);
   d_rnw = den_r(y,:);
   d_snow = den_s(y,:);
   d_graupel = den_g(y,:);
   d_ice = den_i(y,:);
```

```
   i_temp = find(d_rnw~=0.);
      lambda = 0;
      lambda = ((pi*r_r*Nr)./(d_rnw(i_temp))).^(0.25);
      N = Nr*exp(-lambda'*0.002*rad');
      den_pop = N.*(((0.001*rad).^4)*ones(size(i_temp)))';
      denr(:,i_temp)          =          (den_pop.*((d_rnw(i_temp)'./max(sum(den_pop,2),1e-
30))*ones(1,n_radii)))';
   i_temp = find(d_snow~=0.);
      lambda = 0;
      lambda = ((pi*r_s*Ns)./(d_snow(i_temp))).^(0.25);
      N = Ns*exp(-lambda'*0.002*rad_s');
      den_pop = N.*(((0.001*rad_s).^4)*ones(size(i_temp)))';
      dens(:,i_temp)         =         (den_pop.*((d_snow(i_temp)'./max(sum(den_pop,2),1e-
30))*ones(1,n_radii)))';
   i_temp = find(d_graupel~=0.);
      lambda = 0;
      lambda = ((pi*r_g*Ng)./(d_graupel(i_temp))).^(0.25);
      N = Ng*exp(-lambda'*0.002*rad_g');
      den_pop = N.*(((0.001*rad_g).^4)*ones(size(i_temp)))';
      deng(:,i_temp)       =       (den_pop.*((d_graupel(i_temp)'./max(sum(den_pop,2),1e-
30))*ones(1,n_radii)))';
   i_temp = find(d_ice~=0.);
      lambda = 0;
      lambda = ((pi*r_i*Ni)./(d_ice(i_temp))).^(0.25);
      N = Ni*exp(-lambda'*0.002*rad_i');
      den_pop = N.*(((0.001*rad_i).^4)*ones(size(i_temp)))';
      deni(:,i_temp)          =          (den_pop.*((d_ice(i_temp)'./max(sum(den_pop,2),1e-
30))*ones(1,n_radii)))';

   denr = denr(:,2:n_level1);
   dens = dens(:,2:n_level1);
   deng = deng(:,2:n_level1);
   deni = deni(:,2:n_level1);
   r1 = squeeze(rv(y,:,:))';
   r2 = squeeze(rh(y,:,:))';
   [tb1,tb2,stat]=tbscat(t,p,v,cld,ibot,itop,rad,denr,rad,dens,rad,deng, ...
             rad_i,deni,ts,tbc,freq,sc,r1,r2,icefactg,icefacts,icefacti);
   tb_1(y,:) = tb1;
   tb_2(y,:) = tb2;
   status_o(y,:) = stat';
end
% toc

tv = tb_1;
th = tb_2;
zea_mat = propagate_zenith*(pi/180)*ones(1,n_freq);
```

```
tb = ((cos(zea_mat)).^2).*tv+((sin(zea_mat)).^2).*th;
```

B.1.2.3 tbscat.f

This is the FORTRAN code of TBSCAT.

```
      SUBROUTINE TBSCAT(NLEV, TEMP, PRES, H2OVAPOR, CLOUDLIQUID,
     & IBOTTOM, IRAINTOP, NRAIN, NRAIN2, RAINRADIUS_R,
RAINDENSITY_R,
     & RAINRADIUS_S, RAINDENSITY_S, RAINRADIUS_G, RAINDENSITY_G,
     & RAINRADIUS_I, RAINDENSITY_I, TSURF, TBC, FREQ, NANG, SECANT,
     & RV, RH, ICEFACTORG, ICEFACTORS, ICEFACTORI, TBV, TBH, IERR)
C  Copyright (c) 2001 Massachusetts Institute of Technology
C
C  COMPUTES UPWARD-PROPAGATING MICROWAVE BRIGHTNESS
C  TEMPERATURES AT MULTIPLE VIEW ANGLES IN A PLANAR STRATIFIED
C  ATMOSPHERE INCLUDING SPHERICAL DROPS THAT SCATTER.
c
C   P.Rosenkranz - May 22, 2001
C                Aug. 28, 2001 add ice mixture code
c               Aug. 27, 2002 rain density distribution can be matrix
c  CPS          - June 21, 2004 allow different types of precipitation
c               at each level
c  P.Rosenkranz - June 24, 2006 test flags after each call to sedist
c
c  Precipitation occurs in each layer between PRES(IBOTTOM) and
c  PRES(IRAINTOP), with distribution function specified by RAINRADIUS
c  and RAINDENSITY.
c  If TEMP>273.15, precip is assumed to be liquid only;
c  if TEMP<273.15, precip can be supercooled liquid, snow, graupel, or ice
c  and for frozen hydrometeors, the distribution function is adjusted
c  for the ice density given by ICEFACTOR.
C   Supercooled cloud liquid (small non-precip droplets) may occur
c  with temperature below the normal freezing point.
c  Normally IBOTTOM will be at the surface, (i.e.,
c  IBOTTOM=NLEV) but it could be set to other levels for test purposes.
c  CLOUDLIQUID can be set to zeros if not needed.
c  NRAIN2 should either be 1, in which case the same distribution
c  function will be used in all precip layers;
C   or NRAIN2=IBOTTOM-IRAINTOP, to specify separate distributions in
c  each precip layer.
c
      IMPLICIT NONE
C  ARGUMENT SPECIFICATIONS
C   INPUTS
```

```
      INTEGER NLEV        !no. of atmospheric levels
      INTEGER NANG        !no. of angles ( <=MAXANG )
      REAL TEMP(NLEV)     !temperature (K) at each level.
      REAL PRES(NLEV)     !pressure levels (hPa); must be monotonically
c                         increasing.
      REAL H2OVAPOR(NLEV) !H2O vapor density (g/m**3)
      REAL CLOUDLIQUID(NLEV) !H2O liquid density (g/m**3) in small
c           (non-precip) droplets; these are considered non-scattering.
      INTEGER IBOTTOM     !bottom of precip is at PRES(IBOTTOM)
      INTEGER IRAINTOP    !top of precip is at PRES(IRAINTOP)
      INTEGER NRAIN       !no. of elements in RAINRADIUS
      INTEGER NRAIN2      !second dimension of RAINDENSITY
      REAL RAINRADIUS_R(NRAIN)   !values of drop radii (mm); must be >0.
      REAL RAINDENSITY_R(NRAIN,NRAIN2)  !mass density (g/m**3) for raindrops
c                        of radius(i) in layers between PRES(IRAINTOP)
C                        and PRES(IBOTTOM)
      REAL RAINRADIUS_S(NRAIN)  ! melted radii for snow
      REAL RAINDENSITY_S(NRAIN,NRAIN2) ! mass density for snow
      REAL RAINRADIUS_G(NRAIN)  ! melted radii for graupel
      REAL RAINDENSITY_G(NRAIN,NRAIN2) ! mass density for graupel
      REAL RAINRADIUS_I(NRAIN)  ! melted radii for ice
      REAL RAINDENSITY_I(NRAIN,NRAIN2) ! mass density for ice
      REAL ICEFACTORG,ICEFACTORI,ICEFACTORS ! volume filling factors
c           of frozen particles; e.g. 1. for pure ice, 0.4 for graupel
      REAL TSURF          !surface temperature (K)
      REAL TBC(NANG)      !downwelling brightness temperature (K) from
c                       cosmic background or from atmosphere above
c                       highest level in PRES
      REAL FREQ           !frequency (GHz)
      REAL SECANT(NANG)   !secant of propagation angle
c                        (>0 and monotonically increasing)
      REAL RV(NANG)       !surface reflection coefficient at each angle (V-pol)
      REAL RH(NANG)       !surface reflection coefficient at each angle (H-pol)
C   OUTPUTS
      REAL TBV(NANG)      !V-pol brightness temperature (K),
      REAL TBH(NANG)      !H-pol brightness temperature (K) emerging from
c         the atmosphere at the smallest pressure level, at each angle.
      INTEGER IERR        !return code: 0=OK; 1=error in arguments, e.g.
c                 NANG>MAXANG or NRAIN>MAXICE or PRES not increasing,
C                 or RAINDENSITY dimensioned incorrectly;
c                 2=Mie series inaccuracy; 4=Mie series instability;
c                 8=instability in radiative transfer solution
C
C   LIMITATIONS
C   1) POLARIZATION MIXING DUE TO SCATTERING IS NOT CONSIDERED.
```

```
C   2) SPECULAR SURFACE REFLECTION IS ASSUMED. NOTE THAT TB IS NOT
A
C      LINEAR FUNCTION OF SURFACE REFLECTIVITY, DUE TO MULTIPLE
SCATTERING
C      IN THE ATMOSPHERE.
C   3) COMPUTATION INCREASES WITH THE MAXIMUM SECANT VALUE,
AND WITH
C      NANG**3.
C
C   SUBROUTINES CALLED:
C   DILEC5, DILEC9, SEDIST, O2ABS, ABH2O, ABSN2, ABLIQ, TBPS1,
C   DGECO, DGESL
c
c   REFERENCE FOR EQUATIONS: P. W. Rosenkranz, IEEE Trans. Geosci.
C    Rem. Sens.,v.40, pp.1889-1892 (2002)
C
c-------------------------------------------------------------------
c   LOCAL VARIABLES
      INTEGER MAXICE
      PARAMETER (MAXICE=40)
      INTEGER ERR_AC,ERR_ST,ERR_RT,I,LEVEL,INFO,J
      REAL TAV,PAV,WVAV,WLAV,ABSCOEF
      REAL O2ABS,ABH2O,ABLIQ,ABSN2,RG,AB1
      REAL SCATCOEF,EXTCOEF,GDIST,ABPRECIP,DH,SC1
      REAL SUMS_R,SUME_R,SUMG_R
      REAL SUMS_S,SUME_S,SUMG_S
      REAL SUMS_G,SUME_G,SUMG_G
      REAL SUMS_I,SUME_I,SUMG_I
      REAL T_SUMS,T_SUME,T_SUMG
      LOGICAL UNSTABLE,INACC,LAST
      COMPLEX EPS,M
      REAL FAC3
      REAL VOLRADIUS(MAXICE),VOLFRACTION(MAXICE)
c
      IERR = 1
      IF(NRAIN.GT.MAXICE .OR. PRES(NLEV).LE.PRES(1))  RETURN
      IF(NRAIN2.NE.1 .AND. NRAIN2.NE.(IBOTTOM-IRAINTOP)) RETURN
      ERR_AC = 0
      ERR_ST = 0
      ERR_RT = 0
C
C
C  APPLY RT THROUGH LAYERS TO SURFACE
      J = 1
      DO 20 LEVEL=2,NLEV
C  calc. absorption and scattering of layers between levels
```

```
C  (no extinction above the highest level)
C  using average temperature and pressure to compute vertical optical
c  depth of each slab
      TAV = (TEMP(LEVEL) + TEMP(LEVEL-1))/2.
      PAV = SQRT(PRES(LEVEL)*PRES(LEVEL-1))
      WVAV = (H2OVAPOR(LEVEL) + H2OVAPOR(LEVEL-1))/2.
      WLAV = (CLOUDLIQUID(LEVEL) + CLOUDLIQUID(LEVEL-1))/2.
      IF(PAV.LT.PRES(IRAINTOP) .OR. PAV.GT.PRES(IBOTTOM)) THEN
       ABPRECIP = 0.
       SCATCOEF = 0.
       GDIST = 0.
      ELSE
       IF(NRAIN2.GT.1) J = LEVEL - IRAINTOP
       IF(TAV.GT.273.15) THEN
C RAIN ONLY
        CALL DILEC5(EPS,FREQ,TAV)
        M = CSQRT(EPS)
        CALL SEDIST(M,FREQ,NRAIN,RAINRADIUS_R,RAINDENSITY_R(1,J),
     &    T_SUMS,T_SUME,T_SUMG,UNSTABLE,INACC)
        IF(INACC) ERR_AC = 2
        IF(UNSTABLE) ERR_ST = 4
        GDIST = T_SUMG/AMAX1(T_SUMS,1.E-30) !(avoid divide-by-zero)
        SCATCOEF = .75*T_SUMS
        EXTCOEF = .75*T_SUME
       ELSE
C changes made start here
C RAIN
        CALL DILEC5(EPS,FREQ,TAV)
        M = CSQRT(EPS)
        CALL SEDIST(M,FREQ,NRAIN,RAINRADIUS_R,RAINDENSITY_R(1,J),
     &    SUMS_R,SUME_R,SUMG_R,UNSTABLE,INACC)
        IF(INACC) ERR_AC = 2
        IF(UNSTABLE) ERR_ST = 4
C SNOW
        CALL DILEC9(EPS,FREQ,TAV,ICEFACTORS)
        M = CSQRT(EPS)
C        ADJUST ICE DISTRIBUTION TO ACTUAL
        FAC3 = ICEFACTORS**.333333
        DO I=1,NRAIN
         VOLFRACTION(I) = RAINDENSITY_S(I,J)/ICEFACTORS
         VOLRADIUS(I) = RAINRADIUS_S(I)/FAC3
        END DO
        CALL SEDIST(M,FREQ,NRAIN,VOLRADIUS,VOLFRACTION,SUMS_S,
     &    SUME_S,SUMG_S,UNSTABLE,INACC)
        IF(INACC) ERR_AC = 2
        IF(UNSTABLE) ERR_ST = 4
```

```
C GRAUPEL
          CALL DILEC9(EPS,FREQ,TAV,ICEFACTORG)
          M = CSQRT(EPS)
C         ADJUST ICE DISTRIBUTION TO ACTUAL
          FAC3 = ICEFACTORG**.333333
          DO I=1,NRAIN
           VOLFRACTION(I) = RAINDENSITY_G(I,J)/ICEFACTORG
           VOLRADIUS(I) = RAINRADIUS_G(I)/FAC3
          END DO
          CALL SEDIST(M,FREQ,NRAIN,VOLRADIUS,VOLFRACTION,SUMS_G,
    &     SUME_G,SUMG_G,UNSTABLE,INACC)
          IF(INACC) ERR_AC = 2
          IF(UNSTABLE) ERR_ST = 4
C CLOUD ICE
          CALL DILEC9(EPS,FREQ,TAV,ICEFACTORI)
          M = CSQRT(EPS)
C         ADJUST ICE DISTRIBUTION TO ACTUAL
          FAC3 = ICEFACTORI**.333333
          DO I=1,NRAIN
           VOLFRACTION(I) = RAINDENSITY_I(I,J)/ICEFACTORI
           VOLRADIUS(I) = RAINRADIUS_I(I)/FAC3
          END DO
          CALL SEDIST(M,FREQ,NRAIN,VOLRADIUS,VOLFRACTION,SUMS_I,
    &     SUME_I,SUMG_I,UNSTABLE,INACC)
          IF(INACC) ERR_AC = 2
          IF(UNSTABLE) ERR_ST = 4
C
          T_SUMS = SUMS_R+SUMS_S+SUMS_G+SUMS_I
          T_SUME = SUME_R+SUME_S+SUME_G+SUME_I
          T_SUMG = SUMG_R+SUMG_S+SUMG_G+SUMG_I
          SCATCOEF = .75*T_SUMS
          EXTCOEF = .75*T_SUME
          GDIST = T_SUMG/AMAX1(T_SUMS,1.E-30)
C
C end changes made
        ENDIF
        ABPRECIP = AMAX1((EXTCOEF-SCATCOEF) ,0.)
      ENDIF
      ABSCOEF = ABPRECIP + O2ABS(TAV,PAV,WVAV,FREQ) +
    &   ABH2O(TAV,PAV,WVAV,FREQ) + ABSN2(TAV,PAV,FREQ) +
    &   ABLIQ(WLAV,FREQ,TEMP)
      RG = .0293*(1. + .00174*WVAV*TAV/PAV)
      DH = RG*TAV*ABS(ALOG(Pres(LEVEL)/Pres(LEVEL-1)))
      AB1 = ABSCOEF*DH
      SC1 = SCATCOEF*DH
      LAST = LEVEL.EQ.NLEV
```

```
       CALL TBPS1(LAST,NANG,RV,RH,TSURF,TBC,TEMP(LEVEL-1),
     &  TEMP(LEVEL),AB1,SC1,GDIST,SECANT,TBV,TBH,INFO)
       IF(INFO.LT.2) GOTO 30
20     CONTINUE
30     CONTINUE
      IF(INFO.EQ.-1) RETURN
      IF(INFO.EQ.1) ERR_RT = 8
      IERR = ERR_AC + ERR_ST + ERR_RT
      RETURN
      END
```

B.1.2.4 dilec5.for

```
      SUBROUTINE DILEC5 (EPS,FREQ,TEMP)
C   COMPUTES THE COMPLEX DIELECTRIC CONSTANT FOR FRESH WATER
      IMPLICIT NONE
c     ARGUMENTS (OUTPUT):
      COMPLEX EPS ! DIELECTRIC CONSTANT
c     ARGUMENTS (INPUT):
      REAL  FREQ ! (GHZ)  (VALID FROM 0 TO 1000 GHZ)
      REAL  TEMP ! WATER TEMPERATURE  (KELVIN)
C
C    REFERENCES:
C    LIEBE, HUFFORD AND MANABE, INT. J. IR & MM WAVES V.12, pp.659-675
C     (1991);  Liebe et al, AGARD Conf. Proc. 542, May 1993.
c
C    REVISION HISTORY:
C       PWR 8/3/92   original version
c       PWR 12/14/98 temp. dependence of EPS2 eliminated to agree
c                  with MPM93
C       PWR 10/4/99  pulled out dielectric section from abliq
c       pwr 8/22/02  use exponential dep. on T, eq. 2b instead of eq. 4a
C
      REAL THETA1,EPS0,EPS1,EPS2,FP,FS
      THETA1 = 1.-300./TEMP
      EPS0 = 77.66 - 103.3*THETA1
      EPS1 = .0671*EPS0
      EPS2 = 3.52                ! from MPM93
cc      FP = (316.*THETA1 + 146.4)*THETA1 +20.20  ! eq.4a
      FP = 20.1*EXP(7.88*THETA1)  ! from eq. 2b
      FS = 39.8*FP
      EPS = (EPS0-EPS1)/CMPLX(1.,FREQ/FP) +
     & (EPS1-EPS2)/CMPLX(1.,FREQ/FS) +EPS2
      RETURN
```

```
      END
```

B.1.2.5 dilec9.for

```
      SUBROUTINE DILEC9 (EPS,FREQ,TEMP,ICEFACTOR)
C     COMPUTES THE COMPLEX DIELECTRIC CONSTANT FOR FRESH-WATER
ICE
C     IN AN AIR MATRIX
C     P.ROSENKRANZ, 6/1/04
C
      IMPLICIT NONE
C
c     ARGUMENTS
c     INPUTS:
      REAL  FREQ ! (GHZ)  (VALID FOR .001 TO 1000 GHZ)
      REAL  TEMP ! TEMPERATURE  (KELVIN) (VALID RANGE 233-273)
      REAL ICEFACTOR ! volume filling factor of ice material;
c                    e.g. 1. for pure ice, 0.4 for graupel
C     OUTPUT:
      COMPLEX EPS ! DIELECTRIC CONSTANT (DEFINED WITH NEGATIVE
C                 IMAGINARY PART)
C
C     REFERENCE FOR ICE DIELECTRIC CONSTANT:
C     G. HUFFORD, INT. J. IR & MM WAVES V.12, pp.677-682 (1991).
C     REFERENCES FOR MIXING THEORY:
c     A. SHIVOLA, IEEE TRANS. GEOSCI. REM. SENS. V.27, PP.403-415 (1989),
C     K. KARKKAINEN, A. SHIVOLA, K. NIKOSKINEN, IEEE TRANS. GEOSCI.
REM.
C      SENS. V.39, PP.1013-1018 (2001).
c
C     LOCAL VARIABLES
      REAL THETA,ALPHA,BETA,EPSI
      REAL NU,B,C,EPSREAL,EPSIMAG
C
      THETA = 300./TEMP - 1.
      ALPHA = (50.4E-4 + 62.E-4*THETA)*EXP(-22.1*THETA)
      BETA = (.502E-4 - .131E-4*THETA)/(1.+THETA) +
     & .542E-6*((1.+THETA)/(THETA+.0073))**2
      EPSI = ALPHA/FREQ + BETA*FREQ
C
C     Shivola's raisin-pudding model for ice (epsilon 3.15) in air matrix
      NU = ICEFACTOR*(2.5*ICEFACTOR -3.55) + 2.35
      B = 5.15 - 2.*NU - 2.15*ICEFACTOR*(1.+NU)
      C = 5.15 - NU + 2.15*ICEFACTOR*(2.-NU)
      EPSREAL = .5*(SQRT(B*B + 4.*NU*C) -B)/NU
```

```
      EPSIMAG = EPSI*((1.-EPSREAL) +
     & ICEFACTOR*(EPSREAL + 2. + NU*(EPSREAL-1.))) /
     & (5.15 + 2.*NU*(EPSREAL-1.) - ICEFACTOR*(1.+NU)*2.15)
      EPS = CMPLX(EPSREAL,-EPSIMAG)
      RETURN
      END
```

B.1.2.6 sedist.f

```
      SUBROUTINE SEDIST(M,FREQ,NRAD,RADIUS,DENSITY,SUMS,SUME,
     & SUMG,UNSTABLE,INACC)
C
C     SCATTERING AND EXTINCTION FROM A DISTRIBUTION OF SPHERICAL
DROPS
C     SPECIFIED AS A DIFFERENTIAL VOLUME-FRACTION FUNCTION OF
RADIUS
C     11/3/00 P.ROSENKRANZ
c     8/28/01 pwr - revised comments
c     June 21,2004  CPS - allow different types of precip at a given level
c     June 26,2006  PWR - revised comments
C
      IMPLICIT NONE
c
C   ARGUMENT SPECIFICATIONS
C    INPUTS
      COMPLEX M ! index of refraction for drop material
      REAL FREQ ! GHz
      INTEGER NRAD ! number of elements in radius and density vectors
      REAL RADIUS(NRAD) ! values of radii (mm) (> 0)
      REAL DENSITY(NRAD) ! volumetric density (cm**3/m**3) occupied by
c              drops of radius(i) (= fractional volume *10**6)
C    OUTPUTS
C
      REAL SUMS
      REAL SUME
      REAL SUMG
! SCATTERING COEFFICIENT (NEPERS/KM) = .75*SUMS
! EXTINCTION COEFFICIENT (NEPERS/KM) = .75*SUME
! SCATTERING ASYMMETRY FACTOR FOR THE DISTRIBUTION =
SUMG/SUMS
c     Range -1 (backward scattering) to +1 (forward scattering);
c      0 is isotropic scattering
      LOGICAL UNSTABLE ! sum of L1 flags from KSPH
      LOGICAL INACC    ! sum of L2 flags from KSPH
C----------------------------------------------------------------
```

```
c subroutine called: KSPH
C
C    LOCAL VARIABLES
     REAL X,KSC,KEX,G,SC,EX
     LOGICAL L1,L2
     INTEGER I
C
     SUMS = 0.
     SUME = 0.
     SUMG = 0.
     UNSTABLE = .FALSE.
     INACC = .FALSE.
C
     DO 10 I=1,NRAD
      IF(DENSITY(I).LE.0.) GOTO 10
C     COMPUTE INTEGRANDS
      X = 6.283185*RADIUS(I)*FREQ/300.
      CALL KSPH(X,M,KSC,KEX,G,L1,L2)
      UNSTABLE = UNSTABLE .OR. L1
      INACC = INACC .OR. L2
      SC = KSC*DENSITY(I)/RADIUS(I)
      EX = KEX*DENSITY(I)/RADIUS(I)
      SUMS = SC +SUMS
      SUME = EX +SUME
      SUMG = SC*G + SUMG
10   CONTINUE
     RETURN
     END
```

B.2 Program AP (AMSU Precipitation Retrieval)

This program retrieves surface precipitation rates [mm/h], water-paths [mm] for rain water, snow, graupel, and the sum of water, snow, and graupel, cloud liquid water, and peak vertical wind [m/s] from AMSU observations. This version of AP works with AMSU aboard NOAA-15, -16, and -17.

The program was written in MATLAB and it performs retrievals orbit by orbit. The retrieval is 15-km resolution, which is the resolution of AMSU-B FWHM at nadir. It took ~24 sec to retrieve all parameters described above for an AMSU orbit using a conventional 2.8-GHz PC. The program does not require much memory. Inputs required by the program are AMSU-A and AMSU-B orbit data that could be found from http://www.class.noaa.gov/. The main program to run and plot out surface precipitation rate estimates is AP_plot.m, which will call AP.m to perform retrievals. All necessary files, i.e., neural networks, scripts for surface classification and brightness perturbation, etc., are in /usr/barrett1/surusc/AP/. AP_plot.m and AP.m are shown below.

B.2.1 AP_plot.m

```
% Chinnawat Surussavadee coded on 08/08/2006
% last modified 11/04/2006
% This script is to read in AMSU data, call AP.m for retrievals, and plot outputs

addpath /usr/barrett1/surusc/AP
amsudir = '/usr/barrett1/surusc/AMSU/2002/207/';
amsudir = '/usr/barrett1/surusc/AMSU/2003/051/';

sat_id_amsufile = {'NK', 'NL', 'NM'};
sat_dir = {'N15', 'N16', 'N17'};

% Satellite number: 1 for NOAA-15, 2 for NOAA-16, 3 for NOAA-17
sat_num = 1;

%% Select files for processing
[status files] = unix(['find ' amsudir ...
  ' -name "NSS.AMAX.' sat_id_amsufile{sat_num} '*" -print']);

idx = regexp(files, [amsudir]);

amsuafiles = cell(length(idx),1);

for i=1:(length(idx)-1)
  amsuafiles{i} = files(idx(i):(idx(i+1)-2));
end
amsuafiles{end} = files(idx(end):(end-1));

amsuafiles = sort(amsuafiles);

tmp_a = {};
tmp_b = {};
j=1;
for i=1:length(amsuafiles)
   [status_xxx files_xxx] = unix(['find ' amsudir ' -name "' amsuafiles{i}(36:41) 'B'
amsuafiles{i}(43:77) '*" -print']);
   idx_xxx = regexp(files_xxx,amsudir);
   tmp_xxx = files_xxx(idx_xxx(end):(end-1));
   if ~isempty(tmp_xxx)
      tmp_a{j} = amsuafiles{i};
      tmp_b{j} = tmp_xxx;
      j=j+1;
   end
end
```

```
amsuafiles = tmp_a;
amsubfiles = tmp_b;

% retrieval
for i = 1:length(amsuafiles)
    i
    try
        [orbit,process] = read_amsu(amsuafiles{i},amsubfiles{i});
        if process
                out{i} = AP(orbit);
        end
    end
end

% plot o/p
varlist = {'RR','int_rnw','int_snow','int_graupel','int_precip','int_clw','int_ice','wp'};
for i_var = 1:length(varlist)
    figure;orient landscape;wysiwyg;colormap(zebra);
    axesm('mapprojection', 'bsam', 'maplatlimit', [-90 90], 'maplonlimit', [-180 180], ...
          'grid', 'on', 'plinelocation', 30, 'mlinelocation', 30, ...
          'parallellabel', 'on', 'meridianlabel', 'on', ...
          'plabellocation', 30, 'mlabellocation', 30);
    coast = load('coast');
    plotm(coast.lat,coast.long,'k')
    for i=1:length(out)
        if ~isempty(out{i})
            lat = out{i}.lat;lon = out{i}.lon;
            lat(find(out{i}.status_flag~=0)) = nan;lon(find(out{i}.status_flag~=0)) = nan;
            eval(['tmp = out{i}.' varlist{i_var} '_est;']);
            surfm(lat,lon,tmp);
            set(gca,'CLim',[0.2 10]);colorbar('horiz');

set(gca,'fontsize',17,'fontweight','bold');setm(gca,'fontsize',17,'fontweight','bold');axis off;
            hold on;
        end
    end
end
```

B.2.2 AP.m

```
% Chinnawat Surussavadee coded on 08/08/2006
% last modified 11/04/2006
% This is the main function for AP precipitation retrieval
```

```
function out = AP(orbit)

addpath /usr/barrett1/surusc/AP
nntwarn off;

[surf_class,t_surf] = surface_class_pop9(orbit); % Grody's classification

[num_spots_a num_scans_a] = size(orbit.amsua.lat);
[num_spots_b num_scans_b] = size(orbit.amsub.lat);
num_pixel_a = num_spots_a*num_scans_a;
num_pixel_b = num_spots_b*num_scans_b;

% land/sea flag
load landsea990729
land = double(land);
land_flag = ltln2val(land,topolegend,orbit.amsub.lat,orbit.amsub.lon);

% terrain height
load topo
topo_out = ltln2val(topo,topolegend,orbit.amsub.lat,orbit.amsub.lon);

% ------------------------------------------------------------------------
% AMSU TB's
a = orbit.amsua;
b = orbit.amsub;

tbamsua_50km_angle = [];
bias = [0 0 0 0 0.71 0.63 -3.25 -0.65];
for ch = 1:8
   tbamsua_50km_angle = [tbamsua_50km_angle reshape(a.tb{ch}-
bias(ch),num_pixel_a,1)];
end

tbamsub_15km_angle = [];
for ch = 1:5
   tbamsub_15km_angle = [tbamsub_15km_angle reshape(b.tb{ch},num_pixel_b,1)];
end
zenith_angle_a = reshape(a.satz,num_pixel_a,1);
zenith_angle_b = reshape(b.satz,num_pixel_b,1);

% ------------------------------------------------------------------------
% estimate amsua and amsub tb's at nadir
pa = [tbamsua_50km_angle sec(zenith_angle_a*pi/180)]';
for ch = 1:8
   load(['net_amsua_nadir_ch_' int2str(ch)]);
   pnewn = trastd(pa,meanp,stdp);
```

```
    anewn = sim(net,pnewn);
    est = poststd(anewn,meant,stdt);
    est(find(est<0)) = 0;
    tbamsua_50km_nadir(:,ch) = est;
    clear *newn net meanp stdp meant stdt est
end

pb = [tbamsub_15km_angle sec(zenith_angle_b*pi/180)]';
for ch = 1:5
    load(['net_amsub_nadir_ch_' int2str(ch)]);
    pnewn = trastd(pb,meanp,stdp);
    anewn = sim(net,pnewn);
    est = poststd(anewn,meant,stdt);
    est(find(est<0)) = 0;
    tbamsub_15km_nadir(:,ch) = est;
    clear *newn net meanp stdp meant stdt est
end

for ch = 1:8
    tmp1 = amsua2b(reshape(tbamsua_50km_nadir(:,ch),num_spots_a,num_scans_a));
    tbamsua_15km_nadir(:,ch) = reshape(tmp1,num_pixel_b,1);
end

% ----------------------------------------------------------------------
% find pertamsua
pertamsua_15km_all                                                    =
perturb_02052006(tbamsua_15km_nadir,tbamsub_15km_nadir,num_spots_b,num_scans
_b);

% ----------------------------------------------------------------------
% sea pc's
x = [tbamsua_15km_nadir tbamsub_15km_nadir];
load('pc_sea');
mean_x = repmat(pc.mean_x,size(x,1),1);
x_wo_mean = x-mean_x; % remove mean
pc_sea = (x_wo_mean*pc.coeff);
clear pc x

% land pc's
x = [tbamsua_15km_nadir(:,1:5) tbamsub_15km_nadir(:,[1 2 5])];
load('pc_land');
mean_x = repmat(pc.mean_x,size(x,1),1);
x_wo_mean = x-mean_x; % remove mean
pc_land = (x_wo_mean*pc.coeff);
clear pc x
```

```
% ----------------------------------------------------------------------
% flag

% 1. check for any errors in TB's
tmp = [tbamsua_15km_nadir tbamsub_15km_nadir];
xxx1 = zeros(size(tmp));
xxx1(find(tmp<50 | tmp>400)) = 9999;
xxx2 = sum(xxx1,2);

% 2. check for any errors in TB's
xxx3 = zeros(size(surf_class));
xxx3(find(surf_class==5)) = 9999;
xxx3 = reshape(xxx3,num_pixel_b,1);

% 3. don't use if tbamsua ch. 5 < 242K
t53 = tbamsua_15km_nadir(:,5);
xxx4 = zeros(size(t53));
xxx4(find(t53<242)) = 9999;

% 4. consider only for terrain height satisfying criteria
xxx5 = zeros(size(topo_out));
xxx5(find(topo_out>2000 & abs(orbit.amsub.lat)<60)) = 9999;
xxx5(find(topo_out>1500 & abs(orbit.amsub.lat)>=60 & abs(orbit.amsub.lat)<70)) =
9999;
xxx5(find(topo_out>500 & abs(orbit.amsub.lat)>=70)) = 9999;
xxx5 = reshape(xxx5,num_pixel_b,1);

xxx7 = xxx2+xxx3+xxx4+xxx5;
inx_not_ok = find(xxx7~=0);

% ----------------------------------------------------------------------
% estimate precip separtely land and sea

% land i/p
p_land = [pc_land(:,2) tbamsub_15km_nadir(:,3:4) pertamsua_15km_all
sec(zenith_angle_b*pi/180)]';

% sea i/p
p_sea = [pc_sea(:,[2:5]) pertamsua_15km_all sec(zenith_angle_b*pi/180)]';

inx_land = find(land_flag==1);
inx_sea = find(land_flag==0);

varlist = {'RR','int_rnw','int_snow','int_graupel','int_precip','int_clw','int_ice','wp'};

for i = 1:length(varlist)
```

```
    % land net
    load(['amsu_mm5_' varlist{i} '_land_net']);
    pnewn = trastd(p_land(:,inx_land),meanp,stdp);
    anewn = sim(net,pnewn);
    est_land = poststd(anewn,meant,stdt);
    est_land(find(est_land<0)) = 0;
    clear *newn net meanp stdp meant stdt

    % sea net
    load(['amsu_mm5_' varlist{i} '_sea_net']);
    pnewn = trastd(p_sea(:,inx_sea),meanp,stdp);
    anewn = sim(net,pnewn);
    est_sea = poststd(anewn,meant,stdt);
    est_sea(find(est_sea<0)) = 0;
    clear *newn net meanp stdp meant stdt

    est = zeros(size(land_flag));
    est(inx_land) = est_land;est(inx_sea) = est_sea;
    est(inx_not_ok) = 0;
    eval(['out.' varlist{i} '_est = est;']);
    clear est;
end

% return code
status_flag = zeros(size(out.int_rnw_est));
inx_1 = find(xxx2+xxx3~=0);
status_flag(inx_1) = status_flag(inx_1)+1;
inx_2 = find(xxx4~=0);
status_flag(inx_2) = status_flag(inx_2)+2;
inx_3 = find(xxx5~=0);
status_flag(inx_3) = status_flag(inx_3)+4;
inx_4 = find(surf_class==2 | surf_class==4);
status_flag(inx_4) = status_flag(inx_4)+8;

out.lat = orbit.amsub.lat;
out.lon = orbit.amsub.lon;
out.status_flag = status_flag;
out.tbamsua_15km_nadir = tbamsua_15km_nadir;
out.tbamsub_15km_nadir = tbamsub_15km_nadir;
out.topo = topo_out;
out.land_flag = land_flag;
out.surf_class = surf_class;
out.p_sea = p_sea;
out.p_land = p_land;
out.t_surf = t_surf;
out.inx_not_ok = inx_not_ok;
```

```
out.time = orbit.amsub.time;
out.sdate = orbit.amsub.sdate;
```

Bibliography

[1] C. Surussavadee and D. H. Staelin, “Comparison of AMSU millimeter-wave satellite observations, MM5/TBSCAT predicted radiances, and electromagnetic models for hydrometeors,” *IEEE Trans. Geosci. Remote Sens.*, vol. 44, no. 10, pp. 2667-2678, Oct. 2006.

[2] C. Surussavadee and D. H. Staelin, “Millimeter-wave precipitation retrievals and observed-versus-simulated radiance distributions: sensitivity to assumptions,” *J. Atmos. Sci.*, submitted for publication, 2006.

[3] D. H. Staelin and C. Surussavadee, “Precipitation retrieval accuracies for geo-microwave sounders,” *IEEE Trans. Geosci. Remote Sens.*, submitted for publication, 2006.

[4] C. Surussavadee and D. H. Staelin, “Global Millimeter-Wave Precipitation Retrievals Trained with a Cloud-Resolving Numerical Weather Prediction Model,” *IEEE Trans. Geosci. Remote Sens.*, in preparation for publication, 2006.

[5] C. Surussavadee, D. H. Staelin, V. Chadarong, D. McLaughlin, and D. Entekhabi, “Comparison of NEXRAD, AMSU, AMSR-E, TMI, and SSM/I Surface Precipitation Rate Retrievals over the United States Great Plains,” *J. Hydrometeorology*, in preparation for publication, 2006.

[6] J. Dudhia, D. Gill, K. Manning, W. Wang, and C. Bruyere, (2005, Jan.) *PSU/NCAR Mesoscale Modeling System Tutorial Class Notes and Users’ Guide (MM5 Modeling System Version 3).* [Online]. Available: http://www.mmm.ucar.edu/mm5/documents/tutorial-v3-notes.html

[7] P. W. Rosenkranz, “Radiative transfer solution using initial values in a scattering and absorbing atmosphere with surface reflection,” *IEEE Trans. Geosci. Remote Sens.*, vol. 40, no. 8, pp. 1889-1892, Aug. 2002.

[8] F. J. Wentz, C. Gentemann, and P. Ashcroft, “On-orbit calibration of AMSR-E and the retrieval of ocean products,” *83rd AMS Annual Meeting*, Amer. Met. Soc., Long Beach, CA, 2003. Available: www.remss.com

[9] R. Adler, T. Wilheit, Jr., C. Kummerow, and R. Ferraro. 2004, updated daily. AMSR-E/Aqua L2B Global Swath Rain Rate/Type GSFC Profiling Algorithm V001, March to June 2004. Boulder, CO, USA: National Snow and Ice Data Center. Digital media.

[10] C. Grassotti, R. N. Hoffman, E. R. Vivoni, and D. Entekhabi, “Multiple-Timescale Intercomparison of Two Radar Products and Rain Gauge Observations over the Arkansas—Red River Basin,” Wea. Forecasting, vol. 18, pp. 1207-1229, Dec. 2003.

[11] J. R. McCollum, and R. R. Ferraro, “Next generation of NOAA/NESDIS TMI, SSM/I, and AMSR-E microwave land rainfall algorithms,” *J. Geophys. Res.*, vol. 108, no. D8, pp. 7-1-7-16, Mar 2003.

[12] F. T. Ulaby, R. K. Moore, and A. K. Fung, *Microwave remote sensing: active and passive*, Addison-Wesley Pub. Co., Reading, MA, 1981.

[13] D. Deirmendjian, *Electromagnetic scattering on spherical polydispersions*, American Elsivier Publishing Co., New York, NY, 1969.

[14] B. T. Draine and P. J. Flatau, (2005, Oct. 11), *User Guide for the Discrete Dipole Approximation Code DDSCAT 6.1.*, [Online]. Available: http://arxiv.org/abs/astro-ph/0409262

[15] H. J. Liebe, G. A. Hufford, and T. Manabe, "A model for the complex permittivity of water at frequencies below 1THz," *Inter. J. Infra. and Mill. Waves*, vol. 12, no. 7, pp. 659-675, 1991.
[16] G. Hufford, "A model for the complex permittivity of ice at frequencies below 1 THz," *Inter. J. Infra. and Mill. Waves*, vol. 12, no. 7, pp. 677-682, 1991.
[17] A. H. Shivola, "Self-consistency aspects of dielectric mixing theories," *IEEE Trans. Geosci. Remote Sens.*, vol. 27, no. 4, pp. 403-415, Jul. 1989.
[18] K. Karkainen, A. Sihvola, K. Nikoskinen, "Analysis of a three-dimensional dielectric mixture with finite difference method," *IEEE Trans. Geosci. Remote Sens.*, vol. 39, no. 5, pp. 1013-1018, May 2001.
[19] D. H. Staelin, Receivers, Antennas, and Signals in Communication and Sensing Systems, MIT 6.661 Course Note, Jan. 2005.
[20] J. Lenoble, Radiative Transfer in Scattering and Absorbing Atmospheres: Standard Computational Procedures, A. DEEPAK Publishing Co., Hampton, VA, 1985.
[21] J. Lee, "Blind noise estimation and compensation for improved characterization of multivariate processes", Ph.D. dissertation, Massachusetts Institute of Technology, Department of Electrical Engineering and Computer Science, March 2000.
[22] *Neural Network Toolbox User's Guide*, The Mathworks, Inc., Natick, MA, 1998.
[23] T. Mo, "Prelaunch calibration of the Advanced Microwave Sounding Unit-A for NOAA-K," *IEEE Trans. Microwave Theory Tech.*, vol. 44, no. 8, pp. 1460-1469, Aug. 1996.
[24] R. W. Saunders, T. J. Hewison, S. J. Stringer, and N. C. Atkinson, "The radiometric characterization of AMSU-B," *IEEE Trans. Microwave Theory Tech.*, vol. 43, no. 4, pp. 760-771, Apr. 1995.
[25] H. H. Aumann, M. T. Chahine, C. Gautier, M. D. Goldberg, E. Kalnay, L. M. McMillan, H. Revercomb, P. W. Rosenkranz, W. L, Smith, D. H. Staelin, L. L. Strow, and J. Susskind, "AIRS/AMSU/HSB on the Aqua mission: design, science objectives, data products, and processing systems," *IEEE Trans. Geosci. Remote Sens.*, vol. 41, no. 2, pp. 253-264, Feb. 2003.
[26] C. Muth, P. S. Lee, J. C. Shiue, and W. A. Webb, "Advanced Technology Microwave Sounder on NPOESS and NPP," Proceedings, *IEEE Trans. Geosci. Remote Sens. Symp. 2004*, Anchorage, Alaska, IEEE Geosci. Remote Sens. Soc., pp. 2454-2458, 2004.
[27] S.-Y. Hong, and H.-L. Pan, "Nonlocal boundary layer vertical diffusion in a medium-range forecast model," *Mon. Wea. Rev.*, vol. 124, pp. 2322-2339, 1996.
[28] C. Cohen, "A comparison of cumulus parameterizations in idealized sea-breeze simulations," *Mon. Wea. Rev.*, vol. 130, pp. 2554-2571, 2002.
[29] J. S. Kain, "The Kain-Fritsch convective parameterization: An update," *J. Appl. Meteor.*, vol. 43, pp. 170-181, 2004.
[30] W.-K. Tao, and J. Simpson, "Goddard cumulus ensemble model. Part I: Model description," *Terres., Atmos. Ocea. Sci.*, vol. 4, pp. 35-72, 1993.
[31] J. Reisner, R. J. Rasmussen, and R.T. Bruintjes, "Explicit forecasting of supercooled liquid water in winter storms using the MM5 mesoscale model," *Quart. J. Roy. Meteor. Soc.*, vol. 124, pp. 1071-1107, 1998.
[32] P. Schultz, "An explicit cloud physics parameterization for operational numerical weather prediction," *Mon. Wea. Rev.*, vol. 123, pp. 3331-3343, 1995.

[33] Y.-L. Lin, R. D. Farley, and H. D. Orville, “Bulk parameterization of the snow field in a cloud model,” *J. Clim. Appl. Meteor.*, vol. 22, pp. 1065-1092, 1983.
[34] F. W. Chen and D. H. Staelin, “AIRS/AMSU/HSB precipitation estimates,” *IEEE Trans. Geosci. Remote Sens.*, vol. 41, no. 2, pp. 410-417, Feb. 2003.
[35] P. W. Rosenkranz, “Retrieval of temperature and moisture profiles from AMSU-A and AMSU-B measurements,” *IEEE Trans. Geosci. Remote Sens.*, vol. 39, no. 11, pp. 2429-2435, Nov. 2001.
[36] E. A. Smith, P. Bauer, F. S. Marzano, C. D. Kummerow, D. McKague, A. Mugnai, and G. Panegrossi, “Intercomparison of microwave radiative transfer models for precipitating clouds,” *IEEE Trans. Geosci. Remote Sens.*, vol. 40, no. 3, pp. 541-549, Mar. 2002.
[37] A. G. Voronovich, A. J. Gasiewski, and B. L. Weber, “A fast multistream scattering-based Jacobian for microwave radiance assimilation,” *IEEE Trans. Geosci. Remote Sens.*, vol. 42, no. 8, pp. 1749-1761, Aug. 2004.
[38] G. Liu, “Approximation of single scattering properties of ice and snow particles for high microwave frequencies,” *J. Atmos. Sci.*, vol. 61, pp. 2441-2456, 2004.
[39] P. Bauer, A. Khain, A. Pokrovsky, R. Meneghini, C. Kummerow, F. Marzano, and J. P. Poiares Baptista, “Combined cloud-microwave radiative transfer modeling of stratiform rainfall,” *J. Atmos. Sci.*, vol. 57, no. 8, pp. 1082-1104, 2000.
[40] A. Heymsfield, “Ice crystal terminal velocities,” *J. Atmos. Sci.*, vol. 29, pp. 1348-1357, 1972.
[41] P. V. Hobbs, S. Chang, and J. D. Locatelli, “The dimensions and aggregation of ice crystals in natural clouds,” *J. Geoph. Res.*, vol. 79(15), pp. 2199-2206, 1974.
[42] C. I. Davis, “The ice-nucleating characteristics of various AgI aerosols,” Ph.D. dissertation, Dept. Mech. Eng., Univ. Wyoming, Laramie, 1974. p. 267.
[43] H. J. Liebe, P. W. Rosenkranz, and G. A. Hufford, “Atmospheric 60-GHz oxygen spectrum: new laboratory measurements and line parameters,” *J. Quan. Spec. and Rad. Trans.*, vol. 48, pp. 629-643, 1992.
[44] P. W. Rosenkranz, “Water vapor microwave continuum absorption: a comparison of measurements and models,” *Radio Sci.*, vol. 33, no. 4, pp. 919-928, 1998.
[45] J. L. Schols, J. A. Weinman, G. D. Alexander, R. E. Stewart, L. J. Angus, and A. C. L. Lee, “Microwave properties of frozen precipitation around a North Atlantic cyclone,” *J. Appl. Meteor.*, vol. 38, pp. 29-43, 1999.
[46] L. Zhao, and F. Weng, “Retrieval of ice cloud parameters using the Advanced Microwave Sounding Unit,” *J. Appl. Meteor.*, vol. 41, pp. 384-395, 2002.
[47] S. J. English and T. J. Hewison, “Fast generic millimeter-wave emissivity model,” *Proc. of the Inter. Soc. Opt. Eng.*, vol. 3503, pp. 288-300, Aug. 1998.
[48] F. Karbou, C. Prigent, L. Eymard, and J. R. Pardo, “Microwave land emissivity calculations using AMSU measurements,” *IEEE Trans. Geosci. Remote Sens.*, vol. 43, no. 5, pp. 948-959, May 2005.
[49] M. T. Hagan and M.B. Menhaj, “Training feedforward networks with the Marquardt algorithm,” *IEEE Trans. Neural Net.*, vol. 5, no. 6, pp. 989-993, Nov. 1994.
[50] D. Nguyen and B. Widrow, “Improving the learning speed of 2-layer Neural Networks by choosing initial values of the adaptive weights,” *Proc. of the Inter. Joint Conf. on Neural Net.*, vol. 3, pp. 21-26, 1990.

[51] S. Rosenfeld and N. Grody, "Anomalous microwave spectra of snow cover observed from Special Sensor Microwave/Imager measurements," *J. Geoph. Res.*, vol. 105, no. D11, pp. 14913-14925, Jun. 2000.
[52] R. R. Ferraro, F. Weng, N. C. Grody, L. Zhao, H. Meng, C. Kongli, P. Pellegrino, S. Qiu, and C. Dean, "NOAA operational hydrological products derived from the Advanced Microwave Sounding Unit," *IEEE Trans. Geosci. Remote Sens.*, vol. 43, no. 5, pp. 1036-1049, May 2005.
[53] F. J. Solman, D. H. Staelin, J. P. Kerekes, and M. W. Shields, "A microwave instrument for temperature and humidity sounding from geosynchronous orbit," Proceedings, *IEEE Int. Geosci. Remote Sens. Symp. 1998,* Seattle, WA, IEEE Geosci. Remote Sens. Soc., pp. 1704-1707, 1998.
[54] B. Bizzarri, A. J. Gasiewski, and D. H. Staelin, "Initiative for MW/mm sounding from geostationary orbit," Proceedings, *IEEE Int. Geosci. Remote Sens. Symp.* 2002*,* Toronto, Canada, IEEE Geosci. Remote Sens. Soc., pp. 548-552, 2002.
[55] E. A. Smith, P. Bauer, F. S. Marzano, C. D. Kummerow, D. McKague, A. Mugnai, and G. Panegrossi, "Intercomparison of microwave radiative transfer models for precipitating clouds," *IEEE Trans. Geosci. Remote Sens.,* vol. 40, no. 3, pp. 541-549, Mar. 2002.
[56] M. Grecu, and E. M. Anagnostou, "Overland precipitation estimation from TRMM passive microwave observations," *J. Appl. Meteor.*, vol. 40, no. 8, pp. 1367-1380, Aug. 2001.
[57] P. Bauer, E. Moreau, and S. DiMichele, "Hydrometeor retrieval accuracy from microwave window and sounding channel observations," *J. Appl. Meteor.*, vol 44, no. 7, pp. 1016-1032, Jul. 2005.
[58] A. Tassa, S. D. Michele, A. Mugnai, F. S. Marzano, P. Bauer, J. Pedro, and J. P. V. P. Baptista, "Modeling uncertainties for passive microwave precipitation retrieval: evaluation of a case study," *IEEE Trans. Geosci. Remote Sens.,* vol. 44, no. 1, pp. 78-89, Jan. 2006.
[59] C. Kummerow, W. S. Olson, and L. Giglio, "A simplified scheme for obtaining precipitation and vertical hydrometeor profiles from passive microwave sensors," *IEEE Trans. Geosci. Remote Sens.*, vol. 34, no. 5, pp. 1213-1232, Sep. 1996.
[60] A. J. Gasiewski, and D. H. Staelin, "Statistical precipitation cell parameter estimation using passive 118-GHz O_2 observations," *J. Geophys. Res.*, vol. 94, no. D15, pp. 18,367-18,378, Dec. 1989.
[61] M. S. Spina, M. J. Schwartz, D. H. Staelin, and A. J. Gasiewski, "Application of multilayer feedforward neural networks to precipitation cell-top altitude estimation," *IEEE Trans. Geosci. Remote Sens.,* vol. 36, no. 1, pp. 154-162, Jan. 1998.
[62] R. V. Leslie, and D. H. Staelin, "NPOESS aircraft sounder testbed-microwave: observations of clouds and precipitation at 54, 118, 183, and 425 GHz," *IEEE Trans. Geosci. Remote Sens.*, vol. 42, no. 10, pp. 2240-2247, Oct. 2004.
[63] W. J. Blackwell, J. W. Barrett, F. W. Chen, R. V. Leslie, P. W. Rosenkranz, M. J. Schwartz, and D. H. Staelin, "NPOESS aircraft sounder testbed-microwave (NAST-M): instrument description and initial flight results," *IEEE Trans. Geosci. Remote Sens.,* vol. 39, no. 11, pp. 2444-2453, Nov. 2001.

[64] D. Staelin, J. Kerekes, and F. J. Solman, “Final report of the geosynchronous microwave sounder working group,” prepared for NOAA/NESDIS GOES Program Office by MIT Lincoln Laboratory, Lexington MA, August 22, 1997.
[65] B. Lambrigtsen, S. Brown. T. Gaier, P. Kangaslahti, A. Tanner, W. Wilson, “GeoSTAR: a new payload for GOES-R,” American Meteorological Society Annual Meeting, Jan. 2006.
[66] M. E. MacDonald, private communication.
[67] J. W. Waters, et al., "The Earth Observing System Microwave Limb Sounder (EOS MLS) on the Aura satellite," *IEEE Trans. Geosci. Remote Sens.*, vol. 44, no. 5, 1075-1092, May 2006.
[68] F. J. Solman, private communication.
[69] A. Thompson, J. M. Moran, and G. W. Swenson, Jr., *Interferometry and Synthesis in Radio Astronomy*, John Wiley & Sons, New York, N.Y., 1986, 534 pp.
[70] A. B. Tanner, W. J. Wilson, B. H. Lambrigsten, S. J. Dinardo, S. T. Brown, P Kangaslahti, T. C. Gaier, C. S. Ruf, S. M. Gross, B. H. Lim, S. Musko, and S. Rogacki, "Initial Results of the Geosynchronous Synthetic Thinned Array Radiometer (GeoSTAR)", *Proc. IGARSS*, Denver, CO, USA, August 2006, pp. TBD.
[71] C. Cho and D. H. Staelin, “Cloud clearing of atmospheric infrared sounder hyperspectral infrared radiances using stochastic methods,” *J. Geophys. Res.*, vol. 111, no. D09S18, 2006. DOI: 10.1029/2005JD006013.
[72] D. H. Staelin and F. W. Chen, “Precipitation observations near 54 and 183 GHz using the NOAA-15 satellite,” *IEEE Trans. Geosci. Remote Sens.*, vol. 38, no. 5, pp. 2322-2332, Sep. 2000.
[73] J. P. Hollinger, J. L. Peirce, and G. A. Poe, “SSM/I instrument evaluation,” *IEEE Trans. Geosci. Remote Sensing*, vol. 28, no. 5, pp. 781-790, Sep. 1990.
[74] C. Kummerow, W. Barnes, T. Kozu, J. Shiue, and J. Simpson, “The tropical rainfall measuring mission (TRMM) sensor package,” *J. Atmos. Oceanic Technol.*, vol. 15, pp. 809-817, Jun. 1998.
[75] P. Gloersen, and F. T. Barath, “A Scanning Multichannel Microwave Radiometer for Nimbus-G and SeaSat-A,” *IEEE J. Oceanic Eng.*, vol. OE-2, no. 2, pp. 172-178, Apr. 1977.
[76] AIRS Level 2 Standard Retrieval Data Set [Online]. Available: http://daac.gsfc.nasa.gov
[77] P. W. Rosenkranz, “Rapid radiative transfer model for AMSU/HSB channels,” *IEEE Trans. Geosci. Remote Sensing*, vol. 41, no. 2, pp. 362-368, Feb. 2003.
[78] N. C. Grody, F. Weng, and R. R. Ferraro, “Application of AMSU for obtaining hydrological parameters,” Microwave Radiometry and Remote Sensing of the Earth’s Surface and Atmosphere (P. Pampaloni and S. Paloscia, editors), VSP, pp. 339-352, 2000.
[79] R. Kistler et al., “The NCEP-NCAR 50-year reanalysis: monthly means CD-ROM and documentation,” *Bull. Amer. Meteor. Soc.*, vol. 82, no. 2, Feb. 2001.
[80] T. Kawanishi, T. Sezai, Y. Ito, K. Imaoka, T. Takeshima, Y. Ishido, A. Shibata, M. Miura, H. Inahata, and R. W. Spencer, “The Advanced Microwave Scanning Radiometer for the Earth Observing System (AMSR-E), NASDA’s contribution to the EOS for global energy and water cycle studies,” *IEEE Trans. Geosci. Remote Sens.*, vol. 41, no. 2, pp. 184-194, Feb. 2003.

[81] C. Kummerow, Y. Hong, W. S. Olson, S. Yang, R. F. Adler, J. McCollum, R. Ferraro, G. Petty, D.-B. Shin, and T. T. Wilheit, “The evolution of the Goddard Profiling Algorithm (GPROF) for rainfall estimation from passive microwave sensors,” *J. Appl. Meteor.*, vol. 40, pp. 1801-1820, Nov. 2001.
[82] E. Kalnay, *Atmospheric Modeling, Data Assimilation and Predictability*, Cambridge University Press, 2003.
[83] G. D. Alexander, J. A. Weinman, and J. L. Schols, “The use of digital warping of microwave integrated water vapor imagery to improve forecasts of marine extr4atropical cyclones”, *Mon. Weather Rev.*, vol. 126, pp. 1469-1495, 1998.
[84] C. D. Jones and B. MacPherson, “A latent heat nudging scheme for assimilation of precipitation data into an operational mesoscale mode”, *Meteorol. Appl.*, pp. 269-277, 1997.
[85] K. Puri and G. Holland, “Numerical track prediction models”, in G. Holland (Ed.), *Global Guide to Tropical Cyclone Forecasting*, Bureau of Meteorology Research Center, 2000. [Online]. Available: http://www.bom.gov.au/pubs/tcguide/globa_guide/intro.htm
[86] K. A. Brewster, “Phase-correcting data assimilation and application to storm-scale numerical weather prediction, part i: Method description and simulation testing”, *Mon. Weather Rev.,* vol. 131, pp. 480-492, 2003.
[87] S. Ravela, K. Emanuel, and D. McLaughlin, “Data assimilation by field alignment”, submitted for publication.
[88] E. J. Mlawer, S. J. Taubman, P. D. Brown, M. J. Iacono, and S. A. Clough, “Radiative transfer for inhomogeneous atmosphere: RRTM, a validated correlated-k model for the longwave,” *J. Geophys. Res.*, vol. 102, no. D14, pp. 16663-16682, 1997.
[89] J. Dudhia, “A multi-layer soil temperature model for MM5,” Preprints, The sixth PSU/NCAR Mesoscale Model’s Users’ Workshop, 22-24 July 1996, Boulder, Colorado, pp. 49-50, 1996. [Online]. Available: http://www.mmm.ucar.edu/mm5/mm5v2/whatisnewinv2.html